Development of a biphasic scaffold in the context of rotator cuff repairs

A dissertation submitted to the University of Oxford in partial fulfilment of the requirements for the degree of

Doctor of Philosophy

Rand Tahir Sukkar Alkaissy

St Cross College
Trinity Term 2022

Nuffield Department of Orthopaedics, Rheumatology,
and Musculoskeletal Sciences

Supervisors
Associate Professor Pierre-Alexis Mouthuy,
Associate Professor Sarah Snelling, and Professor Andrew Carr

"It has been an ache and a joy both to look over this big shoulder of mine at all my yesterdays."

- Ethel Waters

Declaration

I certify that this thesis is a true and honest account of my own research, which was conducted ethically, and the results obtained are genuine. Where I have drawn on the work, ideas, and results of others, this has been appropriately acknowledged in this thesis.

Rand Tahir Sukkar Alkaissy

Acknowledgements

At this time of writing, I am five weeks away from submitting my thesis and I think it would take me about that long to thank every person that has contributed, in small and big ways, and that has been a part of my life in Oxford for the past four years. Completing a PhD thesis in normal circumstances is already a major achievement but doing so in the midst of a global pandemic seemed nearly impossible. A big thumbs down and many curse words that are not appropriate for an academic thesis, to Covid-19 and Brexit for the chaos, misery and uncertainty that have clouded the past two years. Having said that, a number of people deserve special thanks for keeping me sane throughout and for guiding me towards the light at the end of the tunnel.

Thank you to my supervisors, Prof Carr, Pierre and Sarah, and Afsie for your encouragement, patience and guidance and your help in completing this thesis, finally! Thank you to Risto, Nicole, Sahand, Claudia and Hamez for being a constant support and for motivating me to push through when I could not possibly see how. Thank you to Zai, who transcended from housemate to life-long friend and lifted me up when I needed it and to Andrew, who believed in me when I did not and who became my home away from home. Thank you to Bets, Emma and Eva for the years of friendship and being my wing women in every sense of the word. Thank you to Sarah, Edyta and Zeynep for all your help in the lab and most importantly your kindness and understanding.

Most importantly, thank you to my parents and my sisters and brother, this is for you.

Thank you Oxford, it has been incredible, and I am ready to close this chapter now.

Table of contents

Abstract

Surgical repair of rotator cuff tears is often inadequate and can lead to re-tearing of up to 40% of surgical cases, and ensuing pain and disability. The reason for surgical failure has often been attributed to the poor intrinsic healing qualities of the tendon itself in combination with a lack of congruence at the bone-tendon interface (enthesis). Despite the advances made with surgical materials and techniques, little progress has been achieved in improving the biological response of torn tendons. Tissue engineering and the development of biomaterials offer promising strategies to support the healing process.

The aim of this thesis was to develop a biphasic biomaterial or scaffold, consisting of a soft electrospun part and a hard 3D printed part, in the context of rotator cuff repairs. Electrospun fibres are promising materials to support tendon healing because they can be designed to resemble the hierarchical architecture of native tendon extracellular matrix. In addition, 3D printed structures have well-known applications in bone-tissue engineering because they can be designed with a similar porosity and pore size to bone matrix. The main objectives will be to create a biphasic scaffold consisting of an electrospun soft cuff and a 3D printed hard block, evaluate the biological activity of the electrospun filaments and set the dimensions of the 3D printed part using anatomical measurements and anonymised medical imaging.

To achieve the biphasic scaffold, a layer-by-layer method to insert pre-assembled bundles of electrospun filaments in the 3D printing process was first used. The resulting scaffold was scaled up to increase its mechanical strength and reach a threshold value of 250N that is of clinical relevance. Second, the cuff component was evaluated against a commercial suture and although there was no difference in cell attachment between them, cells were elongated and spindle-shaped on the former and showed a profile of differentially expressed genes related to development and proliferation, angiogenesis, and extracellular matrix organization. Thirdly, the design of the 3D printed component was improved to fit the geometry of the greater tuberosity of the humerus, using medical imaging, resulting in three prototypes with different fixation methods. The prototypes were tested in a porcine model ex vivo and failure mechanisms were identified using physiologically relevant cyclic loadings.

Future work should focus on automatizing the manufacturing process and on further improving the strength of the biphasic scaffold by changing the cuff design and inserting more filaments. Furthermore, the bioactivity and biocompatibility of the soft and hard components should be evaluated more thoroughly with use of clinically relevant cell types in co-culturing systems or by use of bioreactors. Finally, the designs of the proposed biphasic scaffold need to be evaluated in a model system resembling human anatomy, physiology and biomechanics over a prolonged period of time.

In conclusion, this thesis proposes a novel method for the manufacture of a soft-hard scaffold, using state-of-the-art tissue engineering biomaterial technologies, electrospinning and 3D printing. While it shows potential for rotator cuff tendon repair, this work also contributes to the wider research community investigating multiphasic scaffolds for various clinical applications.

Abbreviations

3D	Three-dimensional
ß-TCP	Beta tri-calcium phosphate
CAD	Computer-aided design
CSA	Cross-sectional area
DEG	Differentially expressed genes
DMEM	Dulbecco's Modified Eagle Medium
DNA	Deoxyribonucleic acid
DSC	Differential scanning calorimetry
ECM	Extracellular matrix
EMA	European Medicines Agency
ES	Electrospun
FBR	Foreign body response
FBS	Fetal bovine serum
FDA	Food and Drug Administration
FIU	Fluorescence intensity unit
FDM	Fused deposition modeling
FW	FiberWire
GSEA	Gene set enrichment analysis
HA	Hydroxyapatite
HFIP	1,1,1,3,3,3-hexafluoro-2-propanol
ISO	International Organization for Standardization
lfc	$\log_2$ fold change
µCT	Micro-computed tomography
MHRA	Medicines and Healthcare products Regulatory Agency
MSC	Mesenchymal stem cell
N	Newton
NGS	Next-generation sequencing
NHS	National Health Service
NRU	Neutral red uptake
ORA	Over-representation analysis
P/S	Penicillin/streptomycin
PBS	Phosphate-buffered saline
PCA	Principal component analysis
PCL	Polycaprolactone
PDO	Polydioxanone
PEEK	Polyether ether ketone
PLA	Polylactic acid
PLGA	Polylactic-co-glycolic acid
RCT	Rotator cuff tear
RNA	Ribosomal nucleic acid
ROM	Range of motion
SEM	Scanning electron microscopy
TCP	Tissue culture plastic
UK	United Kingdom
USA	United States of America

List of figures and tables

Preface

This thesis aims to propose a novel soft-hard construct for rotator cuff repair applications using two well-known scaffolding techniques, namely electrospinning and 3D printing, which are both used to create scaffolds that are used clinically. This construct will ideally have sufficient strength to support tendons during healing and will provide biophysical cues at the microscale to influence cell behaviour. It will also have dimensions that are relevant to a clinical setting, e.g., to fit an anatomical location, and have handling properties that are suitable for surgeons and existing surgical equipment. Its composition will involve synthetic polymers that have been previously used in devices cleared by the Food and Drug Administration (FDA).

In the first chapter, an overview of the shoulder and its macro- and microanatomy, specifically the rotator cuff, will be presented and the response of tendons to injury on a molecular level will also be described. Treatment options for tendon tears, non-surgical and surgical, will be briefly outlined, including what materials are commonly used as suture anchors. Shortcomings of current approaches will be highlighted with the focus on tissue engineering as an emerging discipline that can offer solutions to the lacking biological activity of commercial suture anchors. Electrospinning and 3D printing, the fabrication techniques central to this thesis, will also be introduced. In the second chapter, electrospinning will be used to create submicron polydioxanone fibres that are assembled into bundles and stacked into 3D printed polycaprolactone blocks using a layer-by-layer method. The ultimate load to failure as well as the scale-up potential of these constructs will be evaluated. In the third chapter, the cell response to electrospun sutures and a commercial

equivalent will be compared using a cell viability assay, electron miscroscopy and high-throughput sequencing. Computational analysis is performed to elucidate differences in genetic expression between the two materials and to contextualize functional pathway enrichments. In the fourth chapter, the design of the 3D printed hard block is investigated to approximate the geometry of the greater tuberosity of the humerus. Three design variations will be presented including their method of fixation, using a porcine bone model, and failure mechanism when subjected to cyclic and static load. This will be compared to the failure mechanisms and mechanical properties of currently used sutures in rotator cuff repair.

Finally, in the last chapter, overall discussion points are considered alongside the contribution of this thesis to the development of a soft-hard biphasic construct, including general limitations and potential endeavours for future work.

Chapter 1 Introduction

1.1 The significance of rotator cuff tears

Rotator cuff tears (RCT) are a significant cause of shoulder pain with negative consequences in the global work force, but also in sports-related activities and daily life resulting in a loss of overall productivity (*1*). Over 460,000 rotator cuff repairs are done annually in the United States, expected to surpass 570,000 by 2023, making them the second most common orthopaedic soft tissue repair procedure performed after hip arthroscopies (*2*), see Section 1.3.2 on treatment modalities. The cost of repair is rising significantly as well, which means an increase in pressure on health services (*3*). The estimated annual costs of rotator cuff surgery in the United States was reported to be $1.2-1.6 billion, whereas in the United Kingdom the total cost in the NHS has been reported to be over £60 million (*4*). With a population that continues to age it is expected that the severity of RCTs will be worse, including the pain and disability experienced. Small rotator cuff tears can sometimes be treated conservatively with adequate physiotherapy. However, tears often progress in size leading to a decline in muscle quality and fatty degeneration which hinder a successful surgical outcome (*5-7*). Another important reason for early surgical intervention is to limit pain and prevent shoulder arthropathy, which could lead to further disability. A commonly used approach to repair RCTs is using suture anchors to fix the tendon to the bone. The details of surgical intervention are presented in Section 1.3. This intervention restores some of the function but does little to support the tissues in healing and regeneration, this can lead to re-rupture of the tendon causing poor functional outcomes (*8*), see Section . Indeed, failure rates have been reported to be between 13-94% (*8*). Conversely, the success rate in hip and knee total joint replacements has been reported to be over 90% with follow-ups of over 10

years after implantation (*9*). It therefore begs the questions of what makes RCT repair outcomes so much worse and what can be done to improve it? Different failure mechanisms have been described that range from suture anchor properties to inadequate tissue healing to different modes of rehabilitation (*10, 11*). Rotator cuff surgeries were first performed in the 1980s by Neer et al and despite a considerable increase in research and advances in surgical materials and techniques over the years, the rate of surgical success has not improved significantly (*12*). The pain, disability, and strain that RCT cause on health care systems is only set to increase and neither surgical nor conservative treatment currently result in acceptable long-term outcomes for patients with re-tears of their rotator cuff (*13*). Much research is currently being devoted to tissue engineered scaffolds that focus on the biology and regenerative abilities of the native tissues. Indeed, the mechanical superiority of clinically used sutures and anchors has been proven many times (*14*), but this is fruitless in case of impaired healing of the tendon, and it is necessary to find a compromise between mechanical strength and biological function.

1.2 The shoulder structure and function

1.2.1 Macroanatomy of the shoulder

The human shoulder consists of three bones: the humerus, scapula and clavicle that articulate to create movement. The connection between bones are joints and the shoulder consists mainly of the glenohumeral (GH) joint – a ball and socket joint which gives it a wide range of motion. It connects the head of the humerus to the shallow socket of the scapula called the glenoid fossa (i.e. cavity). To increase its depth and provide more stability for the humerus, the glenoid fossa is surrounded by fibrocartilaginous tissue around its margin. This is a soft, rubbery tissue called the glenoid labrum. Other important joints in the shoulder are between the scapula and clavicle (acromioclavicular, AC), the clavicle and sternum (sternoclavicular, SC) and the scapula and thorax (scapulothoracic, ST). The shoulder joint is kept stable by the

organization of soft tissues that prevent dislocation of the bones, e.g. a forceful pull in the wrong direction could cause the humerus to be popped out of its socket. These soft tissues include muscles, tendons, and ligaments. The most important muscles contributing to shoulder movement and stability are the supraspinatus, infraspinatus, teres minor and subscapularis, all originating from the scapula and inserting onto the proximal humerus. Their tendons pass over the GH joint and come together in a musculotendinous collar that wraps around the humeral head. This is the rotator cuff and is the site of rotator cuff tears and injuries. These muscle-tendon units perform abduction and rotation of the shoulder, accounting for a significant part of the shoulder's total ROM. Indeed, the supraspinatus muscle is responsible for initiating abduction (i.e., moving the arm away from the body), and damage to this muscle or tendon can have a significant impact on activities in daily life. Figure 1.1 gives an overview of the described structures in an anterior and posterior view. Figure 1.1D gives a superior view of the humeral head with the attachment of the supraspinatus and infraspinatus tendons highlighted on the greater tuberosity.

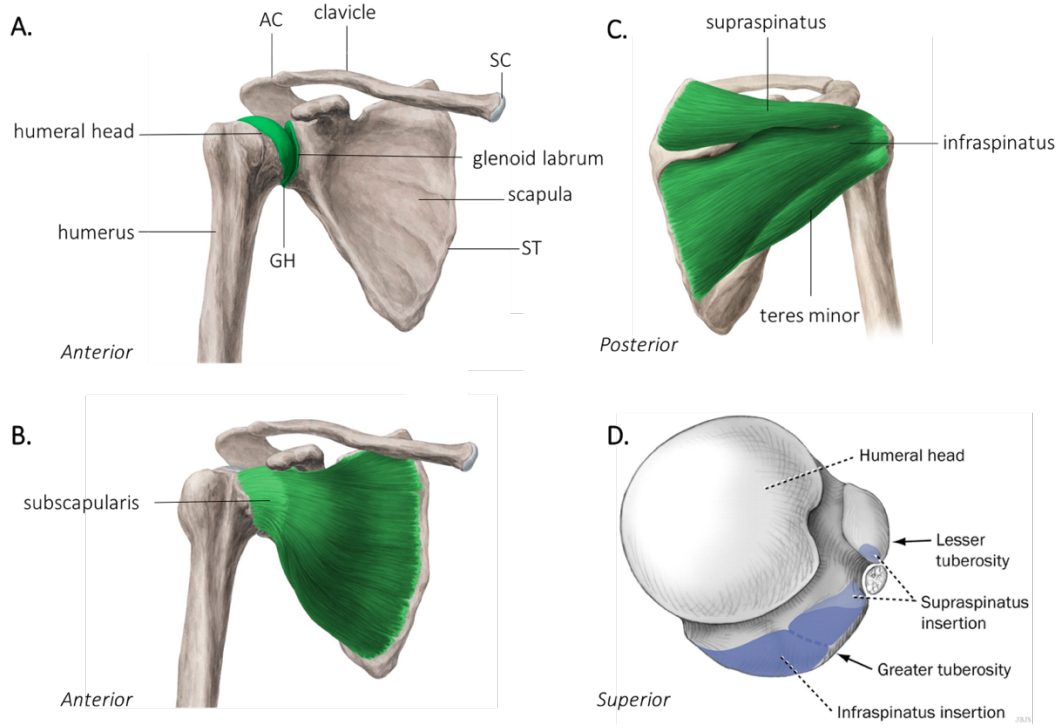

Figure 1.1 Musculoskeletal landmarks for the rotator cuff of the shoulder. For clarity, other structures in the shoulder are not visualized here. Images A-C adapted from Kenhub (*15*), and image D reprinted from Mochizuki et al (*16*) with permission from Wolters Kluwer Health, Inc.

1.2.2 The rotator cuff tendon and footprint

Tendons form the attachment between muscle and bone and move the joints by transmitting force. Rotator cuff tears occur in the tendons that insert onto the humerus and mostly happen at the interface of tendon to bone, called the enthesis (*17*). The mechanisms underlying rotator cuff tears are discussed in section 1.3.1. To understand more about the impact of damage it is necessary to take a closer look at the anatomy of the tendon and enthesis. The focus will be on the supraspinatus tendon as this is the one most commonly injured. The attachment of rotator cuff tendons on the humeral head is also known as the 'rotator cuff footprint' and has been the subject of many cadaveric studies, causing conflicting statements about the footprint structure and its dimensions (see Table C.1, Appendix C). This could be attributed to several reasons. Information about the cadaveric specimens in these studies mostly include age and sex at the time of passing. The age range is quite significant, since most specimens are from older donors (>60 years old). Most authors checked their specimens for gross anomalies and often had prior medical history at hand to be able to exclude those with rotator cuff tears, bony irregularities, or osteoarthritis. Some studies commented on the racial distribution of their specimens but considering the scarcity of human donors in many places this was often not a priority. No study commented on former occupation status or level of athleticism, which is undeniably useful information but cannot be made available to preserve the donors' identity (*18*). Although most authors measured the tendons using similar methods and reference points, the range of measurements is still quite broad. This can be caused by anything from the differences in specimens, to how these were preserved, prepared, and dissected and which specific instruments were used. More detail about this is presented in Chapter 4. However, clinicians and scientists alike do agree that the tendons of the rotator cuff overlap significantly as they insert onto the tuberosities of the humerus (*16, 19, 20*). About 15 mm proximal to the insertion, the supraspinatus and infraspinatus tendons

join to form a common attachment on the greater tuberosity of the humeral head (*19, 21*), see Figure 1.1D. The tendon of the supraspinatus has been described as consisting of an anterior 'strap-like' and a posterior 'rope-like' portion that consist of collagen fibres packed together in primary bundles (sub fascicle) that are grouped into secondary bundles (fascicle) and are then collated into tertiary fibre bundles (*22*). The tendon is made up of these collected tertiary fiber bundles and are surrounded by a loose connective tissue called the epitenon. All these bundles run parallel to the axis of muscle tension (*22*). The wrapping of the bundles in connective tissue (epitenon and endotenon) allows the individual bundles to slide past each other and transfer mechanical load between fibrils (*23*). This hierarchical architecture of tendon makes it particularly well suited to withstand high forces (Figure 1.2).

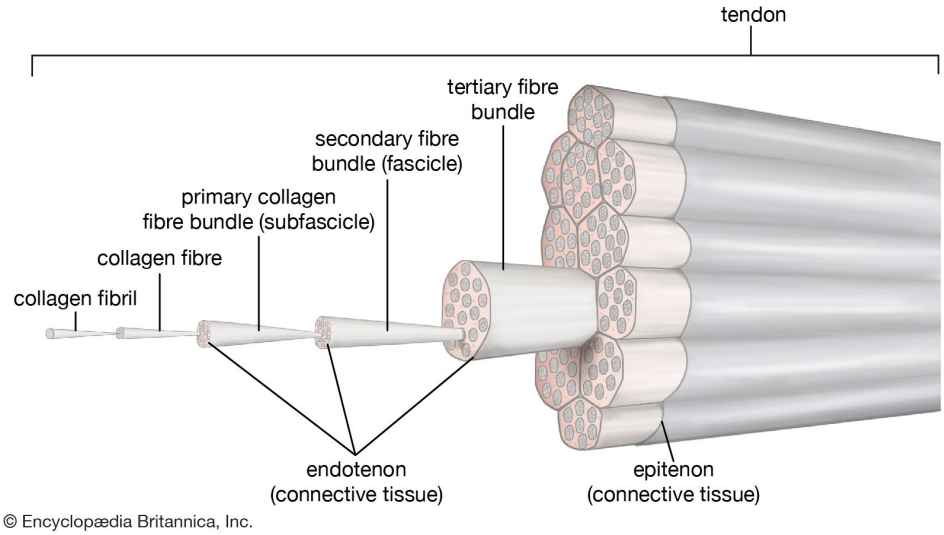

Figure 1.2 The hierarchical structure of a tendon. Image reprinted from Encyclopaedia Britannica with permission specified in Section 1: 'Use of Content' in the Terms of Use (*24*).

1.2.3 The tendon on a molecular level

Tissues and organs are composed of cells which are held together by the extracellular matrix (ECM) – a 'physical scaffolding' (*25*). The composition of the ECM is tissue-specific, but inherently consists of water, proteins, and polysaccharides (*25*). It is a dynamic environment that is continuously being remodelled to support tissue or organ function, development, and repair (*26*). In tendons, the ECM is mainly composed of water, and collagen which accounts

for 60-85% of its dry weight (*27*). Tenocytes, resident fibroblasts that make up tendons, are also embedded in the ECM. Proteoglycans are proteins in the ECM that trap water to lubricate the collagen fibrils as they slide past each other (*28*). Collagen type I, which provides the tendon with its tensile strength (*29, 30*) is the main type that can be found (~95% of collagen). The rest is made up of proteoglycans and other proteins including elastin, and small amounts of inorganic substances (*27*). Collagen type I is a triple helix made up of one α1-chain and two α2-chains, which have a recurring pattern of amino acids responsible for the structure and link of the helix (*31*). Every third position in this motif is occupied by glycine (Gly), which acts as the stabilizer and brings the chains close together (*27*). The strength in the collagen comes from proline, which causes kinks in the individual chains and forces a left-handed confirmation of the helix which increases potential crosslinking and binding sites. The third amino acid is lysine, which causes further crosslinking by hydroxylation, increasing the strength even more. The collagen helices then self-assemble into fibrils, once they have been discharged into the extracellular space, which form the building block of tendon, see Figure 1.3 (*27, 32*). Macroscopically, tendon is a white tissue, due to its avascular state which is an important contributor to its poor repair capabilities.

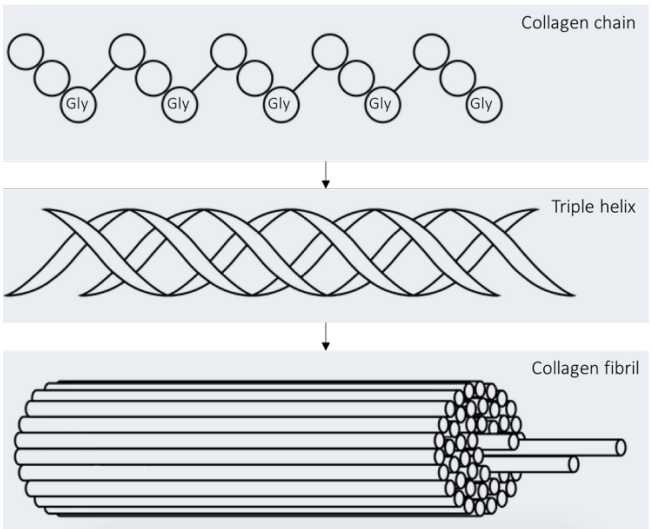

Figure 1.3 The structure of collagen type I. Figure adapted from Sana Amsterdam(*33*).

The cells within the matrix are called tenocytes, or tendon fibroblasts and constitute less than 5% of the volume of tendon tissue (*34*), which makes repair and remodelling quite challenging, see Section 1.3.1. They are located between the parallel chains of collagen fibrils where they produce ECM (*35*). However, this is a slow process as they are sparsely distributed and proliferate at a low rate (*36*), in addition to having only a small number of tendon-progenitor stem cells in the matrix (*35*), this makes healing and regeneration of tendon tissue particularly difficult (*35*). Tenocytes are terminally differentiated fibroblast that are highly elongated in shape and sensitive to extracellular cues to communicate with each other and produce and maintain tendon matrix (*27, 37, 38*).

Tenocytes attach to the ECM through integrin receptors which are transmembrane proteins that link the actin cytoskeleton of the cell to specific ECM components (e.g., fibronectin) (*39, 40*). During cell migration, focal complexes form through these integrins upon first contact with the ECM (*39*). The vitronectin receptor is an important integrin that recognizes proteins in the ECM through peptide motifs (*39*). Once the cytoskeleton of a cell is anchored, a clustering of integrins occurs that matures the focal complex into focal adhesions (*40*). Focal adhesions are reliant on mechanical stress signals for their maturation and maintenance (*39*) and once contact is established, integrins can mediate signalling by inside-out and outside-in pathways, the latter which is involved in many fundamental cellular processes (*41*). If a cell fails to attach to the ECM or lose contact to it, it will undergo apoptosis (*40*). Indeed, the cytoskeleton of the tenocyte is responsible for maintaining homeostasis within the tendon by continuously communicating to the ECM via the integrins (*42*).

1.2.4 The interface between tendon and bone

The enthesis is the insertion of the tendon into bone and has an important role in the transmission of mechanical forces during motion (*43*). It is made up of four different zones in the longitudinal direction: bone (IV), calcified fibrocartilage (III), uncalcified fibrocartilage (II) and tendon (I), each with their respective cell populations (*44, 45*). The mineralisation of the enthesis increases towards the attachment at the bone while collagen fibres become increasingly sparse (Figure 1.4). Bone and tendon are both rich in collagen type I, but the interface between them consists predominantly of collagen type II which, in contrast, is only present in small amounts in bone and tendon (*46, 47*). Indeed, the collagen fibres of the tendon undergo a transformation in composition and geometry before attachment to bone that allows them to unravel and fan out (*46*). This arrangement means that the mechanical properties of the enthesis are different throughout the enthesis zones which makes it particularly well suited for transmitting forces from tendon to bone. It is often the site of injury (e.g., rotator cuff tears) and due to its poor ability to regenerate, damage can lead to a loss of functionality (*8, 48*). In fact, damage and consequent repair attempts will result in a fibrous construct of disorganised scar tissue that is inferior to the mechanical properties of a healthy enthesis (*43, 49*). This disorganised tissue is most likely due to elevated expression of collagen type III which is not normally present in the enthesis, and may indicate that a remodelling takes place in which the abundant collagen types I and II are replaced by collagen type III (*50, 51*). This is thinner than collagen type I, has been found to be increased at rupture sites of Achilles tendon (*52*) and is associated with a low degree of alignment and inferior mechanical properties (*47*). It was also found that the cells presiding in the enthesis changed their shape and did not align to collagen fibres in a parallel orientation anymore (*51*), this reduces adequate force transmission from bone to muscle and translates in reduced and painful motion. Poor outcomes after rotator cuff tears are perpetuated by the current

surgical techniques where torn tendon is directly fixed to the bone, negating the complicated transitional structure of an enthesis that is so crucial to the overall rotator cuff functionality. To fully understand the interplay between rotator cuff tendon tears and structural damage to the enthesis, the response to injury of tendons will be discussed in the next section.

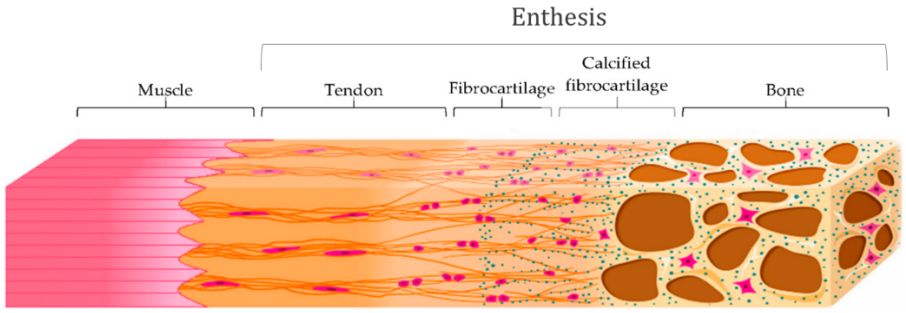

Figure 1.4 A schematic overview of the enthesis as a functional unit in the attachment of tendon to bone. Image adapted from Bianchi et al (*53*) under the Creative Commons Attributions License 4.0.

1.3 Rotator cuff injury

1.3.1 Pathophysiology at the molecular level

Injury to a tendon is referred to as tendinopathy that can be caused by degenerative or traumatic causes and can progress to tendon tears in the absence of treatment (*54*).

The most commonly injured tendon of the rotator cuff muscles is the supraspinatus, which is essential for abduction, with partial involvement of the infraspinatus (*55-57*). Rotator cuff tears are multifactorial but key risk factors for the development of tendinopathy are increased age, smoking (*54*) and repetitive over-use (*58*). Trauma can also occur due to high-energy impact or overuse in overhead athletic activities (*59*). The ECM undergoes changes from a macro- to micro-scale when the tendon is subject to load to facilitate crimping, uncrimping and realignment of the fibres and to allow transfer of strain from the ECM to tenocytes (*60*) via their actin cytoskeletons. Crimp refers to the arrangement of the collagen fibrils in a wavy pattern that buckle and unbuckle during longitudinal loading (*61*). A typical stress-strain curve for a tendon is presented in Figure 1.5 (*62*), in which an initial toe-region represents the stretching of the fibres that increases linearly as the stress increases (linear region). At about

4% strain, i.e. elongation, the collagen fibres lose their crimp and exhibit microscopic failure that progresses into macroscopic failure and eventual tendon rupture beyond 8% strain (*62*). Strain is defined as the difference in the original fibre length and length after being stretched, divided by the original length, e.g. if a fibre measures 1 mm in length and is stretched up to 1.08 mm this would translate as 8% strain. The homeostasis of the tendon is therefore dependent on mechanical feedback loops that range from the macro- to nanoscale and are implicated in rotator cuff tears (Figure 1.6), due to inappropriate mechanical stimulation, and can thus affect transcription and induce different cell responses related to inflammation, migration, proliferation, and differentiation (*63-66*). Damage to tendon fibrils due to high stresses results in a mechanical under-stimulation of the cell cytoskeleton attached to the ECM and can lead to apoptosis of tenocytes, a muted remodelling and ineffective healing response (*60, 67-69*). The actin cytoskeleton maintains its shape and tension by transmitting load through cell surface receptors (*70*). Repetitive overload of the tendon is linked to a difference in cell morphology – with a rounded rather than elongated shape – and an increase in inflammation and ECM degradation markers (*71*). Indeed, there is an increasing amount of evidence indicating a role of inflammation in tendinopathy and the response to injury can be divided into three overlapping stages (*72*): inflammation, proliferation and remodelling. After injury, the acute phase (hours to days) is characterised by the influx of inflammatory cells into the site of injury. Then, in the proliferative phase (weeks to months) fibroblasts start producing collagen so that mechanotransduction can take place. This is also signalled by the release of growth factors (e.g., TGF-β) that stimulate tenocytes to proliferate and synthesise collagen (*73*). In the last phase, remodelling, the newly synthesized collagen fibres cross-link to increase the overall tensile strength of the tendon, in a process that can take up to a year (*74*). The healing process is primarily regulated by matrix metalloproteinases (MMPs) that are responsible for ECM degradation, whereby specific types of MMPs are also responsible

for the degradation or remodelling of collagen (*75*). However, as briefly mentioned before, this remodelling phase results in tendon tissue that is inferior to the healthy tendon, and which is characterised by the disorganised and thinner collagen type III fibres, accumulation of proteoglycans and a decrease in tenocytes (Figure 1.7). The presence of proteoglycans is associated with an increase in water content, contributing to tissue swelling and disruption of the collagen fibre network (*76*).

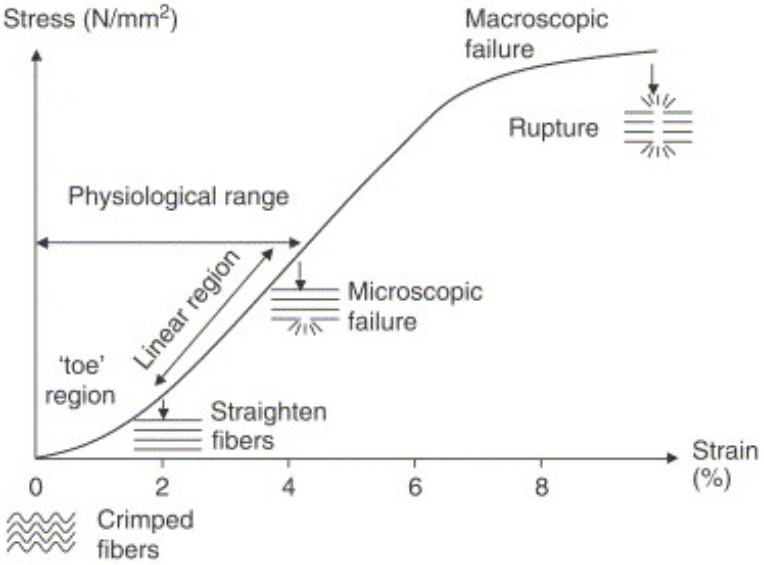

Figure 1.5 Stress-strain relationship in healthy tendon and at the point of failure. Image reprinted from Wang et al (*62*) with permission from Elsevier.

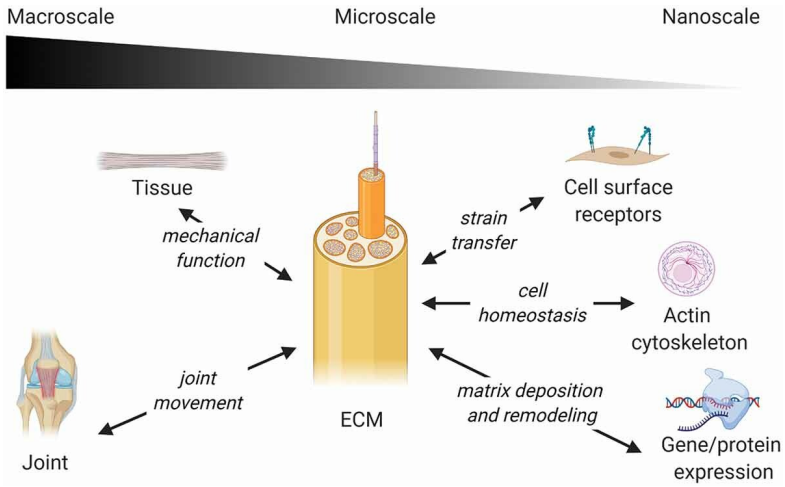

Figure 1.6 Maintenance of tendon homeostasis through multi-scale feedback loops. Image reprinted from Chatterjee et al (*42*) with permission from Taylor & Francis under the Creative Commons Attribution License 3.0

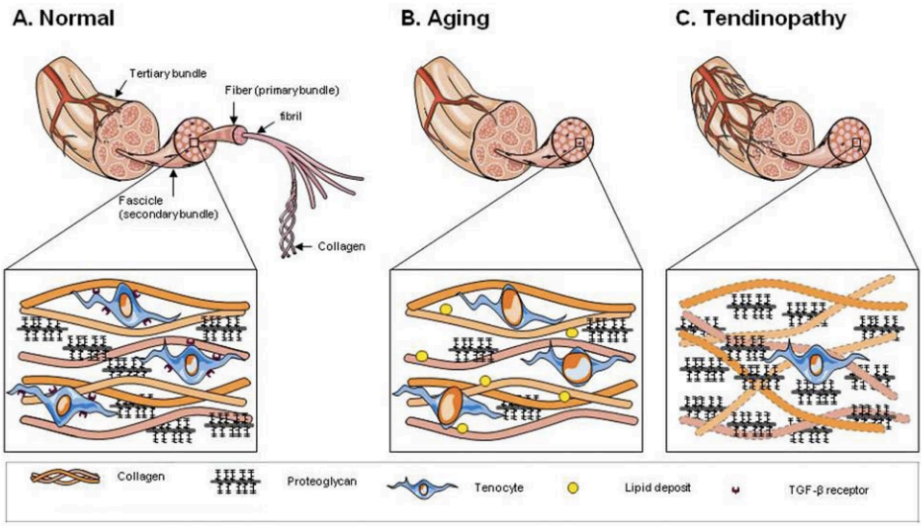

Figure 1.7 Cellular changes in healthy tendon (A) due to aging (B) and disease (C). Figure reprinted from Nourissat et al (*77*) under the Creative Commons Attribution 3.0 License.

1.3.2 Treatment of rotator cuff tears

Patients presenting with complaints of the rotator cuff are most often treated conservatively, especially if it involves an atraumatic presentation. Young and active persons that suffered high-impact trauma are usually treated surgically (*78*). Conservative treatment includes pain relief and rehabilitation through physiotherapy (*79*). Analgesia also includes corticosteroid injections into the glenohumeral joint which have gathered considerable controversy about its efficacy and impact on the tendon tissue (*80-82*). In fact, in a meta-analysis conducted by Mohamadi et al (*80*), the authors conclude that these injections only provide minimal pain relief at best, with no improvement after three months and are thus not cost-effective. Another systematic review by Puzzitiello et al (*81*) highlighted the adverse effects of corticosteroids on tendon tissue, which include decreased cellular proliferation, altered ECM and collagen synthesis and increased apoptosis on a molecular level. Furthermore, they highlighted a significant decrease in load to failure and stiffness in tendons treated with corticosteroid injections, in combination with a decreased bone volume density of the greater tuberosity, which manifested as a decreased suture anchor pull-out strength (*83-85*). Other injectable treatments that have gained popularity include the use of platelet-rich plasma

(PRP) and growth factors (TGF-β), but results are highly variable, not well reported, and inconclusive (*82, 86*). Physiotherapy essentially leaves the tear unrepaired and there is a wide variety of different approaches with a high variability of results (*87*). However, there is still much debate in the wider orthopaedic community of the benefits of conservative versus surgical treatment. In a recent review by Narvani et al (*4*), conservative and non-conservative treatment were discussed, and it was found that although patients benefit from physiotherapy, surgical intervention is warranted in patients with full thickness tears to prevent progression in tear size, muscle atrophy and fatty infiltration to the point it becomes irreparable (*56*). A randomized clinical trial comparing outcome measures of patients with small and medium-sized rotator cuff tears concluded that surgical repair of the tendon resulted in better functional outcomes than physiotherapy after 1, 5 and 10 years of follow-up (*88-90*). Furthermore, the cost-effectiveness of rotator cuff repair is reported to save $3.44 billion annually when accounting for hospital- and theatre costs, as well as costs of lost income due to the inability to work (*91*). Although much is known now about the biology of tendon in healthy and injured state and we have made considerable advances in treating tendon injuries, the intricacy and complexity of the tendon-bone unit means that we are still not able to fully restore tendons to pre-injury conditions.

1.3.3 Surgical repair of the rotator cuff

Rotator cuff tears can be partial or full-thickness tears depending on how deeply affected the tendon is. They can be categorised according to various systems, including, but not limited to: size (Cofield), shape (Ellman), location (Snyder), level of retraction (Patte), and degree of muscle atrophy (Thomazeau), or fatty degeneration (Goutallier) (*92*). A standard classification system does not exist, however tears are often geometrically described as it allows for better communication and comparison of different repair techniques (*93*), see

Figure 1.8. Type 1 tears are crescent-shaped and the tendon can usually be directly fixed to the bone. Type 2 tears can be L- or U-shaped and are longer and require side-to-side repair first, i.e., margin convergence, to reduce the tension on the repair construct (*94*). Type 3 are massive contracted tears that are too large to be pulled towards the tendon-bone edge and often require involvement of a graft patch to bridge the remaining defect (*95*).

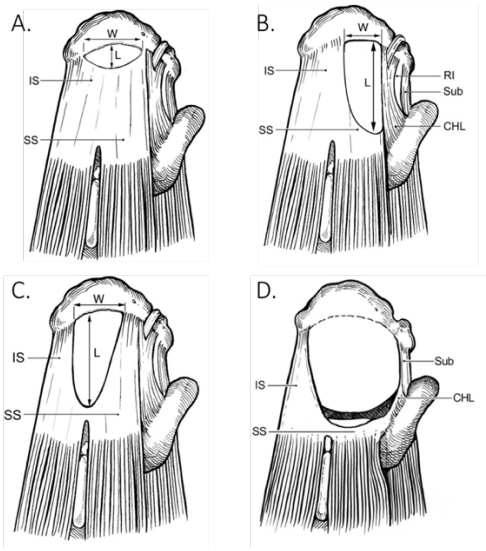

Figure 1.8 Geometric classification of tendon tears: crescent-shaped (A), L-shaped (B), U-shaped (C) and massive (D). W = width, L = length, IS = infraspinatus, SS = supraspinatus, Sub = subscapularis, RI = rotator interval, CHL = coracohumeral ligament. Image adapted from Davidson and Burkhart (*93*).

The main goals of surgical repair are to restore function and mobility to the shoulder and limiting pain. Repair of a massive rotator cuff tear is performed by inserting bone anchors into the head of the humerus and reattaching the remaining tendon via sutures, also known as a transosseous fixation. Briefly, the tear is identified and frayed tissue is removed to keep a healthy cuff edge (debridement). Then, the edge of the tear is grasped and mobilised to its normal position and the tendon is fixed to the bone using suture anchors (*96*). Rotator cuff repair was first reported in the late 1800s but did not become mainstream until 1911 when the American surgeon Codman first described a surgical technique to repair lesions of the supraspinatus (*97*). Nowadays, a variety of techniques exist that can broadly be classified as single-row, double-row and suture-bridge fixations, depending on the size of the tear (Figure

1.9), with usually 1 cm of distance between anchors. The overarching aim is to restore the tendon to its original footprint on the humerus without compromising the original tendon anatomy (*98-101*). These repairs can be performed through arthroscopic or open repair and although arthroscopy is associated with less complications and reduced time in hospital, there is no difference in postoperative outcome between them (*12*). However, arthroscopic repairs have been reported to cost £675 more than open repairs, mainly due to costs of surgical consumables (*102*).

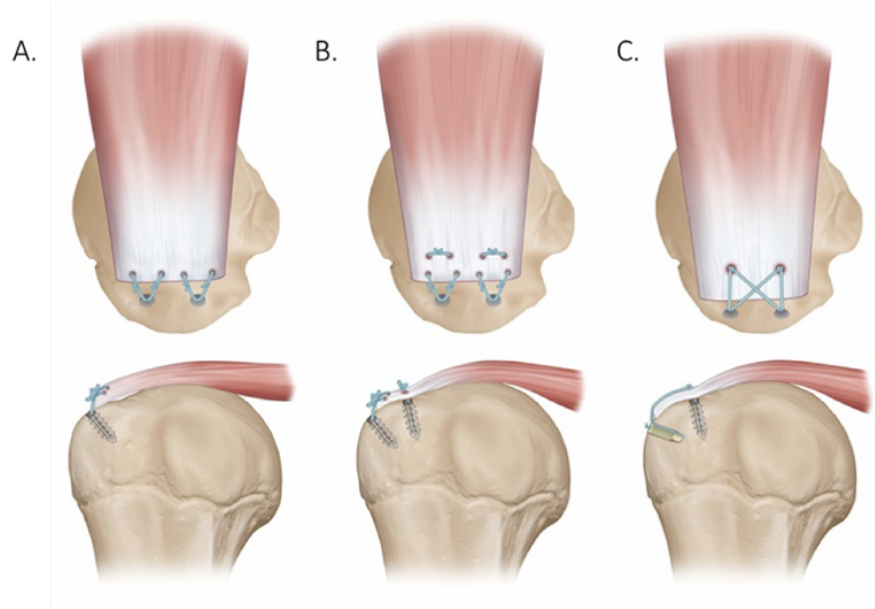

Figure 1.9 Rotator cuff repair using a single-row (A), double-row (B) and suture-bridge (C) method. Image adapted from Bedeir et al (*103*).

To maximise the strength of the repair construct it has been suggested that it should be spread out over a larger area (*99*) to increase the ultimate load to failure (*104*) and the contact pressure of tendon to bone (*105*), much like the fanning out of collagen fibrils in the attachment of the enthesis, as described previously. An important caveat in footprint restoration is not to overstretch the remaining tendon (*106*). A retrospective study reviewing 90 patients undergoing full thickness supraspinatus tears found that tendons repaired under tension had a significantly higher re-tear rate than those repaired without tension, but they did not have significantly different outcomes, as measured by ROM and questionnaires relating

to pain and function (*107*). A considerable number of studies have therefore investigated different repair techniques for optimal footprint coverage while preserving the remaining tendon length and this remains a topic of debate. Although double row fixation seems to be preferred because it has an increased load to failure, better contact and pressure with the footprint area and less gap formation (*108*), evidence is highly dependent on surgical technique, tendon quality and material selection and has not been shown to be statistically significant in outcomes compared to single row fixation (*108*). Furthermore, it is important to stress that these anchors are expensive and can add £149 in the UK and up to $1249 in the US per anchor to the surgical costs involved in rotator cuff surgeries, which makes double-row or even triple-row repairs quite cost-ineffective (*109, 110*).

1.4 Materials used in rotator cuff surgeries

1.4.1 Commercially available clinical sutures

Current sutures used in rotator cuff surgeries can broadly be classified into non-absorbable (FiberWire), partly absorbable (OrthoCord) and completely absorbable (PDS, Ethicon Inc.) (*111, 112*). There is no guideline for choosing a suture type, but guiding factors can include the severity of the tear, the quality of the remaining tissue and most importantly, the patient involved. As mentioned previously, there are a host of intrinsic and extrinsic factors that contribute to the outcome of a rotator cuff injury and repair and the type of suture used is therefore important to consider. Properties such as strength, ease of use and abrasiveness are relevant to selecting the appropriate suture (*113*). Braided and non-absorbable sutures such as FiberWire and Ethibond are mostly preferred because of their strength and because they are less likely to slip and cause anchors to displace compared to absorbable monofilament sutures such as PDS (*114*). Indeed, the type of suture used can be of considerable importance to the biomechanical behaviour of the suture-tendon interface (*115*), which remains one of the most

common failure points in re-tears (*104, 115, 116*), due to the mismatch of material properties between a suture and a tendon. The use of high-strength materials, especially ultrahigh-molecular-weight-polyethylene (UHMWPE) sutures has meant that suture breaking is less likely to be the primary mode of failure but the flipside is that they can be more abrasive to the surrounding soft tissues of the rotator cuff (*111, 117, 118*). A comparison of braided polyester sutures versus monofilament sutures in experimental set-ups has shown that the former result in increased abrasion and cutting through the remaining tendon, especially for the popular FiberWire suture manufactured by Arthrex, compared to not only smooth monofilament sutures but also other UHMWPE containing equivalents such as OrthoCord, FiberTape, Ethibond, UltraBraid and DynaCord (*104, 116, 119-122*). A major consideration for non-absorbable sutures is their increased likelihood over time to generate an adverse reaction from the body or to affect the surrounding tissues in a negative way. A non-absorbable suture will be encapsulated by fibroblasts to form a fibrous capsule as part of the foreign body reaction (FBR) (*123*). The body attempts to degrade the fibrous capsule and, in this process, attract a repertoire of cells, including macrophages and cytokines, that can quickly devolve into an inflammatory response (*124*). Absorbable synthetic sutures degrade in a linearly over a period of weeks to months by enzymatic or hydrolytic degradation, so that there is little formation of fibrous capsule and therefore no sustained FBR (*123*). See also section 1.5.5. The perfect suture type would be easy to handle, strong and absorbable, losing its tensile strength at the same rate that native tissue regains it, completely inert and elicit no tissue reaction. Although we have come very close to this with modern sutures, there is not a single type that fits all criteria, yet.

1.4.2 Use of suture-anchors in rotator cuff surgeries

There are also a variety of commercially available suture anchors for rotator cuff repairs. A suture anchor for rotator cuff repair must adhere to the following criteria: 1) secure fixation of suture to the bone, 2) no migration during static or cyclic stresses, 3) easy to implant, 4) have multiple sutures and 5) not cause adverse short- or long-term events, but the selection depends mostly on surgeon experience and preference (*125*). The anchor is inserted into the bone with the sutures emerging through the eyelet (Figure 1.10). It can be made of a metal (e.g., titanium, stainless steel, alloys), or a polymer (e.g., PEEK, PGA and PLA) and is shaped like a screw (*126*). Several modes of failure can be distinguished that range from suture failure, eyelet breakage and migration of the anchor to improper distribution of load at the various interfaces (*127*). Biocomposite anchors consists of a biodegradable polymer and a calcium phosphate mineral, most commonly β-tricalciumphosphate (β-TCP) or hydroxyapatite (HA), and they have recently become more popular due to their increased osteoconductive properties.

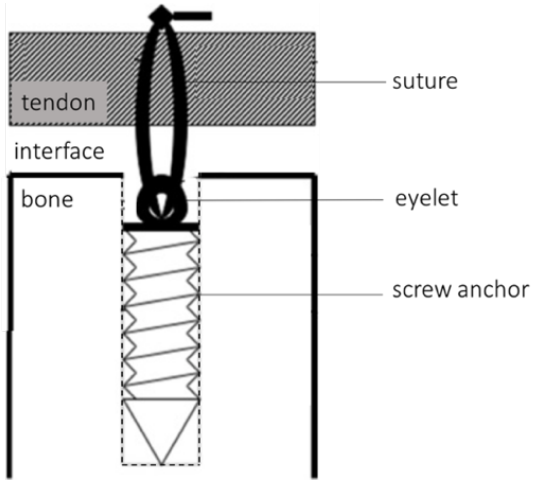

Figure 1.10 The basic concept of the screw-like suture-anchor. Image adapted from Chaudhry et al (127).

A novel type of anchor is the all-suture anchor, which as the name suggests, only consists of sutures. They offer some advantages to the classic anchors in arthroscopic surgery and since there is no solid component, there is less risk of migration and joint damage. Furthermore, it

is smaller and therefore occupies less space in the bone. However, compared to 'traditional' anchors they have a decreased load to failure and show an increased total displacement (*128*). Nowadays, almost all anchors are made from non-metallic materials due to concerns in post-operative imaging, difficulty in removing metallic anchors in revision surgeries and intra-articular migration and associated damage (*112*). Indeed, in a review evaluating the complications associated with bioabsorbable suture anchors in the shoulder authors concluded that the scarcity of literature relating to their question in combination with thousands of bioabsorbable anchors implanted every year meant that they are a safe and stable alternative to metallic anchors (*129*). However, absence of evidence is not proof of success, and it is not uncommon for these anchors to remain visible for up to two years after surgery meaning that their degradation is slower than initially assumed (*130*). Current biodegradable anchors are mostly made of poly-lactic acid (PLLA) polymers (e.g., Corkscrew-FT anchor, Arthrex) that degrade slowly through hydrolysis over a period ranging from 30 months to 5 years and complete resorption at 7 years (*111, 131-133*), depending on its structure. This slow degradation is important, because the propensity of an inflammatory response will depend on the rate of polymer breakdown into smaller monomers (*134*). So, if monomers are released slowly into their environment, the inflammatory cascade could be more controlled and subdued. In a recent review, these types of suture anchors were found to have a complication rate of only 0.5% due to eyelet breakage (*134*).

1.4.3 Concluding remark

Modern medicine and engineering have made many advances in the development of sutures and anchors possible. However, if the tendon does not heal or gets more damaged due to surgery, then the particular material used is of little consequence. Indeed, the most likely findings at revision surgeries of failed rotator cuff repairs are that the suture has cut through the tendon (cheese-wiring), or new tears have formed medially to the original one (*135*).

Quality of the tendon itself and proper reduction of the tendon to footprint based on tear pattern are also important to consider in addition to suture configuration and material choice (*136*). The biomechanical properties of suture-tendon interfaces in torn and degenerated RCT are significantly worse than in intact tendon (*137*). Consequently, the suture-tendon interface is the weak link where repair constructs most often fail, followed by the suture-anchor or bone-anchor interface (*99, 104, 115*). The functional transition from tendon to bone therefore remains the major challenge to overcome in the reconstruction of the rotator cuff tendon.

1.5 Tissue engineering in medicine

1.5.1 The introduction of tissue engineering

Tissue engineering (TE) is an interdisciplinary field that combines the life sciences with engineering sciences for the regeneration or repair of tissues by use of cells and materials (*138*). This field has existed for about forty years and has already made significant advances in the medical field, especially in wound repair with progression to commercial products (e.g., DermaGraft, GraftJacket, etc.). Other applications of tissue engineering are found in the musculoskeletal, neurological, cardiovascular, and dental fields with products in the form of cell-based therapies (e.g., growth factors, platelet rich plasma, stem cells, etc.), natural and synthetic polymers (e.g., polylactic acid, silk, chitosan, etc.) or by use of biomaterials (e.g., scaffolds and bioreactors). According to Allied Analytics, the global tissue engineering market was valued at $2,374 million in 2019 and is projected to reach $6,815 million by 2027, registering a compound annual growth rate of 14. 2% from 2020 to 2027. This significant growth is attributed to a rise in chronic diseases as well as an increase in R&D activities (*139*). Most sales are generated by biomaterial-based companies (>99%, $10,000 million (*140*). As of March 2018, 49 public companies currently exist that operate in the TE market that have 66 clinical trials going or completed from 2011-2018 (0.21% of active

clinical trials in the US), largely sponsored by industry (~77%). It is estimated, however, that this rise in tissue engineering activities will be hindered by governmental regulatory bodies (FDA, EMA, MHRA) and high treatment costs. Strict guidelines exist for tissue engineered products to progress into the commercial markets. They either need to be approved to be tested in a clinical trial or should be able to demonstrate a level of equivalence or superiority to existing medical devices (*141*). However, there is no standard route to take, as in the case for pharmaceuticals in which randomised controlled trials are required, which makes this a long and cumbersome process for any tissue engineered device, not to mention the costs required to overcome these obstacles (*142*). Although tissue-engineered research for musculoskeletal applications has been steadily increasing it is clear from the small number of FDA-approved products on the market currently that there is a gap between what is being produced in laboratories and what is being manufactured for clinical use. The focus of this thesis is on the use of FDA-approved polymers to design a biphasic scaffold intended for rotator cuff applications. Scaffolds designed and intended for human tissue replacement and regenerative purposes must adhere to a certain set of specifications (*143*).

1.5.2 Biocompatibility and biodegradability

Biocompatibility refers to the ability of a cell-free scaffold to elicit a host response in a biological system and is an assessment of potential harm to the human body after exposure (*144*). Scaffolds should be non-toxic to their host environment and elicit a minimal or negligible inflammatory or immunogenic response. Host cells should be able to migrate into and attach onto the scaffold and be stimulated to proliferate and deposit extracellular matrix to start repairing the native tissue. The defining characteristic of tissue engineered scaffolds is that they are non-permanent and only serve as a temporary matrix. Degradation of the scaffold is another component of biocompatibility and should be sufficiently tailored to the

rate of new tissue growth. In addition, degradation products should not be harmful and must be able to be metabolised or cleared by the body through other tracts. If an implanted scaffold achieves normal tissue growth around it, with no adverse reaction, then biocompatibility has been achieved (*144*).

1.5.3 Biophysical properties

Tissues in the human body exhibit a wide range of biophysical properties, such as fibre arrangement and orientation, and respond to biophysical cues such as stress, strain, and stiffness (*145*). Cells attach to proteins within the ECM (e.g. collagen, fibronectin and laminin) through integrins, which link the cell cytoskeleton to specific cell binding sites displayed by these proteins, see section 1.2.3). Integrins have an important role in mechanotransduction between the cell and ECM through the cytoskeleton. To promote cell adhesion and proliferation, a scaffold should be designed with similar topographical cues as the ECM of the native tissue it is intended for, i.e. so that integrins can recognise binding sites, while retaining its own form and function upon implantation (*146*). Another important property that dictates cell viability is porosity, i.e., the percentage of 'empty' space in a scaffold, and pore geometry, i.e., the size and shape of the empty spaces. Large pore sizes and a high porosity make cell migration and angiogenesis, and exchange of nutrients and waste easier, whereas a larger surface area for cell attachment is achieved by smaller pore sizes (*146*). The manufacturing process of a tissue engineered scaffold should be able to transcend a research laboratory. It should be possible to upscale the fabrication of a single unit to batch quantities to be used routinely and to become commercially available for clinical settings. This also includes sterilisation, packaging, storage, and transportation. Therefore, the cost-effectiveness of scaffold fabrication should be an important consideration as well (*147*)

1.5.4 Cell-material interactions in rotator cuff repair

The success of a rotator cuff repair construct is wholly dependent on its interaction with the surrounding tissue and the reaction of the body against it, especially when using augmenting grafts or patches (*134, 148, 149*). As mentioned previously, the weakest link in the rotator cuff repair is often the suture-tendon interface (*150*). Since tendon tissue is known to have poor regenerative capabilities (Section 1.2.3), a closer look at the interplay of suture material and cell interaction has recently become more relevant because it can potentially cause early repair failure (*151*). An injury to tendon or muscle is invariably an injury to its cells and ECM – the network of collagens, proteoglycans, elastin, and cell-binding glycoproteins that are linked to form the structure of a tissue and determine its mechanical properties (*145*). When this matrix is damaged, the mechanics it is normally subject to will be insufficient and will result in an inflammatory response cascading into degeneration and apoptosis (*152*). Fibroblasts attach to the ECM by transmembrane adhesion molecules known as integrins (*39*). These proteins connect the cell cytoskeleton to the ECM and convey details from the cell to the ECM and vice versa, also known as 'outside-in' and 'inside-out' signalling (*153, 154*). The cell response to implanted materials is thus dictated by the communication of biophysical information through the integrins and can be manipulated by changing the structure and mechanical properties of the scaffold. Briefly, cell attachment happens in three steps. First, when the migrating cell encounters the ECM, nascent adhesion occurs by integrin ligand binding which recruits intracellular coupling proteins to form a focal adhesion complex (*155*). This complex matures into a focal adhesion by reorganising the actin cytoskeleton into filament bundles known as stress fibres (*156*), depending on appropriate tension force and polymerisation of the actin filaments (*157*). Finally, fibrillar adhesions are pulled out and used to anchor the cell cytoskeleton to fibronectin fibres from the ECM, in a process termed fibronectin fibrillogenesis (*158*). In turn, fibronectin provides ligand binding

sites other ECM proteins, such as collagens and proteoglycans, and other integrins (*159, 160*). Figure 1.11 gives a schematic overview of the cell attachment to ECM. Important to note here is that tenocytes grow slowly and the inherent repair capabilities of tendon are poor as well, so scaffolds function mostly to bridge the gap created by a tear or rupture and to re-establish contact between neighbouring cells.

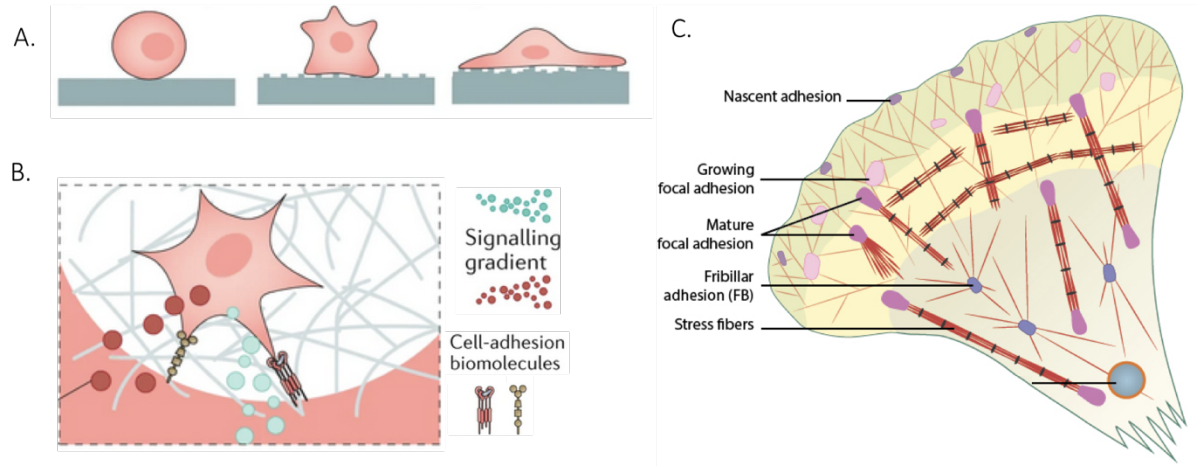

Figure 1.11 Attachment of the migrating cell to the ECM (A) occurs when cell-adhesion biomolecules (e.g., integrins) bind to ligands on the ECM which enables bidirectional communication (B). The cell is anchored by the formation of focal adhesions and fibrillar adhesions that bind it to the fibronectin on ECM (C). Images A-B adapted from (*161*) and image C from (*162*).

1.5.5 The response of cells to biomaterials

Once a scaffold is implanted into the human body it will be surrounded by blood and tissue fluid, which will launch the 'foreign body response' (FBR). This serves three purposes: to stop blood loss, prevent infection, start the wound healing process and protect the body against the foreign material(*163*). Within seconds of implantation, plasma proteins will be adsorbed to the surface of the scaffold which will prompt a layer of host proteins to cover the surface (*164*). Then, inflammatory cells migrate to, and accumulate at, the interface between the scaffold and surrounding tissue to form a fibrin clot (*165*), which can convert to granulation tissue in chronic inflammation. When this happens, monocytes, macrophages and fibroblasts trigger angiogenesis, the formation of new blood vessels, by recruiting fibroblasts to produce collagen and fibrotic tissue (*163*). This is a typical wound healing response that

will replace the granulation tissue with normal ECM components including collagen, glycoproteins, and proteoglycans (*163*). However, persistent inflammatory signals from the implant can lead to a continuous activation of fibroblasts that will encapsulate it into a thick collagenous fibrous construct and shield it off from the rest of the body (*163*). This process can be manipulated in favour of the 'normal' wound healing response rather than the fibrotic response by changing the biophysical cues – i.e., microenvironment – of the scaffold. Indeed, fibronectin fibrillogenesis is mediated by a specific conformation of the integrins to active ligand-binding which is directly affected by the structure of its substrate (*166*). A cell that is seeded on a flat surface, i.e., two-dimensional (2D), will have integrin activation on one side only and flatten along the surface, while cells in a three-dimensional (3D) environment will have integrins activated around all its sides and they can therefore assume 3D characteristics (Figure 1.12). Enhanced focal points with the substrate will also result in increased matrix interaction and ECM production. The construction of a 3D scaffold can be achieved by techniques such as 3D printing and electrospinning, which will be discussed in section 1.6.

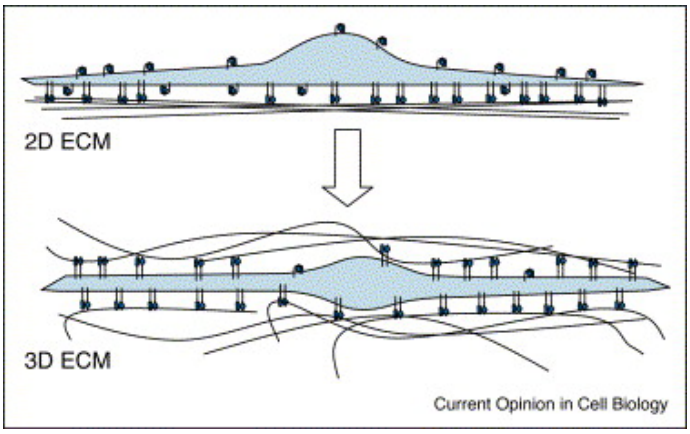

Figure 1.12 Response of cells to a 2D versus a 3D environment. Image reprinted from Larsen et al (*167*) with permission from Elsevier.

1.5.6 A brief segue into molecular biology and its application

One Chapter in this thesis is devoted to the biological response of cells seeded on electrospun scaffolds and commercial sutures. I therefore think it necessary to briefly mention biological concepts that might be familiar to the reader, and which form the basis of the methods used in

Chapter 2. The biological blueprint that contains information on protein synthesis is stored in deoxyribonucleic acid (DNA) inside the nucleus of a cell and consists of four nitrogen bases (adenine, thymine, guanine, and cytosine) that are linked in chains to form strands (*168*). The information in a DNA molecule is read by enzymes that transcribe it into messenger ribonucleic acid (mRNA), which leaves the cell nucleus is then translated into proteins by ribosomes, which is a molecular complex of proteins. This conveyance of information from DNA to RNA and proteins is unidirectional – except where viruses are concerned – and can be highly variable and temporally regulated (*169*). Since the information stored in DNA generally does not change under normal circumstances (i.e., in the absence of abnormal and harmful mutations), it is far more interesting to take a closer look at RNA when comparing samples under different conditions. To understand more about how scaffolds can influence cell behaviour, next-generation sequencing (NGS) has recently emerged to reveal the transcriptome of a cell, i.e., the complete set of RNA transcripts produced by a genome, and to identify genes that are differentially expressed between cells exposed to different conditions (*170*). This is important because RNA is the link between the genome and the proteome – i.e., genetic information from a cell (contained in its DNA) is transcribed into proteins through RNA. This knowledge is superior to the ubiquitous way of interpreting cell behaviour on scaffolds by visualizing morphology, performing viability and toxicity assays and histology. RNA sequencing (RNA-Seq) is a form of NGS that can sequence RNA rapidly and at relatively low cost and is an increasingly widely employed measure for gene expression. Although there is a wide variety of different protocols available, the general steps involve extraction of RNA from experimental samples, reverse transcription of RNA into complementary DNA (cDNA), attaching synthetic oligonucleotides to the ends of cDNA fragments (adapter ligation), amplification and sequencing (*170*). These steps are discussed in more detail in the Methods section of Chapter 3. So far, studies on the transcript level for

cells on electrospun scaffolds have been limited. The first such study evaluated the response of murine fibroblasts seeded on electrospun aligned fibres and used a microarray assay to show an increase in the production of actin and focal adhesion related genes (*171*). Two studies have evaluated the response of human tendon fibroblasts on electrospun PDO filaments and compared these to cells seeded on commercial sutures using RNA-Seq, whereby it was confirmed that the activation of tendon-derived fibroblasts is influenced by the orientation and diameter of the fibres (*172, 173*). It was also concluded that tendon-derived stromal cells showed a transcriptomic response indicating cell proliferation and wound healing(*173*). Studies using RNA-Seq involving electrospun scaffolds for skin wound healing purposes, vascular regeneration, retinal diseases have also seen positive results for aligned electrospun fibers (*174-177*). However, RNA-Seq has not yet been widely applied to the cell response on biomaterials, see Chapter 3.6 for an overview of previous genomic analysis of tendon cell pathways related to biomaterials.

1.6 Tissue engineering for musculoskeletal applications

Most tissue engineered scaffolds concern one type of tissue (e.g., cartilage, bone, or tendon). Tissues that are complex in nature (i.e. the enthesis) are much harder to replicate and although fundamental research and understanding on the enthesis has steadily increased over the years, little has been done to develop scaffolds that are designed to improve its repair and regeneration (*178*). Commercial scaffolds for supraspinatus tendon repairs have a well-established use in clinical settings. These can be synthetic, e.g. Mersilene (polyethylene terephthalate), or biological, e.g. GraftJacket (human dermis), and can be roughly classified into two types: the overlay and the inter-positional graft. The former is positioned *over* the remains of the tendon whereas the latter is placed between the tendon and its attachment to the bone (*148*). Although they are used frequently in rotator cuff repairs common problems

are their inferior mechanical abilities compared to native rotator cuff tendons and non-compliance with the surrounding tissue (*178*). Their re-tear rates are slightly better than for conventional repair remain quite high still. Novel scaffolds are mostly created with the aim of providing a biologically friendly environment for tissue healing but consistently fail in proper mechanical support as well (*179, 180*). There are scaffolds that do progress to clinical trials that are similar in properties to commercial grafts, but they do not amend rotator cuff tears well enough to be considered a valid alternative (*181*). Table 1.1 gives an overview of materials currently used as scaffolds for musculoskeletal purposes including their advantages and disadvantages. The proposed scaffold in this thesis will be composed of synthetic polymers that have been evaluated for cell attachment and toxicity specifically in the context of rotator cuff repairs, see Section 1.6.4 and 1.6.5. The main advantage of synthetic materials is that they are easy to reproduce and to be used for scale up productions as well, limiting manufacturing costs as compared to other materials. Synthetic materials also lend themselves well to alterations to facilitate cell attachment and growth. For example, PCL can be easily mixed with calcium phosphates for bone regeneration applications.

Table 1.1 Common materials used in tissue-engineered scaffolds for musculoskeletal purposes (*146*)

Material	**Example**	**Advantages**	**Disadvantages**
Natural	Proteins or polysaccharides occurring in animals or plants, e.g., silk, alginate, collagen	Biocompatible and biodegradable	Heterogeneity, difficulty extracting, poor mechanical properties
Synthetic	Polyesters, e.g., PLA, PCL, PDO	Cheap, biocompatible, easy to fine-tune, reliable and reproducible	Poor cell attachment, possible toxic degradation products
Xenograft	Mammalian decellularised ECM	Cell attachment	Process is difficult and can alter biomechanical properties, low cell infiltration
Ceramic	β-TCP or HA	Biocompatible and osteoconductive	Poor mechanical properties

Metals	Titanium, stainless steel, cobalt alloys	Superior mechanical properties	Not suitable for new tissue growth, possible harmful by-products
Composites	Combination of above materials	Able to mimic complex native tissues	Difficult to fabricate and keep consistent properties of respective materials

1.6.1 Advances in the design of multiphasic scaffolds

As discussed in the previous section, the attachment of tendon to bone is a complex interplay for different tissues cohesively termed the enthesis. Several studies have investigated the potential of electrospun scaffolds by using varying degrees of alignment and mineralisation to mimic the enthesis, and incorporating drugs and nanoparticles, which have been described at length in an excellent review by Sensini et al (*182*), and of which a few examples are relevant to this thesis. A multiphasic scaffold consisting of a knitted PGA sheet (Phase A), PLGA microspheres (Phase B) and PLGA-bioglass microspheres (Phase C) was manufactured for the junction of anterior cruciate ligament (ACL) to bone with a tri-culture of fibroblasts, chondrocytes and osteoblasts on the respective phases (*183*). The authors found that their construct supported heterotypic cellular interactions *in vivo* and resulted in the formation of continuous but distinct regions. A scaffold consisting of two different pore alignments (anisotropic and isotropic) was manufactured using silk fibroin, by directional freezing, freeze-drying and salt leaching, to which seeded cells expressed different markers related to tendon/ligament, enthesis and cartilage markers (*184*). Pore alignment is important for cell alignment, especially when seeding different types such as tenocytes (anisotropic) and osteocytes (isotropic). Silk was also used to create a hybrid scaffold consisting of aligned electrospun silk fibers and a knitted fibrous mesh to induce fibroblastic differentiation of MSCs (*185*). A real break-through in tissue engineered scaffolds was introduced by Criscenti et al who developed a triphasic scaffold for bone-ligament reconstruction by electrospinning PLGA on top of a 3D printed PCL scaffold, separated by a paper foil to create three different

regions (*186*). Sooriyaarachchi et al (*187*) also fabricated a hybrid scaffold by embedding a layer of electrospun PCL between two 3D printed PLA frames to mimic the native meniscus extracelluar matrix. Two approaches of combining electrospinning and 3D printing have since been described in the literature: a layer-by-layer deposition of 3D printed materials and electrospun nanofibers and 3D printing with material that includes electrospun filaments (*188*). For example, Yu et al made electrospun PCL/gelatin nanofibers and dispersed these into the meshes of a 3D printed PCL scaffold to create a composite scaffold for bone tissue engineering (*189*). However, despite the many advances and encouraging outcomes in musculoskeletal tissue engineering, there is still much to improve on. Thus far, no scaffold has been able to fully reach the complex hierarchical structures of the enthesis, and in fact most of the focus is on the tendon side, rather than the bone side (*182*). The advantage of a combination of approaches to create multiphasic scaffolds is that it considers tissues consisting of multiple phases, e.g. the enthesis. The disadvantage is that it is a more complex endeavour where there is more room for error when managing different manufacturing approaches. Furthermore, mechanical properties of tissue-engineered scaffolds do not approximate that of current native tissues either and are a long way from being clinically relevant (*190*). Indeed, current tissue-engineered scaffolds have not progressed from animal testing and although we have developed a sound understanding of the biology of the enthesis, there is little focus on the mechanical characterisation of scaffolds that transcends to clinically appropriate values. Animal models are frequently used to test scaffolds and evaluate biocompatibility, histology and mechanical properties and are a good choice for understanding tissues on a cellular and molecular basis but are not always sufficient to translate to human use (*191*). Accepted animal models currently consist of quadrupeds, whose biomechanics cannot be directly extrapolated to match musculoskeletal behaviour in humans (*191*) and inducing a tendon injury in a healthy animal will be different to the human

pathophysiology. Acute and chronic injury models in animals exist and have been accepted by the scientific community, but they cannot truly replicate traumatic and degenerative tendon conditions in humans (*192*). However, validated animal models are currently the most relevant method to safely assess novel scaffolds intended for human tendon repair. In contrast, there is a plethora of human cadaver studies investigating native tendon mechanical values for the purpose of evaluating commercial sutures, suture anchors and repair techniques, which could also be translated to tissue engineered scaffolds. There is a pressing need to progress beyond simple histologic and mechanical testing in animals and there should be more efforts into paralleling human outcome measures deemed successful to progress beyond basic science (*193*).

1.6.2 3D printing in tissue engineering

Charles Hull was among the first to describe and patent 3D printing in 1986, introducing it as stereolithography (*194*). Briefly, using this method, a 3D object can be generated by printing layers on top of each other in succession and curing it using ultraviolet light. Sachs et al developed it further with the motivation of reducing the time needed to create and test prototypes of new products to bring to the market (*195*). Since then, several other forms of 3D printing have been described involving natural polymers (e.g., silk, cellulose, chitosan), synthetic polymers (e.g., polyethylene, polyester, epoxy) or a blend of both. Natural polymers can be extracted from plants, animals, and microorganisms, which makes them a renewable resource. This also means a high probability of batch-to-batch variation for large-scale manufacturing processes, however (*196*). Furthermore, extraction and processing of these polymers can alter their properties negatively, for example, when exposed to heat. In addition, their poor mechanical properties make them an unsuitable candidate for hard tissue engineering, and it is difficult to control their degradation (*143*). Synthetic polymers, on the other hand, can be easily tuned for their mechanical properties and degradation kinetics and

can be reproduced quite reliably (*197*). They have become increasingly popular in tissue engineering due to this and have been used in a variety of 3D printing technologies. The simplest and most common method of 3D printing, however, is fused deposition modelling (FDM). Briefly, this involves creating an object using any kind of designing software, i.e., computer-aided design (CAD). This CAD is then translated into a 'G-code', which gives instructions to the 3D printer on movement and action. A (synthetic) polymer is used as raw material, i.e., the filament, and is wound onto a spool. Motors move the spool forward continuously to feed the polymer into the extrusion head where it is heated until it melts. The liquefied filament is then extruded through the nozzle and deposited onto a building platform where it solidifies into shape. This happens on a layer-by-layer basis. The nozzle head can move in three directions (XYZ) to allow for three degrees of freedom, as specified by the G-code. Figure 1.13 gives a simplified overview of this process. No other steps are involved in the creation of the object, except removing support material if needed. This makes FDM by far the easiest and most tunable 3D printing option in tissue engineering. It has been used for tissue engineered scaffolds in many applications, citing its high reproducibility and ease of tunability as the main advantage, especially with the eye on personalized implants (*198*).

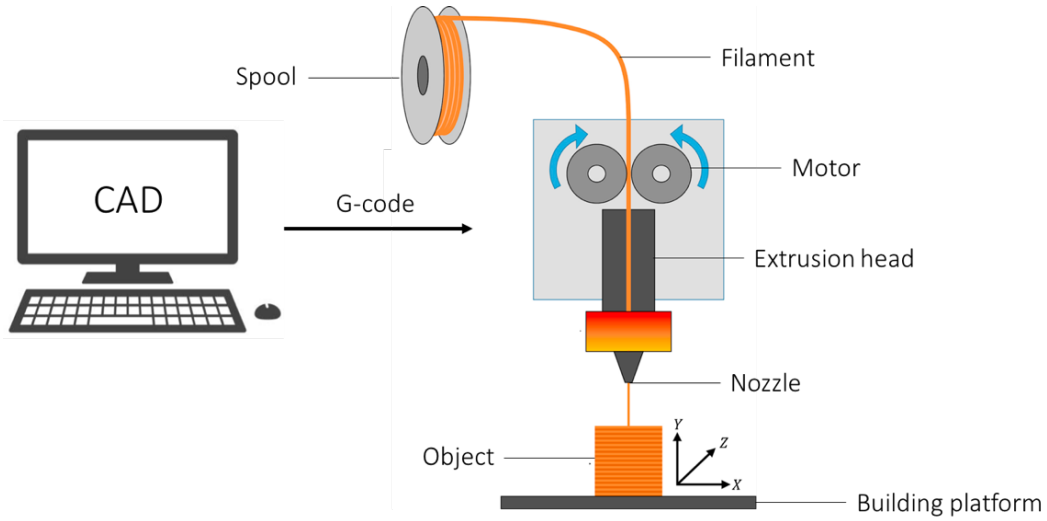

Figure 1.13 A schematic of the FDM process. Image adapted from Stansbury and Idacavage (*199*).

The most commonly used polymers include PCL and PLA because they are cheap, easily available and have a low melting point which does not require post-processing for crosslinking (*188*). However, since these are quite hydrophobic polymers, focus has shifted towards the use of materials that are more hydrophilic and contain bioactive compounds. 3D bioprinting, also known as organ printing, is a more complex method of additive manufacturing in which units of cells and biomaterials are deposited to form tissue-like structures (*200*). The use of multiple nozzle heads can generate complicated structures involving multiple cell types and different biomaterials and PCL is a frequently used polymer (*201*). Advances have been made in the construction of 3D printed scaffolds for bone, muscle, tendon, and ligament tissues but very few have looked at the respective interfaces, predominantly citing the challenge of replicating its microenvironment and its relative complexity compared to other, well-developed techniques (*201*). Other popular 3D printing methods in tissue engineering include stereolithography, which requires the use of a liquid resin bath, and selective laser sintering that is powder-based and requires additional post-processing steps to remove excess powder (*202*).

1.6.3 3D printing of polycaprolactone

FDM is used solely with thermoplastic materials. This is a class of polymers that soften when heated above their glass transition temperature and which can be indefinitely reversed into a solid state by cooling (*203*). A popular polymer that is widely used in bone tissue engineering is polycaprolactone (PCL). This is hydrophobic, semi-crystalline polymer that is synthesized by either condensing 6-hydroxyhexanoic acid or ring-opening polymerisation of ε – caprolactone using a catalyst (Figure 1.14), which is the preferred route because it produces a higher quality polymer (*204*). It is also relatively cheap and easy to synthesize this polymer compared to others (*204*). Another advantage is its low melting temperature of between 59-

64 °C (*205*). This means that at physiological temperatures, it is quite rubbery and has high toughness and strength. PCL has been classed as a biodegradable polyester and is the slowest polyester to degrade, with degradation occurring over a period of months to years – depending on its molecular weight and crystallinity. It breaks down by the cleaving of ester bonds through chain scission, resulting in a loss of mass (*206*). The term biodegradable and bioabsorbable or -resorbable have been used interchangeably in the wider research community but refer to two separate things. Firstly, biodegradable is used in the earth sciences to refer to 'ecological polymers' created for packaging purposes that aim to reduce plastic waste and therefore degrade in natural environments in the presence of, for example, microorganisms, sunlight, or rainfall (e.g., the ocean, forest, mountains etc.). Secondly, bioabsorbable or -resorbable refers to polymers that are intended for implantation in humans and thus degrade within the human body, for example, by enzymes (e.g., sutures, meshes, bone anchors). However, both terms describe the breakdown of a polymer to the point where no trace is left in its original environment, irrespective of degradation process, and either term could therefore be used (*207*). Throughout this thesis, both terms are used interchangeably as well. PCL is biodegradable because it can be broken down by microorganisms in natural environments (*206*) but is mostly referred to as bioabsorbable when used for medical purposes, because it degrades by hydrolysis, i.e., contact with an aqueous solution, and not by enzymatic activity since there are no suitable enzymes to break down PCL within the body (*208*). Bioabsorption of PCL takes much longer than biodegradation, however, because the hydrolytic reaction needs to be instigated first. The degradation occurs by surface or bulk degradation. When the rate of water penetrating the polymer is slower than chain scission of the polymer backbone, we speak of surface erosion (*209*) and this is a predictable process which makes it a promising candidate for drug delivery vehicles because the release rate of a drug can be controlled (*210*). Bulk degradation starts

when the surface has eroded and water can intrude into the polymer, initiating hydrolysis throughout the entire matrix and a decrease in molecular weight, see Figure 1.15. The degradation of PCL results in non-toxic by-products, composed mainly of capronic acid, that are excreted normally (*211, 212*). PCL is a slowly degrading polyester and depending on the geometry and thickness of the scaffold it can take up to a few years for it to be completely degraded.

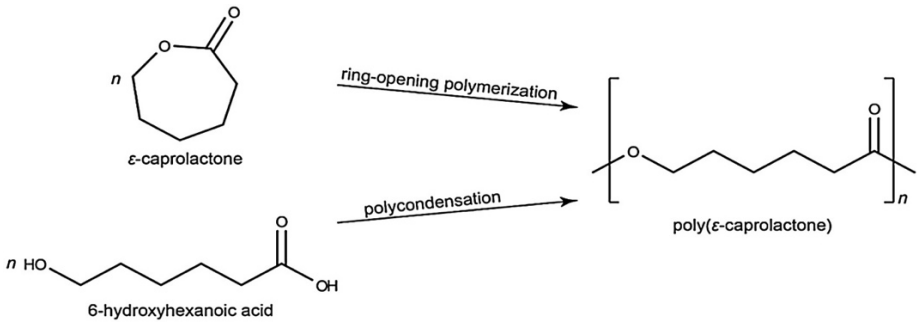

Figure 1.14 Synthesis of polycaprolactone by ring-opening polymerisation or polycondensation. Image reprinted from Bartnikowski et al (*206*) with permission from Elsevier.

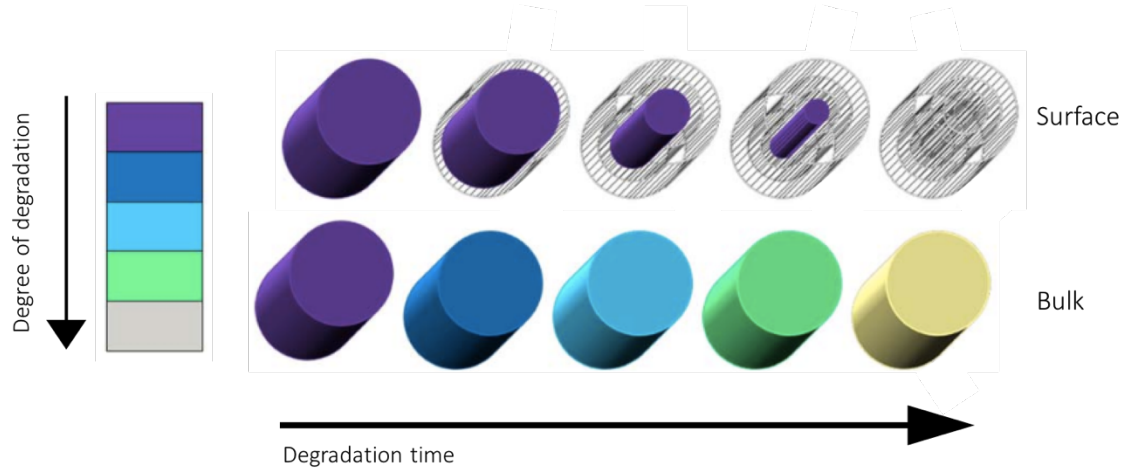

Figure 1.15 Surface and bulk degradation of polycaprolactone over time. Image adapted from Woodruff and Hutmacher (*209*).

However, PCL is quite hydrophobic in nature making cell attachment difficult, and although it is a biocompatible polymer with a slow degradation rate, it is not bioactive and does not have osteoconductive properties. It also does not mimic native bone ECM and has inferior mechanical properties compared to native bone (*213*). However, considerable success has

been achieved to improve its properties by blending it with other compounds, such as hydroxyapatite (HA), a naturally occurring mineral comprising most of the inorganic bone matrix, and β-tricalcium phosphate (β-TCP), a bioceramic that is widely used as bone graft substitutes since its resorption is readily replaced by new bone (*214*). Indeed, the incorporation of HA and β-TCP into PCL has been reported to result in mechanical and biological properties approaching that of native bone tissue (*213, 215, 216*). Furthermore, PCL has a good ability to bear load and compression due to its crystallization structure (*217-220*) and is easily fine-tuned during 3D printing to achieve highly porous scaffolds for cell ingrowth and proliferation (*221, 222*). PCL also has superior rheological and viscoelastic properties compared to other polymers, which makes it very simple to manipulate and use for the manufacturing of scaffolds on a larger scale (*209*). It is especially attractive because it is easily enhanced by adding functional groups to it that could improve its hydrophobicity, bioactivity and biocompatibility (*209*). In fact, the versatility of PCL is such that is has been used for a wide variety of biomedical applications as well. Due to its excellent blending abilities with other compounds and degradation profile, it has been investigated as a drug delivery system as an alternative to traditional methods including oral administration and intravenous injection which are hindered by a short rise in drug concentration in the blood and need repeated intake. A few examples of using a slow biodegradable polymer as PCL as a drug delivery system include the delivery of vancomycin (an antibiotic) in the treatment of chronic osteomyelitis (*223*), the release of prostaglandins from an intraocular PCL film to treat glaucoma (*224*), and the release of hormones in a long-term contraceptive implant (*225*). A sub-dermal contraceptive implant (Capronor) was already patented in 1979 and consisted of a PCL rod that releases the hormone levonorgestrel over a period of 12 months. The degradability of the device was a promising concept because it did not require retrieval of the implant after insertion. It progressed to a Phase II randomized clinical trial but was

unfortunately discontinued due to minor complications (local skin irritation, most likely due to manufacturing residue) and funding problems (*226*).

1.6.4 Clinical use of polycaprolactone

PCL was first cleared by the FDA in 2006 as a bone void filler in craniofacial applications, commercialized as OsteoPore (*227*) and since then, has been implanted in over 20,000 patients globally (*228*). PCL is currently being investigated in reconstructive surgeries as well, notably in the oral and maxillofacial fields. A novel design of a 3D printed PCL/ β-TCP scaffold was introduced for the repair of a critical-sized defect in a canine mandible with favourable results 12 weeks post implantation (*229*). A 3D printed PCL/ β-TCP combination was also successfully used in cranioplasty for patients with deformed skulls (*216*), reconstruction for complex zygomatico-maxillary defects (*230*), and as a 3D printed mesh in rhinoplasty (*231*). 3D printed PCL has already progressed into a variety of other medical procedures as well. It has become a popular polymer in clinical cosmetology and is involved in dermal filler applications due to its collagen-stimulating abilities (*232*). A case-report concerning a female patient suffering from a structural deformity of the sternum and rib cage (pectus excavatum) details how this was reconstructed using a tissue-engineered scaffold (*233*). The scaffold was 3D printed and made from a medical grade polycaprolactone and highly porous so it could be filled with an autologous fat graft during surgery.

The first clinical series using 3D printed medical-grade PCL-TCP scaffolds for novel bone replacement were reported in 2022 (*234*). It involved four patients with large bone defects in the range of 2564-149,285 cm^3 in the tibia, skull and mandible and positive outcomes in the follow-up postoperatively. PCL has also been used to successfully fabricate and implant airway stents in infants born with a disorder causing collapse of the airway during respiration (tracheobronchomalacia), with positive results at 11-, 14-, and 38-months' follow-up for the

three children involved (*235*). All these cases followed a similar simple workflow of obtaining the patient's medical imaging, segmenting it and creating the desired 3D model.

1.6.5 Polydioxanone in a new form

Another interesting polymer that has been used in clinical settings for over forty years, is polydioxanone (PDO), which was specifically developed as a wound closure suture in the 1980s and is marketed as PDS/PDSII in the US by Ethicon Inc (*236, 237*). It also has a use as orthopaedic pins and is on the market as OrthoSorb by Johnson & Johnson International. It is synthesized by ring-opening the monomer paradioxanone (p-dioxanone) using heat and a catalyst (Figure 1.16), and for current use as suture is extruded as a monofilament.

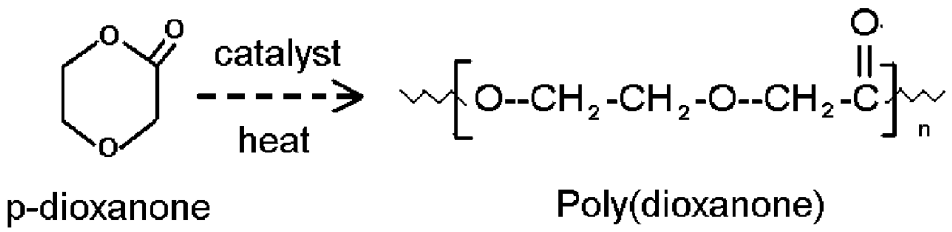

Figure 1.16 The synthesis of PDO using a catalyst and heat. Image reprinted from Boland et al (*236*) with permission from Elsevier.

PDO is also a biodegradable polymer and degrades through similar mechanisms as biodegradable polyesters, by hydrolysis and chain scission. Degradation by-products are non-toxic and excreted mostly via the respiratory tract and partly by the alimentary tract (*238*). The absorption of PDS sutures is stated by the manufacturer to take between 182-238 days, and was reported to result in a loss of 67% of tensile strength after about three weeks of in vitro culture (*239*). PDO has gained new interest in the tissue engineering field because its mechanical properties are similar to those of collagen and elastin, which are two major structural components in soft tissues, such as blood vessels (*236, 240*).

1.6.6 Electrospinning PDO for tendon tissue engineering

The advantage of a polymeric fibrous construct is that the mechanical properties and degradation kinetics can be altered by tailoring its microstructure (*241*). Textile techniques such as braiding, twisting, weaving and knitting have long been used in medical applications (e.g. sutures, grafts) to improve mechanical parameters and consequently have also been adopted in the fabrication of scaffolds for tissue engineering applications (*242*). Important parameters involved in the design of tissue engineered scaffolds based on fibre structures are the fibre diameter, alignment, cross-sectional area and spacing between fibres (*243*). Among different technologies to produce fibre-based scaffold, electrospinning has become one of the most successful methods to be used. Electrospinning dates back to the 1600s (*244*), though recently, efforts are attributed to Anton Formhals, who patented several parts of the process in the late 1930s (*245*). The basic concept of electrospinning has not changed much over the centuries, however. Briefly, it is a process in which micro- and nanoscale fibres can be produced from a polymer solution using electrical charge. A syringe containing the polymer solution and a needle is inserted into a syringe pump which deposits directly onto a metal collector that is connected to a high voltage power supply. The electrical potential increases the surface tension of the polymer solution at the tip of the needle and allows it to form a conical drop, known as the 'Taylor cone' (*246*). As more electrical charge is applied, the surface tension is overcome, and the polymer is drawn out in a jet that settles on the metal collector. The diameter of the resulting fibres can be tuned by changing the polymer, electrical field, flow rate of the polymer, distance between the needle and the tip or the type of collector device used (*247*). A schematic of the basic electrospinning set-up is presented in Figure 1.17 (*246*) including the many variables that can be altered, relating to the environment, polymer solution and electrospinning set-up (*246*). Electrospinning is cheap, simple, easy to adjust and easy to scale-up (*248*). One of the major advantages of

electrospinning in tissue engineering is its ability to create constructs with a high surface-to-volume area, high level of porosity and microporous structure (*242*). Fibrous constructs can be created as single filaments (1D), nanofibrous mats (2D) or 3D scaffolds by stacking fibres in a layer-by-layer fashion (*249*). The latter is the most popular choice as it has better mechanical properties and can support cell adhesion and proliferation similar to native ECM (Figure 1.18) (*250*).

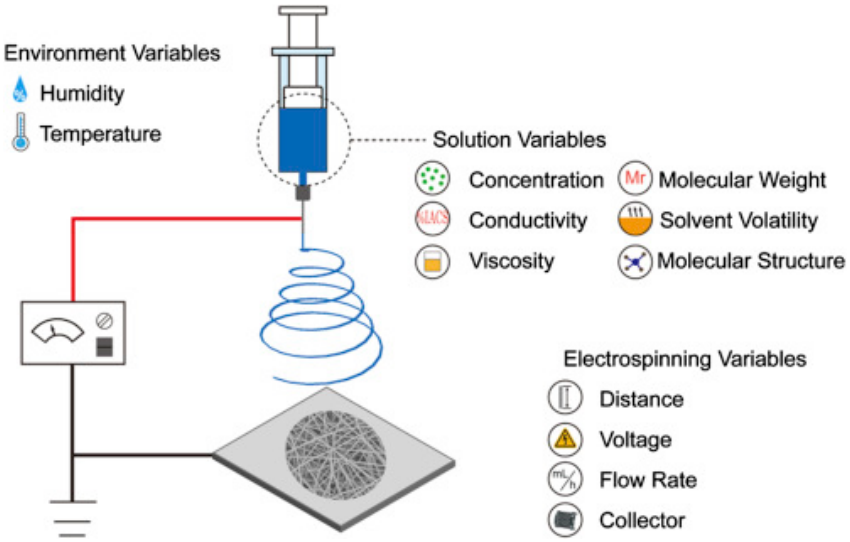

Figure 1.17 The basic electrospinning set-up includes a syringe with a polymeric solution that is deposited through a needle onto a metal collecter, attached to a high voltage system. Many different parameters in this set-up can be altered. Image reprinted from Long et al (*246*) with permission from Elsevier.

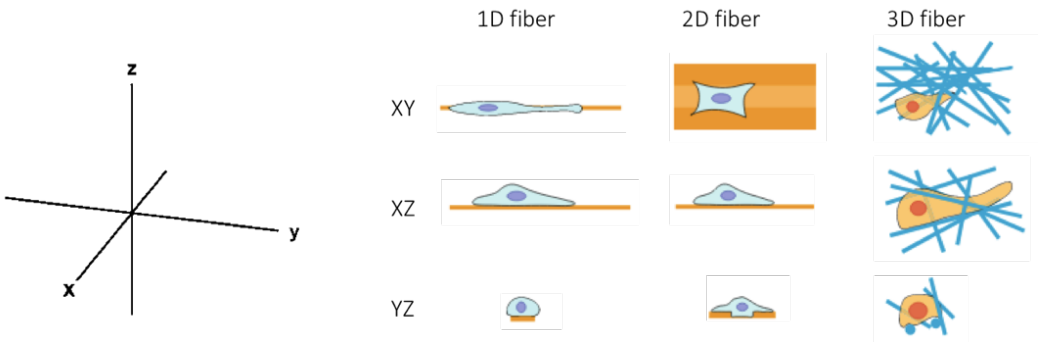

Figure 1.18 Orientation of cells in 1D, 2D and 3D fibre matrices. Image adapted from Jenkins and Little (*251*).

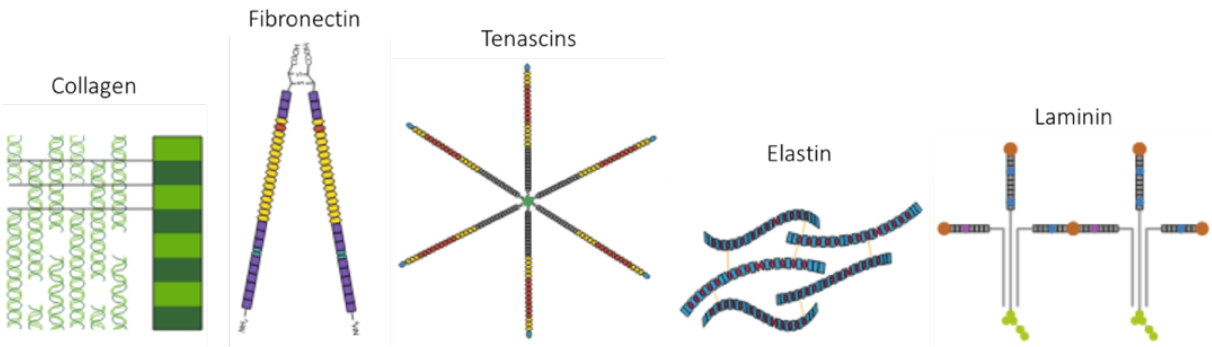

Figure 1.19 The structure of various fibrous proteins that are important for ECM maintenance. Image adapted from Jenkins and Little (*251*).

Tunable electrospinning parameters for a successful cellular response include fibre diameter and alignment, which was further highlighted in a recent review by Jenkins et al (*251, 252*). The ECM consists of mainly fibrous proteins – meaning they have polypeptide chains organized in parallel along an axis, thereby producing long fibres (*253*), including collagens, glycoproteins (e.g., fibronectin and tenascin-C), elastin and laminins (Figure 1.19) (*251*), which are thus responsive to scaffolds that have a similar architecture. Indeed, fibre alignment as contact guidance has shown a positive regulation of cell behaviour in electrospun scaffolds for anterior cruciate ligament, with significantly more collagen deposition and cells with a spindle-shaped morphology and oriented in the direction of the fibres (*254*). It has also been shown to positively direct cells towards muscle and tendon lineages (*255-257*). In combination with mechanical stimulation, mesenchymal stem cells seeded on aligned electrospun nanofibers have also been successfully guided to differentiate into ligament fibroblast-like cells (*258*). Different kinds of synthetic polymer are currently used in electrospinning for tissue engineered applications, including PLA, PCL and PDO. Boland et al were the first to use PDO for electrospinning. They dissolved commercial PDS sutures in 1,1,1,3,3,3-hexafluro-2-propanol (HFIP) and electrospun it into nanofibrous structures to control their fibre diameter and orientation and thus improve their mechanical properties and potential for cell attachment (*236*). Recently, PDO was investigated as an

electrospun patch for tendon cell adhesion and the potential for rotator cuff applications, showing promising results (*259*). The difference in response between diseased and healthy tenocytes was also evaluated on these scaffolds and it was found that both responded positively and showed similar morphologies after seven days in culture medium(*260*). Consequently, a woven and electrospun PDO/PCL patch was evaluated in a sheep tendon injury model to evaluate whether it could induce a positive endogenous fibroblast response (*261*). Results were encouraging and tendon healing was enabled without a prolonged local or foreign body response. However, the inherent mechanical properties of electrospun filaments remain quite low (*262*) and inspiration has been drawn from textile industry to improve these (*263*). Braiding electrospun filaments into multifilament yarns have shown mechanical properties similar to native tendons and has been shown to induce differentiation of human MSCs into tenogenic phenotypes, i.e. an elongated cell shape with expression of key tenogenic biomarkers such as scleraxis and tenomodulin, but without expression of chondrogenic, osteogenic or adipogenic markers (*264-267*). More recently, Calejo et al manufactured PCL/gelatin and PCL/gelatin/HA particles microfibers and knitted them together to create a 3D fibrous scaffold with continuous topographical and compositional mineral gradient (*268*). Indeed, manufacturing continuous electrospun PDO filaments has resulted in upscaling its production by using industrial braiding machines, which could lead to significant advances in electrospun filaments for medical use (*269, 270*).

1.7 Summary

This Chapter provided the context to the work performed in this thesis. Rotator cuff injuries are a significant problem for the patient and place a major burden on healthcare and society due to insufficient repairs leading to pain and disability. This is expected to become worse with an aging and more active population. The structure and function of the rotator cuff was

introduced from macro- to micro level to illustrate the complexity of the hierarchical structure that makes up the tendon and its attachment to bone (enthesis). A disruption in this structure is difficult to adequately repair and poses an unmet clinical need. Tissue engineered biomaterials were introduced as an alternative to currently available suture anchors used in rotator cuff surgeries, because they have the potential to actively influence and support resident cell populations in the healing of native tissues. Electrospinning and 3D printing are particularly interesting because of their ability to use clinically approved polymers to produce constructs with properties similar to tendon and bone. This will form the basis of the methods used in this thesis.

1.8 Thesis aim and hypotheses

The main aim of this thesis is to manufacture a scaffold consisting of a hard (3D printed)- and soft (electrospun) phase that is based on the enthesis anatomy.

The objectives are as follows:

1. Continuous electrospun filaments will be pre-assembled into bundles and combined with 3D printed material by inserting them during the 3D printing process. The number of inserted filaments will be scaled up to increase the overall tensile strength.
2. Fibroblasts will be seeded on electrospun filaments and a commercial competitor and next-generation sequencing will be used to analyse differentially expressed genes between them.
3. A literature study will be conducted to set the dimensions of the 3D printed block in collaboration with a medical manufacturer, using anonymised medical imaging.

The hypotheses are as follows:

1. The fabrication and scale-up of soft-hard constructs is possible by combining electrospun polydioxanone filaments within 3D-printed polycaprolactone blocks. This construct will reach a threshold of mechanical strength that is clinically relevant.
2. Fibroblasts will attach and proliferate more on electrospun filaments than on their commercial competitor (FiberWire), which does not involve submicron physical cues. The former will promote fibroblasts to elongate along the filaments and express genes related to proliferation and differentiation.
3. The 3D printed hard part of the biphasic construct can be shaped to fit the specific anatomical location of the supraspinatus footprint on the humerus and can be inserted and fixated using existing surgical equipment.

Chapter 2 Manufacture of soft-hard scaffolds

2.1 Abstract

Rotator cuff tendon tears are common injuries of the musculoskeletal system that often require surgical repair. However, re-tearing following repair is a significant clinical problem, with a failure rate of up to 40%, notably at the transition from bone to tendon. The development of biphasic materials consisting of soft and hard components, which can mimic this interface, is therefore promising. Here, we propose a simple manufacturing approach that combines electrospun filaments and 3D printing to achieve scaffolds made of a soft polydioxanone cuff embedded in a porous polycaprolactone block. The insertion area of the cuff was based on the supraspinatus tendon footprint and the size of the cuff was scaled up from 9 to 270 electrospun filaments to reach a clinically relevant strength of 227N on average. Our biological evaluation showed that the biphasic scaffold components were non-cytotoxic, and that human fibroblasts and osteoblast-like cells could be grown on the cuff and block, respectively. Overall, these results indicate that combining electrospinning and 3D printing is a feasible and promising approach to create soft-to-hard biphasic scaffolds that could improve the outcomes of rotator cuff repair.

2.2 Introduction

In the musculoskeletal system one of the most common injuries are rotator cuff tendon tears (RCT) of the shoulder, contributing to 30-70% of all cases of shoulder pain (*271*). Surgical repair failures, i.e. re-rupture, occur mostly at the enthesis, which has an important role in the transmission of mechanical forces during motion (*104, 271-274*). Other reported failure mechanisms are anchor pull-out, eyelet breakage, suture breakage or tendon pulling through sutures (cheese-wiring) (*104, 275, 276*). Recent focus within the biomaterials field has aimed to produce implants that mimic the soft-hard tissue transition seen in the native enthesis (*44, 277*). There has been an increasing interest in using electrospinning and 3D printing technologies to achieve this (*278*). In terms of materials, polycaprolactone (PCL) and polydioxanone (PDO) have been extensively used with both technologies because of their appealing degradable properties, both polymers are degraded by hydrolysis and are metabolised in the body, and track record of safety in patients (*205, 279, 280*). Combining electrospun (ES) and 3D printed (3DP) materials provides an exciting opportunity to engineer biomaterials for multiphasic tissues, such as the enthesis (*184*). So far, it has led to constructs for neuronal cell growth (*281*), bone tissue engineering (*282*), cartilage tissue engineering (*283*) and cranial defects (*284*). A variety of methods have been used which mostly involved 3D printing on top of pre-spun fibres or electrospinning on 3DP structures(*283, 285, 286*). However, none of these methods have been used to design soft-hard implants with a biphasic configuration that mimics the tendon-bone junction. This is mainly because the enthesis is particularly challenging to address as it is exposed to high forces (152.6 - 779.2 N (*178, 287-290*)), and high stresses (11-22 MPa (*287-289*)) during movement of the arm, while ES materials are typically relatively weak (*291*). Currently, a combined electrospun and 3D printed scaffold does not exist for clinical use.

Here, we propose a new strategy to combine 3D printing and electrospinning and create robust soft-hard structures for potential as rotator cuff repair implants. Our strategy consists of embedding a soft cuff made of ES filaments during the 3D printing of a hard base. In this study we investigate the use of PCL and PDO polymers and the effect of filament configuration on the mechanical properties of the cuff material. We also explore the impact of increasing the size of the cuff to reach clinically relevant mechanical strengths. Finally, we perform cell-based assays to assess the potential of the ES-3DP biphasic implant as a medical device.

The specific Chapter objectives are as follows:

1. To electrospin continuous PDO and PCL filaments and 3D print PCL on top of them to create the biphasic scaffold.
2. To evaluate the mechanical properties of the scaffold by subjecting it to uniaxial tensile load and thermal analysis.
3. To assess the biological activity and cytotoxic properties by seeding cells on the electrospun soft cuff and the 3D printed hard cuff, separately.
4. To scale up the potential of the biphasic scaffold by increasing the number of electrospun filaments that can fit in the 3D printed block.

The hypotheses are:

1. It is possible to combine electrospinning and 3D printing to create a biphasic scaffold that does not require additional post-processing steps, whereby electrospun filaments within the block will be able to maintain their integrity.
2. Cells will be able to attach to and proliferate on the two components of the biphasic scaffold and it will not be a cytotoxic environment.
3. It will be possible to increase the number of filaments within the 3D printed block to reach a clinically relevant threshold force.

2.3 Materials and methods

2.3.1 Preparation of polymer solution

PDO (Riverpoint Medical, USA) and PCL (Ashland Specialities Ireland, Laboratory A, Synergy Centre, Institute of Technology Tallaght, Ireland) granules were dissolved into 1,1,1,3,3,3-hexafluoroisopropanol (HFIP, Apollo Scientific Limited, UK) at concentrations of 7% and 17%, respectively (weight-to-volume ratios), based on optimization work performed previously(*292, 293*). Pyridine (EMSURE ACS, Germany) was added to the PDO solution at 1 ppm prior to spinning as described in previous work (*292*). The polymer solutions were put on a roller for at least 72 hours at room temperature to ensure all granules were dissolved. Concentrations were selected based on optimization work previously carried out with the goal of creating submicron fibres that displayed no beading (*270*).

2.3.2 Electrospinning of filaments

The filaments were produced from the polymer solutions as described previously (*270*). Briefly, electrospinning was performed with a single nozzle electrospinning setup and a wire collector (100μm in diameter, Goodfellow, Huntingdon, UK) using a high voltage power supply system (30 kV, SL30P30/230, Spellman, West Sussex, UK) and a syringe pump (World Precision Instruments Limited, Florida, US). The metal wire was cleaned three times with 70% ethanol prior to use and was moving linearly at 0.5 mm/s during electrospinning. The solutions were spun with a voltage of 7.0-9.0 kV and were deposited onto the wire using a static nozzle. The material flow rate was 1 mL/h, spinning at a room temperature of 21°C and 30% humidity. Following the exit of the metal wire (coated with the PCL material) from the glove box, the electrospun fibrous mesh was detached as a continuous filament and placed on a separate spool. The filament spool was removed at the end of the process and stored in a desiccator prior to stretching.

2.3.3 Preparation of electrospun (ES) filaments

After electrospinning, the filaments were manually stretched in a clean environment and at room temperature, at a ratio of about 1:3 and 1:7, respectively for PDO and PCL. This was done to prevent plastic deformation during further use, as well as to increase the strength of the fibres, reduce the fibre diameter and align the microfibers (*270, 279, 294*). The ends of the electrospun filaments were tied together whenever a break occurred to keep its continuity. They were wound on a spool and stored at room temperature in a desiccator before use.

2.3.4 Filament assembly: parallel and twisted configurations

The ES filaments were prepared in two configurations: parallel and twisted. For the parallel configuration, individual filaments were cut in 20 cm pieces and laid next to each other to ensure the fibres would not overlap or cross each other using tape. A minimum of 9 and a maximum of 27 parallel filaments were used per layer. They were then spanned onto aluminium U-frames which were created in-house (measuring 15 cm in length and width). The frames with the filaments were then stored in the desiccator until use. For the twisted configuration, an industrial twisting machine (Mini Twister AMT 2S-Marui Textile Machinery Co. Ltd.) was used (*293*). Three spools of stretched filaments were loaded onto a feeder stand and twisted in the S-direction at a spindle speed of 500 turns/minute to produce 3-plied yarns. Three spools of 3-plied yarns were then loaded onto the feeder again and twisted in the Z-direction at a spindle speed of 250 turns/minute to produce a cabled yarn. These yarns were then also cut into 20 cm pieces and spanned across the frames using tape.

2.3.5 3D printing parameters

The three-dimensional design of the block was created using computer-aided design (Autodesk Meshmixer, Autodesk Inc., San Rafael, CA, USA). The block dimensions were 5 x 15 x 10 mm (unless mentioned otherwise), with a lattice structure having an infill density of

60%. This denotes the amount of material that is printed within the overall object surrounded by an exterior wall. Samples were printed from PCL granules (Ashland Specialities, Ireland) with an Ultimaker 3 Extended 3D printer (3D4Makers, Haarlem, The Netherlands), operated by 3DLifePrints (Oxford, UK). The material was extruded at 110 °C and deposited in layers of 150μm. No build plate heating was used in the PCL 3D printing process and all parts were printed at room temperature. A solvent free glue stick (chemical base: modified starch) was used to adhere the PCL print to the glass build plate of the 3D printer and prevent warping.

2.3.6 Incorporating the ES filaments during 3D printing to create the biphasic constructs

An overview of the incorporation process of the ES filament into the 3D printed blocks is shown in Figure 2.1. Following electrospinning and assembly of the filaments onto the frames, 3D printing was initiated. The printing was automatically stopped to insert the ES filaments or yarns across according to the pre-defined number of layers (see Table 2.1). The pre-assembled fibres were quickly transferred from their U-frames and taped down on the printing platform to ensure that the movement of the nozzle would not disrupt their alignment. For the twisted yarns, the last 2 cm was untwisted and frayed so that each individual fibre would have maximum contact with the extruded material. Printing was then resumed, and the process was repeated until completion of the pre-defined number of steps to produce the biphasic construct, consisting of a soft cuff made of ES filaments or yarns and a hard 3D printed block.

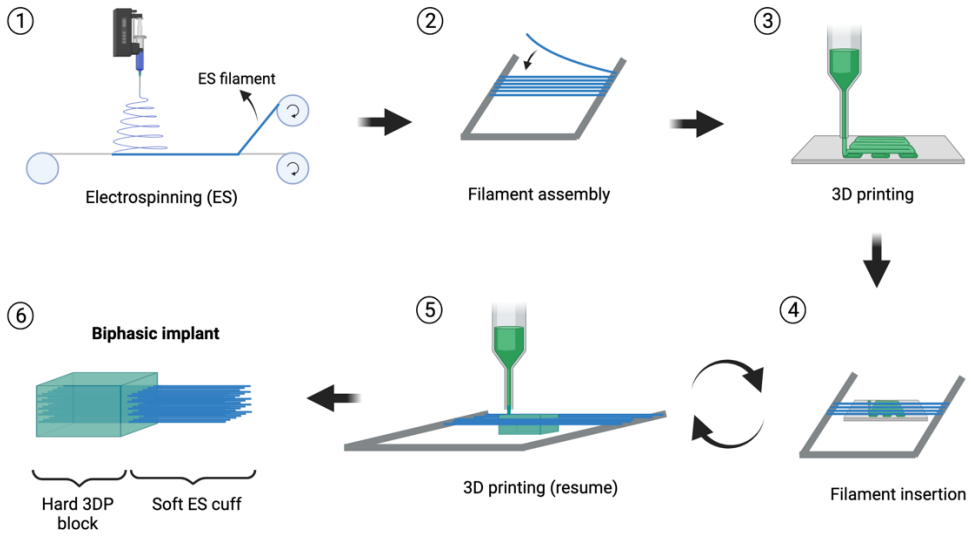

Figure 2.1 Schematic overview of the proposed approach to create soft-hard biphasic implant using electrospinning and 3D printing: (1) filament electrospinning, (2) assembly of the filaments onto U-frames, (3) initiation of the 3D printing, (4) interruption of the 3D printing to insert the ES filaments or yarns, (5) resuming of the 3D printing, (6) completed biphasic implant with an ES cuff and a 3DP block. Note that (4) and (5) are repeated as many times as needed.

Table 2.1 Interruption of the 3D printing based on the number of ES filaments layers. The minimum height of printed materials between layers was 0.45mm and the final height of the blocks was 5mm.

# of layers of filaments in the print	Height at which the printing was interrupted (mm)
1	2.70
5	0.50, 1.40, 2.30, 3.20, 4.10
10	0.50, 0.95, 1.40, 1.85, 2.30, 2.75, 3.20, 3.65, 4.10

2.3.7 Scanning electron microscopy (SEM)

Samples were cut and mounted on an aluminium stub (Agar Scientific, Essex, UK) with use of a carbon adhesive (Agar Scientific) and gold coated for 120 seconds with use of the SC7620 Mini Sputter Coater System (Quorum Technologies Ltd, UK). They were imaged by SEM (Carl Zeiss Evo LS15 Variable Pressure Scanning Electron Microscope) at various magnifications to examine the morphology of the samples. Measurements were taken using ImageJ software (National Institutes of Health, Bethesda, USA).

2.3.8 Tensile testing

Samples were tested to failure with a tensile testing machine (Zwick Roell Group, Ulm, Germany) using a 5 kN load cell and custom-made clamps that were previously described (*269*). The initial grip-to-grip separation was set at 10 cm and the test was then performed at a

rate of 20 mm/min. The force at failure and change in distance between the grips were recorded with the testXpert II software (Zwick Roell Group, USA). The stress applied to the scaffold was calculated as $\sigma = F/A$ whereby F is the force (N) applied over the initial area A (mm^2). An apparent cross-sectional area of 0.3 mm^2 and a porosity of 67% per filament were used to calculate the area of the filaments, based on work performed by Abhari et al in which porosity of PDO filaments was calculated using mercury porosimetry (*269*). The strain was defined as $\varepsilon = (L_0+L_i)/L_i$, whereby L_0 is the displacement value and L_i is the initial grip-to-grip distance. Six samples were tested per experimental condition to compare the different polymers and parallel and twisted configurations, whereas four samples were tested in the scale-up experiments.

2.3.9 Thermal analysis

To assess the potential effect of the 3D printer nozzle's high temperature on the filaments during the printing process (in particular, at the exit of the printed block), PCL and PDO filaments were heated at different temperatures (60, 80, 90, 100, 110 and 120°C) in an oven (Fisherbrand Gravity Convection Oven) for 1 minute. These samples were not tested for tensile properties. Fibres stored at room temperature were used as controls. A differential scanning calorimeter (TA Q2000-1275 Differential Scanning Calorimeter, DSC) was then used to evaluate the thermal properties of the samples. For each condition, approximately 5 mg of sample was fitted in an aluminium pan (TZero Aluminium), along with an empty tin as the reference standard. The pans were heated a heating rate of 10 °C/min in a nitrogen atmosphere, from 0 °C to 90 °C and -20 °C to 135 °C for PCL and PDO, respectively. A second heating and cooling cycle was performed to erase the thermal history of the sample and any residual solvent. From the DSC thermogram of the first cycle, the melting temperature (T_m), measured area of the thermal capacity (ΔH_m) and, if available, measured area of the annealing peak (ΔH_a)

and of the recrystallization peak (ΔH_c) were determined (*295*). Recrystallization is observed as an exothermic peak just before the melting peak(*296*). Heat of fusion (ΔH_f) was calculated by averaging ΔH_m and considering the melting enthalpy of the recrystallization (ΔH_c) and of the annealing (ΔH_a) peaks, if observed (Hf = (Hm-Hc)+Ha) (*295, 297*). Crystallinity was calculated by dividing the resulting heat of fusion by the theoretical heat of fusion of a 100% crystalline sample (ΔHf°) for PDO (141.2 J/g) and PCL (139.3 J/g), respectively (*297, 298*), see equation below:

$$\% \, crystallinity = \frac{\Delta Hf}{\Delta Hf^{\circ}} \; x \; 100\% \qquad (1)$$

2.3.10 Cell culture and maintenance

Human foreskin fibroblasts (HFF-1 cell line, ATCC) were used to seed on the electrospun soft cuff, and were maintained in growth medium DMEM F12 (Lonza, UK) supplemented with 15% foetal bovine serum (FBS, Biosera UK) and 1% penicillin–streptomycin solution (P/S, Gibco, UK), according to the supplier's instructions. A human osteoblast-like cell line was used (MG-63, Sigma Aldrich, UK) to seed on the 3D printed hard cuff. For the neutral red uptake assay, mouse BALB/c 3T3 fibroblast cells (Merck, Germany) were maintained at 37°C, 5% CO_2 in Dulbecco's Modified Eagle Medium (DMEM, Sigma-Aldrich, UK) supplemented with 10% new-born calf serum (NCS, Sigma-Aldrich, UK), 4 mM L-glutamine (Thermo Fisher Scientific, UK), 20 mM 4-(2-hydroxyethyl)-1-piperazineethanesulfonic acid (HEPES, Thermo Fisher Scientific) and 1% penicillin/streptomycin (Gibco, UK). Cells were cultured in T-75 flasks (Thermo Fisher Scientific) with a fresh media change every two to three days. Once cells had reached approximately 90% confluency, they were split at a ratio of 1:3 and sub-cultured under the same conditions to allow proliferation with a maximum passage of 15 (BALB/c 3T3) and 20 (HFF-1 and MG-63). Cellular morphology and adherence was assessed prior to each

media change and prior to cell seeding by light microscopy. In cases of unusual morphology and slow growth densities (i.e. round instead of flat and elongated cells) the flask was discarded. Culture medium was regularly tested for mycoplasma using a MycoAlert testing kit (Lonza, UK) according to the manufacturer's instructions.

2.3.11 Assessment of cell seeding efficiency and proliferation over time

Scaffolds (n = 3, biological repeats) were prepared for cell seeding by being soaked in culture media (DMEM F12 supplemented with 15% FBS and 1% P/S) for two hours at 37 °C, 5% CO_2. Once cells had reached >90% confluency, they were mechanically scraped and counted using a hemacytometer counting-chamber device and seeded at different densities and volumes (Table 1). A standard curve was generated by seeding cells in triplicate (n = 3) at densities of $1x10^4$, $2.5x10^4$, $5.0x10^4$ and $1x10^5$ in a 48-well plate (Corning Inc., Corning, NY, USA). To estimate cell numbers from this curve a simple linear regression was applied using GraphPad Prism version 9 (GraphPad Software Inc, San Diego, USA). After seeding cells onto the scaffolds, the plate was placed in the incubator for two hours to allow cells to attach (the seeding plate). Then, the scaffolds were transferred to a new 48-well plate and topped up with fresh culture medium. The seeding plate was saved to assess attachment of the cells on day 1. This was approximated by using a PrestoBlue assay (Invitrogen, Paisley, UK) to measure metabolic activity (*299*). This is an oxidation-reduction-based assay in which resazurin, a blue non-fluorescent dye, is taken up by live cells and reduced to resorufin, a highly fluorescent component. This change in colour can be detected by measuring fluorescence in a microplate reader and obtaining a change in fluorescence intensity units (FIU) over time. It can therefore technically be used to quantify cellular proliferation and has the advantage of being non- destructive to cells so the same cell population can be evaluated across specified time points. Briefly, culture medium in each relevant well was replaced with

400 µL of a 10% PrestoBlue solution (v/v in DMEM) at selected time-points (day 1, 4, 7, 14 post-seeding) and incubated for 1 hour at 37°C, 5% CO_2. Afterwards, 100 µL of each sample was transferred in triplicate to a white, flat-bottom 96-well plate (Corning, UK). Fluorescence was measured at 485nm excitation and 520nm emission using a FLUOstar optima microplate reader (BMG Labtech, Germany). A well containing just the PrestoBlue solution was used to correct for background signal. The scaffolds were then rinsed with PBS and transferred to new 48-well plates containing fresh, pre-warmed cell culture media. Scaffolds were placed into new 48-well plates with fresh medium every two to three days to exclude cells that had attached to the bottom of the well plates. The percentage of cells that had successfully attached to scaffolds was quantified by determining the ratio of the microplate readings (FIU) of the seeding plate and the scaffolds after day 1, corrected for background, see equation below. The estimated cell number was then calculated using the calibration curve.

$$\%\ cell\ attachment = \frac{FIU\ day\ 1\ plate}{(FIU\ day\ 1\ plate + FIU\ seeding\ plate)}\ x\ 100\% \quad (2)$$

2.3.12 Assessment of cytotoxicity

The neutral red uptake (NRU) assay for cytotoxicity was used according to previously published work (*293*). It is an established method to indirectly evaluate toxicity in the biological evaluation of medical devices guided by the ISO 10993-5:2009(*300*). Prior to carrying out the assay, 0.1 g of each sample (PDO ES filaments, PCL 3DP samples, FiberWire sutures, polyethylene caps, rubber bands) was weighed out and submerged in 70% ethanol for two hours. They were then washed with sterile phosphate buffered saline (PBS, Sigma-Aldrich, UK) three times, transferred to separate 10-cm petri dishes, and left to dry overnight. The next day, samples were extracted at a ratio of 0.1 mg/mL (guided by the extraction ratios outlined

in ISO 10993-12 for irregularly shaped devices) in medium consisting of DMEM as described above but consisting of 5% NCS instead of 10%. The samples were incubated in the medium at 37 °C for 72 hours under agitation. Next, BALB/3T3 cells were seeded into 96-well plates (without samples) at a density of 1x 10^4 cells/well and left to adhere for 24 hours to form a sub-confluent monolayer. The different extraction media, corresponding to the testing materials, was added to the wells as undiluted, 2-fold and 4-fold dilutions. The plate was incubated for another 24 hours before neutral red uptake was determined and compared to control wells (cells exposed to DMEM only). Absorbance was measured at 540 nm using the FluoStar Optima microplate reader (BMG Labtech, Ortenberg, Germany). Cell viability was calculated as the percentage of values obtained for the cell culture medium only (control). Three technical repeats were used per experiment (n = 3). As recommended by the ISO 10993-12, sodium lauryl sulphate (SLS, Sigma-Aldrich, UK) was used as positive control and tested in a four-concentration scale (*300*). Rubber bands were used as a secondary positive control. Polyethylene caps were used as a negative control. Finally, FiberWire sutures (Arthrex, Naples, Florida, US) were used as a comparator to the PDO and PCL materials.

2.3.13 Statistical analysis

Statistical analysis was performed with GraphPad Prism version 9 software (GraphPad Software Inc, California, USA). Data in graphs are expressed as means with standard deviations. A standard one-way ANOVA with Tukey's multiple comparisons testing was used to examine statistical differences between groups. Results were considered statistically significant for $p < 0.05$. Experiments were performed in six repeats for the mechanical testing, except for the scale-up manufacturing which was done in four repeats due to the amount of material it required. The thermal analysis was done in triplicate for both polymer types. Cytotoxicity assessments were performed in triplicate.

2.4 Results and discussion

2.4.1 Manufacturing biphasic scaffolds: PDO soft cuff *versus* PCL soft cuff

The approach described in the method section (Figure 2.1) was successfully applied to create soft-hard scaffolds consisting of a 3DP PCL block with an integrated ES cuff. As shown in Figure 2.2, the biphasic scaffolds could be produced with either a PDO or a PCL ES cuff. Prototypes were created with 60 filaments in total over four layers (15 filaments per layer). For the tensile tests shown in Figure 2.2 I-L, the number of filaments per scaffold was downscaled to nine filaments per block for this initial stage to limit the use of electrospun filaments that were needed for the experiments throughout this thesis. SEM images indicate that, while the PDO cuff morphology remained intact during the assembly, the micro-fibrous morphology of the PCL cuff was lost near the insertion zone into the 3DP block. This suggests that fibres melted as consequence of the melting point of PCL filaments (~57°C) being much lower than the temperature of the extrusion melt (~110°C) used during the 3D printing process. This means that PCL fibres could not be used in combination with PCL 3D printed material and it was decided to continue the experimental phase with PDO electrospun fibres instead.

In terms of mechanical properties, biphasic scaffolds with a PDO cuff led to slightly higher breaking forces compared to the scaffolds with a PCL cuff ($p= 0.0177$, Figure 2.2I). However, controls performed with the ES cuff material only (no block) indicated that for both PDO and PCL, the insertion of the cuff in the block had a significant effect on its mechanical properties ($p<0.0001$, Figure 2.2I). This is also evident from the respective stress and strain values ($p<0.0001$, Figures 2.2J and 2.2K). A decrease in all properties was observed for the PCL cuff and this was expected because of the melting of the PCL filament near the insertion zone. For PDO, similar observations were made. While no melting was observed, this effect can be explained by annealing of the region of the filaments near the insertion.

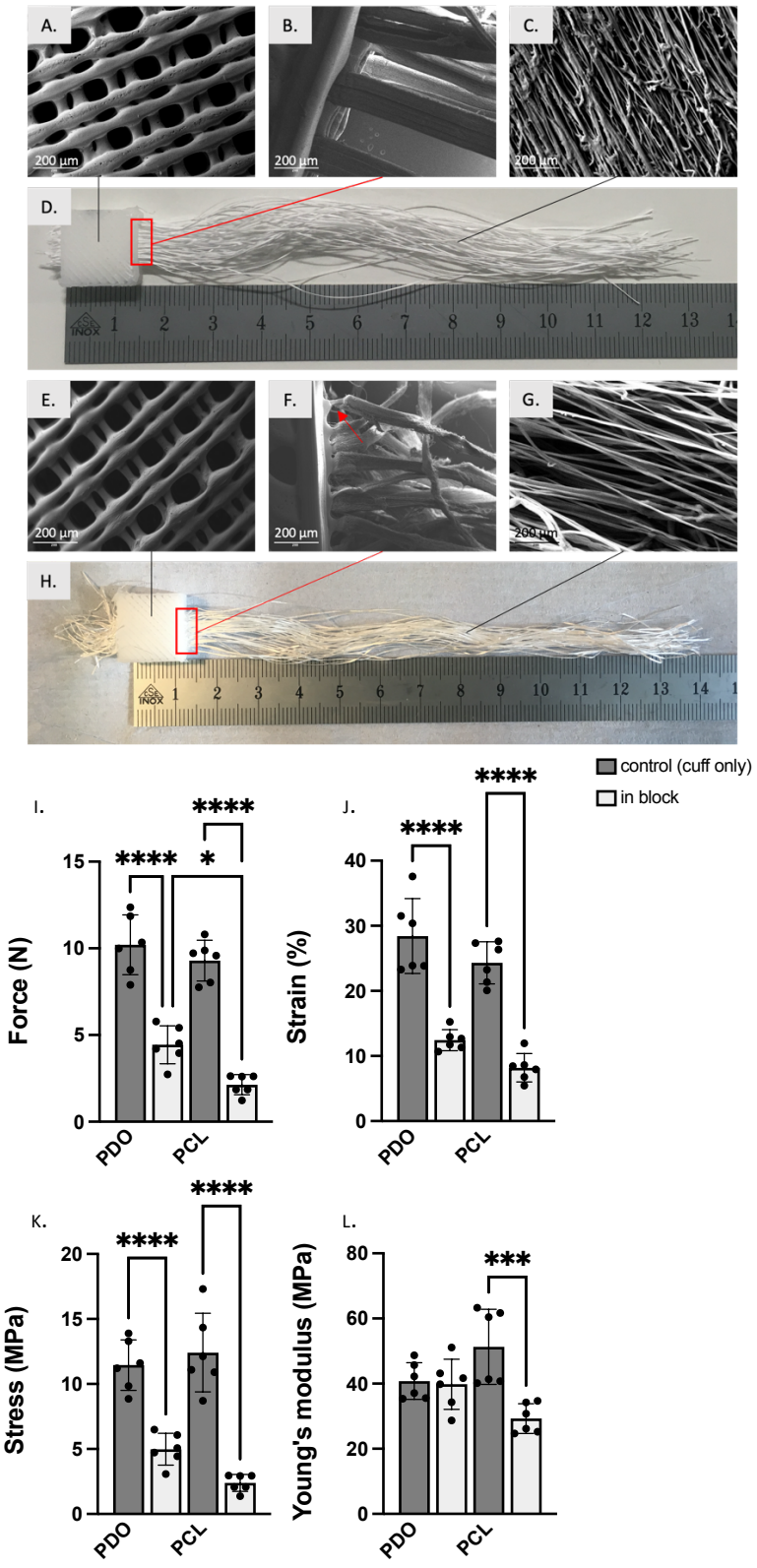

Figure 2.2 Soft-hard scaffolds made of a 3DP printed PCL block and either a PDO (A-D) or a PCL (E-H) ES cuff. SEM images are taken of prototype scaffolds consisting of 60 filaments in four layers. A) SEM image showing the 3DP lattice (made of PCL) embedding the PDO cuff; B) SEM image showing the interface between the 3DP block and the PDO cuff; C) SEM image showing the submicron fibres within the PDO filaments; D) gross appearance of the biphasic scaffold with PDO cuff; E) SEM image showing the 3DP lattice (made of PCL) embedding the PCL cuff; F) SEM image showing the interface between the 3DP block and the PCL cuff ; G) SEM image showing the submicron fibres within the PCL filaments; H) gross appearance of the biphasic scaffold with PCL cuff. I-L) Tensile properties of the biphasic scaffolds and control cuffs, each involving 9 filaments in one layer: force at failure (I), maximum strain (J), maximum stress (K), Young's modulus (L), n = 6. Scale bars = 200 µm. P-value of <0.05 is denoted as *, p<0.001 as *** and p<0.0001 as ****.

2.4.2 Thermal analysis

Annealing occurs when PDO is exposed to high temperature (*295*). As shown in Table 2.2, a thermal analysis of the PDO filaments subjected to temperatures ranging from 60 to 120°C for 1 minute (to roughly mimic the contact with the extrusion melt before cooling down) indicated that the polymer crystallinity was affected by a short exposure at 90°C and above (increase at 90°C, decrease at 100-120°C). Annealing, and the subsequent change in crystallinity can affect the mechanical properties and degradation kinetics (*295*). The fact that all samples (PCL and PDO ES cuffs) failed at the interface between the soft and hard components is consistent with the explanations provided above. The thermographs of the differential scanning calorimetry (DSC) for the PDO and PCL samples heated at different temperatures compared to room temperature (RT) are shown in Figure 2.3. The graphs show the heat flow associated with the transitions of the polymer as a function of time and temperature and have a few identifiable regions. The main melting peak of PDO is around 106°C and is similarly shaped for most samples (Figure 2.3A). Small endothermic peaks can be observed around 40°C, corresponding to an annealing peak with a shift in temperature. A clear exothermic peak is observed around 80°C just before the melting peak for samples heated at 100°C, 110°C and 120°C, indicating recrystallisation of the samples. For the PCL samples, no annealing or recrystallisation peaks are present (Figure 2.3B). The main melting peak is around 58°C and shows a difference in the narrowness and elongation of the peaks for all samples with an onset of melting around 30°C. There is a trend of a broader and shorter peak for samples heated at increasing temperatures, with the broadest and shortest peak for samples heated at 120°C. Table 2.2 shows the calculated heat of fusion and corresponding crystallinity for PDO and PCL, as compared to the values of a 100% crystalline sample, as well as onset of melting, melting point, and relevant heat enthalpies. Change in crystallinity is also visualised in Figure 2.4 for PDO and PCL, respectively. Crystallinity decreases for PDO samples initially, but peaks for samples heated

at 90°C ($p = 0.0042$), followed by a significant dip at 100°C ($p = 0.0006$) and a consistently lower value for 110°C and 120°C ($p = 0.0114$ and $p = 0.0057$, respectively. Onset of melting seems to be at slightly higher temperatures with increasing treatment temperature, but it decreases for samples heated at 100°C and over. For the PCL samples, crystallinity is lower for all samples compared to room temperature (RT) and there is a shift in onset of melting as well to a slightly higher temperature, although not significantly.

PDO and PCL are both a semi-crystalline polymer, meaning that they consist of an amorphous and crystalline region, have a highly ordered molecular structure and exhibit a sharp melting point when exposed to heat (*238*). Higher crystallinity increases the intermolecular bonding resulting in higher strength (*301*). Although the calculated heat of fusion and crystallinity is decreased for both polymer samples as they are heated at higher temperatures (Table 2.2), it only translates in a significant loss of mechanical properties for the PCL samples. This can be explained by the differences in melting temperature, as the range of temperatures used in this experiment exceeded the melting point of PCL (~58°C), but only noticeably altered PDO samples around its own melting point (~106°C). However, heat treatment (annealing) can improve the mechanical properties of polymers because it influences the proportion and organization of amorphous and crystalline regions resulting in an increase in crystallinity. It has been shown previously that mechanical properties of electrospun PDO change marginally when exposed to heat for longer periods (*295*) and this might explain why these filaments are also only marginally affected by the printing process. During a heating and cooling cycle, crystallisation events can occur before the melting point as polymer chains become more mobile during the heating cycle and give off energy (i.e., heat) when moving into a more stable phase. This is referred to as recrystallisation or cold crystallisation and can be observed in the PDO thermograms around 80°C, just before the melting peak. It only occurs for samples that were pre-heated at 100, 110 and 120°C and has been previously observed in PDO and PLLA

samples that were subject to annealing (*297, 302*). The small endothermic peaks around 40°C are annealing peaks and give information about the previous heat history of the sample (*303*). The location of the peaks depends on the annealing temperature and time (*304*) and has been reported in semicrystalline polymers undergoing annealing as well (*295, 296*). This peak in the samples indicates the formation of crystals that partially melt and recrystallise during the heating cycle until they are completely molten in the main melting peak observed (*305, 306*). In the second heating and cooling cycle, after the thermal history has been erased, this peak disappears, as well as the recrystallization peak and all samples show the same single melting peak. For all PCL samples there is an absence of any other endo- or exothermic peaks, bar the melting peak, which could be explained by the fact that the temperatures used to heat the samples were above the melting point of PCL and thermal degradation could therefore not be captured by the DSC experiment, i.e., the samples were already fully molten before being analysed by DSC. It could also mean that the time exposed to the heat was not long enough to capture any significant events (*305*).

Table 2.2 Thermal properties of PDO and PCL filaments subjected to high temperatures (ranging from 60 to 120°C) for 1 minute. P-values refer to RT control values.

	Treatment	T_m (℃)	$T_{m,\ onset}$ (℃)	ΔH_m (J/g)	T_c (℃)	ΔH_c (J/g)	T_a (℃)	ΔH_a (J/g)	ΔH_{total} (J/g)	Crystallinity (%) (p-value)
PDO cuff	**RT control**	105.8±0.1	87.8±0.7	74.2±2.2	-	-	47.2±0.7	3.8±0.9	78.0±2.1	55.2±1.5
	60℃	106.3±0.3	89.1±1.3	77.3±2.2	-	-	-	-	77.3±2.2	54.8±1.6 (0.9998)
	80℃	106.1±0.2	91.8±0.9	77.2±0.9	-	-	-	-	77.2±0.9	54.7±0.6 (0.9996)
	90℃	105.9±0.3	92.0±0.6	85.0±2.3	-	-	43.3±1.0	1.7±0.4	86.7±2.3	61.4±1.7 **(0.0042)**
	100℃	106.7±0.1	90.8±1.1	68.7±1.1	89.4±1.4	3.4±1.7	41.0±0.9	2.0±0.5	67.2±2.3	47.6±1.6 **(0.0006)**
	110℃	106.6±0.2	83.1±1.4	74.9±4.3	80.0±2.8	8.5±1.3	43.7±0.8	3.8±0.4	70.3±3.5	49.8±2.5 **(0.0114)**
	120℃	106.4±0.3	79.8±1.7	73.9±1.6	77.9±0.2	8.3±0.4	41.1±0.5	3.9±0.3	69.6±1.4	49.3±1.0 **(0.0057)**
PCL cuff	**RT control**	56.8±0.2	30.7±0.9	79.3±0.2	-	-	-	-	80.1±2.1	57.4±1.5
	60℃	53.6±0.7	32.0±0.1	74.9±0.9	-	-	-	-	73.6±1.8	52.7±1.3 (0.1669)
	80℃	53.1±0.7	32.2±0.3	74.7±1.0	-	-	-	-	73.9±2.3	52.9±1.7 (0.1372)
	90℃	53.5±0.5	33.0±0.6	74.7±0.7	-	-	-	-	72.6±1.1	52.0±0.8 (0.1409)
	100℃	52.1±1.7	33.9±0.8	72.7±2.3	-	-	-	-	71.6±3.5	51.3±2.5 **(0.0153)**
	110℃	53.9±2.9	33.3±0.4	75.2±4.1	-	-	-	-	75.2±4.1	53.9±2.9 (0.2298)
	120℃	52.4±1.3	33.9±0.5	73.2±1.8	-	-	-	-	70.2±2.9	50.3±2.1 **(0.0265)**

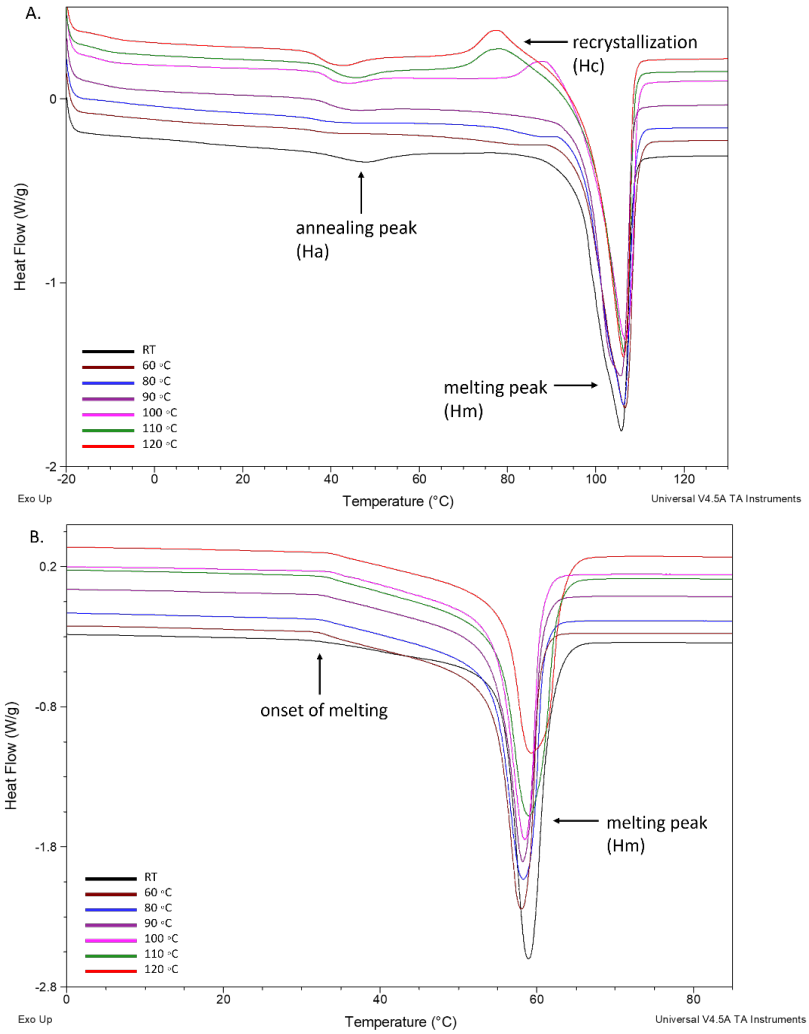

Figure 2.3 DSC thermographs for PDO samples (A) and PCL samples (B) at room temperature (RT) and heated at temperatures ranging from 60-120°C for one minute. Small endothermic peaks are seen around 40°C for PDO. The samples heated at 100, 110 and 120°C show a clear exothermic peak just before the melting peak indicating cold crystallinity. No annealing or crystallinity peaks are present for the PCL samples. All samples have a similar onset of melting but differ in the elongation and narrowness of their respective melting peaks, n= 3.

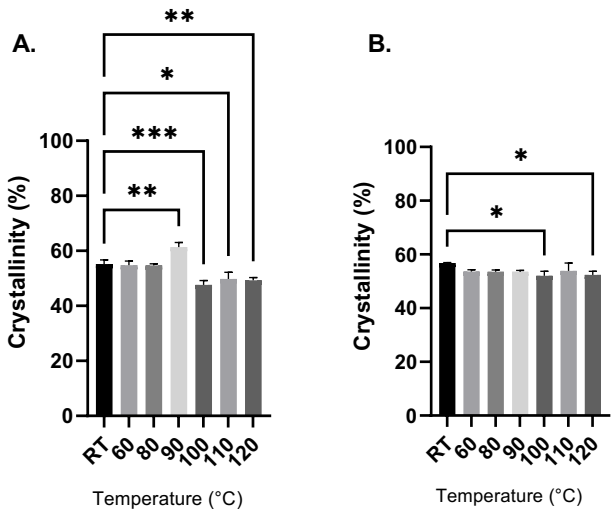

Figure 2.4 Crystallinity values for PDO (A) and PCL (B) across different temperatures. Values of $p<0.05$ are considered significant. P-value of <0.05 is denoted as *, $p<0.01$ as ** and $p<0.001$ as ***.

2.4.3 Cuff design: parallel filaments *versus* multifilament yarns (PDO cuff)

To investigate the effect of ES cuff design on the mechanical properties of the biphasic scaffolds, we compared twisted ES yarns to the parallel ES filaments previously presented (Figure 2.5A-D). Twisting was done to improve the ultimate force of the filaments within the blocks and was done using the PDO filaments only, due to the melting of PCL filaments described in the previous section, which made them unsuitable for use in the biphasic construct. While possible, layering the twisted yarns was considerably more challenging than the parallel filaments because of the difficulty of maintaining alignment of the frayed ends and preventing individual filaments from crossing over each other and sticking together during printing due to the movement of the printer head. Therefore, the fabricated biphasic scaffolds with twisted yarns were of lesser quality and did not provide sufficient adhesion in the 3D printed layers. This was also evident when testing the scaffolds composed of twisted yarns to failure, as they appeared to be slipping out of the blocks rather than breaking (as observed for the parallel filament configuration), indicating the smaller contact area between filaments and the 3D printed block, not sufficient to obtain proper adhesion. All samples (twisted and parallel) failed just past the interface point, at a maximum of 10.2 ± 1.6 N, and while the failure behaviour differed, it is worth noting that – apart for the Young's modulus, which was slightly higher for twisted cuffs – the overall force, stress and strain of biphasic implants did not change with the ES cuff design (Figure 2.5E-H). However, slippage of the twisted cuff means that those samples may have led to higher mechanical properties. Therefore, despite ES twisted yarns being more challenging than parallel filaments to embed in the 3DP block, it could still be a strategy worth exploring in the future to create stronger structures. Further work should investigate better cuff designs for example by optimising the number of twists within yarns. Indeed, the control cuffs (*i.e.* cuffs without a block), showed a negative effect of the twist on its mechanical properties: parallel cuffs were stronger than twisted yarns with an ultimate

tensile strength of 10.2 ± 1.6 N and 5.7 ±1.7 N respectively ($p < 0.0001$, Figure 2.5E). This was unexpected as twisted yarns tend to perform better in terms of ultimate tensile strength due to the increased adhesions between filaments and thus higher frictional forces within the bundle (*294*). Such difference could be due to the degree of twisting being too high, resulting in (micro)fibre damage which potentially could have reduced the overall strength of the yarn (*307*). Furthermore, because the individual filaments within the yarn are not aligned to the axis in which load is applied, fibre obliquity can occur and this may also reduce the overall strength (*308, 309*). Looking into these aspects were however out of the scope of this study and will be addressed in the future.

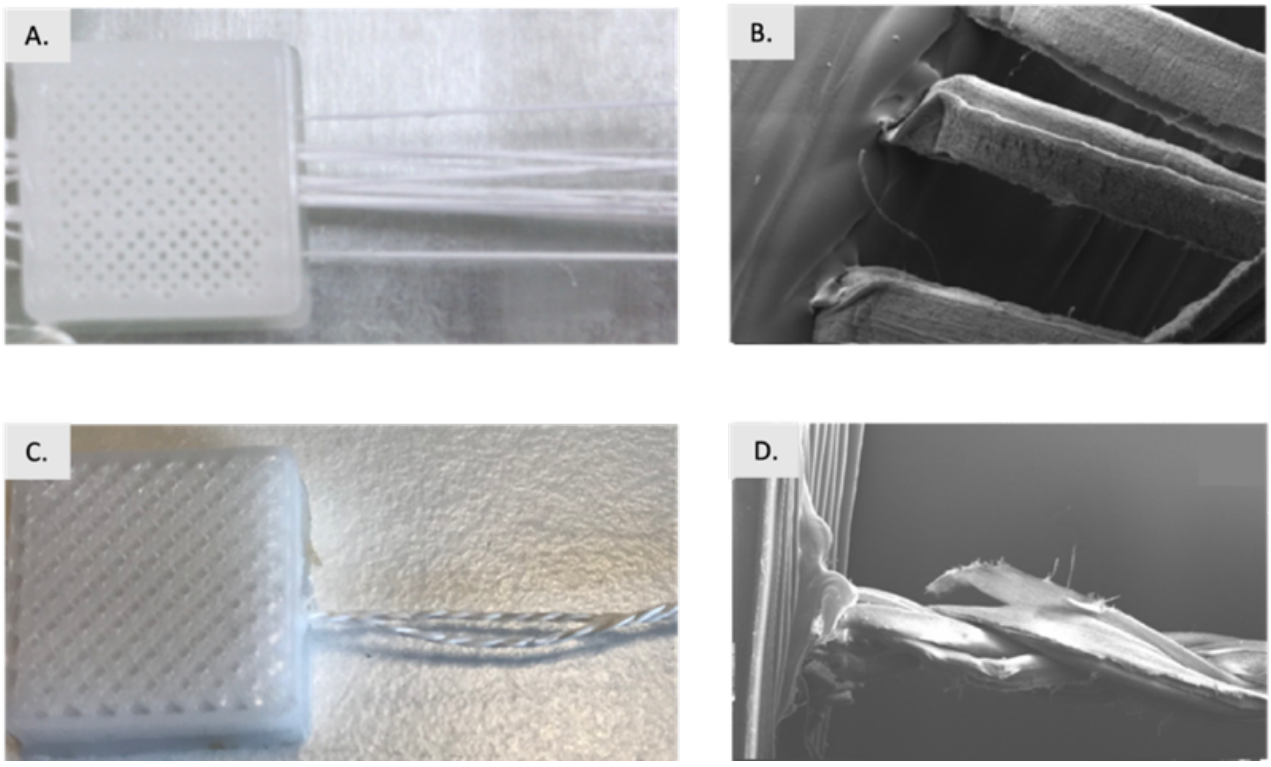

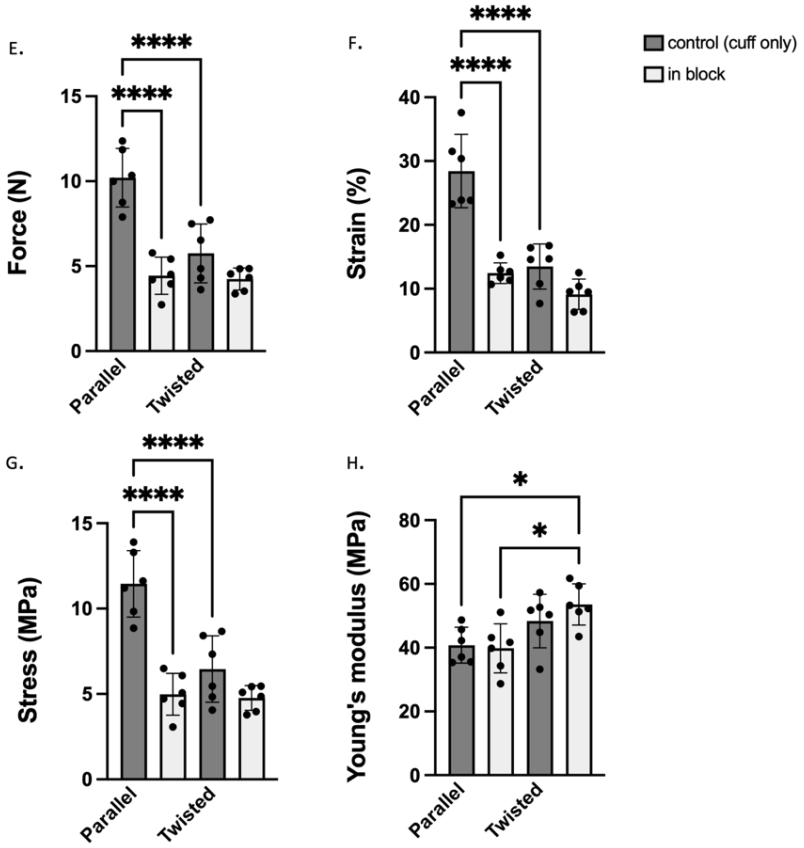

Figure 2.5 ES-3DP biphasic scaffolds with ES filaments in a parallel or twisted configuration. A. gross appearance of scaffolds with parallel filaments, B. SEM image showing nine parallel filaments in one layer emerging from the block, C. gross appearance of scaffolds with twisted filaments, D. SEM image showing a twisted yarn (made of 9 filaments) emerging from the block. E-H: mechanical properties of the biphasic scaffolds and cuff controls, involving 9 filaments in either twisted or parallel configuration. This included force at failure (E), maximum strain (F), maximum stress (G), Young's modulus (H) n = 6. P-value of <0.05 is denoted as * and p<0.0001 as ****.

2.4.4 Scaling-up the ES cuff size to reach clinically relevant forces

Figure 2.6 demonstrates the possibility to significantly increase the number of embedded filaments for the ES cuff to reach higher failure forces. Up to 27 ES filaments could be inserted across the width of the 3DP structure while 10 stops could be executed with the 3D printer, meaning that a maximum of 270 filaments could be embedded into the block. Figure 2.6A-C shows a single layer of 9, 18 and 27 filaments respectively and in Figure 2.6D-F the number of layers was increased to 5 to reach 90 filaments (5x18), and then to 10 to reach 180 filaments (10x18) and 270 filaments (10x27), respectively. A minimum of 0.45 mm of extruded material (corresponding to 3 passages of the printer head) was necessary between each layer of cuff material to ensure the lattice structure would not be compromised during printing. It was

observed that reducing the layer height more than this would result in disruption of the lattice order. The force at failure of the scaled-up scaffolds exhibits a relatively linear relationship for the number of filaments inserted, as expected (Figure 2.6G). The maximum force of the scaffold including 270 filaments was 226.8 ± 46.9 N. The stress, strain, and Young's Modulus (Figures 2.6H-J) increased only marginally with the increase in filament number. The calculated cross-sectional area did not take into account the spaces between inserted filaments which could have led to a variation in tension during tensile testing (*310*). Figure 2.7A shows a schematic illustration of the concept of the biphasic scaffold inserted into the footprint area of the supraspinatus tendon on the humeral head. The soft ES component would attach the tendon to the hard 3DP component embedded into the bone.

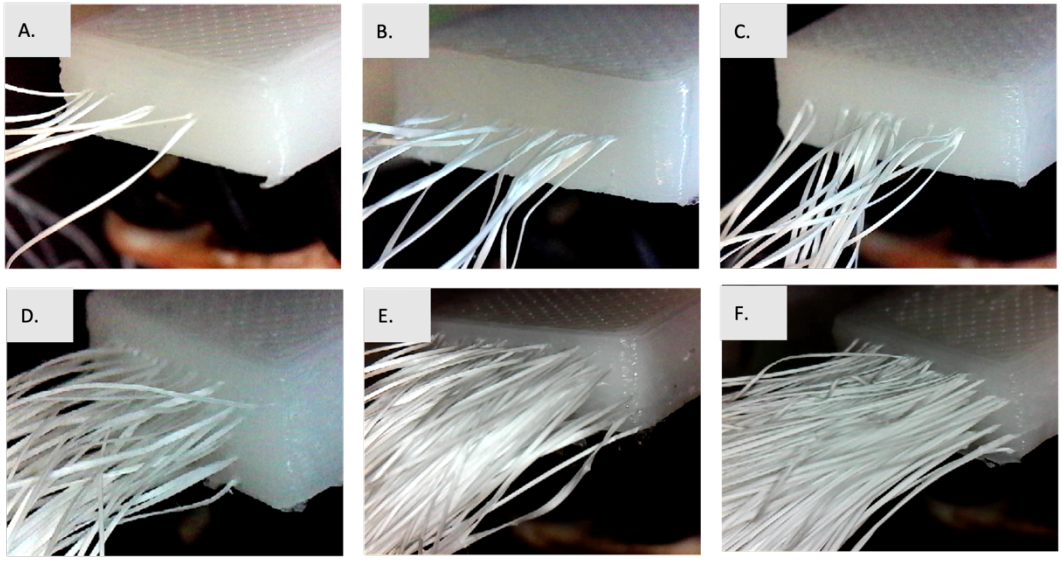

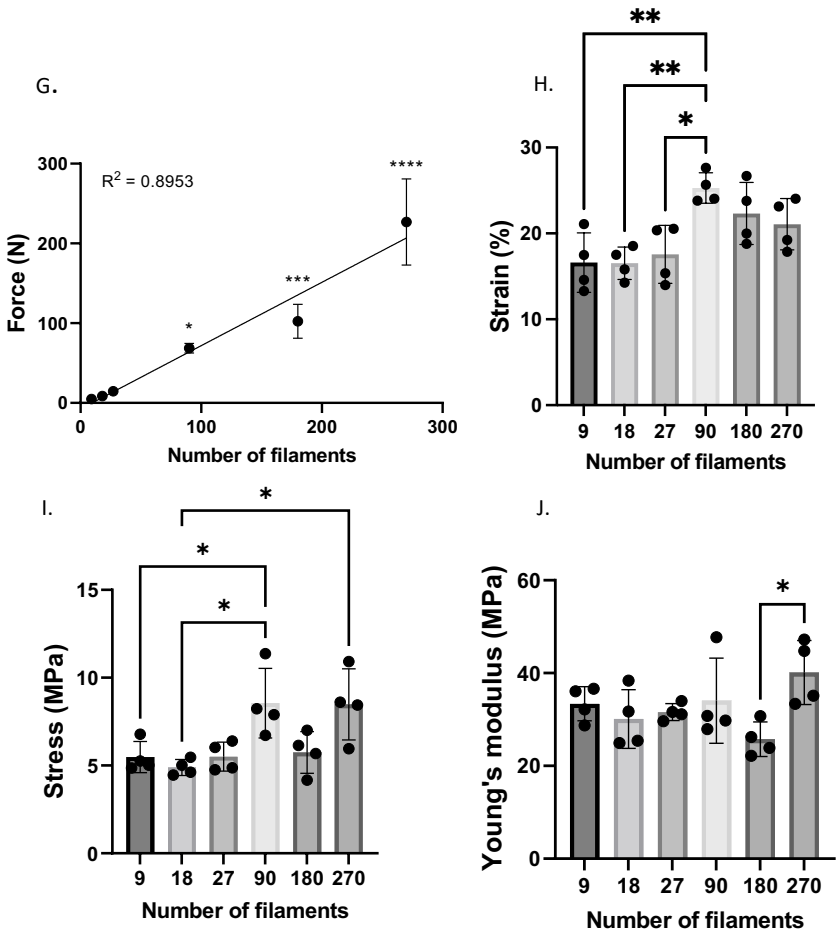

Figure 2.6 Increasing the cuff size to reach clinically relevant forces and demonstrate the scale up potential of the proposed approach. Figure A-F shows the number of filaments increased over the width (A-C) and height (D-E) with a maximum of 270 in 10 layers (F). Mechanical properties are portrayed in figures G-J with force at failure (G), strain (H), stress (I) and Young's Modulus (J) per filament number, n = 4. P-value of <0.05 is denoted as * and p<0.01 as ** .

2.4.5 Biocompatibility of the soft and hard components

To determine the cytotoxicity of the ES cuff (made of PDO) and 3DP block (made of PCL), an indirect NRU assay was performed. In this assay, guided by ISO 10993-5:2009, a relative cell viability above 70% indicates a non-cytotoxic material. As shown in Figure 2.7B, a viability of 82.8% and 81.9% (relative to control culture medium) was observed in the neat extract for the cuff and block, respectively, confirming that both components are non-cytotoxic. Positive controls (rubber and SLS) and negative controls (PE caps) were performed alongside the test samples to ensure that the assay was reliable. Furthermore, the compatibility of the ES cuff and 3DP block were compared to FiberWire, a well-known suture material used clinically in

musculoskeletal tissue repair and no significant differences could be seen between those materials. These results were expected as both PDO and PCL have a clinical record of safety (*311, 312*) and are used at medical grade in this work. They confirm that the manufacturing methods, in particular the use of organic solvent during electrospinning, did not impact on the cytotoxicity of the implant. Solvent residuals can indeed be a source of toxicity (*313*) and these results suggest that residual levels within the filaments were minimal.

The attachment, proliferation and morphology of fibroblasts and osteoblast-like cells on the ES cuff and 3DP block, respectively, are shown in Figure 2.7C-D. Fibroblasts were used to mimic behaviour of tenocytes and osteoblast-like cells to mimic that of osteoblasts. Seeding efficiency is 35% and 20% for the cuff and block, respectively (Figure 2.7C), similarly Savić et al found a seeding efficiency of around 25% for their electrospun filaments and Salerno seeded to around 30-50% efficiency on 3D printed PCL scaffolds of varying porosities (*293, 314*). This relatively low seeding efficiency may be explained by the highly hydrophobic nature of the material (*205*) and the presence of large pores in the structure tested (gaps between filaments or in the 3DP lattice), which resulted in most of the cell suspension flowing down to the bottom of the well-plate. Fibroblasts and osteoblasts proliferated similarly in terms of relative fold change on ES Cuff and 3DP respectively over 14 days (Figure 2.7D). Cells present on the materials are aligned along materials on the SEM images of Figures 2.7E-F. Cells on the ES cuff showed an elongated morphology (Figures 2.7F). These observations are consistent with the literature: primary cells seeded on electrospun filaments exhibit a fibroblast-like morphology by aligning themselves in the direction of the microfibers (*293, 315*) and while encouraging, future work is needed, using primary cells and co-culture models, to demonstrate cell migration within the materials and looking at their gene expression profile will be important to assess the healing potential of the biphasic scaffold (*173, 270, 279, 316, 317*).

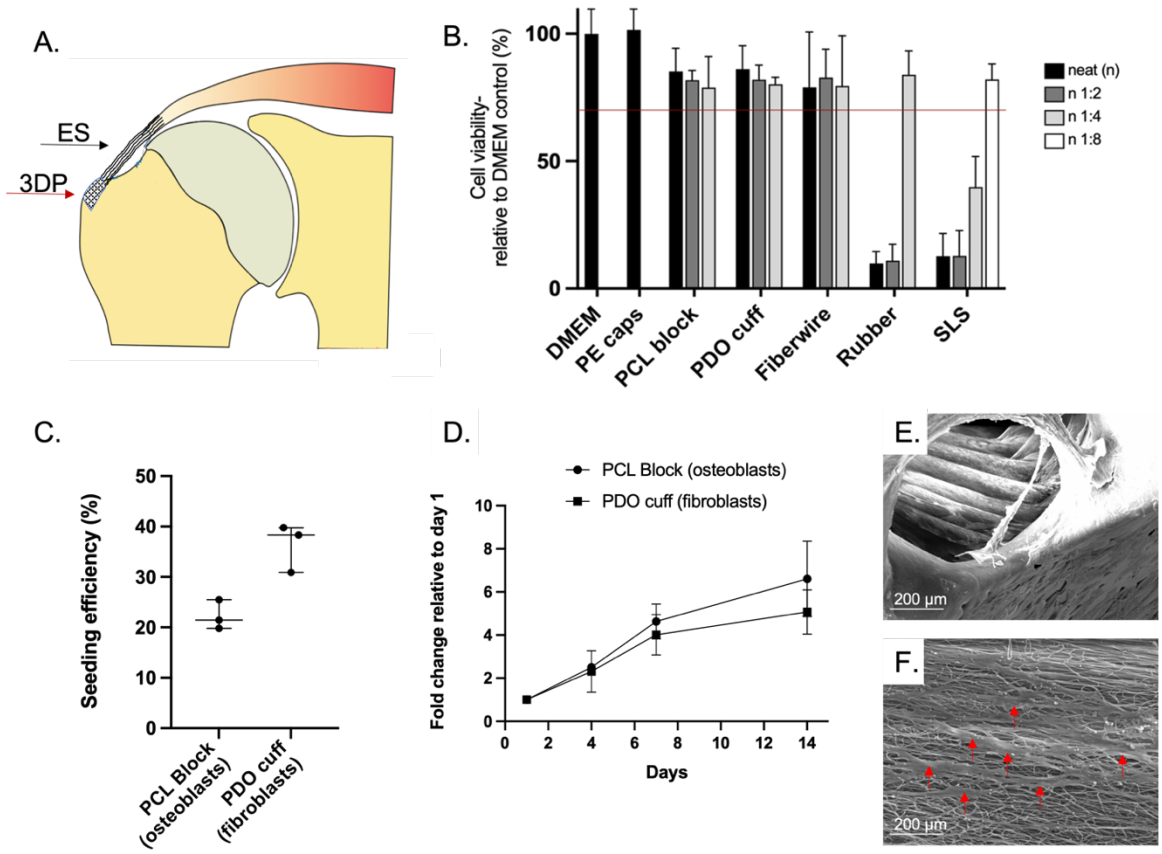

Figure 2.7 Cellular assays performed on the soft and hard components of the ES-3DP scaffold. A. Schematic of how the biphasic scaffold would fit into the shoulder joint, with arrows pointing to the individual components. B. NRU assay demonstrating the lack of cytotoxicity of the block and cuff component of the biphasic scaffold: cell viability was measured as a percentage of the vehicle medium (DMEM) and the materials were compared at undiluted concentrations (neat), 1:2 and 1:4 neat extract (Polyethylene (PE) caps were used as negative controls, rubber bands and SLS served as positive controls and commercially available FiberWire sutures were used as a clinical material control). C. Cell seeding efficiency on the ES cuff and 3DP block fibroblast and osteoblasts cell lines, respectively. D. Relative cell growth on the materials over 14 days E – F. SEM images showing cell morphology and spreading on the 3DP block and ES cuff (red arrows) at day 14, respectively. Scale bars = 200 µm

2.5 General discussion

This study aimed to create soft-hard biphasic scaffolds that could be used for enthesis repair by combining electrospinning and 3D printing. The presented approach can be used to produce biphasic implants that approach forces needed for clinical translation and is safe to use according to preliminary cell viability assays.

Efforts to recreate this interface in synthetic biomaterials have mainly focused on using chemical gradients, such as through increasing mineralization content with ß-tricalcium phosphate or hydroxyapatite particles, and structural gradients, such as through progressive fibre alignments (*318-323*). Multiphasic or hierarchical scaffold strategies are particularly

popular in the bone tissue engineering fields, but examples consist mostly of fibre-based scaffolds of differing diameters, and multi-layered or multiphasic scaffolds condensed into a single unit (*190, 324, 325*). They do not reflect the two distinctly separate materials relating to the enthesis (bone and tendon) nor possess the mechanical properties required to support repair of the entheses of the shoulder joint. Furthermore, designs do not account for whether they would be able to fit into the desired implant location (*326*). For example, the native supraspinatus enthesis is incredibly small and therefore requires very concise scaffold dimensions to be able to fit an implant here. Since many orthopaedic procedures are strictly arthroscopic this can pose a significant constraint as well (*262*). Another consideration is the biomechanics of the implant location, which can pose considerable geometric limitations (*327*). For example, an implant designed to fit into the supraspinatus area should be embedded completely level within the bone to prevent impingement happening when the shoulder abducts. Current suture and bone anchors are designed with this in mind.

Hybrid scaffolds made by electrospinning and 3D printing are currently being developed in the musculoskeletal field. Several strategies have been proposed, including: alternating between electrospinning and 3DP printing (*282*) electrospinning onto 3DP structures (*285*), printing on ES scaffold (*281, 284*)(*328*), assembling existing ES and 3DP components (*189, 283*) . However, most of these strategies focus on bone applications and none attempted to recreate a soft-hard biphasic scaffold for application to entheses (*e.g.,* at the rotator cuff).

Here we demonstrate that ES-3DP scaffolds with an ES cuff made of up to 270 filaments can be created. The ES cuff was embedded into a region of 150 mm^2 (10x15mm), an area that roughly reflects the dimensions of the footprint of the supraspinatus tendon enthesis, measured from human cadaveric specimens (*16, 329*). The ES cuff had a maximum force of failure of 226.8 ± 46.9 N, indicating a clear potential for clinical application from a mechanical point of

view. Indeed, sutures used for rotator cuff surgeries typically fail in the range of 184 – 359 N (*14, 330-332*), although this is heavily dependent on suture material, suture configuration, and tissue quality (tendon and bone). In future work, however, reaching loads of 250 N might be beneficial as it has been suggested that such levels of strength are needed for early passive motion in post-operative rehabilitation (*330, 331*). Data from human cadavers suggest that native supraspinatus tendon stresses and strain are between the ranges of 1.1-23 MPa (*178, 287, 289, 333-335*) and 1.4-28% (*178, 290, 333, 336*), respectively. This broad range can be attributed to the different experimental setups and the quality of the specimens tested. However, the stress and strain values reported of the tested scaffolds in this work fall within this range. Very limited data exists on the Young's Modulus, but is in the range of ~150 MPa for native supraspinatus tendon (*178*).

Several factors can be considered to further increase the maximum failure load of the ES cuff in the biphasic scaffold. Firstly, this could be done by improving the strength of the PDO filaments produced such as by decreasing the speed of the wire (to deposit more material) or increasing the concentration of pyridine in the polymer solution (*292*). Another factor to consider is textile design: although our attempt to use twisting to improve the ES cuff strength has been unsuccessful, assembly parameters were not explored in depth. Textile techniques such as braiding, twisting, weaving and knitting have long been used in medical applications (e.g., sutures, grafts) to improve mechanical parameters and consequently have also been adopted in the fabrication of biomaterials (*242, 243, 337*). Thirdly, since the high temperature of the nozzle and extruded melt was identified as a potential issue leading to decreased strengths (through annealing), approaches that reduce the melt temperature or shield the filaments from heat during incorporation may lead to better results. Alternatively using an additive manufacturing process that does not involve melt deposition might be worth

considering. Finally, modifying the print structure or working with a printer with better resolution might enable finer layers of material to be deposited and, as such, allow for the incorporation of more filaments and lead to higher strength values.

Overall, this study suggests that electrospinning and 3DP can be combined to produce biomaterials with robust soft-hard junctions that could help to regenerate entheses. However, it suffered from several limitations. Firstly, all scaffolds were fabricated by manually inserting filaments during the 3D printing process, leading to some variability between samples. Also, considering cost and time of manufacture of the scaffold components, the number of repeats for each sample was limited to either 4 or 6. Future work will benefit from more repeats while a more automated and efficient process will ensure more consistent scaffolds. Secondly, because of the large number of fibres required for building the biphasic scaffolds (*e.g.* 54 m per sample for those involving 270 filaments), filaments were often used from different batches and stored for prolonged periods of time (up to 3 months in desiccator). Batch-to-batch variations and degradation could account for differences observed in our mechanical datasets. Furthermore, while we performed mechanical test to failure, it would have been valuable to assess the scaffolds under cyclic loading regimes. It has been previously established that cyclic loads of between 100 N and 180N occur in supraspinatus tendon (*117, 330, 338*) and material fatigue is a common failure mechanism among orthopaedic implants. Fourthly, the design and materials used for the print and filament involved very little variations. There are many variations of the 3DP block or ES cuff that could be explored, in terms of structure, geometry, chemistry, etc. For instance, we only printed the base from PCL, which is a polymer well known for its clinical use, but which is highly hydrophobic and leads to relatively low cell attachment when unmodified. Gradients of hydroxyapatite might improve the cellular response to scaffold as it would resemble the gradual transition of tendon to bone in the enthesis. Also, we did not investigate the fixation of the implants. Fixation of the 3DP block in bone and the

fixation of the ES cuff to tendon will be important to address in future work to further highlight the clinical potential of the biphasic scaffolds. Furthermore, the biocompatibility assays remained very basic. Future biological characterisation will potentially require the use of primary cells of the supraspinatus tendon and bone, co-cultures, and next-generation sequencing to assess biological response and repair-potential of the scaffolds. Finally, sterilisation of our materials was achieved using ethanol. Methods used in medical device manufacture, such as ethylene oxide sterilisation, will need to be investigated at a later stage as these can have critical effects on the implant's biological, mechanical and degradation properties.

2.6 Conclusion

3D printing and electrospinning can be combined to produce biphasic implant with a robust soft-hard junction for enthesis repair applications. The thermal properties of the polymers used was important since 3D printing involved high temperatures and this affected the mechanical and morphological properties of the ES fibres. The cuff configuration influenced the failure behaviour of the scaffolds as twisted yarns did not adhere to the 3D printed blocks as well as parallel filaments. Up to 270 filaments could be fitted in a footprint area of 50mm^2, similar to that of the enthesis of the supraspinatus tendon, allowing us to reach clinically relevant strength. The scaffold components were confirmed to be non-cytotoxic and cells were shown to proliferate at their surfaces over a period of 14 days. Although promising, future work will be needed to further assess the potential of these synthetic ES cuff - 3DP block biomaterials including investigating more design parameters (chemical and mechanical gradients, cuff configuration, implant geometry, etc.) and utilising further characterisation methods (mechanical and biological). In the next Chapter, the biological activity of the electrospun filaments will be compared to a commercial suture and further assessed by evaluating cell

attachment and proliferation and employing next generation sequencing to test for any differentially expressed genes that might show a more favourable profile for healing and repair.

2.7 Acknowledgments

I am grateful to 3D LifePrints for their help and granting me access to their 3D printing facilities to create the scaffolds, especially Michael Richard. I would also like to express my gratitude to the “Patch team” for providing additional electrospun filaments to Mr James Fisk at the Institute of Biomedical Engineering (IBME), Oxford for his help in creating the aluminium U-frames. This work was funded by the Interreg 2 Seas programme 2014-2020 3DMed, the Lord Nuffield Trust and the NIHR Oxford Biomedical Research Centre.

Chapter 3 Biological evaluation of electrospun filaments

3.1 Abstract

Biomaterials that are implanted into the human body will encounter a foreign body response that can result in failure of the scaffold and chronic fibrosis and inflammation in the native tissue. Several techniques exist to mitigate this effect, most importantly by mimicking the ECM of the target tissue. In this Chapter we evaluate the biological response of electrospun (ES) filaments introduced in Chapter 1 to that of commercial FiberWire (FW) sutures commonly used in rotator cuff repair. Human dermal fibroblasts were cultured and seeded on the materials and their cell attachment and proliferation was assessed using a cell viability assay (PrestoBlue) and scanning electron microscopy (SEM) for a duration of 14 days. Differentially expressed genes (DEG) at the end of the culturing period were quantified by using next-generation sequencing and employing computational analysis using the DESeq2 package in R. Results showed similarly low seeding efficiency for both ES filaments and FW sutures, but a difference in cell morphology with fibroblasts seeded on ES filaments exhibiting an elongated and spindle-like shape. DEG analysis revealed similarities between ES and FW materials at day 14 including pathway enrichment for cell migration and motility and angiogenesis. A difference was that DEG on ES filaments related to development and growth while those on FW related to wound healing and inflammation. Results suggests a difference between both materials with a more favourable outcome for the ES filaments that could contribute to a mitigating effect of the FBR upon implantation.

3.2 Introduction

To determine if a prototype scaffold meets the requirements to progress to *in vivo* testing it is paramount to first carry out *in vitro* tests to assess suitability for progression along the translational pipeline. As introduced in Chapter 1, cells will interact differently to an implanted material based on its inherent properties and bioactivity. As a first step, they will be encased in proteins that signal macrophages to activate the foreign body response (FBR). This is a natural protective mechanism of the body and is an unavoidable process, leading to a failure of implants in about 10% of cases (*339*). To mitigate the effects of the FBR, the materials involved in the implant should not induce a reparative response, which can be achieved by changing the physical properties (e.g., mimicking native tissue ECM), incorporating bioactive anti-inflammatory compounds or coating the implant in a biomimetic substance (*339*). *In vitro* tests to assess biocompatibility include assessment of toxicity and cell viability, proliferation, infiltration and differentiation. These are important factors that specify how well a scaffold will integrate into the native tissue (*340*), as attachment will lead to deposition of extracellular matrix which will stimulate cell proliferation and differentiation of native tissue (*340*). Ideally, scaffolds are seeded with primary cells that are isolated from human tissue samples and then expanded in tissue culture plastic prior to seeding. Problems with the use of primary cells are that isolation can be tricky, cell numbers remain limited, and the relatively high risk of infection can set back experiments significantly (*341*). Also, since primary cells can come from a multitude of different patients, donor-to-donor variations are important to take into consideration in terms of obtaining reproducible results. Furthermore, as primary cells have a limited life span and proliferate at a low rate, they can lose their morphology and functionality when they are passaged too many times in an unstimulated environment (e.g., tissue culture plastic) (*342, 343*). Many studies perform initial *in vitro* testing using well-established and reliable cell lines to prove the initial safety and efficacy of

the scaffold by showing cell attachment and proliferation. However, there is no 'correct' or 'standardised' seeding density to use to elicit quantifiable cell responses and to be able to extrapolate *in vitro* results, and this could especially be relevant when going through regulatory pathways to obtain approval for the use of the scaffolds in clinical trials. Seeding efficiency depends on the structure and nature of the scaffold as well as the cell type used, and can be further influenced by seeding volume and seeding density (*344*). The main aim of this chapter is therefore to assess cell attachment, viability, and response to these scaffolds with a secondary aim of establishing a seeding density. Cell seeding can be especially wasteful when precious cells are used, and several studies have been done to evaluate the seeding process – notably in bone tissue engineering – to determine what an appropriate cell seeding number is to be able to confidently say that scaffolds meet basic biological requirements of cell attachment, proliferation, and differentiation. The focus will be on the electrospun materials as described in Chapter 2, that act as the cuff in the biphasic scaffold. They will be compared to the commercial (uncoated) No.2 FiberWire suture, used in rotator cuff repair. The main outcomes will focus on the difference in gene expression of the bulk RNASeq experiment. The objectives of this Chapter are as follows:

1. To evaluate how cell viability is influenced by FiberWire (Fw) sutures or electrospun (ES) filaments.
2. To assess cell morphology of cells seeded on ES fibres versus Fw sutures.
3. To investigate gene expression of fibroblasts seeded on ES filaments versus Fw sutures, specifically relating to cell adhesion and proliferation, stress responses and wound healing.

The hypotheses are

1. Fibroblasts seeded on ES filaments will show a higher percentage of cell attachment and a higher number of cells at the endpoint than those seeded on Fw sutures.
2. The morphology of the seeded fibroblasts will be elongated and spindle-shaped on ES filaments but not on Fw sutures.
3. Fibroblasts seeded on ES filaments will exhibit an increased expression of genes related to cell attachment and proliferation and a reduced expression of genes related to inflammatory responses compared to those seeded on Fw sutures.

3.3 Materials and methods

3.3.1 Material preparation and sterilization

The manufacturing of ES PDO filaments has been described in Chapter 2. The commercial equivalent used as a comparator was the No.2 FiberWire sutures (Arthrex, Naples, FL). The No.2 Ethibond sutures (Ethicon, Somerville, NJ, US) was considered the standard suture in rotator cuff repairs, which is a non-absorbable, braided polyester suture. However, polyblend sutures with an ultrahigh-molecular-weight-polyethlyene (UHMPWE) have quickly taken over in popularity due to their biomechanical excellence (*14, 118, 345*). FiberWire is a non-absorbable, braided suture made from UHMWPE and polyester with a core of UHMWPE yarns and a suture diameter of 0.3-0.339 mm according to the USP size classification. The uncoated suture type was used as the coated sutures have proven to be more abrasive in soft tissue repairs (*116*). Fw sutures and ES PDO fibres were prepared for cell seeding in the same way. Nine sutures and filaments of about 40 cm in length were aligned in a parallel fashion held down by tape on both ends. The rationale for nine filaments was based on the number of filaments needed for the twisted structures in Chapter 2. Knots were tied using the same material at every ~1.5cm interval so that samples could be cut between two knots. A bundle

of nine was chosen because this is the minimum number of filaments used in the scale-up experiments in Chapter 1 and because it meant that there would be enough material available for at least three biological replicates. All samples were then placed in 10 cm petri dishes and sterilized by submerging in 70% ethanol for two hours, washing three times in phosphate-buffered saline (PBS, ThermoFisher, UK), and finally left to dry overnight in sterile conditions. The next day, the petri-dish containing the sterilized samples was sealed with Parafilm and stored in a desiccator until ready for use. Samples were stored for a maximum of a week prior to use.

3.3.2 Cell culture and maintenance

Human foreskin (dermal) fibroblasts (HFF-1 cell line, ATCC) were maintained in growth medium DMEM F12 (Lonza, UK) supplemented with 10% foetal bovine serum (FBS, Biosera UK) and 1% penicillin–streptomycin solution (Gibco, UK). Due to the ongoing Covid-19 pandemic no primary cells could be used for the purpose of this experiment and therefore a cell line was chosen that exhibits similar properties to tenocytes. Dermal fibroblasts are an ideal candidate because they are easy to harvest and culture and are similar to tenocytes with regards to their morphology and gene expression, namely production of collagen type I which constitutes the major collagen component of tendon fibrils (*37, 346*). They have been hailed as a promising cell source for tendon engineering endeavors as well (*347-349*). In fact, in a recent review by Chu et al. a pilot investigation into microarray data comparing dermal fibroblasts and tendon fibroblasts revealed striking similarities at gene expression level (*37, 350*). Cells and culture medium were regularly tested for mycoplasma using a MycoAlert testing kit (Lonza, UK) according to the manufacturer's instructions. Cells were used before passage 10 and were not cultured for longer than two weeks from the moment they were taken out of the freezer until they were used for seeding (*351*).

3.3.3 Cell seeding

Unless mentioned otherwise, the static cell seeding method was used throughout this Chapter (Figure 3.1). Scaffolds (n = 4, biological repeats) were prepared for cell seeding by being soaked in culture media for two hours at 37 °C, 5% CO_2. The FBS used in the culture medium provided a protein coating for the materials that benefits cell attachment. Fibronectin and vitronectin are the two main adhesive proteins in the serum (*352*). These are glycoproteins that support cell attachment by activating integrin receptors on the surface of a cell. This then triggers a cascade of intracellular proteins to form focal adhesions, which are important integrin receptors that communicate between the ECM and the actin cytoskeleton within the cell to facilitate attachment (*353, 354*). Once cells had reached >90% confluency, they were mechanically scraped from the tissue culture plastic and counted using a hemocytometer counting-chamber device, before seeding on the scaffolds at different densities and volumes.

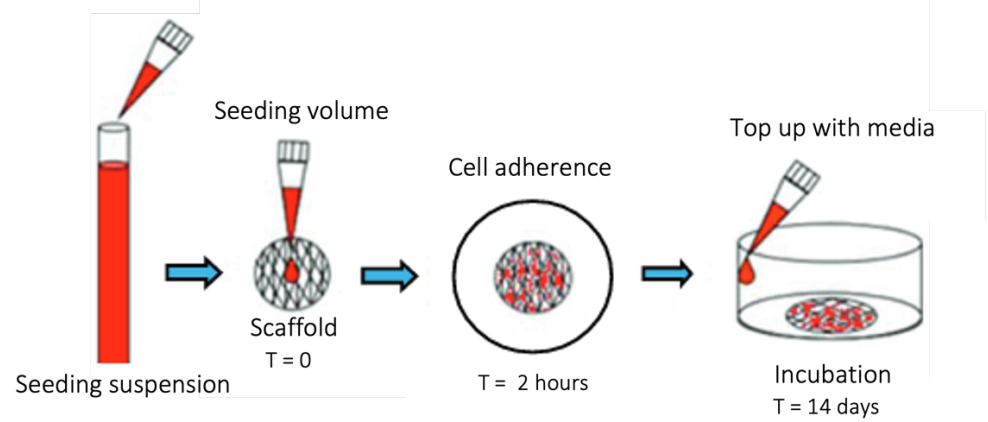

Figure 3.1 The static cell seeding method. Adapted from Kurzyk et al (*355*).

3.3.4 Assessment of initial cell attachment and proliferation

After seeding cells onto the scaffolds, the plate was placed in the incubator for two hours to allow cells to attach (the seeding plate). Then, the scaffolds were transferred to a new 48-well plate and topped up with fresh culture medium. The seeding plate was saved to assess

attachment of the cells on day 1 by comparing the number of cells remaining in the seeding plate and those that were on the scaffold. This was approximated by using a PrestoBlue assay (Invitrogen, Paisley, UK) to measure metabolic activity, using a protocol previously established (*299*). This is an oxidation-reduction-based assay in which resazurin, a blue non-fluorescent dye, is metabolized by live cells and reduced to resorufin, a highly fluorescent component. This can be detected by measuring fluorescence in a microplate reader and obtaining a change in fluorescence intensity units (FIU) from day 1 to day 4, day 7 and day 14 (endpoint). It can therefore be used as a surrogate measure of cellular proliferation since it is non-destructive to cells and so the same cell population can be evaluated at specified time points. Briefly, culture medium in each relevant well was replaced with 400 µL of a 10% PrestoBlue solution (v/v in DMEM) at selected time-points (day 1, 4, 7, 14 post-seeding) and incubated for 1 hour at 37°C, 5% CO_2. Afterwards, 100 µL of each sample was transferred in triplicate to a white, flat-bottom 96-well plate (Corning, UK). Fluorescence was measured at 485nm excitation and 520nm emission using a FLUOstar optima microplate reader (BMG Labtech, Germany). A well containing just the PrestoBlue solution was used to correct for background signal. The scaffolds were then rinsed with PBS and transferred to new 48-well plates containing fresh, pre-warmed cell culture media. Scaffolds were placed into new 48-well plates with fresh medium every two to three days to exclude cells that had attached to the bottom of the well plates. Furthermore, they were placed in new plates prior to every PrestoBlue addition and then again transferred to a clean plate afterwards. The percentage of cells that had successfully attached to scaffolds was quantified by determining the ratio of the microplate readings (FIU) of the seeding plate and the scaffolds after day 1, corrected for background, see equation below. The estimated cell number at each time point was then calculated using the calibration curve mentioned previously described.

$$\% \, cell \, attachment = \frac{FIU \, day \, 1 \, plate}{(FIU \, day \, 1 \, plate + FIU \, seeding \, plate)} \, x \, 100\% \quad (3)$$

3.3.5 Imaging samples

At day 1, 7 and 14, samples were fixed in 10% glutaraldehyde for one hour. They were then washed in PBS and dehydrated in a series of ethanol washes for 10 minutes (40%, 50%, 70%, 90%, 100%, 100%). Finally, they were left in hexamethyldisilazane (Alfa Aesar, Haverhill, MA, USA) overnight and the plate was sealed with Parafilm and stored in a desiccator until ready for SEM imaging according to the method described in Chapter 2, section 2.3.7. Measurements were taken using ImageJ software (National Institutes of Health, Bethesda, Maryland, USA).

3.3.6 RNA extraction

At the endpoint (day 14), scaffolds were taken from the wells and transferred to sterilised Eppendorf tubes containing 500 µL of TRIzol using sterile forceps (Invitrogen, Paisley, UK) and stored in a -80°C freezer until ready for use. RNA extraction was performed using an RNA Clean & Concentrator-5 kit with DNAse treatment (Zymo Research, USA) according to the manufacturer's protocol (*356*). This protocol was adapted from the manufacturer's protocol and work done previously in this group (*357*) and is briefly summarized in Figure 2. Each sample was thawed and topped up with 500 µL of TRIzol, to have a total volume of 1 mL of TRIzol. This was then transferred to a new, sterile GentleMACS M-tube (Miltenyi Biotec, USA). The tube was inverted and placed in a gentleMACS dissociater (Miltenyi Biotec, USA), set to run on a pre-defined agitation protocol and then centrifuged at $3.9x10^1$ g for 5 minutes at 4°C. The agitation and centrifugation were then repeated to maximize extraction of RNA. Following this, the sample was centrifuged at $4.2x10^4$ g for 8 minutes at

4°C after which the supernatant was transferred to a new tube and 400 µL of 1-bromo-3-chloropropane (Sigma-Aldrich, US) was added. This solution was briefly vortexed, incubated for 5 minutes at room temperature and then centrifuged at $4.2x10^4$ g for 20 minutes at 4°C. The clear aqueous phase was transferred to a new tube, taking care not to take anything from the intermediate phase, and an equal volume of 100% ethanol was added (Fisher BioReagents, US). The solution was vortexed and transferred to a new Zymo-Spin IC column with a collection tube. DNAse I treatment was added prior to eluting the RNA. This was done to remove impurities in the sample caused by DNA contaminations and to prevent these from being amplified in the sequencing run (*358*). One microliter of eluted RNA was used to quantify the RNA concentration and purity of the samples on a NanoDrop 10000 Spectrophotometer (ThermoFisher Scientific, USA). Prior to each set of measurements, a blank sample consisting of nuclease-free water was used. Four biological repeats were used for each set, making a total of 24 samples. Cells seeded on tissue culture plastic (TCP) were also added to the experiment and RNA was extracted from them as well. This was done to compare the RNA concentration on the scaffolds using a baseline – since cell attachment was not considered a problem for this group, but they were not further analysed for differential gene expression. RNA was also extracted for samples at day 0. The absorbance at 280 (proteins and phenolic compounds), 260 (nucleic acids) and 230 nm (organic compounds) was measured, and a ratio was calculated of 260/280 and 260/230 per sample. The first ratio is used to assess the purity of RNA and a ratio of ~2.0 is considered acceptable as a rule of thumb but is highly dependent on the composition of nucleic acid in the sample. Anything less than 2.0 could indicate contaminations with proteins or phenol which absorb at 280 nm. Another reason for a low ratio could mean that there is a very low concentration of nucleic acid to measure (> 10 ng/µL). The second ratio indicates the purity of nucleic acid which should be in the range of 2.0-2.2 (indicated by a horizontal dotted line in Figure 14B), with a

lower value suggesting contaminants in the sample that absorb at 230 nm. For example, TRIzol is a phenolic solution which absorbs at 230 nm (*359*). The samples were then diluted to 100ng in 50mL nuclease-free water in a LoBind 96-well plate (Sigma-Aldrich) and stored in -20°C until ready for the next step. The extraction method is briefly summarized in Figure 3.2.

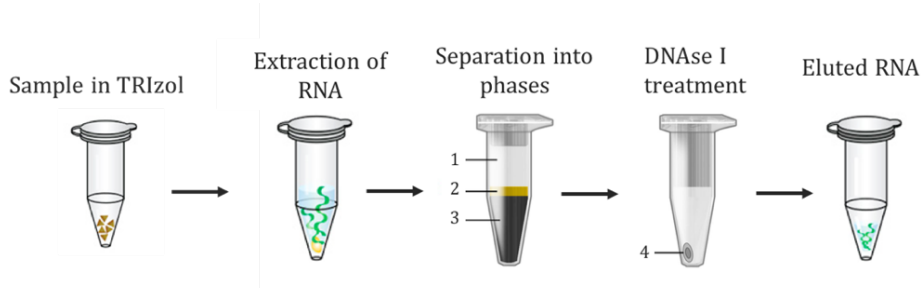

Figure 3.2 Schematic of the RNA extraction protocol based on separation the RNA into an aqueous (1), intermediate (2) and organic (3) phase. DNAse treatment is applied to the isolated RNA (4) to elute it. Finally, each sample is diluted and stored in a LoBind plate. Samples here mean the scaffolds seeded with cells.

3.3.7 RNASeq library preparation and sequencing

About 90% of RNA originating from human cells consists of ribosomal rNA (rRNA), which needs to be removed prior to sequencing to achieve reads from the relevant messenger RNA (mRNA) and to gain information about gene expression at a lower sequencing depth (*360*). This can be done using either the RNA depletion method (negative selection) or the polyadenylated RNA (polyA) method (positive selection) (*361*). The latter was used for the library preparation of the samples in this thesis. Briefly, mRNA was isolated by binding of its polyA tail to oligo-(dT) magnetic beads. These consist of chains of deoxythymine (dT) nucleotides which are complimentary to the 3' end of the polyA-tail of the mRNA molecules. Any particles without a polyA-tail, such as rRNA, can therefore be discarded. RNA library preparation was performed using the NEBNext Ultra II Directional RNA Library Prep Kit for Illumina with polyA selection (New England Biolabs, MA, USA), following the manufacturer's instructions. All reagents were purchased from New England Biolabs, USA. First, the samples were isolated from rRNA, see Figure 3.3. Oligo-dT beads were washed using RNA Binding Buffer (2X) and 50 µL of beads were added to individual (diluted)

samples to isolate the mRNA (Figure 3.3, step 1). This was then placed in a thermal cycler (Veriti 96-well Thermal Cycler, Applied BioSystems, ThermoFisher, UK) set at 65°C for 5 minutes with a cool-down to 4°C to denature RNA and facilitate binding of mRNA to the beads (Figure 3.3, step 2). The beads were then washed in 200 µL of Wash Buffer to remove RNA that had not bound, and the supernatant was discarded. Then, 50 µL of Tris Buffer was added and the sample was placed in the thermal cycler (80°C for 2 minutes, held at 25°C with a heated lid set at 90°C) for the first elution of mRNA from the beads. To allow mRNA to re-bind to the beads, 50 µL of RNA Binding Buffer (2X) was added and the sample was incubated at room temperature for five minutes (Figure 3.3, step 3). The supernatant was discarded, and washing was repeated with 200 µL of Wash Buffer. To prepare for fragmentation and priming, mRNA was eluted from the beads by adding 13 µL of First Strand Synthesis Reaction Buffer and Random Primer Mix (2X) to the sample, incubating at 94°C for 15 minutes and holding at 4°C in the thermal cycler. Random primers have a short, random sequence of nucleotides (usually 6) and are used as unbiased candidates to bind to RNA fragments to ensure that most of the strand is covered so that it can be amplified in the PCR reaction later on (*362*). The supernatant, containing the now fragmented and primed RNA (without beads), was transferred to a new PCR tube, and placed on ice (Figure 3.3, step 4).

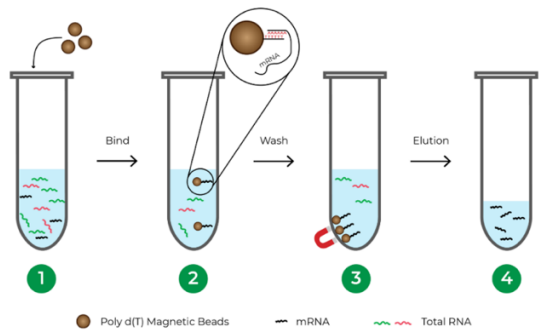

Figure 3.3 Schematic depicting the rRNA removal process by adding oligo-dT beads (1) that bind to the polyA-tail of mRNA molecules (2) so that the supernatant containing unwanted particles can be discarded (3) and the mRNA can be used (4). Image reprinted with permission from the Zymo Research Corporation.

Strand Specificity Reagent and First Strand Synthesis Enzyme mix was added to the RNA and the sample was incubated in the thermal cycler for 10 minutes at 25°C, 15 minutes at 42°C, 15 minutes at 70°C and then held at 4°C. Second Strand Synthesis Reaction Buffer (with dUTP Mix 10X), Second Strand Synthesis Enzyme Mix and nuclease-free water was then added, and the sample was incubated for 1 hour at 16°C. The dUTP (deoxyuridine triphosphate) method is used to generate double-stranded cDNA from the first-strand cDNA. Briefly, this involves the incorporation of uracil nucleotides into the second strand, so that it can be marked for degradation before the PCR amplification step later. This ensures that only the first strand, containing the original RNA information, will be sequenced (*363*). To purify the double-stranded cDNA, 144 µL of Sample Purification Beads were added to the sample, incubated for five minutes at room temperature, and washed twice with 200 µL of freshly prepared 80% ethanol. The beads were air dried for five minutes before eluting the DNA with 55 µL of 0.1X TE buffer. Finally, 50 µL of the supernatant (containing the synthesized double-stranded cDNA) was removed and transferred to a clean PCR tube to which the End Prep Reaction Buffer (10X) and End Prep Enzyme Mix were added to finalize the preparation of the newly formed cDNA library by adding a non-templating 'A'-base to the 3'-end (dA-tailing) of the synthesized fragments. This was incubated in the thermal cycler for 30 minutes at 20°C, 30 minutes at 65°C and held at 4°C. See Figure 3.4 for a simplified overview summary of the RNA library preparation workflow thus far.

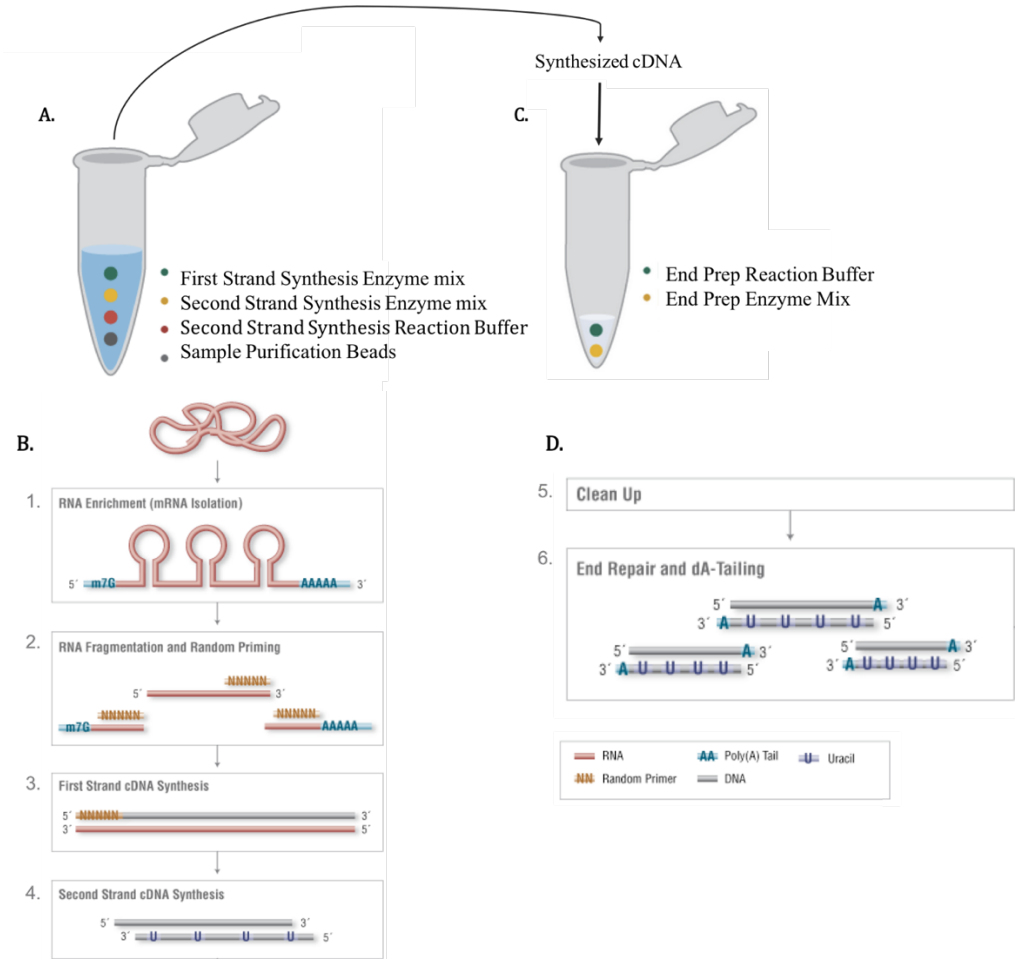

Figure 3.4 A simplified summary of the cDNA synthesis reaction. The enzyme mixes are added to the mRNA (A) that has been cleared of rRNA (B1), fragmented and primed (B2) so that the cDNA synthesis can take place (B3 and 4). After purification, the library prep is finalized (C) by dA-tailing (D6) to prepare for adaptor ligation. Image B and D reprinted from www.neb.com (2022) with permission from New England Biolabs, Inc.

The newly synthesized end prepped DNA was mixed with Adaptor Dilution Buffer (50-fold dilution), Ligation Enhancer and Ultra II Ligation Master Mix and incubated for 15 minutes at 20°C for adaptor ligation. Briefly, in this process oligonucleotides with known sequences (adaptors) are attached to both ends of cDNA fragments, looping them together. Then, USER Enzyme was added, and the sample was incubated again for 15 minutes at 37°C.

To purify the ligation reaction, 87 µL (0.9X) of Sample Purification Beads was added to the sample, incubated for 10 minutes at room temperature, and washed with 200 µL of freshly prepared 80% ethanol twice. Supernatant was removed and the DNA was eluted by adding 19 µL 0.1X TE buffer to the beads. Proceeding to the PCR amplification, 15 µL of the supernatant was transferred to a clean PCR tube. Ultra II Q5 Master Mix, Universal PCR

Primer (i5) and Index (X) Primer (i7) were added to the adaptor ligated DNA sample and incubated for 30 seconds at 98 C for initial denaturation, eleven cycles of 10 seconds at 98 C for and 75 seconds at 65 C for denaturation and annealing, and five minutes at 65 C for the final extension. The i5 and i7 primers add unique indexing sequences to the DNA samples and add P5 and P7 sequences, which allow the Illumina sequencing platform to recognize the libraries and bind them to the correct location in the flow cell. The i7 primer also allows each sample to have an individual barcode attached that will make it identifiable in the down-stream analysis. The PCR amplification serves to increase the size of the library for downstream processing. Then, 45 µL (0.9X) of Sample Purification Beads were added to the sample, which was incubated at five minutes and supernatant was removed to purify the DNA. The beads were washed with 200 µL of freshly prepared 80% ethanol twice, DNA was eluted by adding 25 µL 0.1X TE Buffer and 20 µL of the supernatant was transferred to a clean PCR plate. See Figure 3.5 for a simplified summary.

Quality and size of the libraries (24 in total) was determined using the Agilent 4150 TapeStation (Agilent Technologies) with high-sensitivity D1000 tape, using 1uL of library. After confirming that the electropherogram showed a narrow distribution with a peak size at around 300 base pairs, the libraries were pooled. As a final step prior to sequencing, the pooled libraries were denatured with freshly diluted 0.2 N NaOH and 200 mM Tris-HCl, pH 7 to 20 pM and diluted to 1.8 pM with a prechilled HT1 hybridization buffer, according to the Illumina NextSeq system manufacturers protocol. This denatured and diluted library was then run on an Illumina NextSeq 500 sequencer using the 75 cycles NextSeq 500/550 High Output kit (Illumina). The sequencing data was saved directly to the BaseSpace Sequence Hub, a cloud-based genomics computing environment (Illumina).

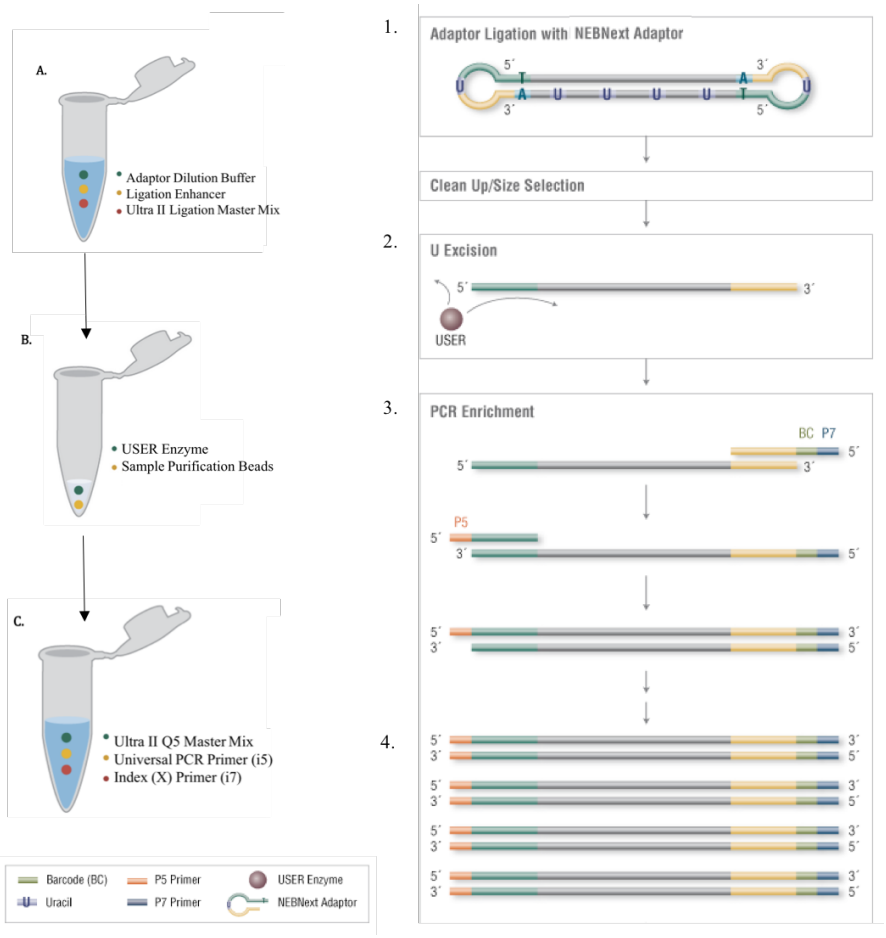

Figure 3.5 A simplified summary of the adaptor ligation and PCR amplification. The enzyme mixes are added to the end prepped DNA (A) to attach the adaptors (1). Then, the USER enzyme is added (B) to remove the uracil nucleotides (2) and prepare the strands for the i5 and i7 primer attachment (C). This allows the P5 and P7 sequences, including barcode to attach (3) for the PCR enrichment to increase the library size (4). Image 1-4 reprinted from www.neb.com (2022) with permission from New England Biolabs, Inc.

3.4 Data analysis

3.4.1 Cell seeding and proliferation data analysis

Data analysis for this Chapter was performed solely by me. GraphPad Prism 9 (GraphPad Software Inc, San Diego, CA, USA) was used to analyse the cell attachment and proliferation data. Data is plotted as mean ± standard error of the mean (SEM). This was used because the individual replicates (n = 4) had three technical repeats per experiment and each repeat is an average value of those replicates. The standard error therefore reflects the average of the standard deviation of the separate experiments. A one-way ANOVA with a Tukey's post-hoc test was used to determine differences between seeding volumes within each material group

and to test whether between the same seeding volume there was any difference in seeding numbers. A two-way ANOVA with a Tukey's post-hoc test was used to determine any differences between cell numbers and fold change at specific time-points and between materials. A simple linear regression was performed to calculate the approximate number of cells that had attached to the materials.

3.4.2 RNASeq analysis

The complete RNASeq workflow used in this Chapter is summarized in Figure 3.6. Sequencing was performed using Illumina equipment and kits and raw FASTQ files were downloaded from BaseSpace. The next steps involved computational analysis using the FASTQ files as input. These were processed using the Miniconda package derived from Anaconda (*364*), based on the Python programming language (Python Software Foundation, https://www.python.org/), and their quality was assessed using the Java-based quality control tool FastQC (Babraham Institute, University of Cambridge), for high throughput sequencing data(*365*). Quality control reports were generated with the FastQC and MultiQC tools (*366*). Using kallisto (*367*), a pseudoalignment tool that quantifies on a transcript level instead of a gene level, reads were then mapped to the GRCh38.p13 reference transcriptome (*368*) that was downloaded from the Ensembl Project (*369*). Exploratory data analysis, differential expression and pathway analysis was performed in R and R Studio (R Foundation for Statistical Computing, Vienna, Austria) using the DESeq2 package (*370, 371*) and by following online tutorials (*372-374*). Data was visualised using the EnhancedVolcano (*375*) and ggplot2 packages (*376*). Gene set enrichment analysis was performed using the clusterProfiler package (*377*). Other packages that were used are cited throughout this Chapter where applicable. The full reproducible code for analysis conducted in Python and R is available in Appendix A, with reference to the online tutorials as well.

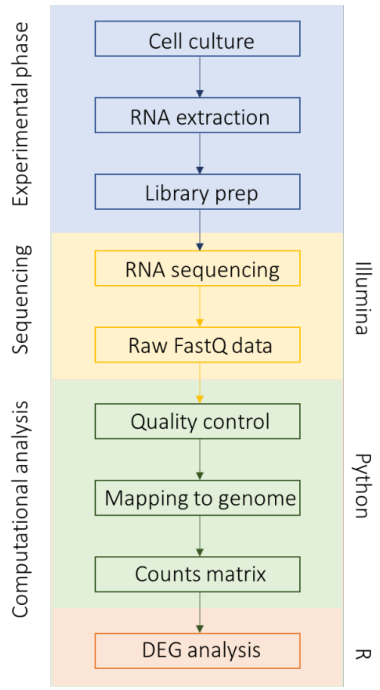

Figure 3.6 Workflow of RNASeq performed in this Chapter, consisting of three separate phases and commodities.

3.4.3 Normalising gene counts

Differential expression (DE) analysis was performed using the DESeq2 package (*371*) by normalising the raw counts, estimating dispersion, fitting data with generalised linear models, and applying the Wald test to the designed formula. Prior to the analysis, the dataset was pre-filtered to remove genes that had less than 10 counts across all samples. This allows accurate examination of DEGs by removing outliers, increasing the number of DEGs, and speeding up the analysis by reducing the size of the data required for computation (*378*). Using a single command, DESeq2 estimates size factors, gene-wide dispersion and fits a model to the data. The assumption underlying the methodology is that genes that are similarly expressed will have a similar dispersion, and thus DESeq2 'shares' information across these genes to accurately estimate dispersions using maximum likelihood estimates (*371*). The *'ashr'* method was used to apply shrinkage of logarithmic fold change (*379*). It is stressed here that data pre-processing has been found instrumental in refining the differential expression analysis for RNA-Seq data and often involves a series of procedures (*371, 380*). For example,

DEGs can be identified inaccurately due to poorly normalised data that is skewed by not considering many contributory factors such as sequencing depth (library size), library (RNA) composition, and gene length (*381*). Therefore, the normalization technique used during the DE analysis was performed based on the median of a ratio method (introduced below) by considering these factors to avoid over- or under-estimated normalization counts caused by unequal sequencing depth or highly expressed genes in some samples. This makes it the preferred method over other normalization methods such as reads per kilobase million (RPKM), fragments per kilobase million (FPKM) and transcripts per kilobase million (TPM) (*382-385*). Suppose there is sample A and B with respective counts for gene X, Y and Z (Figure 3.7). For each gene, DESeq2 calculates a pseudoreference value by multiplying the counts (*i.e.*, geometric mean) across the two samples and taking the square root of it. Then, for each gene, the sample ratios are calculated by dividing the count of this gene in sample A and B by their pseudoreference values, respectively. Since many genes will not be differentially expressed, these values will likely look similar across the genes in a sample. After, the normalisation factor for each sample (size factor) is calculated by taking the median value of all ratios for genes within the sample.

1. Raw counts table

	sample A	sample B
Gene X	143	2912
Gene Y	32	17
Gene Z	112	3

2. Calculate pseudoreference

	sample A	sample B	pseudoreference
Gene X	143	2912	$\sqrt{(143 * 2912)} = 645.30$
Gene Y	32	17	$\sqrt{(32 * 17)} = 23.32$
Gene Z	112	3	$\sqrt{112 * 3)} = 18.33$

3. Calculate size factors

	sample A	sample B	pseudoreference	ratio sample A	ratio sample B
Gene X	143	2912	$\sqrt{(143 * 2912)} = 645.30$	143/645.30 = **0.22**	2912/645.30 = **4.51**
Gene Y	32	17	$\sqrt{(32 * 17)} = 23.32$	32/23.32 = **1.37**	17/23.32 = **0.73**
Gene Z	112	3	$\sqrt{112 * 3)} = 18.33$	112/18.33 = **6.11**	3/18.33 = **0.16**

← 4. Find median (size factor)

4. Normalize gene counts

	sample A	sample B	pseudoreference	ratio sample A	ratio sample B	normalized count sample A	normalized count sample B
Gene X	143	2912	$\sqrt{(143 * 2912)} = 645.30$	143/645.30 = **0.22**	2912/645.30 = **4.51**	**143/1.37 = 104.38**	**2912/0.73 = 3989.04**
Gene Y	32	17	$\sqrt{(32 * 17)} = 23.32$	32/23.32 = **1.37**	17/23.32 = **0.73**	**32/1.37 = 23.34**	**17/0.73 = 23.29**
Gene Z	112	3	$\sqrt{112 * 3)} = 18.33$	112/18.33 = **6.11**	3/18.33 = **0.16**	**112/1.37 = 81.75**	**3/0.73 = 4.11**

Figure 3.7 Worked example for normalization using fictional numbers and gene names.

The median is also used to prevent the value from being swayed by extreme numbers too much in one direction. Due to the scarcity of extremely overexpressed genes appearing in the samples, one can imagine that the normalization factors of most of genes will be tightly distributed around 1. The normalised count of a gene in either sample is therefore given by dividing its raw count by its normalisation factor. Furthermore, log transformation (log base 10) is applied to the normalized counts to compress the largely varying data into comprehensive plots (see Results). Once the gene expression data is pre-processed, DESeq2 estimates gene-wide dispersions and measures the data variability by adopting a negative binomial distribution (Gamma-Poisson) that models the gene counts using the following equation (*371*):

$$K_{ij} \sim NB(\mu_{ij}, \alpha_i) \quad (4)$$

whereby

K_{ij} = raw count for gene i in sample j
μ_{ij} = the fitted mean

α_i = one dispersion per gene

The DESeq2 model fits estimating coefficients ($\log_2$ fold changes) and standard errors for each sample group. To compare this outcome between groups, the Wald statistic is used based on the dispersion and coefficient parameters. There is no differential expression in genes between the compared groups if the null hypothesis made for the DE analysis is accepted, while at least one DEG is detected between the compared groups if the null hypothesis is rejected. It has been suggested that the significantly large number of statistical tests can expand the likelihood of false positives, especially for RNA-seq data. This is also known as the multiple testing problem. The adjusted p-value (padj) is introduced to correct for multiple testing and is calculated here using the Benjamini-Hochberg (BH) correction of 5% false discovery rate (FDR). The FDR leads to increased p-values, making them less likely to be significant. The BH method orders all p-values from smallest to largest and gives them a rank (*i*). Then, each p-value's BH critical value is calculated as such:

$$\left(\frac{i}{n}\right) \cdot Q \tag{5}$$

whereby the p-value's rank (*i*) is divided by the total number of tests performed (n) and multiplied by the FDR (*Q*), which is set to 0.05. This cut off means that the proportion of false positives in the differentially expressed genes will be no more than 5%. To enhance visualisation of the distance and clustering of samples, the normalized gene counts were transformed first to control the variance across the mean. Because the current dataset is small, regularized logarithm transformation (*rlog*) was applied rather than variance-stabilizing transformation *(vst)*. Note that the transformation was blinded to the type of samples. This transformed object was then used for the following methods. Principal component analysis (PCA) has been widely used as a linear dimensionality reduction technique to identify major

components that characterize a given data matrix by projecting the data onto axes where the data variance can be maximized (*386, 387*). We used this technique to find differences between the samples and for visualisation purposes we showed the major components in two-dimensional space. Briefly, the data is reduced by shrinking it to a minimized number of variables that are not correlated ('principal components') and can represent the raw data as completely as possible. This results in the data being summarized from a high dimensional space into a 2D graph that can easily be interpreted (*370, 388*). PCA measures the correlation between all variables by breaking down the matrix geometrically into a magnitude (eigenvalue) and direction (eigenvector). The way PCA works is that the first PC accounts for the largest variation, the second for the second largest variation and so on – if they are unrelated to each other. These PCs can be selected based on the eigenvalue criterion, the proportion of variance criterion or the scree plot criterion (*389*). The sum of the variables entered in to the PCA should be equal to the sum of the eigenvalues calculated; the eigenvalue criterion states that only eigenvalues with a value greater than 1 should be kept. The proportion of variance criterion is achieved when the cumulative variance of the chosen PCs exceeds >80%. Hierarchical clustering was performed by calculating the Euclidian distances between genes using the *rlog*-transformed data. The Euclidian distance measures the distance between two points in Euclidian space and is calculated using Pythagoras' theorem (*390*). Consider, as an example of projection into 2D space, the coordinates of samples A (x_1, x_2) and B (y_1, y_2) where x_1 and x_2 represent the normalized counts of gene 1 and gene 2 in sample A and y_1 and y_2 represent the normalized counts of gene 1 and gene 2 in sample B. The Euclidian distance (d) between them is then calculated as:

$$d = \sqrt{((x_1 - y_1)^2 + (x_2 - y_2)^2)} \quad (6)$$

3.4.4 Quantification of alignment

Quality control of the dataset was performed prior to analysis in R. Kallisto works on the premise of pseudoalignment (*367*). Briefly, kallisto maps reads to a known transcriptome (in this case human) by searching for specific strings of *k* nucleotides in a DNA sequence (k-mer). An index is built firstly of all k-mers in the transcriptome. Then, kallisto deconstructs a given sample into k-mers and finds the corresponding k-mer in the index, which makes the alignment process much faster and lighter. Figure 7 shows the alignment score of the individual samples. The blue bar indicates the percentage of reads that kallisto was able to map to the transcriptome, while the red bar are reads that have not been aligned. Generally, reads from a sample with the percentage of mapped reads below 50% are considered a low-quality alignment. In this dataset, there is one sample from the FW0 group that scores just below 50%, but it was not excluded from further analysis. Overall, it can be seen in Figure 3.8 that reads from most of the samples are mapped in high quality with alignment scores exceeding 85%.

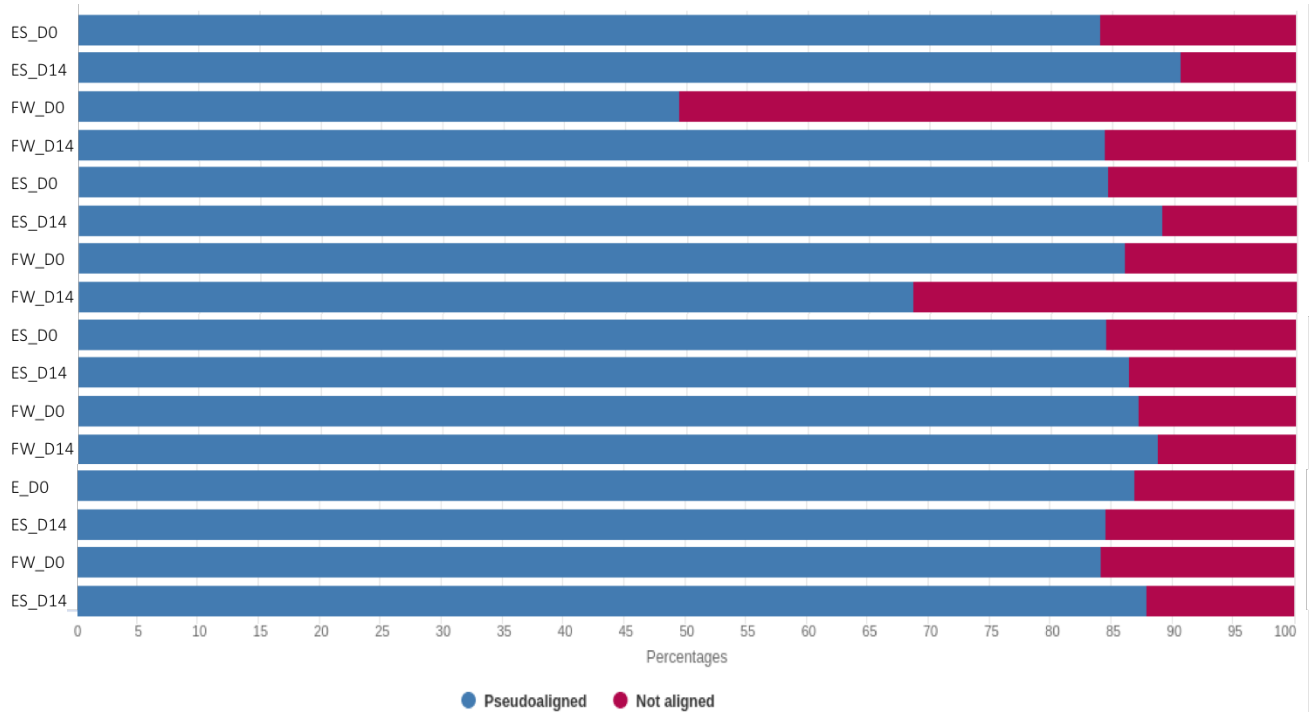

Figure 3.8 Alignment scores provided by kallisto. The blue bar indicates the percentage of pseudoalignment, whereas the red bar indicates the counts that were not aligned.

3.4.5 Exploratory data analysis

As shown in Figure 3.9, DESeq2 yields a model that fits our dataset uniformly and smoothly (most of the data changes are clustered around the red line), which indicates good dispersion estimates. The dispersion estimates of the genes (black dots) are plotted against the mean values of normalized counts and are parameters for the negative binomial models with which DESeq2 fits the available data (red line). The blue dots represent the corrected dispersion estimates of the genes after being shrunk towards the fitted line, with the outliers visualised as black dots encased in blue. Shrinkage is applied to reduce the likelihood of false positives in the downstream differential expression analysis and is especially important in datasets with small sample sizes (n <3). Dispersion is commonly highest for low read counts and lowest (i.e., the red line plateaus) at higher counts.

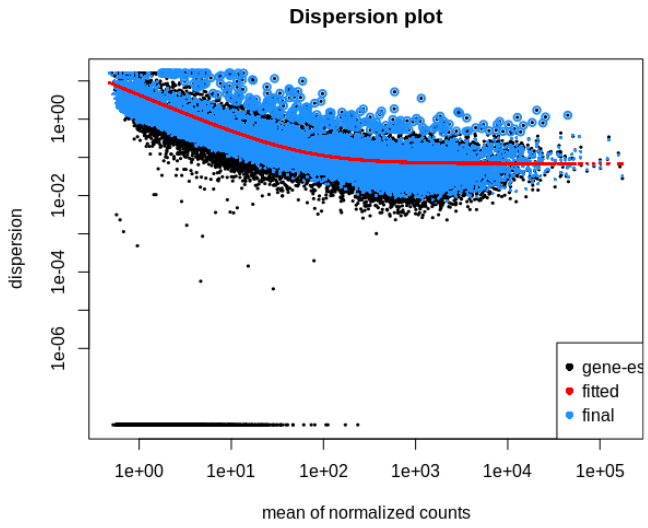

Figure 3.9 Dispersion plot of the current dataset involving all samples.

3.4.6 MA plots

A further diagnostic criterion to roughly check difference in expression levels across all genes is the MA plot, showing the $\log_2$ fold change of genes (M for log-intensity ratio) against the mean of normalized counts (A for log-intensity average) between two groups

(*372*). In this plot, the logarithm to base 2 is used on the y-axis, meaning that a doubling of the gene expression (fold change > 1) is equivalent to a $\log_2$ fold change of 1, whereas a halving of gene expression (fold change < 1) equals a log fold change of -1. Since most genes are not differentially expressed (fold change = 1), they will be clustered at M=0 where the lfc of 1 is equal to 0, which normally renders a trumpet-shaped plot. Therefore, the blue dots above the zero line indicate up-regulated genes, whereas the dots below it indicate down-regulated genes. Figure 3.10 shows four different MA plots for each comparison that is made, with the second term being the group that is compared against the other one of interest (i.e. the 'reference' group). The least expressed genes are seen between electrospun (ES) and FiberWire (FW) samples on day 14. Genes that are expressed at a lfc higher or lower than two are indicated as triangles.

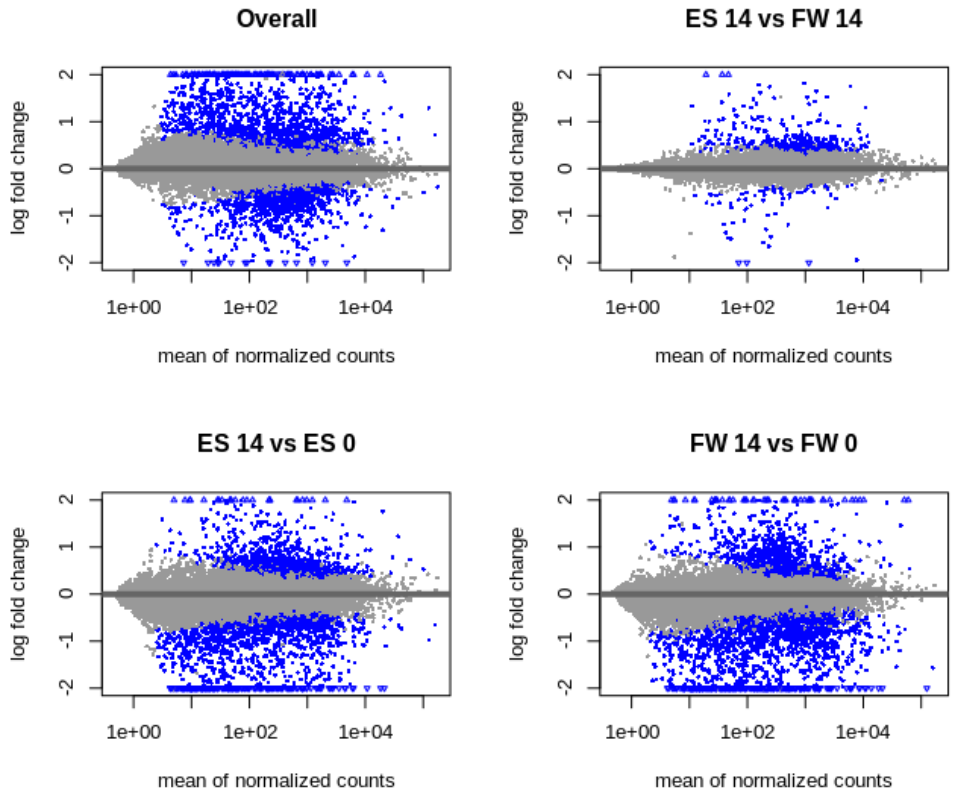

Figure 3.10 MA plots of overall gene expression, between ES14 and FW14, ES14 and ES0 and FW14 and FW 0.

3.4.7 Calculation of volcano plots and heatmaps

Volcano plots are depicted in Figure 19, which are scatter plots with -log(10) of unadjusted p-values (significance) plotted on the y-axis against the $\log_2$ fold change of expressed genes (effect). As described in the MA plot above, the $\log_2$ fold change is used here on the x-axis to represent fold changes, rather than absolute ratios. The $\log_2(x)$ formula denotes that to achieve x, the number 2 must be raised to a specific power, which makes it a more compressive term to use when discussing gene expression levels rather than the native fold change. For example, consider gene A with expression 5 and gene B with expression 10. The fold increase would be B/A = 2, but on a logarithmic scale this value would be displayed at x=1, since $2^1 = 2$. Conversely, if we look at A/B = 0.5, this would be plotted on x = -1 since $2^{-1} = 0.5$. Vertical dashed lines are drawn at x = 1 and x= -1 to indicate these points. Using the $\log_2$ base over absolute numbers centres the values around 0, makes them symmetrical and is therefore easier to see any changes in the positive or negative direction. This symmetry is then visualized as a volcano plot. P-values are plotted on the y-axis and are converted into $-\log_{10}(p)$ first so that lower p-values are plotted towards the top. By default, the p-value cut-off is set at 10^{-6}, translating to $-\log_{10}(0.00001) = 5$, which is shown as the horizontal dashed line. The raw p-value is used rather than the adjust p-value (also known as q-value) to preserve all information at this stage. Genes plotted in the top left- or top right quadrant (down-regulation or up-regulation) are those of interest, specifically the ones marked in red.

The sample-to-sample distance heatmap (Figure 18) was plotted using Pearson's correlation coefficient. This is used to quantify the linear relationship (i.e., distance) between two points in a single metric. The coefficients range from -1 to 1, with the two boundaries indicating a perfect negative correlation and a perfect positive correlation, respectively. Dots of two samples residing on the diagonal correspond to a coefficient of 1. The heatmap clustering samples according to DEGs was generated using the 'pheatmap' package (*391*), with clusters

displayed on the left-hand side and sample names on the bottom row (Figure 20). Briefly, after clustering of the samples, normalization is applied to the raw gene expression values using the Z-score value, given by:

$$Zscore = \frac{(gene\ count\ in\ sample\ X) - (mean\ count\ across\ all\ samples)}{SD\ of\ all\ measured\ counts\ across\ all\ samples} \quad (7)$$

These values are reflected by the colour scale bar on the right-hand side of the heatmap. The goal is to visually qualify differences between samples but not to quantify the difference in gene expression. The scale is set from 4 (red) to -4 (yellow), whereby a positive Z-score means that the expression of a gene for a particular sample is above average across all the samples and a negative score means that the gene expression is below average. In other words, this method is used to centre the data and to visualize the variance between the data, i.e., how gene expression values deviate from the mean indicated as 0 in the colour scale. Any blocks that are coloured '0' are therefore genes that are at an average expression level compared to other samples.

3.5 Results

3.5.1 There is no difference in proliferation rate of cells on ES filaments and Fw sutures

Cells were seeded on ES and Fw in pre-defined densities ($5.0x10^4$, $1.0x10^4$, $2.0x10^5$, and $2.5x10^5$ cells in 5, 10 or 20 µL) to firstly investigate what the proliferation would be over time between ES and Fw sutures and what the optimal number of cells would be to work with for downstream analysis, i.e., would a lower seeding density result in similar cell numbers after 14 days of culture. Initial cell attachment was low across all samples (ES and Fw) and densities (Figure 3.11). Cell numbers increase over time across all samples, but, overall, absolute cell numbers were the highest for samples seeded with $2{,}5 \cdot 10^5$ cells in 20 µL ($5.8x10^4$ for Fw vs. $2.1x10^4$ for ES, Figure 3.12).

Results for RNA concentration across the samples are given in Figure 3.13A. The ES groups have the lowest overall concentration of RNA (10 ng/µL), while the TCP groups have the highest (80 ng/µL). However, the differences between the samples in the FW0, FW14 and TCP0 groups are comparable. The ratio of absorbance is given in Figure 3.13B, with the dark grey bars indicating the 260/280 ratio and the light grey bars indicating the 260/230 ratio. Most samples have an acceptable 260/280 ratio, except for FW day 0, which is most likely due to a low concentration of RNA since samples were collected two hours post-seeding which leaves little chance of cell attachment or proliferation. The 260/230 ratio is below the dotted line for many samples with no obvious pattern per material or time-point. The most likely cause is that traces of the reagents used in the extraction process (most notably TRIzol) remained after the washing steps. Considering that cell numbers were quite low to start with, no samples were excluded from sequencing.

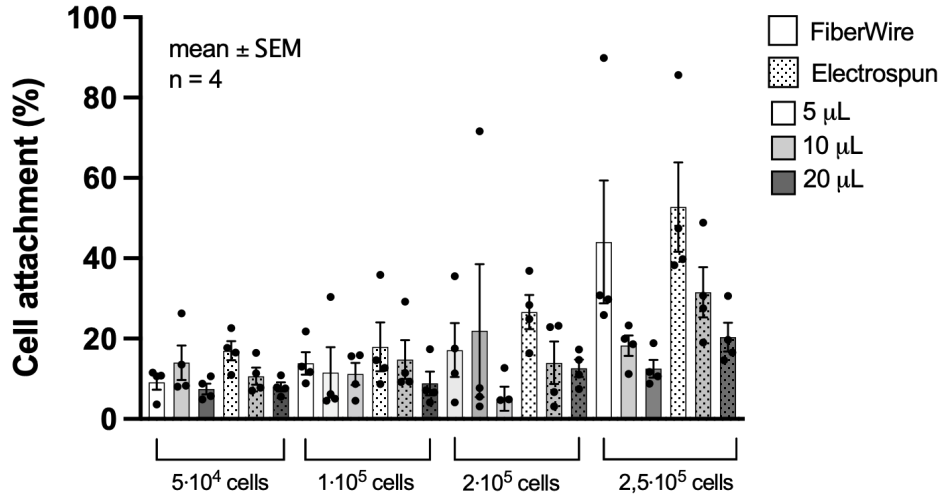

Figure 3.11 Seeding efficiencies for ES filaments and Fw sutures for different seeding densities.

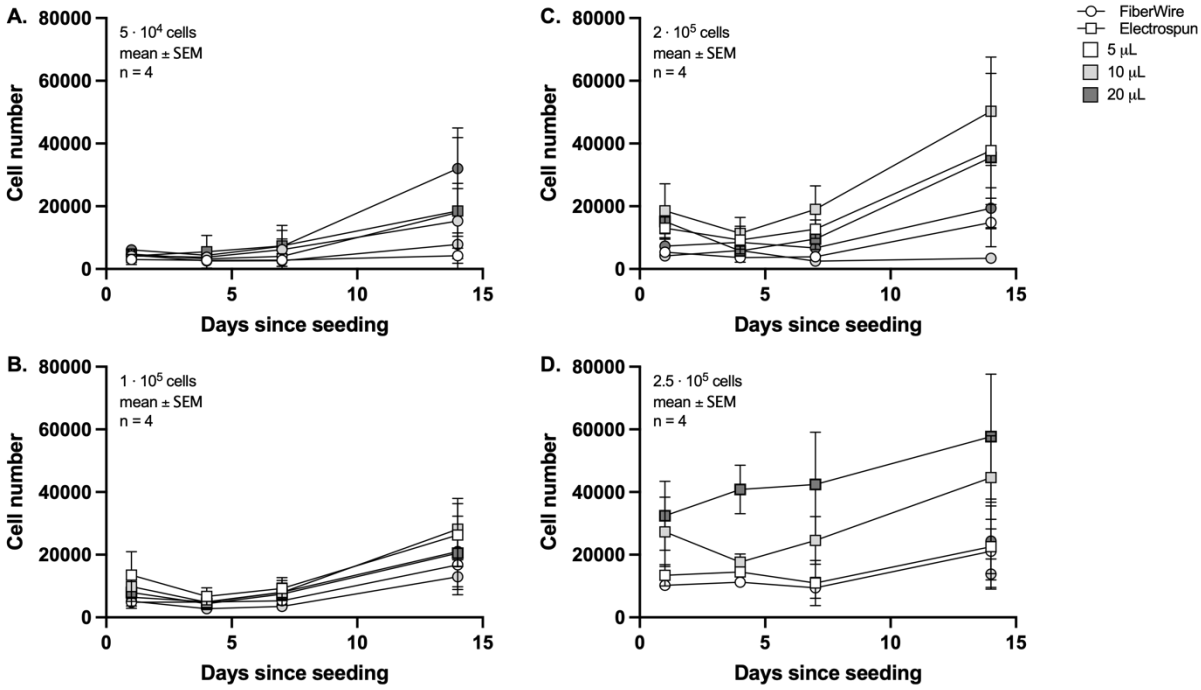

Figure 3.12 Change in cell number over the 14-day culturing period with derived absolute cell numbers for ES filaments and Fw sutures in different seeding densities per time-point (day 1, 4, 7 and 14).

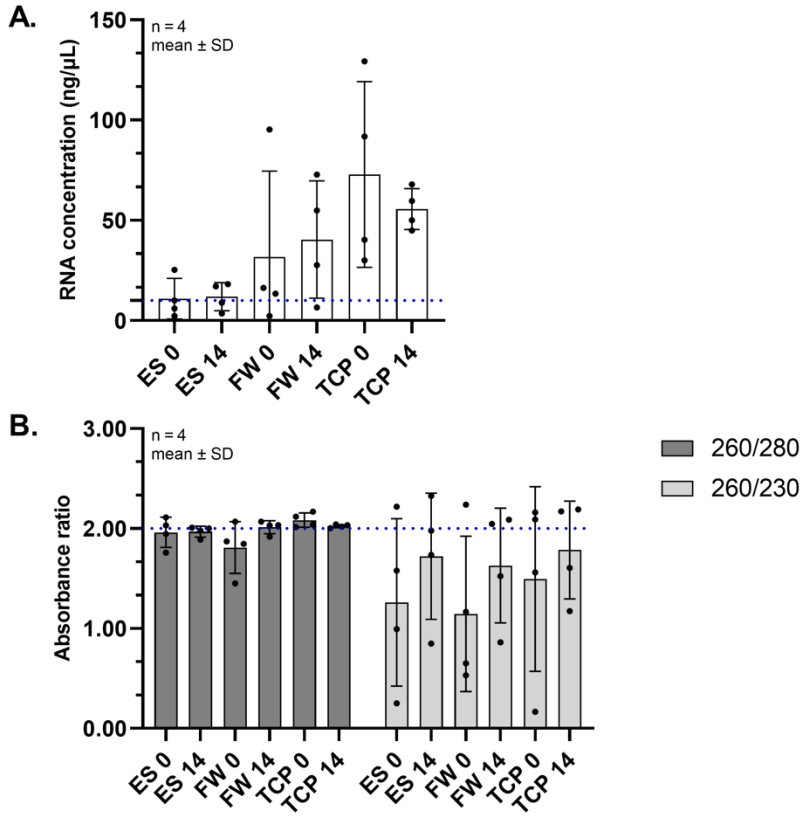

Figure 3.13 RNA concentrations (A) and absorbance ratios of 260/280 and 260/230 (B) measured for each sample after RNA extraction and prior to library preparation. The blue dotted line indicates the lowest RNA concentration possible to sequence (A) and an acceptable ratio of purity (B). ES = electrospun filaments, FW = FiberWire sutures, TCP = tissue culture plastic, 0 = day 0, 14 = day 14.

3.5.2 At the endpoint, cells display an elongated shape on ES sutures

Figure 3.14 shows the images of seeded scaffolds on day 1, 7 and 14 for FiberWire sutures (top row) and electrospun sutures (bottom row). Scaffolds are seeded with $2{,}5 \cdot 10^5$ cells in 20 µL and imaged at a magnification of 750x. Cells are pointed out with red arrows. The shape of fibroblasts seeded on electrospun filaments is noticeably different from the ones on FW sutures – they are more elongated and spindle-shaped across the time points compared to their counterparts on the FW sutures, resembling the morphology of resident tenocytes within tendon ECM. The diameter of individual filaments was measured using ImageJ and was 22.4 µm ± 1.6 for a filament within a FW suture and 3.9 µm ± 0.6 for that within an ES suture.

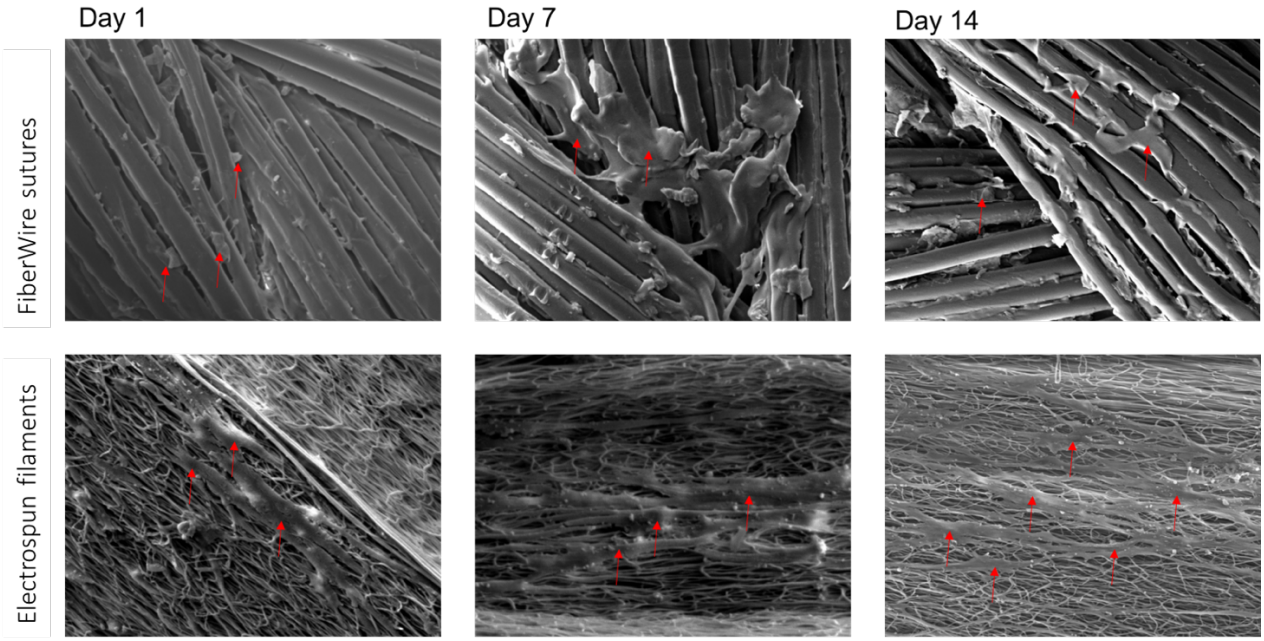

Figure 3.14 SEM imaging of cells seeded on ES filaments and Fw sutures over a 14-day period. These are seeded with $2{,}0 \cdot 10^5$ cells in 10 µL. Red arrows point to cells on the respective scaffolds. Images taken at a magnification of 750x.

3.5.3 Samples mostly cluster according to time-point rather than material type

The principal component analysis (PCA) is plotted in Figure 3.15. The calculation behind this is explain in Section 3.4.3. Clustering is defined as follows: each dot represents an individual sample and is coloured according to the group it belongs to (see key). There are four groups in total, with two different materials ('electrospun' and 'fiberwire') and two different time-points (day 'zero' and 'fourteen'). The two principal components (PC) plotted here together account for 68% of the variance in the dataset, with most of the variance plotted along PC1 (50%). The time-points are the main contributors for the spreading of the data-points, whereas the material type does not seem to influence the clustering behaviour. There is little separation along the y-axis (PC2), accounting for 18% of variance. This PCA accounts for less than 80% of the total variance, meaning that there might be unknown confounding factors in the experimental design that could explain the missing variance (*392*). A screeplot was generated to elucidate the data variance (Figure 3.16). Cumulatively, it seems that 6-7 of the PCs would account for >80% of the variance.

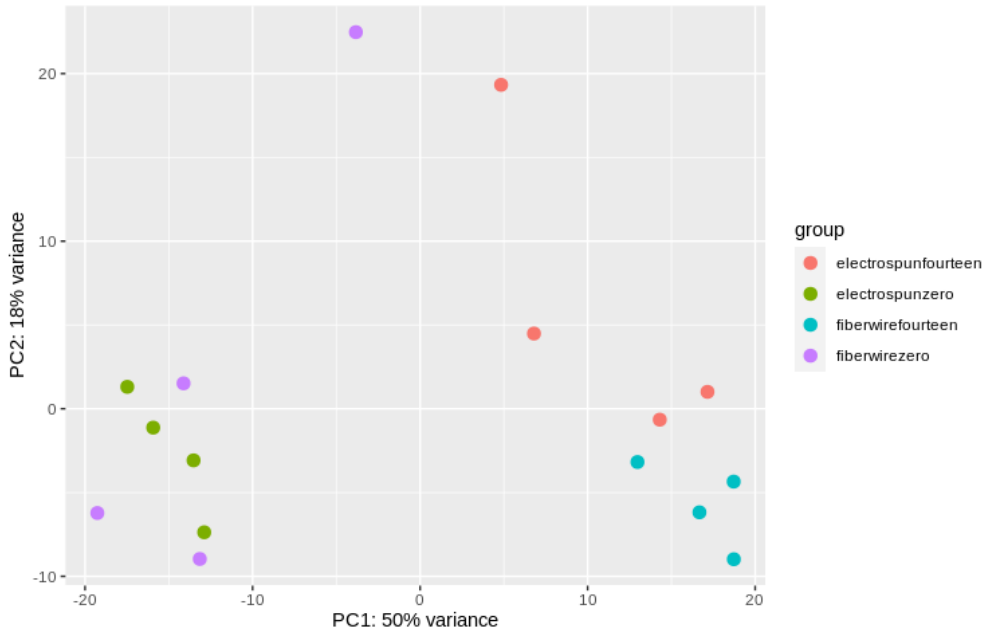

Figure 3.15 PCA plot of the current dataset, with samples split per group. Group 'electrospunfourteen' marks samples of ES filaments harvested on day 14 of cell culturing, whereas 'fiberwirezero' would be samples of Fw sutures harvested on day 0 of cell culturing, etc.

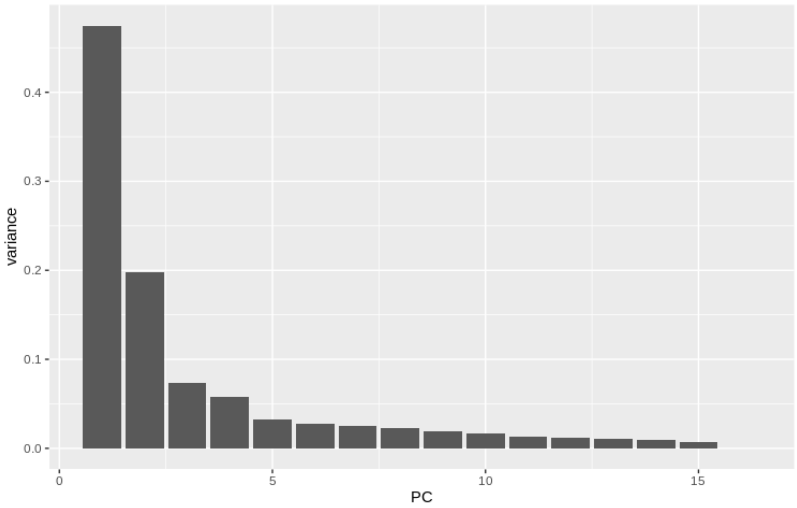

Figure 3.16 Screeplot of the current dataset. The main principal components are PC1 en PC2 which relate to time-point and material, respectively.

Data was further explored by hierarchical clustering and visualised in a dendogram and heatmap presented in Figure 3.17. The cluster distance ("Height) is portrayed on the left-side of the dendogram, which indicates the (dis)similarity between clusters. The higher the value, the less similar the clusters are. There are two main branches which hold all the time-point

fourteen samples on the left-hand side and the time-point zero samples on the right-hand side. The right-hand branch splits into two with the right-hand branch holding two samples from the ‘electrospunfourteen’ group, and one outlier which is a ‘fiberwirezero’ sample. The heatmap (Figure 3.18) gives a slightly different clustering compared to the dendogram. Again, the two main groups seem to be split into the different time-points, with the left-hand side of the map holding nearly all the time-point fourteen samples. The only exception is one electrospun fourteen sample, similar to the dendogram except the latter sample is further apart. The calculations for the dendogram and heatmap are explained in Section 3.4.3. In summary, there is no clear separation of all samples into the four respective groups. All samples were handled in the same manner before, during and after sequencing. However, RNA extractions, RNA library prep and sequencing was performed over the course of a few days, meaning confounding factors could have been introduced that might have influenced the outcome of the experiments.

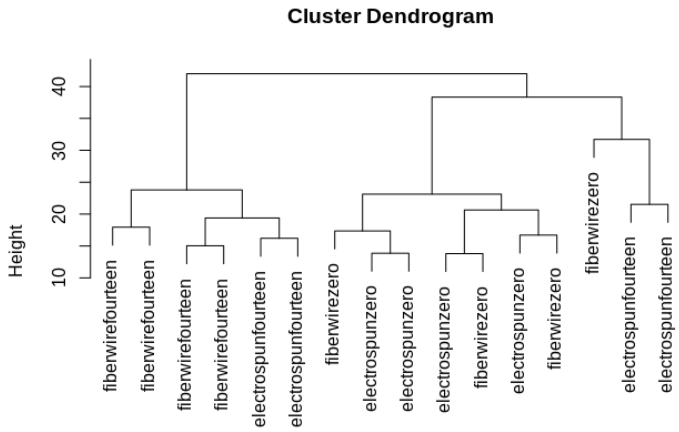

Figure 3.17 Dendogram of the current dataset. Samples are named according to which group they belong to, e.g., ‘fiberwirefourteen’ refers to a FW suture at day 14.

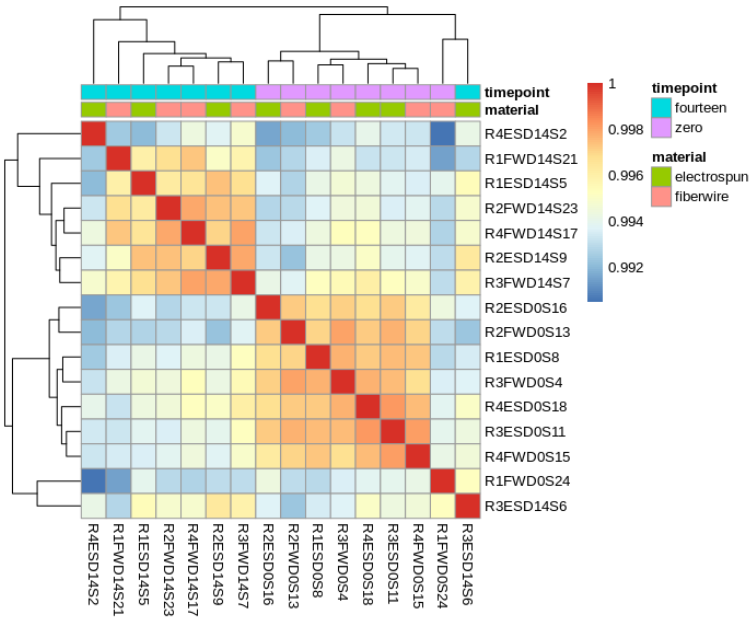

Figure 3.18 Sample-sample distance heatmap. The sample names are indicative of the repeat (R1-R4), material type (FW or ES), time-point (D0 or D14), and number of sample in the batch (S1-S16). Time-point ('fourteen' and 'zero') and material type ('electrospun' and 'fiberwire') are indicated in the top bars of the map.

3.5.4 There are few DEGs between ES and FW sutures at day 14

Each comparison is plotted in a separate volcano plot (Figure 3.19). The second term in the title is the group that is compared to and used as baseline, e.g., ES 14 vs FW 14 means that the cluster of electrospun samples at day 14 is compared against those of FiberWire at day 14. A total of 21999 genes were tested (padj < 0.05), of which 4265 (19.0%) were not included due to a low mean count, 1279 (5.8%) were up-regulated and 1080 (4.9%) were down-regulated (Figure 3.19A). These results were then split to focus on differentially expressed genes (DEGs) between groups. The materials compared at endpoint (ES14 v FW14, Figure 3.19B) yielded 324 (1.5%) up-regulated and 73 (0.33%) down-regulated genes. For ES 14 v ES 0 (Figure 3.19C) there were 1123 (5.1%) up-regulated genes and 1327 (6.0%) down-regulated. This was similar to FW 14 v FW 0 (Figure 3.19D) with 957 (4.4%) up-regulated and 1606 (7.3%) down-regulated genes. The null hypothesis for each gene in the dataset is that there is no differential expression of genes between electrospun and FW sutures at the endpoint (day 14).

A heatmap was generated to see how samples cluster according to DEGs (Figure 3.20). It is evident that the samples cluster well in their respective time-points, but not with respects to the material. The samples in time-point fourteen all cluster together in the middle, for electrospun and fiberwire alike, whereas time-point zero samples show a mix of electrospun and fiberwire on the left- and right-hand side. This pattern is similar to the PCA plots, dendogram and sample-to-sample heatmap shown previously.

Then, the top 20 differentially expressed genes were then ranked by padj per comparison and plotted by their normalised count values using the logarithm base 10 (see Methods). The first plot (Figure 3.21A) shows the genes that are most expressed across all samples. Each dot represents a sample and is coloured according to the group it belongs to, similar to the PCA plot. Along the bottom row the gene names are shown in alphabetical order. The RP11 genes are manually annotated genes from the Vertebrate Genome Annotation (Vega) database and do not have approved symbols available for the gene locus yet (*393*). Furthermore, gene names including 'orf' (e.g., *C15orf52*), relate to an 'open reading frame' meaning that this sequence does not include a stop codon and therefore does not code for a protein (*394*). Lastly, the *CH507* gene is uncharacterized and will not be discussed in this Chapter. All $\log_2$ fold changes (lfc) are given with respect to the second group in the title. For example, if gene X is up-regulated in a plot of group A vs. B, this means it is up-regulated in group A compared to group B. ES 14 is compared to FW 14 in Figure 3.21B. Most genes are up-regulated in the former group apart from collagen type VII α1 chain (*COL7A1*) and zinc activated ion channel (*ZACN*) which are both down-regulated (lfc -1.94 and -2.53 respectively). Intestinal cell kinase (*ICK*) is highly expressed in every sample in the FW14 group but is severely down-regulated in the ES14 group (lfc -21.00). Figure 3.21C shows the DEGs between ES14 and ES0. More genes are up-regulated in the ES0 group, except for

actin binding LIM protein family member 3 (*ABLIM3*, lfc 2.56), cyclin D1 (*CCND1*, lfc 1.76), integrin subunit alpha 2 (*ITGA2*, lfc 2.39), 5'-nucleotidase ecto (*NT5E*, lfc 1.96), neurotrimin (*NTM*, lfc 2.39), progestin and adipoQ receptor family member 5 (*PAQR5*, lfc 2.10), and tripartite motif containing 55 (*TRIM55*, lfc 2.88). The largest difference in expression between these groups is in semaphorin 4A (*SEMA4A*, lfc -4.53) and Wnt family member 2 (*WNT2*, lfc -3.86), which are all down-regulated in ES14 compared to ES0. FW 14 is compared to FW0 in Figure 3.21D, in which nearly all genes are up-regulated in the latter group. *ITGA2* (lfc 2.33) and *NTM* (lfc 2.84) are the only ones that are up-regulated in the FW14 group. The largest differences are in the expressions of carboxypeptidase A4 (*CPA4*, lfc -4.92), protein tyrosine phosphatase receptor type Q (*PTPRQ*, lfc -6.26) and *SEMA4A* (lfc -4.78), all down-regulated in the FW14 group. The significance and relevance of these genes is further elaborated on in the Discussion part of this Chapter. Gene expression analysis was also performed on cells cultured on tissue culture plastic as a baseline comparator, but to condense the data presented in this Chapter and to keep the focus on the difference between the ES and FW materials, it was decided not to include it. This data is freely available upon request.

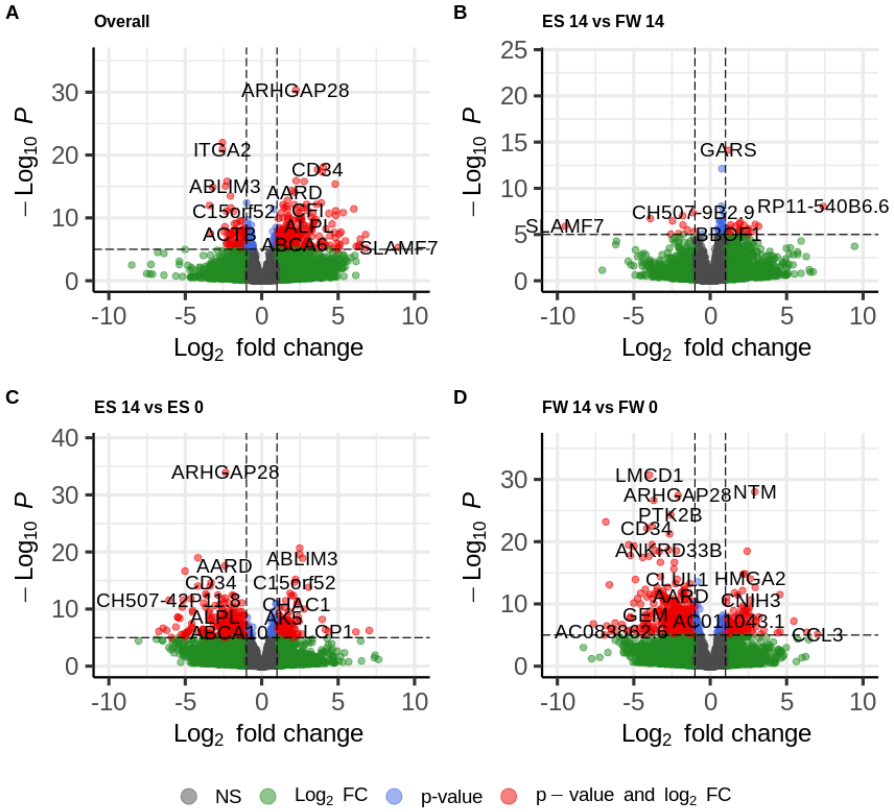

Figure 3.19 Volcano plots of overall gene expression (A), ES vs FW at day 14 (B), ES at day 14 vs day 0 (C) and FW at day 14 vs day 0 (D). Grey dots are non-significantly expressed genes, green dots indicate genes with a significant lfc >|2| (indicated by the vertical lines), blue dots indicate those with a p-value $<10^{-6}$ (indicated by the horizontal line), and finally, red dots indicate genes that have both a significant lfc and p-value.

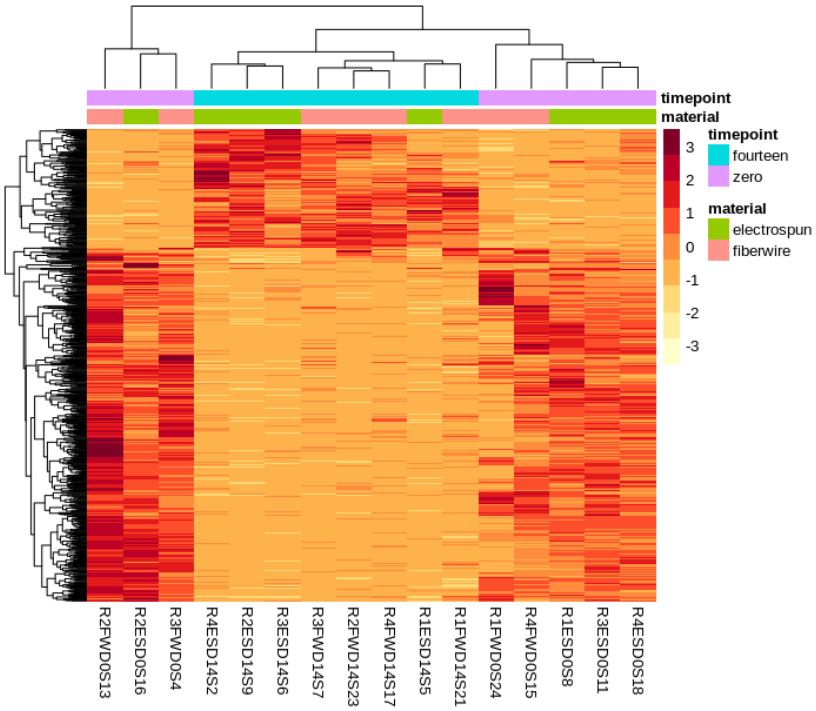

Figure 3.20 Heatmap of differentially expressed genes. The statistical test used by DESeq2 to query this is the Wald test. To reduce the rate of false positives, the Benjamini-Hochberg method is used. An adjusted p-value of 0.05 (padj) and a log fold change of 1 ($\log_2(2) = 1$) was set as threshold to keep significantly expressed genes.

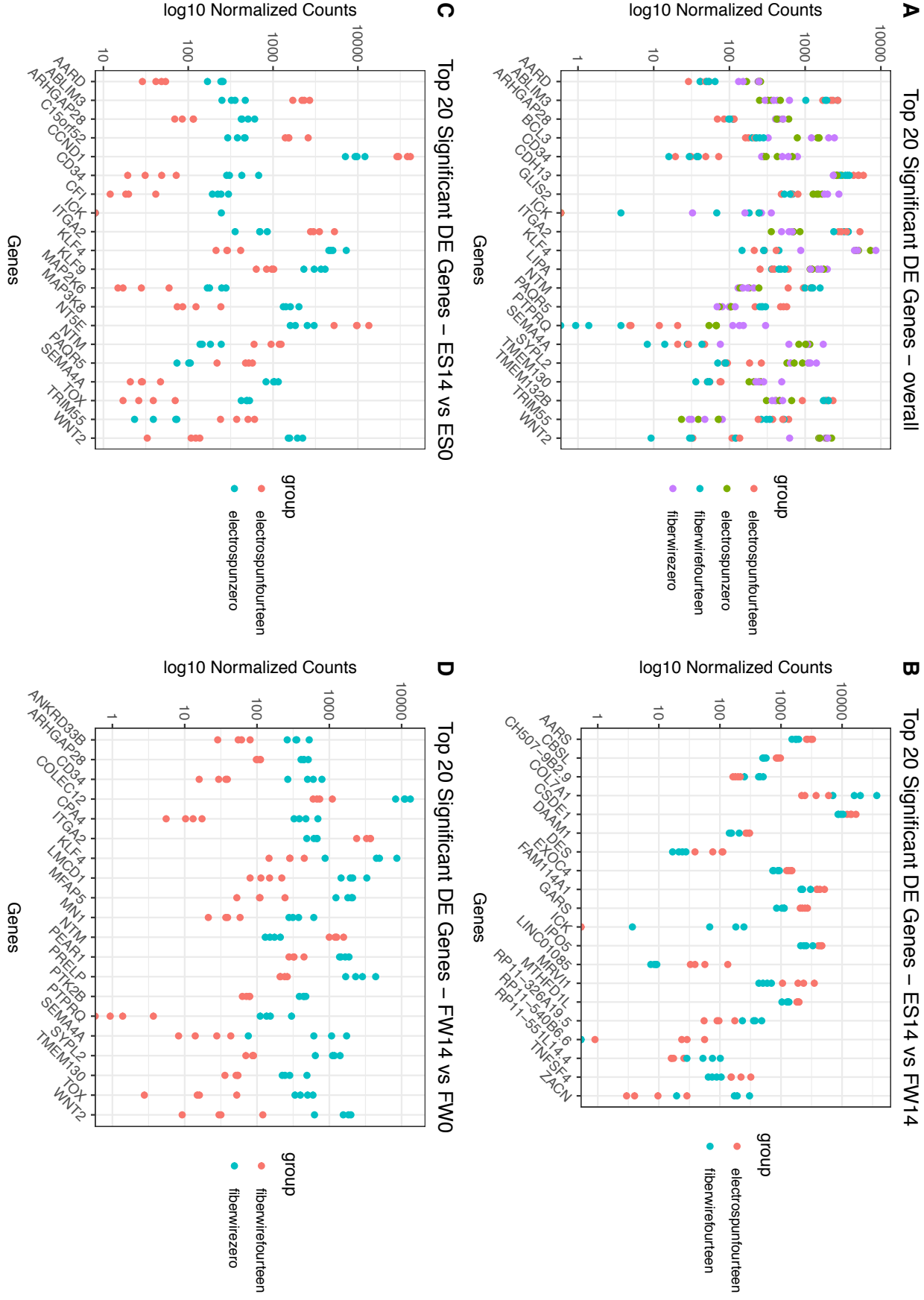

Figure 3.21 Top 20 differentially expressed genes between comparisons. The significance and relevance of these genes is further elaborated on in the Discussion part of this Chapter.

3.5.5 ES sutures induce changes in genes involved in development, while FW sutures induce changes in those involved in wound response

Pathway analysis was carried out to put the list of differentially expressed genes (DEGs) into a biological context. Please refer to the Appendix for more detail on the methodologies used here. The clusterProfiler package was used to perform an over-representation analysis (ORA). A threshold was set to include only significant genes with a padj < 0.05. For each comparison, a dotplot was generated to visualise the top 25 over-represented gene ontology (GO) terms (Figure 3.22-3.23). There were three enriched terms between ES14 and FW 14 (Figure 3.22), which include muscle system process, establishment of cell polarity and sprouting angiogenesis. The enriched terms between ES14 and ES0 are plotted in Figure 3.23A and those for FW14 v FW0 in Figure 3.23B. Most of the enriched terms in the ES group relate to development and proliferation, while those in the FW group are more involved in cell cycle processes and extracellular matrix organisation. Both groups show enrichment in positive regulation of cell migration, cell motility, and angiogenesis. In addition, the ES group shows enrichment in the ameboidal-type cell migration whereas the FW group has an enrichment in response to wounding. Additionally, the Gene Set Enrichment Analysis (GSEA) tool was used to further query the gene expressions. This was done for a couple of reasons. Firstly, the advantage of GSEA over ORA is that it does not need a user-defined threshold (e.g., padj <0.05) and takes all genes in the dataset into account which means it can detect small differences that might contribute to a given gene set. Also, ORA assumes that genes are independent of each other when performing statistical operations. In biological systems, this is not true since genes can influence each other and therefore this analysis can be more prone to errors. The GSEA output is plotted in Figure 3.24, with the normalised enrichment (NES) score visualised as a colour scale from blue (negative) to red (positive). The NES are plotted against the -log10(p-value) to indicate significance. There are a few enriched terms between ES 14 and FW14, with the most

interesting being adherens junction, vascular smooth muscle contraction and gap junction (Figure 3.24). Similarities in enriched terms for ES and FW groups are for proteasome, ribosome biogenesis, nucleocytoplasmic transport, and spliceosome. The most enriched gene set for ES14 v ES0 is the herpes simplex virus 1 infection pathway, which is not expressed in the FW14 v FW0 group. Other pathways which are only expressed in the ES group include pathways in cancer, and cytokine-cytokine receptor interaction. Unique pathways expressed in the FW14 vs FW0 group include the rheumatoid arthritis, IL-17 signalling and Fanconi anemia pathways. Overall, terms expressed in the FW group have more significant NES than those expressed in the ES group.

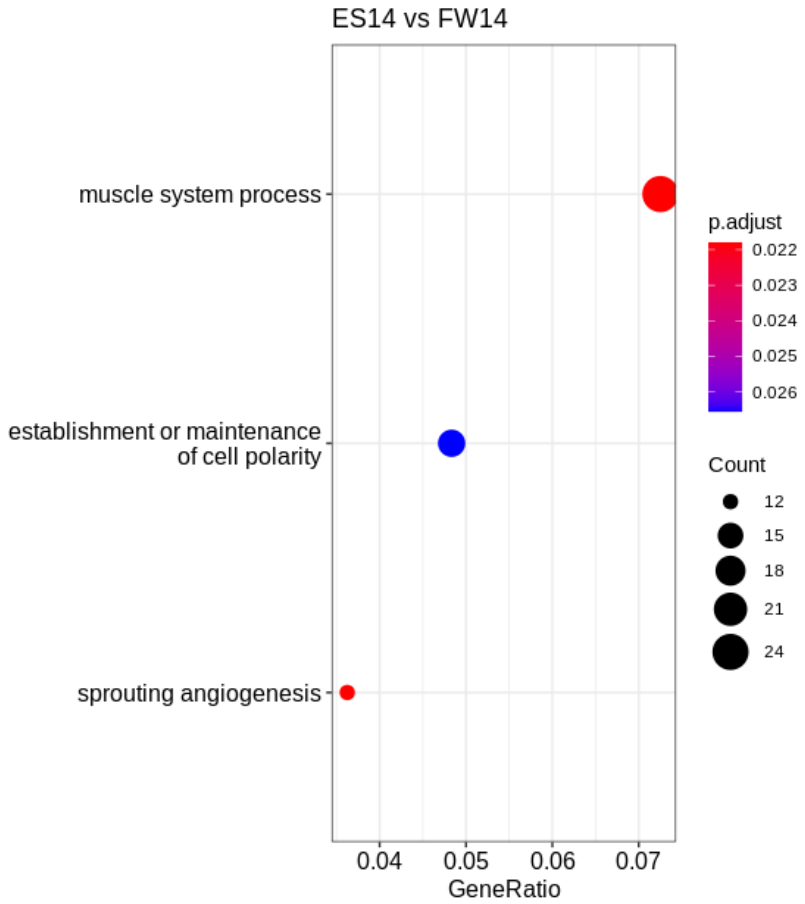

Figure 3.22 Over-representation analysis between ES14 and FW14. The pathways are plotted by gene ratio, which is the number of genes associated with a GO term divided by the total number of significant genes (14759). Thus, the higher the ratio the more genes are associated with the specific term and vice versa. The size of the dots is a measure of frequency; they represent how many genes in the dataset are in the pathways specified on the left-hand side. The colour scale is indicative of the significance, with high p-values in blue and low p-values in red. The adjusted p-value is used to rank the genes as calculated above.

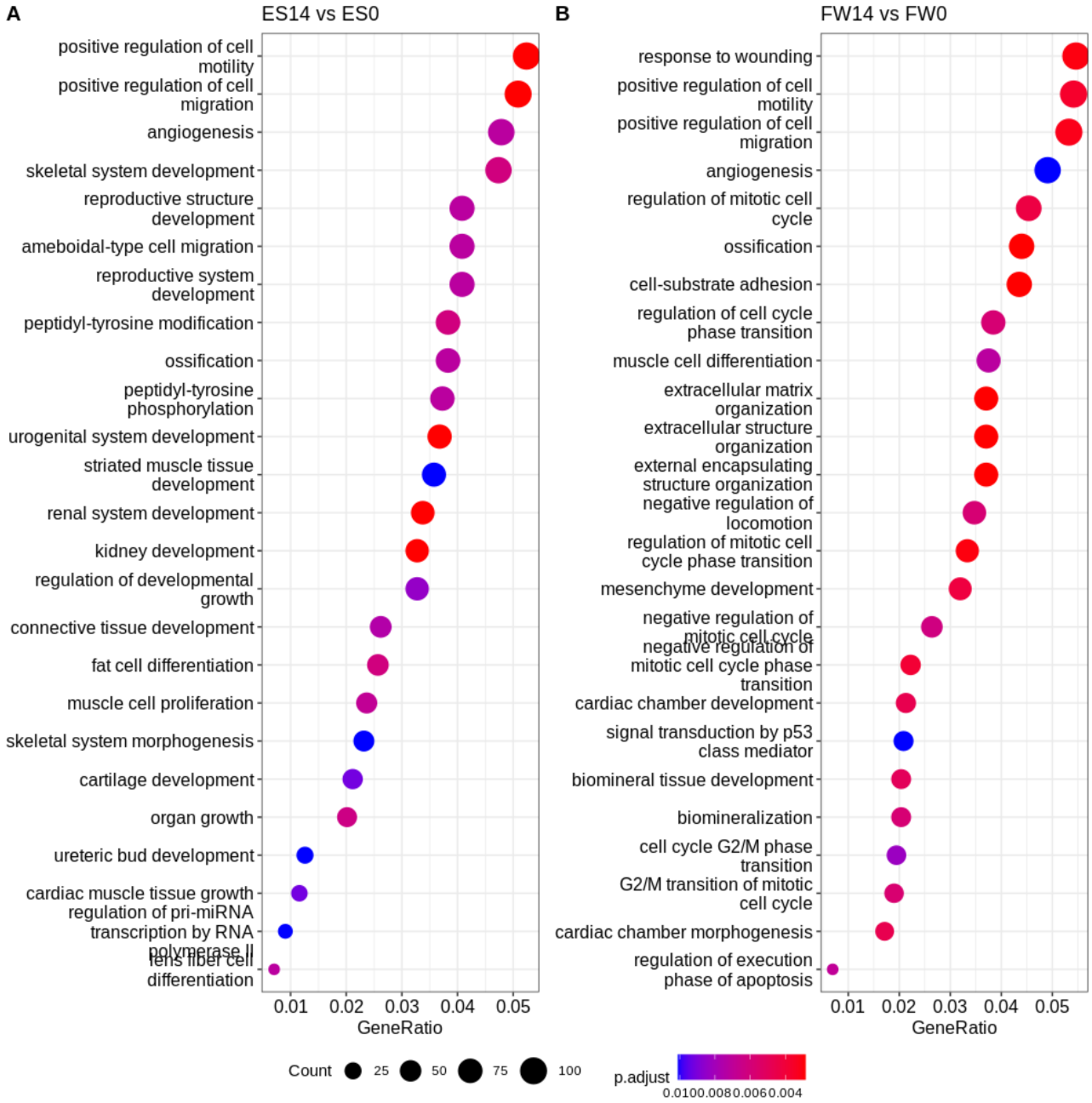

Figure 3.23 Over-representation analysis between ES 0 vs ES 14 (A) and FW 0 vs FW 14 (B).

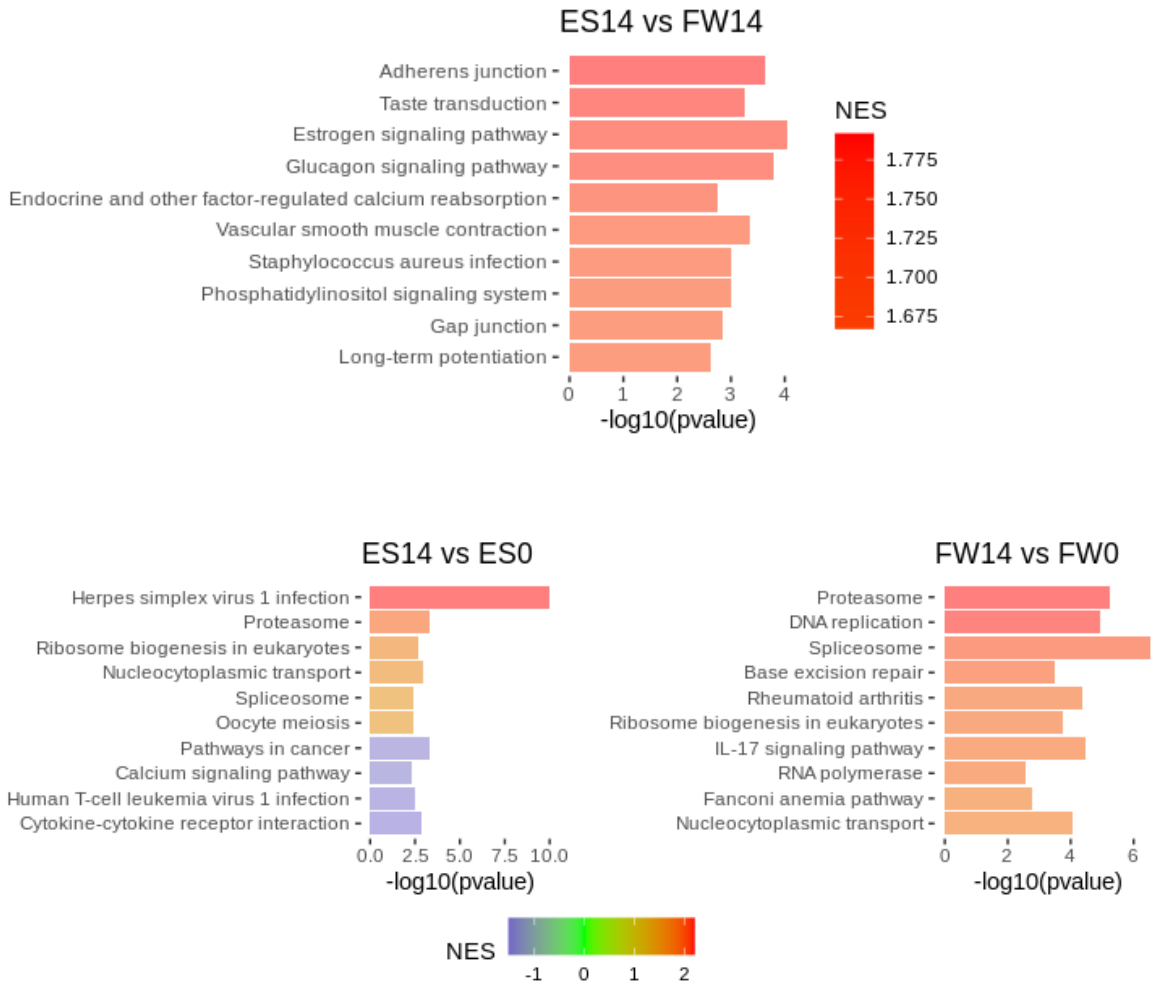

Figure 3.24 GSEA output for each comparison.

3.6 Discussion

In this Chapter the seeding of cells on ES filaments was compared to cells seeded on Fw sutures with respect to their attachment, proliferation and gene expression at the start and end of the culturing period. Initially, nine different seeding densities were tested to determine cell numbers after 14 days of culture and pick the highest value, which would garner a sufficient concentration for RNASeq experiment. Cell seeding efficiency was low for both materials across the different densities used and no significant differences were found in terms of absolute cell numbers or relative fold change. However, cell morphology had changed on the ES filaments compared to the Fw sutures from the first time-point (day 1) onwards. Furthermore, RNASeq showed a difference in gene expression between ES filaments on day 0 and day 14, and between Fw sutures on day 0 and day 14, limited changes between ES filaments and Fw sutures on the final time-point.

3.6.1 Cell attachment and proliferation similar on ES filaments and Fw sutures

Although it was expected that the highest seeding density would result in the highest cell attachment, it was important to understand how large this difference would be. For the materials used in this thesis, seeding less than 200,000 cells, regardless of seeding volume, seems to be a wasted effort as the cell attachment is quite low. It was expected that a higher seeding efficiency would be achieved with cells seeded in a very small volume, but by the end of the experiment there was no statistical difference in absolute cell numbers between the different materials at the end-point. Although no statistical significance was reached between ES filaments and Fw sutures either, there are a couple of interesting aspects to their inherent properties that could have resulted in quite similar cell attachments. Firstly, their surface chemistry is quite different. The ES filaments are manufactured from the highly hydrophilic polydioxanone, which should have facilitated cell attachment. In fact, a micro-drop of media was easily absorbed by the entire scaffold. However, because the suture consists of aligned

micro- and nanoscale fibres it is also highly porous and the drop of media containing the cell suspension largely filtered through to the bottom of the cell plate during seeding. In contrasts, Fw is hydrophobic in nature and has an intricate braided design with an inner structure, making it quite a dense suture. Fibroblasts attach to the ECM by integrin receptors and a successful coupling creates a bi-directional signalling through the integrin - i.e. signals are transmitted from outside of the cell to inside and vice versa – which results in changes to gene expression, (re)organization of the cytoskeleton and cell proliferation (*395*). The opposite of cell attachment is termed *anoikis* – a neologism inspired by the Greek, translating to 'without house' – and is a specific type of cell-death thought to be signalled by the cytoskeleton (*396*). Cell attachment mediated through the integrin receptors are crucial to this process, therefore inadequate contact between the cell and ECM would result in *anoikis* and is the most probable cause for low seeding efficiency and a significantly lower number of cells at the end-point than originally seeded. The shape of the cells seeded on both ES filaments and Fw sutures was evaluated using scanning electron microscopy during the culturing period. The images were compared to each other per time-point they were taken at. Although cells are present on both samples at every time-point, also confirming cell attachment, there is a striking difference in the cell morphology, with those seeded on ES filaments exhibiting an elongated and spindle-like shape from the first time-point, whereas those on Fw sutures remain rounded and flat and do not change their shape much throughout the two-week culturing period. This can be explained in several ways. Firstly, it is a well-known fact in the tissue engineering world that cells respond to environmental cues (*397*). In fact, research concerning scaffolds that are designed primarily for tendon end-goals is now more and more focused on providing instructive cues for cells. Native tendon topography is one of the most important properties of a scaffold that contributes to the phenotype of a tenocyte (*398*). Electrospinning has been popular because it allows for the fabrication of

fibres on a micro- and even nanoscale (Background, section 1.6) that is similar to morphology in tendon fibrils. The microscopic appearance of the materials was different in diameter, which was considerably larger for the Fw sutures than ES filaments: 22400 and 3900 nanometer (nm), respectively. The mean fibre diameter of collagen fibrils in healthy supraspinatus tendon is 57±3 nm while that in an injured tendon is 51±3 nm (*399*). However, electrospun scaffolds with modulated fibre diameter have been reported to positively regulate tenocyte behaviour (*400*) and aligned scaffolds with a relatively large diameter (>2000 nm) have been shown to induce the spindle-like morphology and a reduced inflammatory response in tenocytes (*172*). When comparing these figures to the experimental dataset presented in this chapter, it is reasonable to assume that the ES filaments, which are aligned as well, fall within the >2000 nm diameter range and therefore presented a positive environment for cells to adhere and respond to. The large diameter of Fw sutures did not prevent cell attachment but also did not induce them to change their shape during the two-week culture. In a similar study by Musson et al (*401*) in which primary human and rat tenoyctes were seeded on different types of scaffolds, cell culture on Fw sutures was unsuccessful as tenocytes did not adhere to the material at all after 14 days in culture. The authors cited its highly hydrophobic nature as the main reason, though the low seeding density used ($2.5 \cdot 10^4$ cells/scaffold) could perhaps also be relevant.

3.6.2 Differentially expressed genes between ES filaments and FW sutures show a different profile with respect to cell attachment and wound healing

RNA-Seq was performed on the seeded dermal fibroblasts to investigate the effects of the ES filaments and FW sutures on gene expression. I investigated differences in gene expression in response to material as well as changes across time. The differentially expressed genes between these groups were investigated first and were related to cell attachment and

proliferation, stress responses and wound healing. *Col7A1* encodes for a type of collagen that is the major component of anchoring fibrils in the skin – these connect the epidermal basement membrane to the dermis (*402*), which makes it vital to the function and stability of the extracellular matrix (*403*). Indeed, a mutated gene results in *epidermolysis bullosa*, a severe skin disorder characterized by blistering due to detachment of the epidermis (*404*). It is down-regulated, but not absent, in the ES14 vs FW14 group, which is interesting given that both cell attachment and cell proliferation was increased in the former group. This raises the suggestion whether the anchoring fibrils were as necessary for attachment in the ES14 group – considering a single cell was able to attach to multiple filaments within the suture, elongate and extend to neighbouring cells. On SEM images it seems that cells on Fw sutures do not induce changes in cell shape and perhaps require a more marked increase in the use of anchoring fibrils that is not induced by cell attachment to Fw. *ICK* regulates the length of primary cilia, which are present in nearly all mammalian cells and are important to detect extracellular cues for proliferation and differentiation. They are essential for many signalling pathways, including *Hedgehog* (Hh) signalling which has been shown to be crucial for tendon enthesis development (*405, 406*). The process of mechanotransduction, by which cells convert mechanical forces into biological signs (*405, 407*) is also dependent on the length of primary cilia. Down-regulation of *ICK* can result in abnormal and extended cilia (*408*). However, the assembly of primary cilium does not start until after mitosis has finished (*409*). In a recent study by Bosakova et al (*408*) it was shown that fibroblast growth factor receptors (*FGFRs*) interact with *ICK* by phosphorylation and can inhibit its activity, thereby down-regulating its expression, with the primary aim of regulating cilia length. This means that a down-regulation of FGFRs would result in an increase of ICK activity. Conversely, since *ICK* was up-regulated in every FW14 sample and down-regulated in the ES14 samples, one could assume that there is a down-regulation of FGFRs in FW14 and an up-regulation in

ES14. In fact, four FGFRs are expressed in the current dataset and are slightly down-regulated, but none of them had a statistically significant differential expression. FGFRs signal fibroblast growth factors (*FGF*) to regulate the migration of keratinocytes in cutaneous wound repair to achieve re-epithelialization (*410*) and can potentially accelerate wound closure by changing the morphology of keratinocytes to be spindle-like (*411*). In fact, FGFs have been successfully tried and tested to reduce scarring in post-surgical wounds and to improve the outcome of diabetic foot ulcers (*412, 413*). This could mean that fibroblasts seeded on ES filaments are more likely to express a phenotype geared towards wound healing than those seeded on Fw sutures. This is partly supported by the pathway analysis as well, as discussed below.

3.6.3 Similarities in gene expression between ES filaments and FW sutures

SEMA4A was down-regulated in all time-point fourteen samples irrespective of material. This gene was found to be up-regulated in patients with lung fibrosis and systemic sclerosis has been found to induce a profibrotic phenotype in primary dermal fibroblasts (*414, 415*). Indeed, fibroblast attachment to ECM is regulated by integrins and culminates in the maturation of focal complexes into focal adhesions (*395*), which mainly consist of focal adhesion kinase (*FAK*). This protein plays an important role in cell migration and has been linked to fibroblast migration in lung fibrosis (*416*). This suggests that cells are more prone to a pro-inflammatory phenotype rather than a pro-fibrotic phenotype when cultured on these materials. However, since both the cell populations exhibited this phenotype one can assume that electrospun sutures do not perform worse than FiberWire sutures in this regard. Furthermore, one gene that is only expressed in the Fw group is *COLEC12,* which is involved in inflammatory responses by clearing glycoproteins released by neutrophils and is overexpressed in fibroblasts of patients with hypermobility syndrome (*417*). It has also been

found to play a role in inflammatory response in osteosarcoma (*418*). This skews the narrative in favour of ES sutures that do not express this gene. *Wnt2* was also down-regulated in all time-point 14 samples as well and is a ligand that is expressed in lung mesenchyme during lung development and plays an important role in airway smooth muscle development (*419*).

3.6.4 Different genes are expressed at time-point 0 and 14 for for ES filaments and Fw sutures, respectively.

A couple of genes were up-regulated in ES14 compared to ES0, but not expressed in FW14 vs FW0. *CCND1* is a transcriptional regulator that controls cell proliferation and has been linked to cancer metastasis – most likely due to its ability to regulate cell adhesion and migration (*420*). Indeed, it has been shown that *CCND1*-deficient cells show less migration and invasion than wild-type cells and are strongly associated with metastasis in breast cancer (*421-423*). Its up-regulation in this experiment might indicate a positive sign of cell proliferation and the invasion of cells in the scaffold as well – an important indicator for the integration and efficacy of a biomaterial. It could also explain why cancer pathways were enriched in the functional pathway analysis with no biological context. *ITGA2* encodes for the α2 integrin subunit. The integrin family consists of 18 α - and 8 β-subunits that can form 24 different heterodimer combinations (*424*). The α2 sub-unit only forms a heterodimer with the β1-unit, resulting in the α2β1 integrin, which is mainly expressed in epithelial and platelet cells and is one of the receptors for type I collagen making it vital for angiogenesis (*425-428*).

3.6.5 Angiogenesis and cell migration are enriched for both ES filaments and Fw sutures

The functional pathway analysis revealed only three enriched GO terms between ES 14 and FW 14. The most interesting term is muscle system process in GO. Similarly, skeletal muscle development is also prominent in the GO term for ES14 vs ES0. Similar enriched terms for ES0 v ES14 and FW0 vs FW14 include positive regulation of cell motility and cell migration, and angiogenesis. Cell migration of fibroblasts is regulated by *FAK* and linked to lung fibrosis through *SEMA4A*, as previously discussed. Fibroblasts play a role in angiogenesis by producing and releasing vascular endothelial growth factor (*VEGF*) to signal the migration of endothelial cells to form new blood vessels (*429*). During wound healing, new blood vessels infiltrate the site of injury together with fibroblasts and macrophages to build new ECM and restore the damaged tissue (*430*). This term is expressed in conjunction with the 'response to wounding' in the FW group. Other interesting terms in the FW group include extracellular structure and matrix organization and cell-substrate adhesion. These three are all linked to attachment of the cell to the matrix, although this was not different between ES and FW sutures in the previously discussed proliferation data. In the early response to rotator cuff tearing, cell proliferation is stimulated by vasoactive factors that initiate angiogenesis (*431*). However, tendon is an inherently avascular tissue which also contributes to the difficulty of the repair response. Signs of angiogenesis in this experiment are probably inherent to the use of dermal fibroblasts rather than tendon fibroblasts, which have an important role in wound healing.

The difference in cellular composition and distribution between healing and injured rotator cuff have been reviewed extensively

3.6.6 Signs of angiogenesis are further enriched for ES filaments, while for Fw sutures it concerns inflammatory processes

The gene-set enrichment analysis revealed several up-regulated pathways for ES14 as compared to FW14. Adherens junctions are present in endothelial and epithelial cells and connect cells to each other by joining actin cytoskeletons together. They are important in maintaining endothelial integrity and vascular homeostasis (*432*). Similarly, gap junctions allow communication between cells by linking the cytoplasm of two cells and forming intercellular channels and serve an important purpose in the homeostasis of many tissues. This is a positive indication of cell-to-cell communication on the ES filaments that is apparently less evident in the Fw sutures. Furthermore, the vascular smooth muscle contraction can be directly linked to the angiogenesis GO term, as discussed in the previous section. A unique GSEA term that is expressed between ES 0 and ES14 is the herpes simplex virus 1 (HSV-1) infection. Since the fibroblasts used here were from a commercial cell line, derived from neonates, there was no infection of any kind during the culturing process and this pathway was not enriched in the FW group it is reasonable to assume that there was not actually an HSV-1 infection present. Interestingly, this pathway was also found to be enriched in the study by Wang et al (*433*), where the authors investigated the difference between the adult and neonatal cardiomyocytes. The HSV pathway was also found to be enriched in microarray analysis of osteoarthritis and rheumatoid arthritis samples (*434*). No further comment on it was made in these studies, however. In the FW group, the pathways for rheumatoid arthritis and IL-17 signalling are enriched, which are both linked to each other and could indicate the presence of inflammatory processes (*435, 436*). This might also be linked to the ‘response to wounding’ GO term, discussed previously. Consequently, the Fancomi anemia pathway is also enriched in the FW group and is needed for the repair of

damaged DNA. It is involved in repairing cytotoxic DNA lesions, which can be caused by aldehydes as a result of many metabolic processes including lipid peroxidation (*437*).

3.6.7 Limitations and future work

There are several limitations to this experiment that should be addressed. Firstly, this experiment was limited by the use of a commercial cell line rather than primary cells. Although they are also fibroblasts and were mainly chosen because they expressed similarities to tendon fibroblasts, the genetic profiling of these cells does not express markers relevant to tendon development and maintenance. However, considering the large number of cells needed to run the experiment in multitude and to gather reliable and reproducible results, it was not possible or feasible in the current time to get enough primary cells explanted from donated tissues.

The fibroblasts were harvested from the foreskin of two male neonates (*438*) and can therefore be considered neonatal fibroblasts. There is a marked difference in the behaviour of adult and neonatal fibroblasts. Indeed, it has been shown that younger fibroblasts tend to be pro-regenerative compared to adult fibroblasts (*439*). A recent single-cell RNA sequencing performed on murine cardiomyocytes revealed a switching from neonatal to adult fibroblasts that regulated cardiomyocyte maturation, which can potentially be manipulated to tackle cardiovascular disease development (*433*). The tendency towards fibrosis or regeneration has been heavily linked to age and the results presented in this Chapter do not necessarily reflect pro-fibrotic markers. However, it is interesting that the FW group expressed genes in response to wound healing pathway, while the ES group expressed mostly terms related to development and proliferation. These differences could be attributed to the difference in the surface topography of the materials. Dermal fibroblasts have a subpopulation of reticular and papillary fibroblasts related to their location in the skin, whereby the former is squarer and

flatter while the latter is thinner and spindle-shaped (*440*). Papillary fibroblasts have also been shown to have increased proliferation compared to reticular fibroblasts (*441*). Furthermore, reticular fibroblasts show GO terms that are mostly involved in the smooth muscle contraction pathways and correlate with cytoskeletal organization and cell motility, while papillary fibroblasts showed enrichment in the immune response (*440*). Papillary fibroblasts also promote angiogenesis (*442*), which was a significantly enriched term both groups. This, in combination with the results of cell morphology, indicates FW and ES sutures have a population of both papillary and reticular fibroblasts. The seeding densities chosen in this work were based on numbers often used in the current lab group when working with electrospun materials (*173, 259, 260, 293*) and were capped at a maximum of 250,000 cells per sample to have enough to run the experiment multiple times. In the literature, there are may examples of seeding densities or concentrations that are $5 \cdot 10^5$-$1 \cdot 10^6$ cells/mL but this figure is not an accurate description of how many cells will be on a scaffold since seeding volumes are nearly always in the order of microliters. Therefore, a scaffold that is seeded in a concentration of $1 \cdot 10^6$ cells/mL and a volume of 20 µL will have 20,000 cells on it at maximum (e.g., if every single cell would stick to the scaffold and the seeding efficiency would be 100%). The figures in this experimental Chapter were therefore deliberately chosen to reflect the number of cells seeded and not the concentration. Low seeding efficiency is another problem often encountered in tissue engineering and is due to the nature of cell seeding. A static seeding method was used here to seed and maintain the cells, which relies solely on gravitational forces. Cells are thus allowed to infiltrate the scaffold without being subjected to mechanical forces resulting in reduced viability, but since infiltration rates can be quite slow in especially dense scaffolds (e.g., the FiberWire sutures), a culturing period of two weeks might not have been long enough. As briefly mentioned before, however, there is a plethora of evidence suggesting a positive influence of mechanical stimulation on cell

behaviour. However, there was no time to establish and test a suitable methodology for different types of seeding, i.e., dynamic seeding using external forces, nor was this the focus of this experiment. In future work, these results may be used as a baseline for testing different seeding methods to see if this might improve initial cell attachment and maintain a higher number of cells during the entirety of the culturing period.

Another factor impacting these experiments is the electrospun material involved. The filaments were manufactured using an in-house electrospinning set-up, which is susceptible to minimal environmental changes (e.g., humidity, air pressure, static energy) that could impact the quality of the fibres on a microscopic level. The fibres were assessed macroscopically for any gross deformities, such as beading (*292*), and by stretching them to evaluate their elasticity. Furthermore, because it was not feasible to spin all the samples in one go, batch-effects could exist that could have affected the surface topography of the scaffolds and thereby cell attachment and genetic expression. This was overcome by using different batches of filaments in a random order to create the sutures used in this experiment. No conclusive evidence of batch-effects could be deducted from the results, however. The FiberWire sutures all came from the same batch and were individually packed and pre-sterilized, so this seems less likely. In addition to the limitations addressed above, there remain a few points that will be interesting for future work. Firstly, the scaffolds used in this work were quite small as there was a limited supply of the material available. This meant that the surface area we worked with was also small and pipetting onto this tiny scaffold contributed to a low seeding efficiency and loss of cells. To circumvent this problem, making bigger bundles (e.g., using the largest number of filaments that were used in Chapter 2) or weaving the fibres into a patch will be a solution. Secondly, in this experimental set-up we pre-soaked the materials to facilitate cell attachment. However, I did not establish what the difference in cell attachment would be without preparing the materials and thus we cannot

say if it contributed or not. It will be interesting to add this to future work and gauge whether it is a necessary step at all. Thirdly, the RNASeq results obtained here are from a two-week cell culture period and this might not have been long enough to elucidate more relevant pathways. As mentioned above, the scaffolds were also not subjected to any mechanical load which could have contributed to enrichment of different pathways as well. In a future experiment, a culture period of at least 28 days including cell stimulation should be attempted. Lastly, the comparator material tested here were the Fw sutures and although it is a relevant material and a popular use in clinical settings, other products are frequently used in rotator cuff surgeries as well (e.g., OrthoCord, EthiBond, UltraTape, etc.). To assess how well electrospun sutures match those used in clinical settings, the current experiment should be expanded to include more comparators.

3.7 Conclusion

This Chapter shows that there is no difference in cell attachment or proliferation between ES filaments and Fw sutures, but fibroblasts seeded on ES filaments were elongated and spindle-shaped compared to those on Fw sutures, indicating a favourable attachment of cells on the ES filaments, resembling the attachment of cells to ECM. This is encouraging because it means cells can adapt to the architecture of the electrospun sutures as they would to the native ECM of native tendon tissue. Enriched pathways mostly related to development and proliferation, angiogenesis, and extracellular matrix organization. ES filaments exhibited a more pronounced profile towards cell proliferation and differentiation whilst Fw sutures had enriched pathways in wound response and inflammatory pathways concerning rheumatoid arthritis and IL-17. The results in this Chapter can provide a baseline for future work, that should focus on the use of a more clinically relevant cell type.

3.8 Acknowledgements

All experiments and data analysis in this Chapter were performed by me. However, a few people deserve a special mention for their help. Thank you to Dr Claudia Paul, Dr Jolet Mimpen and Dr Martin Philpott for help with RNA extractions, library preparation and RNA-sequencing. Thank you to Dr Adam Cribbs, Dr Lorenzo Ramos Mucci and Dr Jianfeng Sun for their explanations of various computational analysis principles and for reading through my analysis. This work was funded by the Interreg 2 Seas programme 2014-2020 3DMed.

Chapter 4 Adapting the design of the 3D printed part of the biphasic scaffold

4.1 Abstract

Current suture anchors used in rotator cuff surgeries commonly comprise a hard part (anchor) and a soft (suture) component and have excellent mechanical properties. However, several modes of failure have been identified that are usually due to improper healing of the native tissue and weakness at the interfaces. This thesis has developed a biphasic scaffold consisting of a hard 3D printed block and soft electrospun cuff, involving bioactive materials that could be beneficial in tendon- and enthesis healing. In this Chapter, the dimensions of the 3D printed component has been adapted to fit the footprint of the supraspinatus tendon on the greater tuberosity of the humerus. This was done using anonymized patient CT scans, in collaboration with 3DLifePrints and resulted in three different designs. Three repeats per design were used (n = 3). The designs were implanted in porcine bones, fixated with screws and subjected to a pre-defined cyclic loading regime. μCT imaging was performed before and after testing. Load-displacement curves, ultimate load to failure and displacement per cycle were calculated from the data provided by the testing software. Failure mechanisms were noted for each sample. The first design had the lowest displacement and was the easiest to fixate, but was quite difficult to print. The second design did not have a successful fixation and got pulled out during cyclic loading. The third design was the most difficult to attach. There is still much room for optimization but this could be an avenue into creating hard-soft anchors for rotator cuff repairs that can be personalized to individual patient anatomy.

4.2 Introduction

Different biomaterials are currently being explored in tissue engineering to act as scaffolds in bone, cartilage and tendon injuries (*443*). An important step in the design is to tailor the dimensions of an implant to the anatomical location it is intended for (*326*), and ensuring that it meets similar mechanical properties as the native tissue, by subjecting it to tensile, compressive or cyclic testing, for example. The main goal of this chapter is to redesign the 3D printed hard part of the biphasic scaffold, introduced in Chapter 2, to fit the greater tuberosity (GT) of the humerus. Briefly, CT-scans of the humerus of anonymized patients will be segmented, i.e. dissected, into a 3D object based on pre-defined anatomical boundaries so that it can be extracted from the model and further developed into an implant. Commercial sutures will be used (Figure 4.1) to test the fixation of the designed prototypes, instead of the electrospun sutures at this stage of the development. They will be subjected to a cyclic loading protocol in which the displacement (i.e., the movement of the prototypes) will be measured. A critical value of 5 mm or more of displacement of an implant, i.e. the implant moving *out* of the bone, can result in gap formation (*117*). When a gap forms between a repaired tendon and the bone there is limited to no contact of the tendon with the footprint area which is necessary for tendon healing and the repair construct will most likely fail (*117, 444, 445*). This occurs predominantly in the postoperative rehabilitation period, 3-6 months after surgery, when the rotator cuff is subjected to low-level loading (*446, 447*). Reducing the gap formation at the tendon-bone interface in this postoperative period could lead to improved tendon healing (*448*).

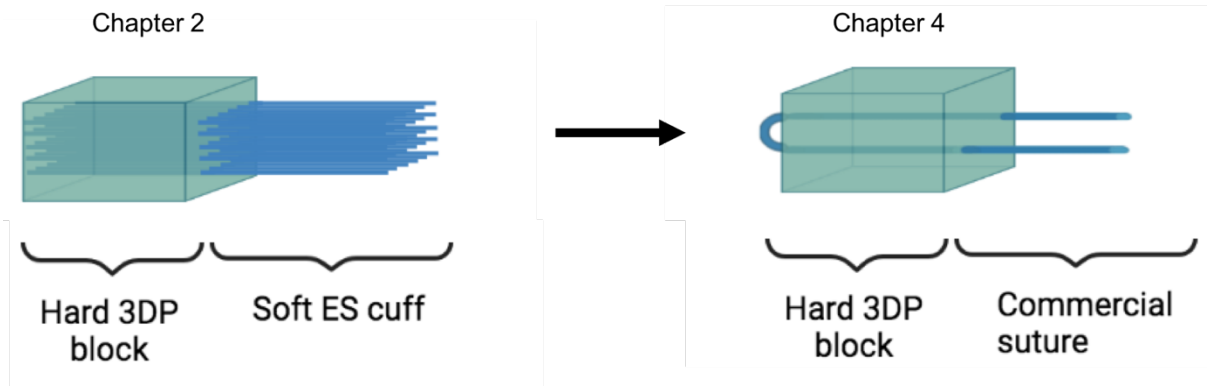

Figure 4.1 A diagram of the biphasic scaffold introduced in Chapter 2 (left) and the adaptations made to carry out the experiments in the current Chapter (right) using commercial sutures instead of electrospun sutures.

The objectives of this chapter are as follows:

1. To adapt the geometry of the hard part of the biphasic scaffold that was introduced in Chapter 2 to correspond to the greater tuberosity of the humerus using anonymized patient CT scans.
2. To assess the feasibility of the designs in terms of insertion and fixation using existing surgical tools and techniques and a relevant bone model.
3. To identify mechanisms of failure by subjecting the inserted prototypes to a cyclic loading regime and static load to failure using a commercial suture type.

The hypotheses are:

1. We can adjust the dimensions of the 3D printed block to fit the geometry of the greater tuberosity of the humerus based on medical imaging – i.e., personalise and individualise the design process of the scaffold.
2. The designed prototypes can be inserted and fixated using surgical equipment and methods that are already employed in common orthopaedic surgeries.
3. The mechanisms of failure identified by the cyclic and static load will be comparable to failure mechanisms of currently used suture-anchors in rotator cuff repairs.

4.3 Materials and methods

4.3.1 Segmentation by 3DLifePrints

Two anonymised CT scans of 42-year-old and 72-year-old female patients (Figure 4.2A) were provided by 3DLifePrints for segmentation using Simpleware ScanIP (Synopsys, California, USA). For this initial design process, the greater tuberosity (GT, see Figure 1.1 in Chapter 1) on the humeral head was defined as the region of interest. Briefly, segmentation means that the region of interest is labelled on the CT scans so that it can be extracted and converted into a 3D model for 3D printing. The supraspinatus and infraspinatus tendons attach onto the greater tuberosity (Figure 4.2B), and the geometrical boundaries were defined as the footprint of these tendon attachments (~5x15 mm) and a depth of 10 mm, corresponding to the average length of a commercial suture length. This volume was then extracted and designed into three different implants (Figure 4.2C).

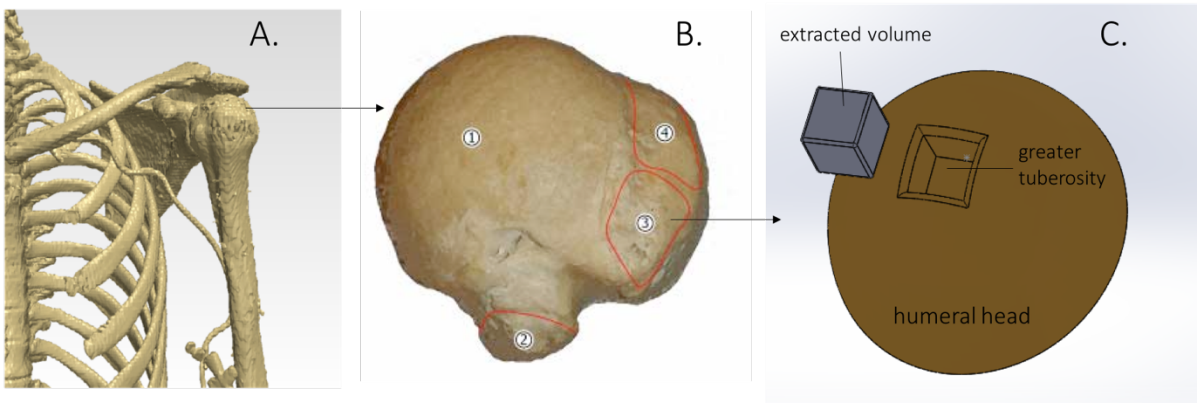

Figure 4.2 A) Anonymised scan of the left shoulder of a 42-year-old female patient. B) Superior view of the humeral head (1) with the lesser tuberosity (2), greater tuberosity where the supraspinatus (3) and infraspinatus (4) tendons attach.

4.3.2 Implant design considerations

The design of the implants was guided by the following:

- Dimensions of the scaffold had been determined (15x10x5 mm) based on a literature review of human cadaveric studies (*16, 21, 178, 288, 290, 449-458*) measuring the supraspinatus tendon footprint on the humeral head, see Appendix C for specifications.

- To avoid impingement of the shoulder during abduction, they were designed to be flush with the surface of the humerus (*327*).
- The total volume of the prototype was also limited to be less than the total volume of four suture anchors (~3000 mm^3(*459*)), which is the average number of suture anchors used in massive rotator cuff repairs (*459, 460*).
- Finally, a 'safe zone' was set to ensure that incorporated fibres would not be affected by any fixation methods.

Three initial prototypes were designed using MeshMixer (Autodesk Inc., California, US) and Netfabb (AutoDesk Inc., California, US).

4.3.3 Implant manufacture

All prototypes were printed using polycaprolactone granules (3D4Makers, Haarlem, The Netherlands) in an Ultimaker 3 Extended 3D printer, operated by 3DLifePrints (Oxford, UK), as mentioned in Chapter 2. A titanium casing to accompany one of the prototypes was printed by an external company (Renishaw plc, Wotton-under-Edge, United Kingdom). Anatomical models of humeral heads were 3D printed, using the same printer, in polylactic-co-glycolic acid (PLGA) with the volume of the prototypes extracted from it to envision their insertion, as per my designs (Figure 4.3)

4.3.4 µCT imaging

To verify the internal structure of the prototypes and to assess them before and after testing they were imaged using micro-computed tomography (µCT), which was performed by me. Each prototype was placed vertically on the holding stub and kept in place with BluTak. The samples were imaged using a µCT scanner (SkyScan 1172, SkyScan, Kontich, Belgium) at a pixel size of 13 µm, 40 kV and 250 mA. No filter was used. The reconstruction of the images

was done using NRecon software (SkyScan 1172, SkyScan, Kontich, Belgium) with a filtered-backprojection (Feldkamp) algorithm, as the μCT uses a cone-beam projection while the stage that the sample is fixed on rotates around its axis to capture it in 360° (*461*). ImageJ software (National Institute of Health, Bethesda, MD, USA) was used to process and stack the images.

4.3.5 Model of implantation

The implant was designed with the human shoulder in mind. However, it was not possible to procure human shoulders or accurate human bone models at the time of performing the experiment. Therefore, porcine shoulder bones (*sus domesticus)* were obtained from a local abattoir. The animals were not sacrificed for the purpose of this experiment. On visual inspection, the bones did not show any obvious inconsistencies, except for a few signs of sharp incisions across the humeral head surface, most likely due to sharp tools used for the dismemberment of the animal. Remaining soft tissue, consisting mostly of muscles, tendons and ligaments, and blood, was removed from the bones using sterile scalpels and forceps. The bones were washed with a solution containing PBS and 5% penicillin/streptomycin/amphotericin B (Sigma Aldrich, UK) and stored in a -20°C freezer. They were then thawed in a cold room (4°C) for at least 24 hours prior to use. This handling of animal tissues was based on similar experiments conducted in the literature and prior defined safety protocols in our facilities. It was not investigated whether a different approach would have led to different outcomes.

4.3.6 Implant insertion

The distal end of each bone was sawed off and a hole was drilled through the remaining shaft so that the bone could be placed in a custom-made grip and locked in place with a custom-cut

3 mm diameter screw of 86 mm length. A bench drill (RS Components, UK) was used to create the insertion hole of approximately 5 mm diameter and 15 mm length, using a 4.8 mm drill bit and a drilling depth of 10 mm for two designs and 25 mm for the third, and the pilot holes for the screws using a 1.7 mm drill bit and drilling depth of 20 mm. A single suture (FiberWire No2.) was looped through each sample before it was manually pushed into the bone until flush with the bone. No hammer or additional excessive force was needed or wanted to prevent damage to the prototype and bone. Stainless steel screws measuring 2 mm in diameter and 20 mm in length (Phillips M2 X 20mm, Accu, UK) were then used to fixate the samples using a manual screwdriver (Wera Tools, Germany). For the third design, the insertion of the screws was done blindly through the lateral wall of the humerus while holding an additional prototype as exterior model, as no custom-made guide was available. Once the bone and the samples were locked and loaded, the custom-made grip replaced the original clamp on the tensile testing machine (Figure 4.7). After testing, the bone was bathed in a 1% Virkon solution for at least 1 hour, stored in a disposable plastic jar and placed in a -80ºC freezer to be safely disposed of by the department's facilities team.

4.3.7 Cyclic loading protocol

A Zwick/Roell tensile testing machine (Zwick Roell Group, Ulm, Germany) and a 10 kN load cell was used for the cyclic loading protocol. No2. FiberWire (Arthrex, Naples, US) were newly purchased (same batch) and were kept in their individual, sterile, vacuum packaging until needed. A new suture was unpacked and used for each test. Prototypes were printed with two central holes to pass the suture through. They were then fixed into the porcine bones as described in the previous section. To ensure that the sutures were tensed and had a similar load from the start, a preload of 10 N was applied to each implant. Then, a cyclic loading programme from 10 N to 180 N for up to 200 cycles was applied based on a previously published protocol that simulates the postoperative rehabilitation phase of rotator

cuff repair (*128, 462*). Displacement was defined as the difference in crosshead position from the peak of the first cycle to the peak of cycles 50, 100, 150 and 200 (*463*). After the final cycle, the prototypes were subjected to load until failure, meaning either the sutures failed, or the implant got pulled out of the bone. Maximum load of failure and displacement were recorded by the tensile testing program (testXpert II; Zwick Roell Group) the same way as described in Chapter 2. Three samples per prototype were used to undergo cyclic loading and mode of failure was recorded for each. Results were recorded by the machine's software and plotted using RStudio (R Foundation for Statistical Computing, Vienna, Austria) and the *ggplot2* package (*376*).

4.3.8 Data analysis

Three samples per prototype were tested (n = 3) making a total of nine samples. Mean displacement per cycle was calculated by taking the displacement value at 40 cycles for each prototype and dividing it by 40 – this number was chosen to be able to include three repeats per prototypes, since not all of them had completed 200 cycles. Displacement at failure was taken as an average of the reported displacement values after the static load to failure, Maximum force at failure was taken as an average of the three samples per prototype. To compare these values between the three groups, a standard one-way ANOVA was used with Tukey's correction for multiple comparisons using GraphPad Prism version 9 software (GraphPad Software Inc, California, USA) was performed. Results were considered significant for $p < 0.05$ and where applicable are indicated with an asterisk (*) on the graphs. In case of non-significant results, no additional symbols are plotted. Graphs are presented with mean ± standard deviation (SD).

4.4 Results

4.4.1 Implant design

The input from the segmentation and the original dimensions provided for the hard part of the scaffold introduced in Chapter 2 were used to shape three different designs (Figure 4.3), which were produced based on the considerations listed in section 4.3.2. The starting point was the extracted volume as depicted in Figure 4.2B. From this initial 'block', different ways of attachment were envisioned that would fit with currently used surgical techniques and equipment and that would also leave room for attachment of the electrospun scaffolds. Design 1 (Figure 4.3A) involves three attachments with room for screws of 2 mm diameter on the medial, lateral, and posterior side of the greater tuberosity (GT). These attachment wings were designed with a thickness of 2 mm to allow for screw tolerances. Design 2 (Figure 4.3B) does not have attachments to hold screws and is fixated by a metal case. This case is fixed in place by screws of 2 mm diameter on the lateral and posterior side of the GT. Design 3 (Figure 4.3C) has an attachment at the bottom that holds space for screws to be fixed into from the lateral wall of the humerus, inferior to the plateau of the GT.

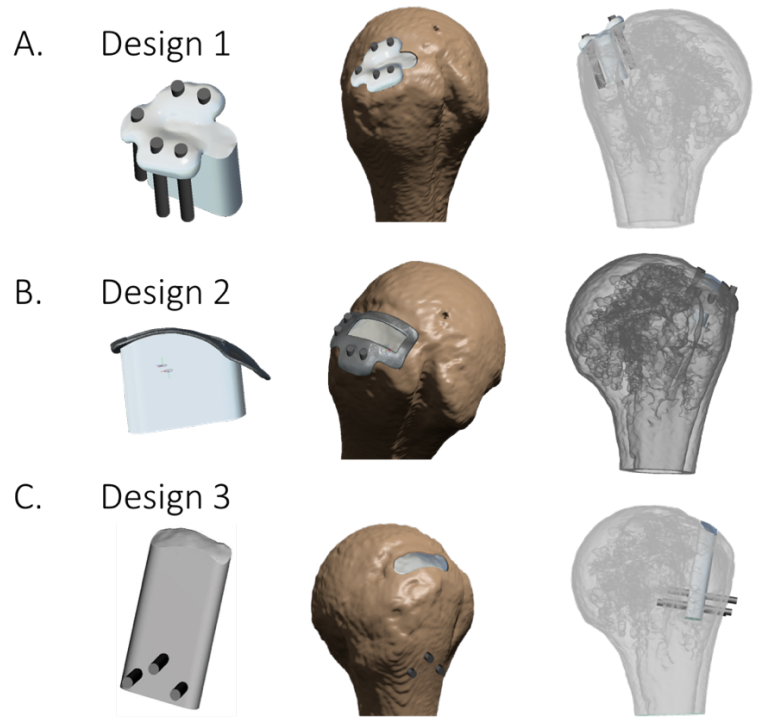

Figure 4.3 Three prototypes designed using a freeform approach, with screws in situ (left column) and visualized in a macroscopic (middle column) and translucent view (right column).

4.4.2 Implant prototyping

The prototypes were printed in PCL using the set-up described in Chapter 2 (Figure 4.4A-C). Several printing parameters had to be adjusted (nozzle size and temperature, extrusion rate, fan speed) to make sure the prototypes were of acceptable finish. The screw holes had to be added manually using a mini hand drill bit after the prints were finished. The anatomical humeral heads printed in PLGA are presented in Figure 4.4D with each corresponding prototype put in place to visualise if and how it matched the surface geometry. Note that all prototypes are imaged without filaments or sutures here and that the material used was not deemed suitable for the experiments in the rest of this Chapter, as it was quite weak in handling and we were unable to print a similar internal structure to native bone. μCT imaging is included in Figure 4.5 for each prototype including a FiberWire suture, to assess the internal printing quality. The central tunnels for passing the suture through and pre-drilled

screw holes are visible in Figure 4.5B and 4.5C, respectively. The metal casing was not imaged.

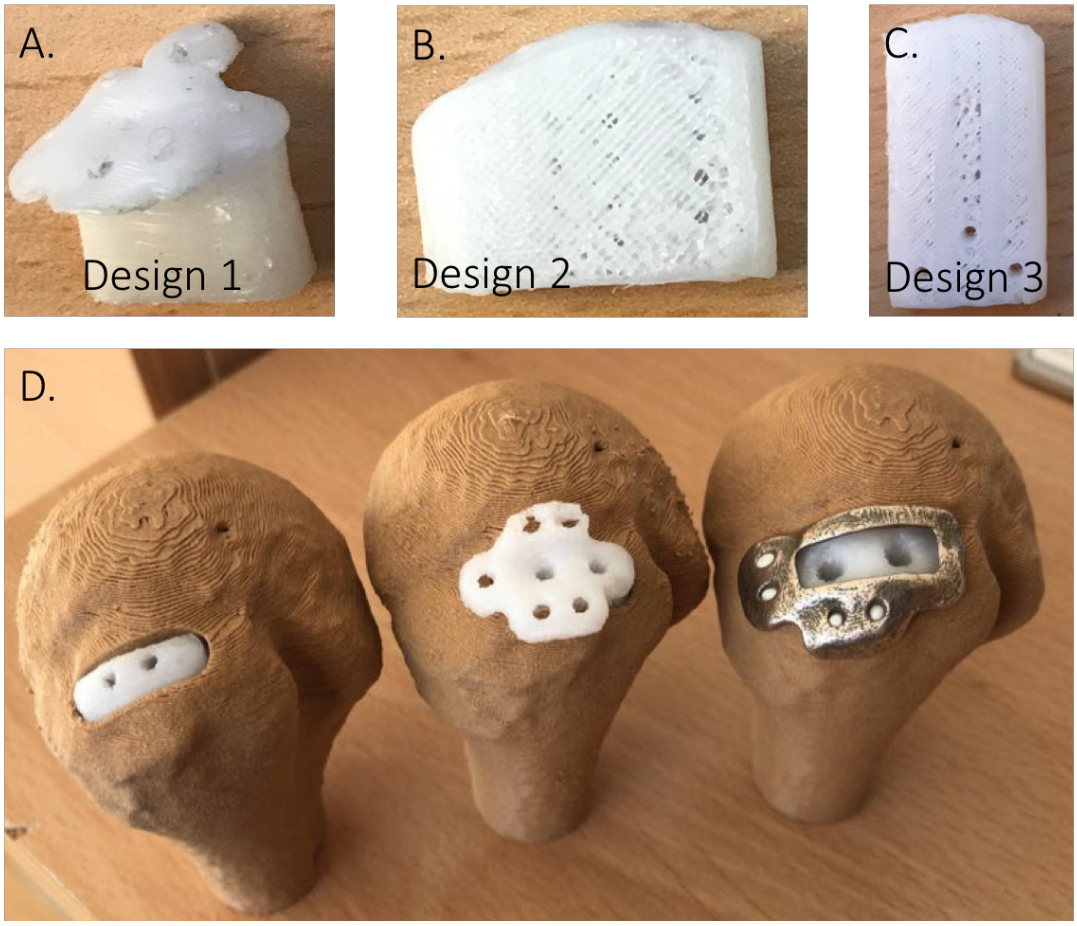

Figure 4.4 3D printed samples of the three designs (A-C) and their insertion into 3D printed models of the humeral head with the volume for the prototypes extracted from the greater tuberosity (D). Design 1 (A) corresponds to the model in the middle of image D, design 2 (B) corresponds to the right model and design 3 (C) corresponds to the left model.

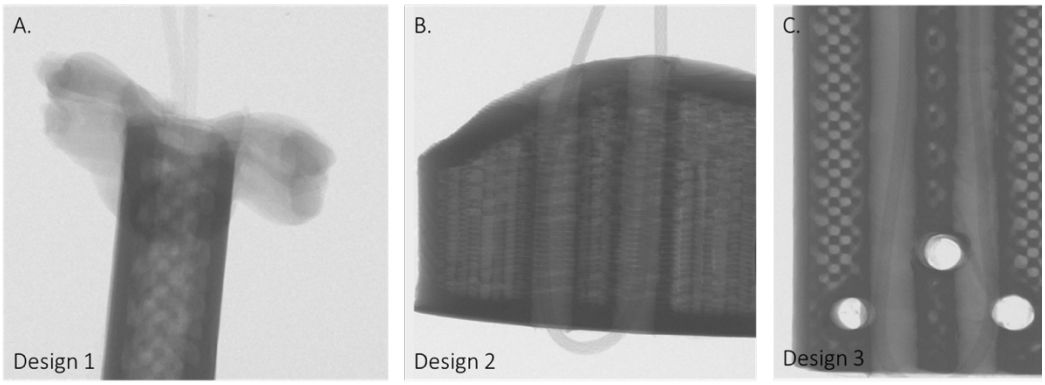

Figure 4.5 µCT imaging of the samples confirming the interior structure and the tunnels through which the suture pass (featured in all three). The suture tunnels and pre-drilled screw holes are visible (C).

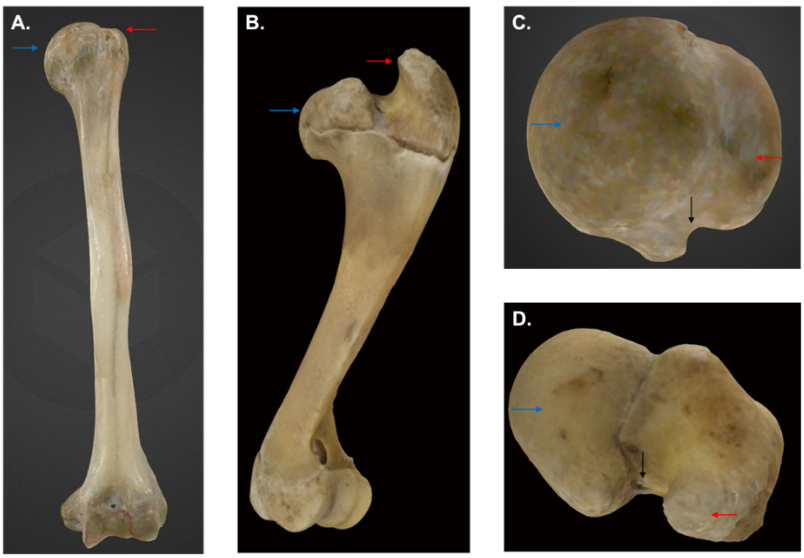

Figure 4.6 Anterior view of the human humerus (A), medial view of the porcine humerus (B) and a cranial view of both, respectively (C-D). Greater tuberosities indicated with a red arrow, humeral heads indicated with blue arrows and the bicipital groove with a black arrow. Images screenshotted from 3D models, freely available online (*464, 465*)

4.4.3 Feasibility of implant fixation into animal bone model

The domestic pig was chosen as a model system to insert the prototypes into, because its bones resemble human ones the most with respect to bone mineral density and biology (*466-468*). Size of the bone was not taken into consideration for this experimental set-up. The location that would most accurately approximate where it would have been implanted in the human bone was utilised. A simplified comparison of the human and porcine humerus is presented in Figure 4.6. The greater tuberosity of the porcine humerus is quite large, narrow, and overhanging the bicipital groove (Figure 4.6B and D), which makes it an unsuitable anatomical landmark to implant in. Another consideration was the direction that the sutures would be pulled in during the cyclic loading regime, which had to resemble the direction of force of the supraspinatus tendon. Each sample was secured into a new bone. Figure 4.7 shows the experimental set-up with the custom-made clamp (Figure 4.7A) and the porcine bone secured in place with the central hole drilled (Figure 4.7B). The location of insertion in the bone was chosen so that the angle of insertion relative to the direction of force was approximately 45° as it would have been using commercial suture anchors (*469*) and so that

the samples would sit as levelled with the bone as possible (Figure 4.8). The third design had a vertical insertion (90°) with the fixation by the screws perpendicular to the insertion. After testing, the samples were removed to assess any damage to them. For every design, the effect of the suture pulling through the relatively soft polymer was observed. The drilling was done using a bench drill. It took some time to ensure that no bony ridges remained in the hole. Furthermore, the drilling of the pilot holes was done after the samples had been inserted, which required precise alignment and was not always successful due to accidentally hitting the scaffold when drilling in the screws. This could have been prevented with a custom-made cutting guide and is commonly used in different kinds of surgeries to prevent damage to surrounding structures.

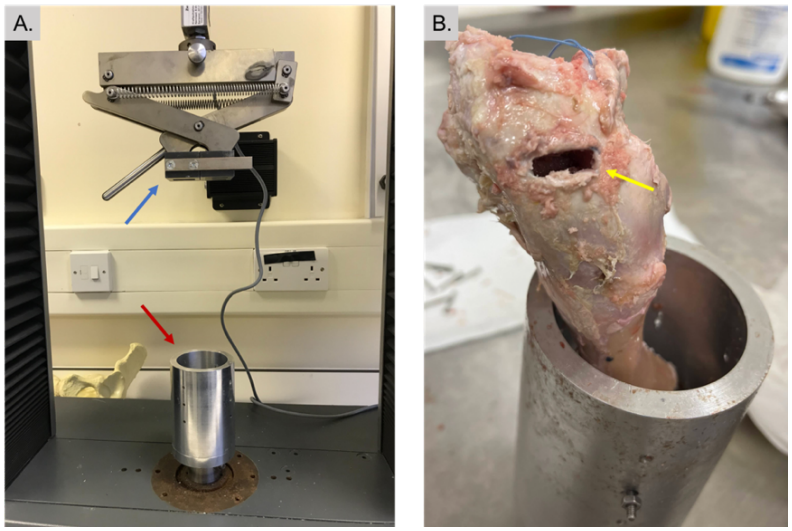

Figure 4.7 The experimental set up (A) using a custom-made cylindrical grip (red arrow) and the standard grip of the machine (blue arrow). A porcine bone secured is in place in the custom-grip (B) with a hole pre-drilled (yellow arrow) to fit the implants.

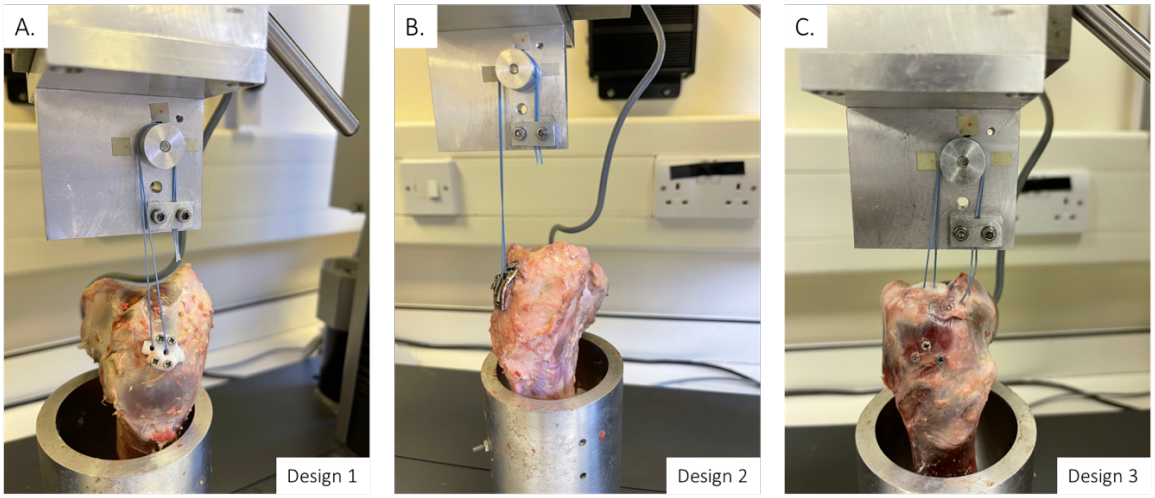

Figure 4.8 The three designs inserted and fixed into the porcine bones with commercial sutures used in lieu of the electrospun cuff.

4.4.4 Cyclic loading behaviour of the implants

Each prototype was tested with three repeats (n = 3). These all underwent a loading regime of 200 cycles and a static load to failure afterwards to evaluate the maximum force they can be subjected to, as an approximated measurement of fatigue in a postoperative rehabilitation setting. The average displacement per cycle, meaning the movement of the implant within the bone, was calculated for each implant and is present in Figure 4.9A as mean ± SD. For design 1 this was 0.031 mm ± 0.003, for design 2 it was 0.052 mm ± 0.021 and for design 3 it was 0.046 mm ± 0.021. These were calculated based on 40 cycles as this ensured that all samples could be compared to each other. There were no significant differences between the groups (p = 0.504, 0.933 and 0.701). The displacement in mm is plotted on the x-axis and the number of cycles on the y-axis for each individual sample (9 in total) in Figure 4.9B. The dotted vertical line indicates where the cyclic loading regime stopped and the static pull to failure started. Three repeats (one of design 1 and two of design 2) did not complete the full 200 cycles and failed prematurely; these are indicated in the plot with the cycle number at which they failed. The load-displacement are shown in Figure 4.9. The dotted horizontal lines on the y-axis indicate the limits set for the loading protocol, which is 10 N pre-load and 180

N. The distance travelled by the grips is the displacement on the x-axis in mm. Each experiment has a complete run including the ultimate load to failure.

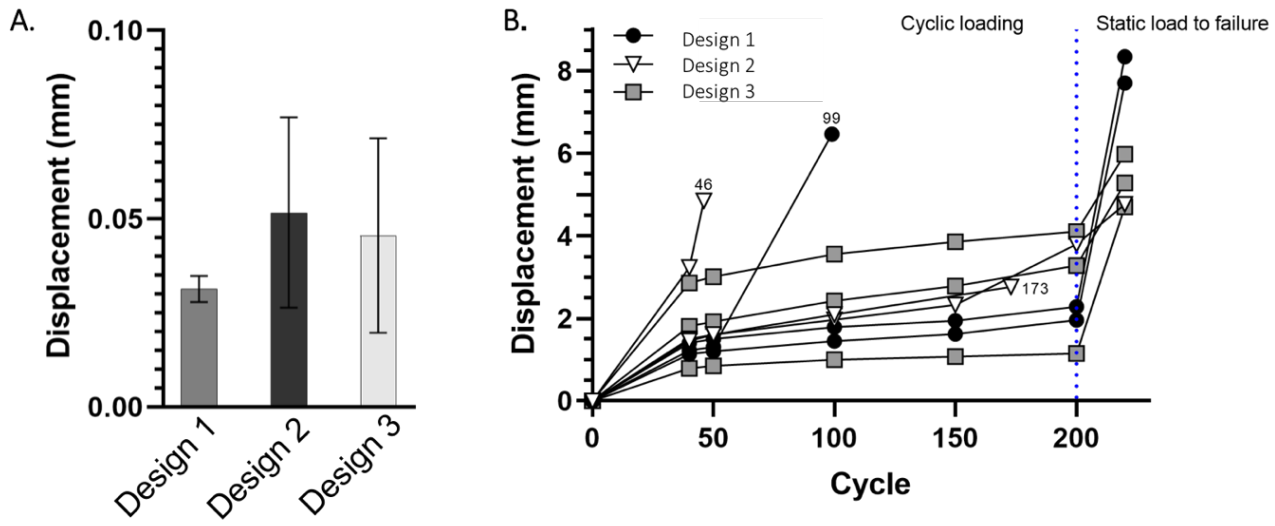

Figure 4.9 Mean displacement per cycle per design (A) and the displacement at every cycle interval for the individual repeats (B). The blue horizontal line in B indicates where the cyclic load regime ended and the static load to pull started. Most samples follow a similar path of steady displacement until a rapid increase at the end. Differences were not statistically significant for either A or B.

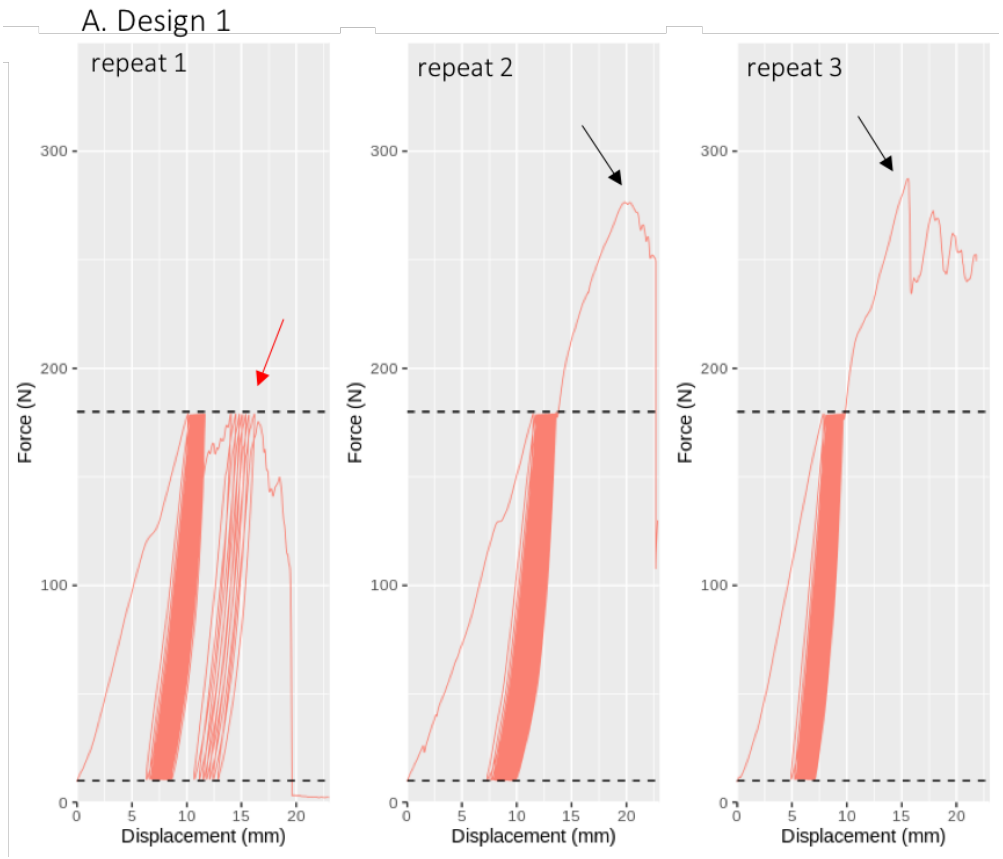

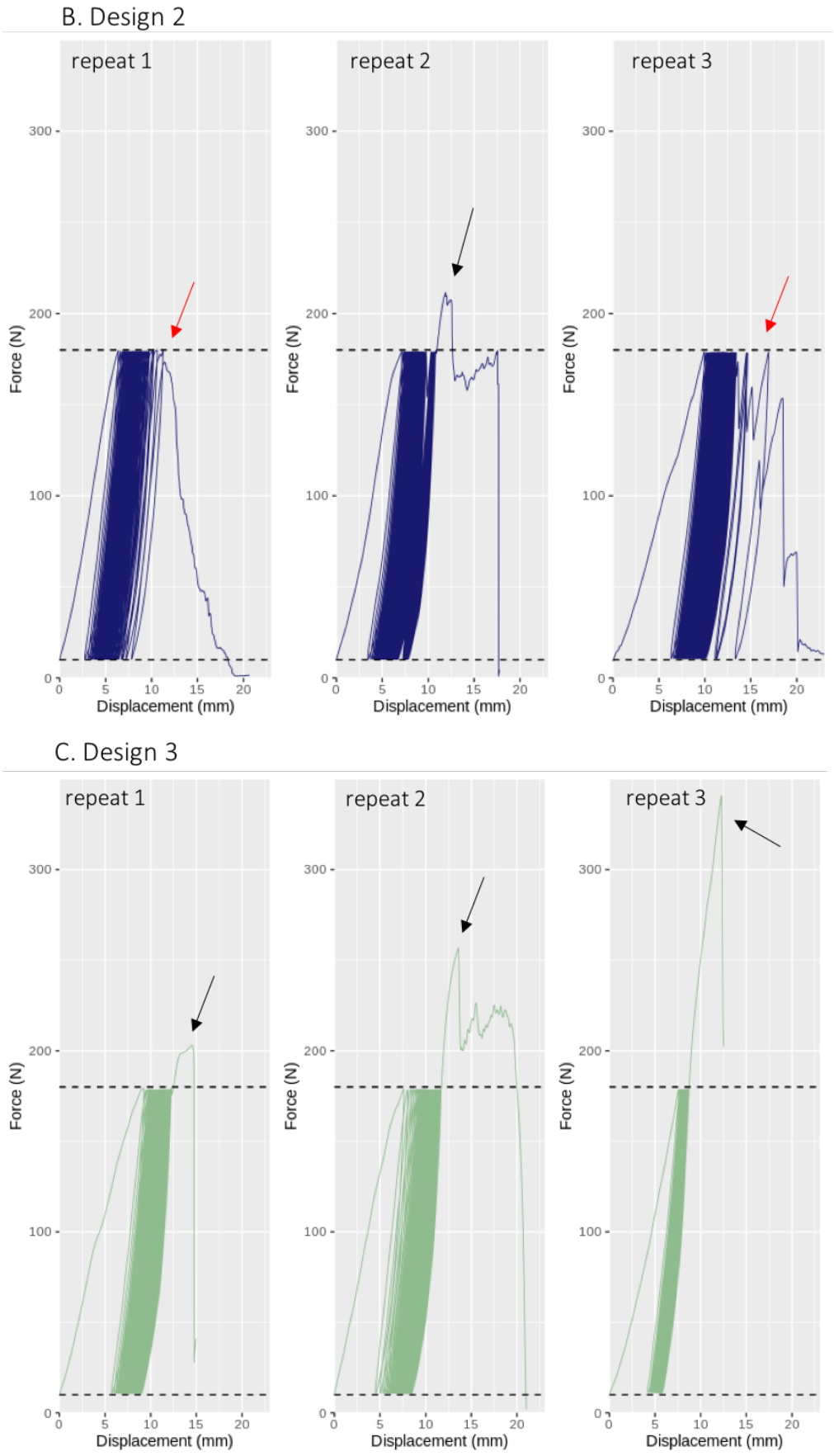

Figure 4.10 Load-displacement curves for design 1 (A), design 2 (B) and design 3 (C), including three repeats for each. After initiating the regime, most samples stabilize quite well and are able to hold for 200 cycles until the final load to failure (black arrows). A few samples failed prematurely (red arrows) and did not complete the static load to failure.

Figure 4.10A represent the three repeats for design 1, Figure 4.10B represent those for design 2 and Figure 4.10C those for design 3. Each plot shows a hysteresis curve with repeated loading and unloading for 200 cycles followed by the maximum load to failure, except for Figure 4.10A repeat 1 and 4.10B repeats 1 and 3, which failed at 173, 99 and 46 cycles, respectively. Each repeat portrayed in the figures stabilised after the initial few cycles, but several interruptions can be noted. These 'jumps' in the curves are the points at which either the sample started to displace, or the suture started failing, and the loading-unloading pattern attempted to re-stabilise itself. For the first repeat of design 1 (Figure 4.10A), two distinct phases in the cyclic loading can be observed but it also failed to completely stabilise after the initial displacement and did not complete the run either. The next two repeats were affected by suture elongation, but this did not cause any disruptions in the loading behaviour, and they showed a steady increase in displacement until failure. In repeat 1 and 3 of design 2 (Figure 4.10B), this was not successful and ultimately the implant pulled out before it was able to finish the full loading program. For the second repeat, the curve is quite broad and there is a slight jump around 6 mm of displacement where the implant starts to move but then re-stabilises and can complete the remaining cycles. In the third repeat of design 3 (Figure 4.10C) there is a very consistent cyclic loading pattern and displacement is minimal, with the narrowest curve, until the point of failure is reached.

4.4.4 Static load to failure of the prototype implants

After cyclic loading the samples were subject to static load to failure. The failure mechanisms were recorded for each and are summarised in Table 4.1, with the absolute displacement after cycling loading and the displacement after load to failure as well. Two samples in design 2 were the only ones that pulled out of the bone all together. The suture failed on two occasions, leading to a premature failure in one sample. The largest values for displacement after loading and displacement after failure were also seen in the samples that did not

complete the cycles. The most common failure mechanism was displacement of the implant, due to improper fixation. The results therefore cannot be compared to commercial equivalents. For a better understanding of the mechanical behaviour of the current scaffolds, the experiment should be repeated with human bone models.

Table 4.1 Summary of failure mechanisms and displacement values per repeat.

	Cycles completed	Displacement after loading (mm)	Ultimate load to failure (N)	Displacement at failure (mm)	Failure mode after static load to failure
Design 1	99	6.45	179.11	6.45	Suture failure
	200	2.28	276.63	8.34	Suture pull through
	200	1.96	287.48	7.71	Suture pull through
Design 2	46	4.85	179.92	4.85	Implant pull-out
	200	3.80	211.48	4.77	Implant displaced
	173	6.98	179.07	6.98	Implant pull-out
Design 3	200	3.28	202.97	5.28	Suture failure
	200	4.11	257.31	5.98	Implant displaced
	200	1.15	340.66	4.71	Implant displaced

The ultimate force at failure for each design is shown in Figure 4.11A. There were no statistically significant differences between the forces expressed per group (p-values of 0.441, 0.264 and 0.901). The mean force at failure was 190.6 N ± 18.48 for design 1, 247.74 N ± 59.68 for design 2 and 284.61 N ± 80.16 for design 3. The total displacement after failure is additionally plotted in Figure 4.11B for each design. For design 1 it was 7.50 ± 0.79 mm, for design 2 it was 5.53 ± 1.02 mm, and for design 3 it was 5.33 ± 0.52 mm. These differences ($p = 0.109$, 0.964 and 0.079) were also not statistically significant. Figure 4.12 shows the different failure mechanisms. Sample pull-out (repeat 1, design 2) is seen in Figure 4.12A which models uniaxial movement, i.e. lifting the arm from neutral to over-head position, while implant displacement (repeat 2, design 3) is seen in Figure 4.12B, noted with a red arrow, and models post-operative rehabilitation exercise, i.e small, repetitive shoulder

movements. The difference between these terms is important because a displaced sample still had some fixation and was not completely pulled out during the static load to failure. Suture pull through (repeat 2, design 1) is seen in Figure 4.12C, marked by the difference in colour of the suture at the red and black arrows, and suture failure in 4.12D, in which the sample (repeat 1, design 3) remained in situ but the suture had snapped off during the experiment.

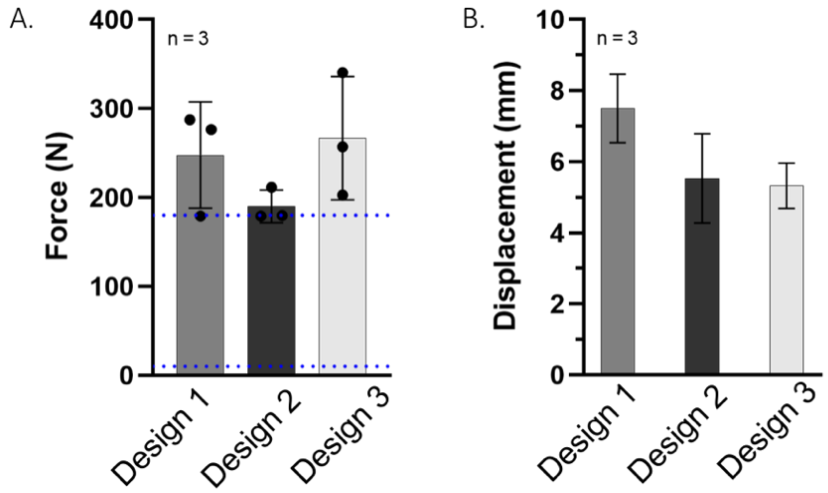

Figure 4.11 The force at failure per design after the final load to failure (A) and the total displacement after failure (B). The blue dotted lines indicate the limits of the loading regime, with pre-load at 10 N and maximum force at 180 N. The three repeats that did not complete the total loading regime are plotted just below this upper limit. Both given as mean ± SD. Differences were not statistically significant.

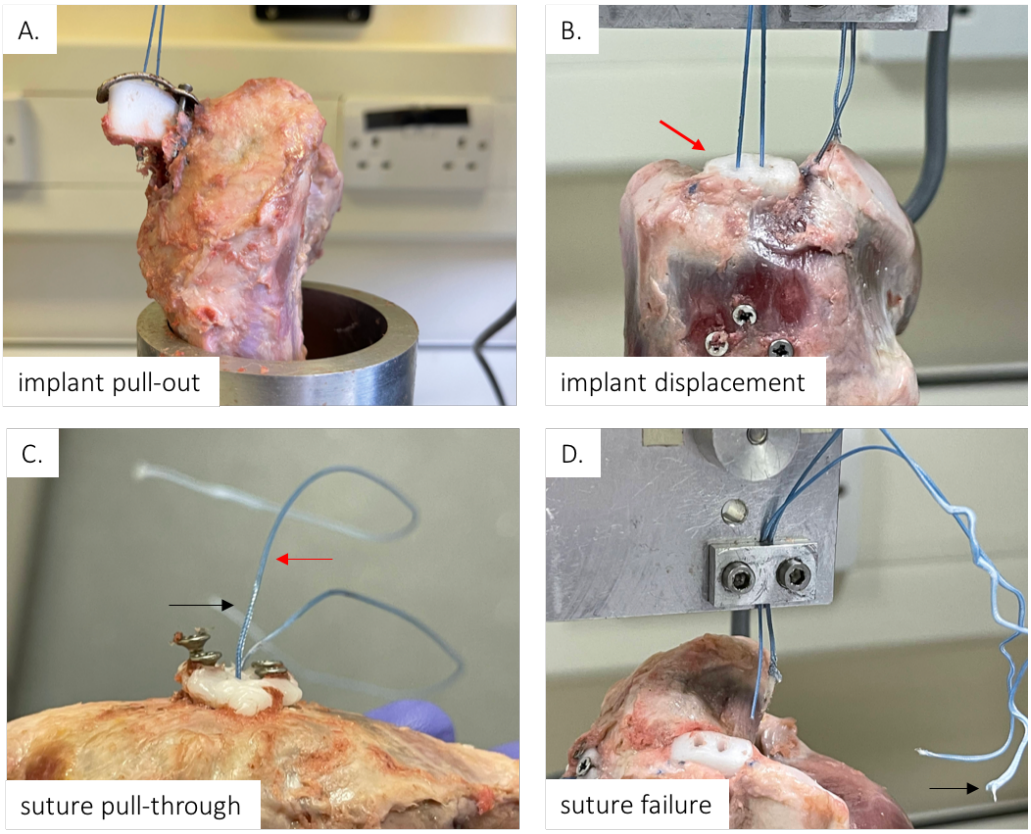

Figure 4.12 Different failure mechanisms visualised: implant pull-out (A), implant displaced (B, red arrow), suture pull through (C, note the difference in suture colour at the red vs the black arrow) and suture failure (D, black arrow).

Finally, µCT imaging was performed to evaluate the effect of the suture pull on the polymer (Figure 4.13). Images of representative samples were taken pre-testing with a FiberWire suture *in situ* (Figure 4.13A-B) and after testing (Figure 4.13C-D). Each sample is pictured with the bottom facing up, i.e., where the suture loops through the two central tunnels. A distinct cheese-wiring effect can be seen in Figure 4.13C-D, indicated by a red arrow, which was also seen on visual inspection after testing. Cheese-wiring is the effect of the FiberWire suture pulling through the soft polymer, essentially dissecting it. Slight damage to the exterior of the sample is seen in Figure 4.13D, also marked with a red arrow, which was caused by the screws. This was seen in nearly all samples of designs 1 and 2.

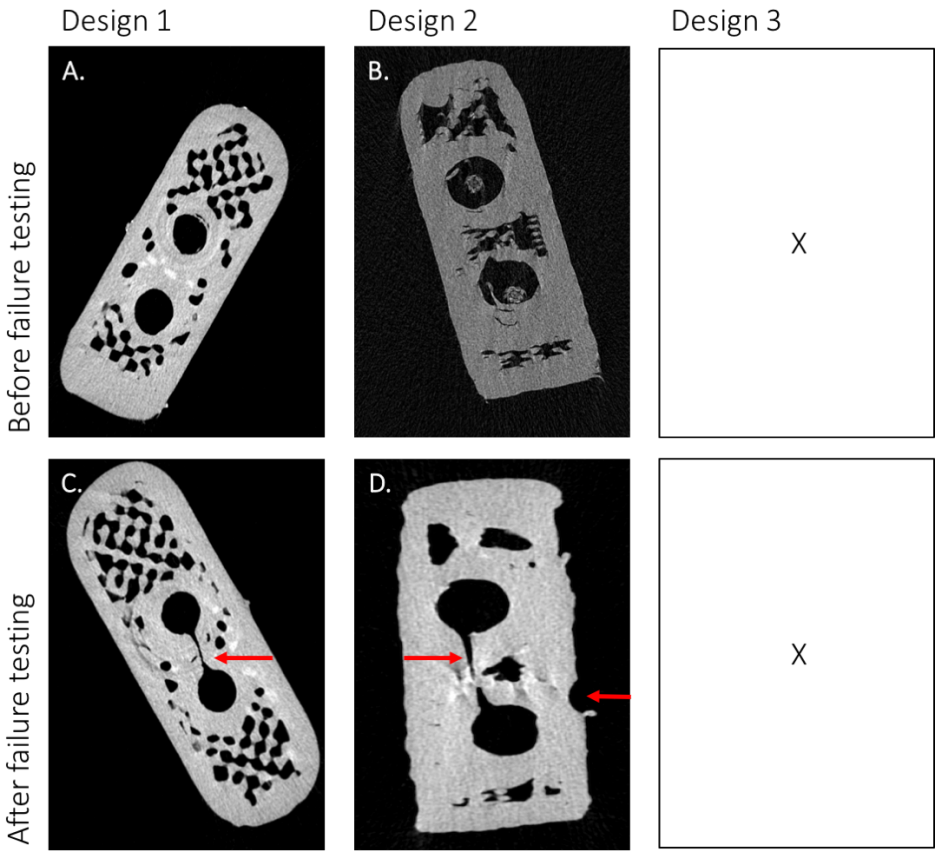

Figure 4.13 µCT imaging of samples before (top row) and after the final load to failure (bottom row) with a communicating channel between the two suture tunnels indicating a cheese-wiring effect (C-D, red arrow), and imprints left by the fixation of the screws on the exterior wall of the implant (D, red arrow). The third design was not imaged as it was accidentally disposed of with the animal waste after testing.

4.5 Discussion

By modifying the dimensions of the 3D printed hard part of the biphasic scaffold introduced in Chapter 2, we were able to design three different prototypes that had clinically relevant dimensions for insertion into the greater tuberosity of the humerus. The mechanical properties were evaluated by inserting the implants into relevant bone models and subjecting them to an established cyclic loading regime and testing them to failure.

4.5.1 The dimensions of the designs are based on a literature review of anatomical studies

The literature study conducted to set the dimensions of the scaffold, resulted in a range of measurements, but the most often cited measurements are of Mochizuki et al (*16*), who also had the largest number of human cadavers available (n = 97). They have disputed the consensus that the greater tuberosity of the humeral head harbours mainly the attachment of the supraspinatus tendon and have shown that this is in fact largely taken up by the infraspinatus tendon as well. This feeds directly into a now more commonly accepted view that isolated supraspinatus tendon tears most likely involve part of the infraspinatus tendon too which increases poor functional outcomes after rotator cuff repair (*16*). Therefore, within the available literature a distinction was made between measurements of solely the footprint of the supraspinatus tendon and those concerning the entirety of the greater tuberosity. The prevailing argument by Mochizuki et al (*16*) means that a greater surface area is available, and it is much easier to mould an implant based on a bony geometry (the greater tuberosity) than on the approximated surface area of a tendon that is not attached anymore. It was therefore possible to adapt the 3D printed part of the scaffold introduced in Chapter 2 to fit the greater tuberosity, while maintaining enough space to incorporate the number of filaments that would achieve clinically relevant mechanical properties. Furthermore, the approach

described in this Chapter of using medical imaging to inform the scaffold dimensions, is a well-suited starting point for a point of care production pipeline (Background, section 1.6.3) since this work was achieved with the collaboration of an in-house medical manufacturing company (3D LifePrints). This meant that adaptations to the design could be communicated quickly and efficiently. The prototypes designed in this Chapter were inserted into porcine humeri using tools that are common in orthopaedic surgery, so that an insertion method could be used that would be surgically feasible and did not necessitate custom-made devices. It also did not compromise surrounding structures, specifically the bicipital tendon and ascending branch of the anterior humeral circumflex artery (*470*). The first step in the insertion involved exposure of the bony surface with the assumption that the greater tuberosity of the (human) humerus would be available as a surface to work with. In massive rotator cuff tears, the infraspinatus is often involved, and it is common practice to mobilise the rotator cuff for adequate footprint coverage and to have an equal distribution of loading when reattaching the tendon (*460*), see also Background, section 1.3. In this experiment, the bones that were obtained from the abattoir had been cleared of most of the soft tissues and the remainder was removed prior to testing. Therefore, no comment can be made about the ease of exposing the bony surface, while preserving important soft tissue structures.

4.5.2 3D printing of the designs required several iterations and was limited by the current 3D printer

The printing orientation of the prototypes was based on the presumption that filaments would be inserted over the total length of the scaffold, i.e., they were printed with the lateral side face down on the printing surface (horizontally). Since design 2 has an accompanying metal casing to secure it in place, the original width was adjusted from 5 to 8 mm to allow for more grip by the case. This also means it will require more space on the greater tuberosity than the

other two scaffolds. The use of pure PCL as a thermoplastic polymer is beneficial for inserting filaments during the printing process as it is slow to solidify, allowing the filaments to stick to the extruded layer. However, the properties of the current 3D printer were a limiting factor, and did not succeed in producing scaffolds with the desired resolution, i.e., level of detail. This was mainly due to the available nozzle diameter which determines the layer height and width of the extruded material, and thereby the finer details of the resulting objected (*471*), see Appendix D for additional figures. This was especially troublesome for printing the attachment wings in design 1. These had been designed with a thickness of 2 mm to allow for screw tolerances, but this came out slightly thicker (~3-4mm) and less defined than originally designed. In this stage of development, these printing size errors were accepted but in the future, the nozzle diameter and layer height should be investigated more thoroughly. Only three samples per design were tested in this experimental phase, to reach at least n = 3, because of the availability of animal bones. Each experiment required an unused bone and we were not able to source more than ten bones of the same species and the same local abattoir (to contest variability between the upkeep of the animals and slaughtering methods), because they were mostly processed for human consumption.

4.5.3 The insertion of the designs into porcine bone models was the easiest for design 1 and the more difficult for design 3

The first design had attachment wings to hold the screws making the insertion and fixation straightforward. However, it occupied more space on the surface of the bone than the width of the inserted part and would only be feasible if it was level with the bone. The second design involved a metal casing that is about 2 mm thick but in patients with reduced sub-acromial space, this could pose a significant problem and lead to shoulder impingement complaints (*472*). This same concern could be raised for the first design. During the

experiment, it was clear that the metal casing did not align properly with the polymer sample, and therefore did not have enough grip to prevent it from being pulled out. The rubbing of the metal casing against the underside of the supraspinatus tendon in abduction can also be a cause of concern in the long run (*472*). Also, this design had wider dimensions than the other two, meaning that a wider hole had to be drilled in the bone. Since the designs all had the same metrics to allow the incorporation of the electrospun filaments, it was not possible to reduce the width and thereby the size of the metal case. Its main attraction here was the insertion of screws in metal rather than the polymer to preserve its integrity and have no interference with the electrospun soft part. Finally, a design that consists of a degradable and non-degradable material is not ideal as the metal casing will cease to serve a purpose once the polymer has degraded and in the long-term could cause adverse reactions in the body (*164*). The same is true for the screws that are used in every design. Future work should explore if the metal casing and screws could be replaced by a biodegradable alternative. The third design occupied the least space externally, but the most internally. This was the more elegant design, since only the electrospun filaments would be emerging from the footprint area and less external space would be occupied than with the other two designs, reducing the risk of impingement. However, in practice this fixation was the most challenging as it not possible to ascertain whether the screws were in position. An additional implant guide would be needed for a secure fixation.

4.5.4 The ongoing debate about the proper insertion angle

All samples were inserted at 45° or 90°. The fixation strength of any type of anchor is dependent on its design, the angle and depth of insertion and the bone density of the patient or specimen involved (*473*). There has been considerable debate about which insertion angle is the most preferred one in rotator cuff repair constructs using suture anchors. The concept

of the 'deadman angle', was first introduced by Burkhart (*469*) and refers to the angle that the suture emerging from the anchor makes to the direction of pull of the rotator cuff. According to Burkhart, this should be equal to or less than 45°, and if it were to approximate 90° it would increase the risk of suture failure due to high tensions. This concept has been disproven over the years with a preference towards an insertion angle of 90° (*473-478*) but has since elicited a strong rebuttal from the original author citing questionable materials and experimental set-ups (*479-481*). In this experiment, the angle of fixation did not result in significant differences across the mechanical properties of the designs. The samples were evaluated mechanically for cyclic loading, ultimate load to failure and displacement of the implant. Hysteresis is the energy spent during loading and unloading of the sample – the unloading curve is different from the loading curve and shifts to the right for each subsequent cycle as it loses energy in the form of heat while it tries to find an equilibrium (*482*). As the loading becomes stabilized, the energy lost is reduced and the curve becomes narrower. It is a measure of the viscoelastic properties of a tissue and is related to its creep abilities, meaning the increase in length (deformation) a tissue undergoes over time while being subjected to constant load (*483*). This can also contribute to gap formation in a repair construct (*484*). The overall displacement for each design was less than 5 mm during cyclic loading but increased steeply to over 8 mm during static pull, meaning they could withstand the former well but not the latter. Also, regardless of design, all samples had a similar increase in displacement during the cycles.

4.5.5 Biomechanical testing of the different designs was most successful for design 1

The first design was the simplest to fixate and apart from the first repeat which suffered from suture failure, the curves look consistently narrow with the least displacement overall. The two successful repeats had similar loads to failure but showed the most displacement during

this final static phase. However, failure here was not due to the design but a failure of the suture. This was noted by the difference in colour of the suture emerging from the implant (wet vs. dry) at the end of the experiment compared to at the beginning, and the displacement at failure which was the largest for these samples. The cheese-wiring effect was also the most pronounced in this set of samples. The second design performed the worst with two premature failures, and this was mostly due to the misalignment of the metal casing on the polymer. Lack of time and funding meant that this could not be attested any further and repeat experiments should be performed to evaluate whether this design is actually worse performing than the other two. The premature failures led to a larger mean displacement per cycle, resulting in broad curves in the load-displacement graphs. Also, the repeat sample that did survive the cyclic loading had quite a low ultimate load to failure compared to the other two and could withstand about 30N past the maximum force during cyclic loading. The suture pulling through the polymer is a similar mode of failure as slipping of the suture in knotless suture anchors (*485*). This type of anchor was developed two decades ago as a solution to the problem of knot tying during arthroscopic rotator cuff repairs (*486*) and served to reduce surgical costs and operating time as well (*487*). Displacement for these samples is therefore perhaps an inaccurate description, as the samples did stay in place during the experiment and would serve better to describe the extension of the sutures. The last design was the most difficult to fixate. It would serve to have a custom-made guide to ensure that the screws penetrate the construct. This was initially considered in the design process but was not further explored here due to lack of time and funding. It was clear that fixation was suboptimal from the start of the experiment, as the samples started moving up and down during the cyclic loading experiment and did not stay fixed in place. The suture failure might have been due to the central screw blocking the suture as it underwent loading, causing friction and eventual failure (*104*). Indeed, this sample had the highest load to failure across

all, and the narrowest cyclic loading curve. In the final biphasic scaffold, the electrospun fibres would not be in direct contact with the screws. With proper fixation techniques and an alternative soft part (electrospun filaments), this design could be a promising candidate compared to commercial suture anchors, especially as it occupies the least space on the humeral head and sits completely within the bone. A cutting guide would serve to prevent the screws from encroaching onto the soft filaments and to accurately visualise the location of the implant from the lateral side.

4.5.6 A comment on current biomechanical loading practices

A final remark is on the cyclic loading regime adopted here. It has been proposed that cyclic loading regimes present a more physiological loading conditions than static, single-pull experimental set-ups and that failure under the former constitutes bone failure whereas the latter is predominantly suture failure (*117*). The cyclic loading protocol (*128, 462*) adapted in this experimental set-up was informative for the fixation method of the biphasic scaffold. Cyclic loading has been widely trialled and tested in the context of rotator cuff repairs and have involved a myriad of different set-ups and materials used. Nagra et al (*128*) tested the mechanical properties of four commercially available all-suture anchors using the same loading protocol as in this Chapter and found them to fail at 103.9-181.0 N with a total displacement of 19.7-33.7 mm. Kim et al (*488*) tested the metal corkscrew anchors by Arthrex loaded with a No2. FiberWire suture and found an ultimate load of 349.7-516.3 N with a gap formation of 1.7-7.6 mm. These ultimate failure loads achieved by the current prototypes (179.07-340.66 N) fall within a similar range, as do the displacement values (4.71-7.71 mm). However, there remains a large variability in the data presented here and in the literature. A landmark study by Barber et al (*14*) testing a wide variety of rotator cuff anchors at a cyclic loading protocol of 10 to 100 N over 200 cycles found a mean pull-out force of

173.3-760.9 N while no anchors reached a displacement value higher than 5 mm. While their materials included several metal anchors, they rightly conclude that the trend of novel suture anchors is towards radiolucent materials, most notably biodegradable and biocomposite polymers (*14*) such as the ones used in this work. However, the cyclic loading and mechanical behaviour of these implant designs was evaluated at time-point zero, meaning that they were implanted and tested directly, as was done here also. After patients undergo rotator cuff surgeries a period of relative immobilisation of 4-6 weeks follows (*489*) to allow the implant to integrate into its surroundings and for the tissues to heal. This does not mean that no movement may occur at all – in fact, small range of motions from the wrist, hand and elbow are encouraged to prevent post-operative stiffness (*489*). By 12 weeks postoperative, unrestricted movements may occur and strengthening exercises are advised (*489*). However, passive motion immediately postoperatively is under debate as recent studies have shown that it could impede tendon-to-bone healing and increase risk of re-rupture (*490-493*). A material with superior mechanical properties (e.g., ultimate tensile strength) will not perform adequately if the tendon does not heal (*135*). It is therefore important to consider the surrounding biology, which is not reflected in the work here or in many biomechanical studies of commercial suture anchors. Although clinical studies involving patient reported outcomes and medical imaging do exist, they are subject to different specifications including the surgical techniques and materials used, the rehabilitation protocol and follow-up period. To effectively design an implant that meets clinical requirements, a more robust method of testing these is necessary that involves more than artificial loading regimens and static pull-out.

4.5.7 Limitations and future work

Several limitations exist to this work. Firstly, due to ethical, financial and time constraints it was not possible to obtain cadaveric human bones or 3D printed bone models of an accurate, bone-mimicking material. Fused deposition modelling (FDM) is one of the main forms of additive manufacturing that is used in patient specific 3D printing, along with laser sintering and stereolithography (*494*). FDM was deliberately chosen in Chapter 2 as the 3D printing modality because it allows for an easy and direct incorporation of the electrospun filaments, and therefore no other 3D printing methods were tested. However, the major limitation was the imprecise printing of the designs due to printing a material with a low melting point and a relatively wide nozzle diameter. This was especially relevant for the first design, which required many iterations to achieve an acceptable quality, meaning the internal lattice structure was preserved and the external features were printed as designed with minimal sizing errors. The printing of the tunnels for the sutures and the holes for the screws was also difficult to achieve and had to be amended manually after printing. This could have been addressed during the course of the DPhil, but unfortunately the 3D printer was largely unavailable during the pandemic years and use of it was charged on an hourly rate, excluding cost of material. This left the data collection for this Chapter quite thin and upon reflection, it would have been much better to purchase our own 3D printer and experiment with all different settings in the time allowed with no extra cost involved. PCL was the optimum choice in this setting, however, as it is widely used in bone tissue engineering applications and is easily miscible with calcium phosphates to increase its osteoconductivity (see Background, section 1.6.3). It is also highly tunable as a thermoplastic in FMD printers. Physical 3D printing was not possible until quite late in the timeframe of this thesis, due to the ongoing pandemic and the unavailability of 3D printing facilities. Exploring different biodegradable polymers or polymer blends (e.g., PCL/hydroxyapatite/ß-TCP, PCL/starch,

PLA) is a consideration for future work, including consequent mechanical and bioactivity testing. Furthermore, the protrusion of the implants would have to be evaluated in a more carefully designed experiment in which shoulder impingement should be quantified as well, for example, using a full model of the shoulder joint (scapula and humerus). Also, due to the limited time and resources available, it was not realistic to provide the samples used here with electrospun materials. The number of filaments per sample (~270 of about 15-20 cm in length, see Chapter 2) requires at least 40 metres of stretched electrospun filaments and roughly 365 metres in total. Also, since the maximum pull-out force for this number of filaments was already tested in Chapter 2, a commercially available and popular suture type used in rotator cuff repairs was used instead. However, since the molecular weight of the polymer used in this work was high (M_w = 50,000 g/mol), it was soft in nature (*495*) and suffered the effect of the abrasive suture pulling through it during testing, similar to a suture pulling through tendon (*116*). This means that the values for displacement as given by the machine might not be entirely accurate, since it involves the length of the suture pulling through the material, as well, rather than just the length of the sample moving in the bone. This effect was seen for every sample, but it is unclear whether this happened during or after cyclic loading, as there was no way of inspecting them prior to the final failure test. This would have required an additional extraction and insertion step which was not feasible. It could be said that this contests the presented data, and the aim is therefore to repeat the experiments in this Chapter with the biphasic scaffold including either a less abrasive suture type, or the electrospun filaments, as originally intended. Future work should also focus on creating scaffolds that approximate the biological and mechanical properties of native bone tissue, which can be achieved by blending PCL with hydroxyapatite or β -TCP (Section 1.6). This was not within the scope of this thesis and was therefore not attempted here. A summary of the main advantages and disadvantages of each design is present in Table 4.2. In the first

design the main advantage is the strong and easy fixation but this also occupies the most space on the external surface of the bone. The second design is similar in this and has an added metal case which is easily misaligned, but which means that the entire polymer block can be used for the electrospun filaments. Finally, the third design is the easiest to print and insert but unless there is a way to visualise it from the outside, fixation remains difficult.

Table 4.2 The main advantages and disadvantages of each design.

	Design	Advantages	Disadvantages
1		- Single unit - Easy insertion - Easy fixation - Strong fixation - Least displacement	- High impingement risk - External space occupation - Difficulty 3D printing - Misalignment of screws
2	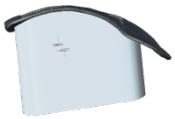	- Easy printing - Easy insertion - Screws fixed in metal rather than polymer - 3DP block dedicated to ES filaments	- High impingement risk - External space occupation - Two separate units - Non-degradable case - Misalignment of casing - Misalignment of screws
3		- Single unit - Easy printing - Easy insertion - Low impingement risk	- Difficult fixation - Internal space occupation

4.6 Conclusion

The overall aim of this chapter was to redesign the hard part of the biphasic scaffold to meet clinically relevant dimensions. The feasibility of the resulting designs was tested by inserting them into bone models using common surgical tools, and evaluating their mechanical properties by subjecting them to cyclic loading and tensile testing. Commercial suture anchors also consist of a hard (bone anchor) and soft part (suture) and have excellent mechanical properties. However, as discussed at length in Chapter 1 and 3, they do little to

encourage native tissues to heal and result in a high failure rate. In this work, the soft cuff is completely embedded within the hard cuff, negating the problem of suture slippage and eyelet breaking, which are frequent modes of failure in traditional suture anchor systems. Also, since the anchor is composed of a polymer with positive reports of its osseointegrative abilities, it could potentially reduce the incidence of failure by migration or pull-out. However, although the theoretical advantages of the current designs are interesting, there is still much to explore in terms of the practicalities. Important focus points are the manufacturing of full prototypes including the soft electrospun cuff and using a representative experimental model for initial testing at time zero and beyond.

4.7 Acknowledgements

I would like to thank Lisa Ferrie, Camille Ribolzi and Michael Richard from 3D LifePrints who procured and segmented the patient CT images. I would also like to thank Dr Edyta Augustyniak and Dr Tania Choreno Machain for reviewing this Chapter. This work was funded by the Interreg 2 Seas programme 2014-2020 3DMed.

Chapter 5 General discussion and conclusions

5.1 Overview of thesis aims

The main aim of this thesis was to design a scaffold consisting of a soft and hard part through the combination of electrospinning and 3D printing for rotator cuff applications. These techniques are increasingly used for tissue engineered multiphasic scaffolds with promising results and have a good potential for scale-up, but have not yet been combined in an effective and straightforward process. In Chapter 2, I introduced a novel strategy by 3D printing on top of pre-assembled electrospun filaments to create soft-hard constructs. The polymers that were used were chosen based on prior FDA approval, a well-established use in clinical and tissue engineering uses and previous experience in the group. The potential for scaling up these scaffolds to meet clinically relevant mechanical requirements was also investigated. We were able to produce a 3D printed PCL scaffold consisting of a maximum of 270 ES filaments divided in 10 layers that was able to meet an ultimate tensile load that approximated a clinically relevant threshold value (226.8 ±46.9 N). In Chapter 3, the soft part of the scaffold consisting of ES PDO filaments was compared to a commercial suture equivalent (FiberWire) and assessed for cell attachment and behaviour using next-generation sequencing and computational analysis. It was hypothesized that fibroblasts seeded on ES filaments would have a higher seeding efficiency, show a different morphology, and exhibit a different genetic expression compared to Fw sutures. Although the initial cell attachment and proliferation rate was low for both materials, cells on electrospun filaments attained an elongated and spindle-like shape compared to cells on Fw sutures that stayed relatively flat and rounded for the duration of the cell culture period. This is most likely due to the similarity of the aligned ES filaments to the arrangement of tendon tissue ECM. Furthermore,

RNA-Seq analysis revealed an up-regulation in developmental and proliferative genes for cells on ES filaments, while those on Fw had an up-regulation of genes in the wound response combined with an upregulation in rheumatoid arthritis and IL-17 pathways. Finally, we focused on improving the geometry of the hard part of the scaffold consisting of 3D printed PCL. This was modified to fit the anatomy of the greater tuberosity of the humerus using anonymized patient CT scans. The pathway from 3D printing to personalised patient implant is becoming increasingly popular and advancing into a well-established pipeline which we used to our advantage. The resulting prototypes were tested for surgical feasibility by implanting and fixing them into porcine bone models and subjecting them to mechanical testing using a pre-defined loading regime. Outcomes were compared to those of suture anchors currently used in rotator cuff surgeries. Although fixation was suboptimal due to the prototypes having a geometry that was intended for human bones rather than porcine ones, this initial experimental set-up provided useful insights into the advantages and disadvantages of each prototype and opened the potential for future work on them.

5.2 Use of electrospinning and 3D printing to fabricate a soft-hard scaffold

5.2.1 A novel layering approach for tissue engineering

Previously, researchers have been depositing random electrospinning nanofibrous meshes by electrospinning directly onto 3D printed layers to produce composite scaffolds in the context of bone, cartilage, and ligament engineering (*285, 496-499*). The work presented in this thesis differs from the previous attempts in several aspects. We used a layering approach by interrupting the 3D printing process to insert pre-assembled electrospun filaments as opposed to electrospinning directing on top of an existing 3D printing block. We also used aligned electrospun filaments that mimics the ECM of tendon as opposed to random electrospun fibres, thereby specifically focusing on the tendon-bone interface. We worked with two

different polymers, PDO and PCL, to take advantage of the higher melting point of PDO to enable its insertion during printing. Finally, our approach is both scalable, i.e., it has the potential to be automated, and tunable as explained in section 1.6.6. PDO, however, is not widely used in the musculoskeletal field, most likely due to its relatively rapid degradation rate compared to other synthetic biodegradable polymers (*148, 172, 173, 259-261*). Other reported uses include electrospun PDO as a drug delivery system and for vascular engineering (*500-502*) and although there are studies investigating combinations of electrospun PDO and electrospn PCL (*261, 500*) and blends of a PDO/PCL polymer (*503*), no reports exist on a combination of electrospun PDO and 3D printed PCL. In this work, we have proposed a plain method of merging these polymers using accessible and simple techniques.

5.2.2 Future opportunities offered by the novel layering approach

5.2.2.1 Increasing the number of layers through improved FDM devices

We used an extrusion-based 3D printing method to manufacture the hard component of the scaffolds because it was compatible with the insertion of electrospun filaments. To keep the consistency throughout the experimental chapters, we only used one 3D printer (Ultimaker 3) based on the FDM method. Although it would not have been time-consuming to do so, I did not investigate different printing resolutions, which would have allowed a more precise and finer product and a more intricate inner design, as the focus was on the layering approach and expanding the number of filaments to insert while maintaining the same dimensions rather than improving the internal structure, at this stage. In addition, the maximum layers of electrospun filaments I could insert into a single scaffold depended greatly on the layer height. I used the minimum possible thickness, but using a different, more advanced printer (such as the Ultimaker S5) could perhaps have allowed us to insert even more filaments and

thereby increase the overall mechanical strength of the biphasic scaffold. Furthermore, we did not explore alternative printing patterns or infill densities which can be used to modulate porosity and pore size. This is known to greatly influence cell attachment and infiltration in tissue engineering and would require a separate project to fully investigate its potential. The effect of different fibre diameters and alignments was not considered in the soft part of the scaffold. To keep the consistency throughout all chapters, the fabrication of the filaments was done using the same set of parameters each time. I used aligned filaments with a diameter (<10 μm) similar to values reported in this group previously for PDO filaments (*173, 292*). In the literature, many different set-ups are used for 3D printing and the integration with different materials. Depending on the intended application, the combination of parameters to create tissue-engineered scaffolds can be changed accordingly and presents a wide range of potential.

5.2.2.2 Automatising scaffold production

Each scaffold was prepared and assembled manually by a single person and was therefore quite time-consuming. Since these techniques are quite well-established and have already been scaled up for various endeavours, the production the separate components could be increased quite easily. A major potential for future work would be the automatizing of the manufacturing process, whereby the bundles of electrospun filaments would be incorporated into the 3D printed scaffold by a robotic arm, for example, rather than manually. This would allow more precision and control of the configuration of the bundles and the printing time between layers and ensure that each scaffold is manufactured the same. Differences in mechanical outputs can then truly be attributed to the materials used rather than to human errors affecting a manual assembly. Adapting existing 3D printers to include an extra assisted device for layering electrospun filaments during printing could be an interesting engineering challenge to investigate. An example of such a design is presented in Appendix E, in which a

similar 3D printer to the one used in this thesis is fitted with additional, removable parts to facilitate the layering of electrospun filaments during 3D printing.

5.2.2.3 Improving the chemistry of the biphasic scaffold for enhanced cell response

In this thesis I chose to 3D print using PCL, which is a highly tunable polymer with a slow degradation rate that has shown considerable promise in bone-tissue applications. One property that was not explored is its easy miscibility with other compounds, including calcium phosphates which have long been used to improve the osteoconductive and mechanical properties of PCL. Calcium phosphates are already being used in clinical biocomposite anchors for the same purpose and would not have to go through extra regulatory pathways to be included. Cell attachment using osteoblasts was only assessed in a limited manner using a human osteoblast-like cell line (MG-63) as a pilot experiment in Chapter 2, see section 2.3.10. We did not attempt to isolate and extract tenocytes from animal or human models in this DPhil as this was too prone to infections and would not yield in enough cells for the experiments needed. Mineralisation of PDO scaffolds has been investigated for bone tissue engineering applications by either incorporating bioceramic particles in the polymer solution for electrospinning or by coating them in mineralisation substances (*504-506*) and remains to be explored in the context of this thesis. Coating the electrospun PDO filaments prior to assembly might facilitate infiltration of osteoblasts into the internal structure, as well as favourably affect the scaffold porosity. It could also create a more gradual transition from the hard 3D printed part to the soft electrospun part and in effect be considered a triphasic scaffold.

5.3 Electrospun filaments induce different transcriptional responses in fibroblasts compared to clinical sutures

5.3.1 Transcriptome-level differences between electrospun filaments and commercial sutures

In our current study, we found an up-regulation of genes relating to the IL-17 pathway in FiberWire, but not in the electrospun filaments. The lack of knowledge of the body's immune response to suture materials was highlighted by Lock et al (*124*) who studied the levels of inflammation produced by seven common suture materials. Pro-inflammatory markers that are expressed early in a foreign body reaction (L-1β, IL-1α, TNFα, IL-8 and CCR7) were up-regulated in four suture types, including FiberWire, with no balance from anti-inflammatory markers (TGFβ1, IL-1RA and CD163), although the cell culture period was only five days. IL-17 is a pro-inflammatory cytokine and is involved in the fibrotic response to synthetic implanted materials, characterized by the influx of macrophages in response to protein adsorption of the implant (*507*). In addition, the response to wounding and angiogenesis were among the most prominent enriched GO term, and in combination with IL-17 would suggest that the foreign body response is simulated (*507*). Angiogenesis is the final step in wound healing and is stimulated by endothelial cells. It was also an enriched term in the electrospun sutures but might have a different context. As mentioned before, PDO blended with collagen or elastin is a commonly used polymer for vascular tissue engineering because it resembles a similar compliance to native arteries (*508, 509*). Heene et al. (*510*) created a macroporous PDO scaffold using salt leaching, coated this with fibrin and co-cultured human umbilical vein endothelial cells (HUVECs) and adipose tissue-derived MSCs to form a vascular network. The fabrication of a microvasculature structure is of interest in growing tissues constructs and could potentially be of interest in the regeneration of the tendon. Indeed, angiogenesis is a key aspect of many repair processes and it is believed that the poor healing

abilities of the tendon are due to its hypovascular state (*511*). Therefore, electrospun PDO filaments could prove to be a positive influence on the ingrowth of new blood vessels and repair of tissues.

5.3.2 Limitations and future work

5.3.2.1 The use of FiberWire as a comparator material

FiberWire is a highly popular choice in rotator cuff surgeries but is not used as a comparator to tissue-engineered scaffolds for musculoskeletal purposes in the literature. For example, the morphology of cells on FiberWire sutures has only been described in two studies (*293, 512*). In fact, other than reporting on biomechanical properties, there seem to be few reports on basic biological properties for clinical sutures, which are often limited to basic cell viability experiments and histological evaluations in animal models (*513*). The use of clinical sutures in the body is associated with a foreign body reaction and there are several case reports involving the use of FiberWire detailing such complications and necessitating a subsequent removal of the suture (*514-517*). Perhaps a further investigation is considered superfluous as they have already passed approval by the major health organizations and have been in circulation for decades with only a small number of published case reports. However, considering the main advantage of biomaterials is their biological superiority it is surprising that they are not more often compared to clinical equivalents in *in vitro* or *in vivo* experiments. In this body of work, only one type of clinical suture was used to perform experiments with. In future work, this could be expanded to include a larger variety of sutures and grafts to have a wider range of comparisons.

5.3.2.2 Implementation of a co-culture model and loading regime

The materials used here were solely tested *in vitro* using commercial cell lines and well-established protocols in a monoculture. A co-culture system, i.e., the seeding of different cell

types to approximate the complexity of the ECM in a single environment, has been used to engineer a variety of heterogeneous tissues in mono- or multiphasic scaffolds to induce differentiation of cell types into the specific populations that make up the interface zone, as briefly described previously. Tendon cells are mechanosensitive and can change their ECM composition based in response to loading stimuli (*518*). With the advent of novel tissue engineered scaffolds, dynamic bioreactors have emerged as a way to apply load under specific conditions. A bioreactor is a device that can reproduce physiological conditions to positively influence cell proliferation and differentiation (*519*). As a step further, in a recent study by our group (*520*), a humanoid robot was integrated with a bioreactor to deliver loading regimes to fibroblasts cultured on bundles of electrospun PCL filaments for the purpose of tendon regeneration. These offer exciting advances for biomaterials and brings an important clinical relevance to tissue engineering.

5.4 The design of a clinically relevant 3D printed block

In the final Chapter we adapted the geometry of the hard part of the biphasic scaffold to fit that of the greater tuberosity of the humerus. The aim was to design prototypes that would fit the number of electrospun filaments described in Chapter 2 to meet mechanical needs and which would be possible to implant in the footprint area of the supraspinatus tendon. This was achieved by collaborating with external medical manufacturers and is a first step in towards the clinical translation of the prototype.

5.4.1 The advantage of a single unit suture-anchor

Compared to currently used suture anchors, the 3D printed part of the proposed prototypes are of relatively large dimensions, but do not occupy more space in the bone in total. Conventional suture anchors are usually placed about 1 cm apart from each other and as

many as eight different sutures can be inserted in the repair of massive rotator cuff tears. Furthermore, there are many options of suitable anchors that can be combined with different types of sutures. Each suture-anchor comes with a different insertion tool and technique as well. This can create quite some variability in the effectiveness of the rotator cuff repair, as it becomes reliant on these materials and the surgeon's expertise. In fact, most research dedicated to surgical rotator cuff repairs involves the comparison of various repair techniques, anchors and sutures and, although insertion method are very similar, there is no standardization in the best practice approach (*521*). Indeed, this will also vary from country to country as different manufacturers will be dominating the market. In our approach, the scaffold can be changed according to patient anatomy and does not require custom-made tools. We presented three different prototypes with basic fixation methods using screws. Although several concerns were discussed in Chapter 4 regarding impingement and the potential difficulty of fixation, we believe there is room for optimization and further development of these types of implants in collaboration with orthopaedic surgeons.

5.4.2 Future aspects worth exploring

5.4.2.1 Fixation of the electrospun cuff to tendon tissue

One avenue that still requires investigation is how to attach the electrospun filaments into the remaining tendon. Currently, the electrospun cuff emerges as a bundle of individual, parallel aligned filaments that can be up to 270 in numbers. Naturally, this is not a practical way of handling this scaffold. In the first Chapter, we briefly experimented with twisted bundles, but this was not further explored due to an unsuccessful incorporation into the 3D printed block. This was entirely due to the difficulty of fraying the twisted ends and making sure the filaments were stuck on the adhesive block individually and did not clump together. Furthermore, the twisted filaments became slack and lost their structure as the ends were

frayed, although we tried preventing this by tying a knot at the end. A better preparation of the bundles prior to printing, combined with a more thorough layering of the bundles would have most likely resulted in a successful merging of the twisted bundles into the 3D printed block. In conventional anchors, the sutures are looped through the eyelet of the anchor and emerge from the bone in single, double, or triple-loaded strands to be passed through the tendon. Knot-tying is an entirely separate discipline as well depending on whether it is an arthroscopic or open repair or a sliding or non-sliding knot and the quality of it depends heavily on what suture is used (*521*). Indeed, a knot of a bulkier suture can occupy too much space in the subacromial space and cause impingement and irritation which can negatively affect soft tissue healing (*521*). Abhari et al (*269*) have recently published on the use of industrial braiding machines to upscale the production of electrospun filaments and assembling them into multifilament yarns, much like conventional sutures, for clinical translation. Embedding multifilament yarns into 3D printed blocks is therefore a possibility for future work and would make the scaffold as presented here much more practical for handling and use in surgical settings. In addition, textile techniques such as braiding, weaving and twisting have been used for millennia to increase the strength of natural fibers (e.g., cotton, wool or silk) and can definitely be used with electrospun filaments as well.

5.4.2.2 A more thorough evaluation of PDO and PCL

The approach taken in this thesis fits well with the advent of 'point of care (PoC)' 3D printing in orthopaedic surgery and traumatology (*522*). The 3D printing technique has become ubiquitous and widely accessible which has attracted health care facilities to incorporate 'in-house' 3D printing laboratory and make the leap towards personalized medicine and custom-made implants (*522*). These are commonly extrusion-based printers and are operated by biomedical engineers who work collectively with surgeons from various

disciplines to design and print patient-specific implants, surgical guides and instruments, and anatomical models. The workflow starts by converting a dataset of medical images (usually CT) into a virtual object that is either designed de novo or is a mirror of a healthy counterpart (*523*). Many different software packages are available to do this, and the virtual object is consequently passed to the 3D printer. The PoC manufacturing model adheres to the regulatory framework surrounding customized 3D printing if the materials used are certified under ISO 10993 – which is the set of guidelines for medical devices that make bodily contact. However, not all European regulations have to be met if the product is used only within the hospital and is not aimed for market release (*523*). Furthermore, if the product is intended for direct contact with patients, sterilization can occur using standard hospital policies (*523*), for example, by use of ethylene oxide as regular hospital steam sterilization (i.e., autoclaving) can damage the 3D printed implant (*523*). We used an indirect cytotoxicity assay in this thesis to evaluate the safety of PDO and PCL in their current state, based on an ISO for medical devices. It is one of the most widely used cytotoxicity assays for biomedical applications (*524*), but is only sufficient as an in vitro assessment. Even though both polymers are FDA-cleared and have translation potential, no device currently exists on the market that is a combination of both and therefore the ISO 10993 regulations will need to be applied more in depth, here. This includes and is not limited to test for local effects after implantation, residuals by ethylene oxide sterilization and tests for the identification and quantification of degradation products (*300*). Therefore, for future work, a more in-depth evaluation of the proposed scaffold is also needed.

5.5 Main limitations in this thesis

Specific limitations to each experiment have been considered per chapter, but there are also a few overall limitations. The impact of the Covid-19 pandemic has also been addressed and posed significant disruptions for the completion of this thesis. As briefly mentioned before,

the continuous supply of materials presented a significant limitation on the extent of the experiments performed. The electrospinning setup in our laboratory could spin high-quality filaments continuously but was highly susceptible to environmental changes and was eventually outsourced to our cleanroom production team in Harwell to ensure filaments were of consistent quality. For the experimental section in Chapter 2, materials were used right away to prevent adverse effects from degradation but for the sections in Chapter 3 this was of less importance. Sufficient material could not be produced for the experimental section in Chapter 4, nor was there availability to produce the full prototype scaffolds at the 3D printing facility, and a commercial suture was chosen instead to represent the cuff. Static load to failure of the biphasic scaffolds with the maximum number of filaments was already performed in Chapter 1, but cyclic loading was not performed and should be considered for future work. Bulk RNA-Seq was performed in Chapter 3 and works best with the assumption of a homogenous cell population. The cells presently used stemmed from a commercial cell line, but this was not verified in-house. They were routinely tested for mycoplasma and no bacterial or fungal infections were present, but cell-line contamination by other species has become an increasingly widely known phenomenon (*351*). Cell line authentication has not yet become standard practice in many laboratories and is one of the major reasons for irreproducibility of results (*525*). It has been estimated that 18-36% of cell lines used in scientific research are cross-contaminated, duplicated or misidentified (*526*). The current cell line was purchased by ATCC and has no reports of contaminations or misidentifications, yet.

5.6 Conclusion

In this thesis we have presented a novel method of combining electrospinning and 3D printing biodegradable polymers that have a track record of safety in patients. This approach can be adapted and improved to design various types of soft-hard implants. The main results are summarised as follows:

- Layering pre-assembled bundles of electrospun PDO filaments during 3D printing of PCL is feasible with minimal disruption to the overall process. The higher melting temperature of PDO meant that the electrospun fibres were compatible with the heating of PCL during printing and were only marginally affected. The resulting soft-hard scaffold can be up-scaled by increasing the number of filaments within the 3D printed block.
- Fibroblasts were able to attach to the electrospun filaments and showed an elongated and spindle-shaped morphology. RNA sequencing of cells on ES filaments revealed differentially expressed genes that exhibited a more pronounced profile towards cell proliferation and differentiation whilst Fw sutures had enriched pathways in wound response and inflammatory pathways concerning rheumatoid arthritis and IL-17.
- The 3D printed block can be designed to fit a specific geometry using point of care principles, in which anonymised medical imaging is used to segment and define the boundaries of the scaffold according to implant location. The resulting designs could be inserted and attached in porcine models using existing tools and could undergo a pre-defined cyclic loading regime resembling the postoperative rehabilitation period.

This thesis contributes to the wider research community investigating multiphasic scaffolds using synthetic polymers by offering an easy, reproducible, and adaptable fabrication method that is relevant for clinical settings.

References

1. C. Grobet *et al.*, Cost-Utility Analysis of Arthroscopic Rotator Cuff Repair: A Prospective Health Economic Study Using Real-World Data. *Arthrosc Sports Med Rehabil* **2**, e193-e205 (2020).
2. U.S. Sports Medicine Market Analysis, Size, Trends | 2020-2026. *iData Research*, (2020).
3. I. Papanicolas, L. R. Woskie, A. K. Jha, Health Care Spending in the United States and Other High-Income Countries. *JAMA* **319**, 1024-1039 (2018).
4. A. Narvani *et al.*, Degenerative rotator cuff tear, repair or not repair? A review of current evidence. *The Annals of The Royal College of Surgeons of England* **102**, 248-255 (2020).
5. S. Moosmayer, A. V. Gartner, R. Tariq, The natural course of nonoperatively treated rotator cuff tears: an 8.8-year follow-up of tear anatomy and clinical outcome in 49 patients. *J Shoulder Elbow Surg* **26**, 627-634 (2017).
6. S. Cheung *et al.*, The presence of fatty infiltration in the infraspinatus: its relation with the condition of the supraspinatus tendon. *Arthroscopy* **27**, 463-470 (2011).
7. B. Melis, M. J. DeFranco, C. Chuinard, G. Walch, Natural history of fatty infiltration and atrophy of the supraspinatus muscle in rotator cuff tears. *Clin Orthop Relat Res* **468**, 1498-1505 (2010).
8. L. M. Galatz, C. M. Ball, S. A. Teefey, W. D. Middleton, K. Yamaguchi, The outcome and repair integrity of completely arthroscopically repaired large and massive rotator cuff tears. *J Bone Joint Surg Am* **86**, 219-224 (2004).
9. M. Marsh, S. Newman, Trends and developments in hip and knee arthroplasty technology:. *Journal of Rehabilitation and Assistive Technologies Engineering*, (2021).
10. P. Desmoineaux, Failed rotator cuff repair. *Orthopaedics & Traumatology: Surgery & Research* **105**, S63-S73 (2019).
11. A. Novoa-Boldo, L. V. Gulotta, Expectations Following Rotator Cuff Surgery. *Curr Rev Musculoskelet Med* **11**, 162-166 (2018).
12. A. Carr *et al.*, Effectiveness of open and arthroscopic rotator cuff repair (UKUFF): a randomised controlled trial. *Bone Joint J* **99-B**, 107-115 (2017).
13. N. S. Shah, E. Suriel Peguero, Y. Umeda, Z. T. Crawford, B. M. Grawe, Long-Term Outcomes of Massive Rotator Cuff Tear Repair: A Systematic Review. *HSS Journal®* **18**, 130-137 (2021).
14. F. A. Barber, M. A. Herbert, Cyclic loading biomechanical analysis of the pullout strengths of rotator cuff and glenoid anchors: 2013 update. *Arthroscopy* **29**, 832-844 (2013).
15. N. Gorman, Supraspinatus muscle. https://www.kenhub.com/en/library/anatomy/supraspinatus-muscle, (2022).
16. T. Mochizuki *et al.*, Humeral insertion of the supraspinatus and infraspinatus. New anatomical findings regarding the footprint of the rotator cuff. Surgical technique. *J Bone Joint Surg Am* **91 Suppl 2 Pt 1**, 1-7 (2009).
17. J. Apostolakos *et al.*, The enthesis: a review of the tendon-to-bone insertion. *Muscles Ligaments Tendons J* **4**, 333-342 (2014).
18. A. Winkelmann, A. Heinze, S. Hendrix, Acknowledging tissue donation: Human cadaveric specimens in musculoskeletal research. *Clinical anatomy (New York, N.Y.)* **29**, (2016).
19. J. M. Clark, D. T. Harryman, Tendons, ligaments, and capsule of the rotator cuff. Gross and microscopic anatomy. *J Bone Joint Surg Am* **74**, 713--725 (1992).
20. H. Minagawa *et al.*, Humeral attachment of the supraspinatus and infraspinatus tendons: an anatomic study. *Arthroscopy* **14**, 302--306 (1998).
21. J. R. Dugas, D. A. Campbell, R. F. Warren, B. H. Robie, P. J. Millett, Anatomy and dimensions of rotator cuff insertions. *J Shoulder Elbow Surg* **11**, 498-503 (2002).
22. J. Fallon, F. T. Blevins, K. Vogel, J. Trotter, Functional morphology of the supraspinatus tendon. *J Orthop Res* **20**, 920-926 (2002).

23. S. Szczesny, D. Elliott, Interfibrillar shear stress is the loading mechanism of collagen fibrils in tendon. *Acta Biomaterialia* **10**, 2582-2590 (2014).
24. E. B. Online. (2021).
25. C. Frantz, K. Stewart, V. Weaver, The extracellular matrix at a glance. *Journal of cell science* **123**, 4195-4200 (2010).
26. F. Gattazzo, A. Urciuolo, P. Bonaldo, Extracellular matrix: A dynamic microenvironment for stem cell niche | Elsevier Enhanced Reader. *Biochimica et Biophysica Acta*, 2506-2519 (2014).
27. M. Kjaer, Role of extracellular matrix in adaptation of tendon and skeletal muscle to mechanical loading. *Physiological reviews* **84**, 649-698 (2004).
28. M. Benjamin, J. Ralphs, Fibrocartilage in tendons and ligaments--an adaptation to compressive load. *Journal of Anatomy* **193**, 481-494 (1998).
29. J. Kastelic, A. Galeski, E. Baer, The multicomposite structure of tendon. *Connective tissue research* **6**, 11-23 (1978).
30. H. Screen, D. Berk, K. Kadler, F. Ramirez, M. Young, Tendon functional extracellular matrix. *Journal of orthopaedic research : official publication of the Orthopaedic Research Society* **33**, (2015).
31. S. Ricard-Blum, The collagen family. *Cold Spring Harb Perspect Biol* **3**, a004978-a004978 (2011).
32. M. Franchi, A. Trirè, M. Quaranta, E. Orsini, V. Ottani, Collagen structure of tendon relates to function. *The Scientific World Journal* **7**, 404-420 (2007).
33. *Collagen Research*. (SANA Amsterdam, http://sana.amsterdam/pages/research).
34. S. Tozer, D. Duprez, Tendon and ligament: development, repair and disease. *Birth defects research. Part C, Embryo today : reviews* **75**, 226-236 (2005).
35. Y. Bi *et al.*, Identification of tendon stem/progenitor cells and the role of the extracellular matrix in their niche. *Nature Medicine* **13**, 1219-1227 (2007).
36. C. Thorpe *et al.*, Aspartic acid racemization and collagen degradation markers reveal an accumulation of damage in tendon collagen that is enhanced with aging. *The Journal of biological chemistry* **285**, 15674-15681 (2010).
37. J. Chu, M. Lu, C. G. Pfeifer, V. Alt, D. Docheva, Rebuilding Tendons: A Concise Review on the Potential of Dermal Fibroblasts. *Cells* **9**, (2020).
38. C. McNeilly, A. Banes, M. Benjamin, J. Ralphs, Tendon cells in vivo form a three dimensional network of cell processes linked by gap junctions. *Journal of anatomy* **189**, (1996).
39. M. Chiquet, L. Gelman, R. Lutz, S. Maier, From mechanotransduction to extracellular matrix gene expression in fibroblasts. *Biochimica et biophysica acta* **1793**, (2009).
40. B. Alberts, A. Johnson, J. Lewis, *Integrins*. Molecular Biology of the Cell (Garland Science, ed. 4, 2002).
41. J. Jones, R. Walker, Integrins: a role as cell signalling molecules. *J Clin Pathol: Mol Pathol* **52**, 208-213 (1999).
42. M. Chatterjee, P. Muljadi, N. Andarawis-Puri, The role of the tendon ECM in mechanotransduction: disruption and repair following overuse. *Connective Tissue Research* **63**, (2021).
43. H. H. Lu, S. Thomopoulos, Functional attachment of soft tissues to bone: development, healing, and tissue engineering. *Annu Rev Biomed Eng* **15**, 201-226 (2013).
44. J. Z. Paxton, K. Baar, L. M. Grover, Current Progress in Enthesis Repair: Strategies for Interfacial Tissue Engineering. *Orthopedic Muscul Sys* **003**, (2013).
45. P. T. Jensen, K. L. Lambertsen, L. H. Frich, Assembly, maturation, and degradation of the supraspinatus enthesis. *J Shoulder Elbow Surg* **27**, 739-750 (2018).
46. L. Rossetti *et al.*, The microstructure and micromechanics of the tendon--bone insertion. *Nature Materials* **16**, 664-672 (2017).
47. M. Buckley *et al.*, Distributions of Types I, II and III Collagen by Region in the Human Supraspinatus Tendon. *Connect Tissue Res.* **54**, 374-379 (2013).
48. L. M. Galatz, L. Gerstenfeld, E. Heber-Katz, S. A. Rodeo, Tendon Regeneration and Scar Formation: The Concept of Scarless Healing. *J Orthop Res* **33**, 823-831 (2015).

49. S. Thomopoulos, C. P. William, D. B. Rifkin, K. A. Derwin, Mechanisms of tendon injury and repair. *J Orthop Res* **33**, 832-839 (2016).
50. L. Galatz *et al.*, Delayed repair of tendon to bone injuries leads to decreased biomechanical properties and bone loss. *Journal of orthopaedic research : official publication of the Orthopaedic Research Society* **23**, (2005).
51. T. Kanazawa *et al.*, Histomorphometric and ultrastructural analysis of the tendon-bone interface after rotator cuff repair in a rat model. *Scientific Reports* **6**, 1-10 (2016).
52. H. A. Eriksen, A. Pajala, J. Leppilahti, J. Risteli, Increased content of type III collagen at the rupture site of human Achilles tendon. *Journal of Orthopaedic Research* **20**, 1352-1357 (2002).
53. E. Bianchi *et al.*, Innovative Strategies in Tendon Tissue Engineering. *Pharmaceutics* **13**, 89 (2021).
54. R. Z. Tashjian, Epidemiology, natural history, and indications for treatment of rotator cuff tears. *Clin Sports Med* **31**, 589-604 (2012).
55. S. Namdari, R. Henn, A. Green, Traumatic Anterosuperior Rotator Cuff Tears: The Outcome of... : JBJS. *The Journal of Bone & Joint Surgery* **90**, 1906-1913 (2008).
56. N. A. Mall *et al.*, Symptomatic progression of asymptomatic rotator cuff tears: a prospective study of clinical and sonographic variables. *J Bone Joint Surg Am* **92**, 2623-2633 (2010).
57. J. Ide, A. Tokiyoshi, J. Hirose, H. Mizuta, Arthroscopic repair of traumatic combined rotator cuff tears involving the subscapularis tendon. *J Bone Joint Surg Am* **89**, (2007).
58. A. Seidler *et al.*, Work-related lesions of the supraspinatus tendon: a case-control study. *Int Arch Occup Environ Health* **84**, 425-433 (2011).
59. A. Bedi, J. Dines, R. Warren, D. Dines, Massive tears of the rotator cuff. *J Bone Joint Surg Am* **92**, (2010).
60. B. R. Freedman *et al.*, Dynamic Loading and Tendon Healing Affect Multiscale Tendon Properties and ECM Stress Transmission. *Scientific Reports* **8**, 1-13 (2018).
61. A. Herchenhan *et al.*, Tenocyte contraction induces crimp formation in tendon-like tissue. *Biomechanics and modeling in mechanobiology* **11**, (2012).
62. J. H. C. Wang, Mechanobiology of tendon. *J Biomech* **39**, 1563-1582 (2006).
63. C. Thomas, J. Collier, C. Sfeir, K. Healy, Engineering gene expression and protein synthesis by modulation of nuclear shape. *Proceedings of the National Academy of Sciences of the United States of America* **99**, (2002).
64. S. Lelièvre *et al.*, Tissue phenotype depends on reciprocal interactions between the extracellular matrix and the structural organization of the nucleus. *Proceedings of the National Academy of Sciences of the United States of America* **95**, (1998).
65. J. Henderson, G. Shannon, A. Veress, C. Neu, Direct measurement of intranuclear strain distributions and RNA synthesis in single cells embedded within native tissue. *Biophysical journal* **105**, (2013).
66. Y. Shi *et al.*, Uniaxial mechanical tension promoted osteogenic differentiation of rat tendon-derived stem cells (rTDSCs) via the Wnt5a-RhoA pathway. *Journal of cellular biochemistry* **113**, (2012).
67. M. Egerbacher, S. P. Arnoczky, O. Caballero, M. Lavagnino, K. L. Gardner, Loss of homeostatic tension induces apoptosis in tendon cells: an in vitro study. *Clinical orthopaedics and related research* **466**, 1562-1568 (2008).
68. A. Scott *et al.*, High strain mechanical loading rapidly induces tendon apoptosis: an ex vivo rat tibialis anterior model. *British journal of sports medicine* **39**, (2005).
69. R. Bell, N. R. Gendron, M. Anderson, E. L. Flatow, N. Andarawis-Puri, A potential new role for myofibroblasts in remodeling of sub-rupture fatigue tendon injuries by exercise. *Scientific Reports* **8**, 1-10 (2018).
70. N. Wang, J. D. Tytell, D. E. Ingber, Mechanotransduction at a distance: mechanically coupling the extracellular matrix with the nucleus. *Nature Reviews Molecular Cell Biology* **10**, 75-82 (2009).
71. C. Thorpe *et al.*, Tendon overload results in alterations in cell shape and increased markers of inflammation and matrix degradation. *Scandinavian journal of medicine & science in sports* **25**, (2015).

72. B. J. Dean, P. Gettings, S. G. Dakin, A. J. Carr, Are inflammatory cells increased in painful human tendinopathy? A systematic review. *Br J Sports Med* **50**, 216-220 (2016).
73. P. Sharma, N. Maffulli, Biology of tendon injury: healing, modeling and remodeling. *Journal of musculoskeletal & neuronal interactions* **6**, (2006).
74. M. Abate *et al.*, Pathogenesis of tendinopathies: inflammation or degeneration? *Arthritis research & therapy* **11**, (2009).
75. P. Riley *et al.*, Matrix metalloproteinase activities and their relationship with collagen remodelling in tendon pathology. *Matrix Biology* **21**, 185-195 (2002).
76. J. Parkinson, T. Samiric, M. Illic, J. Cook, J. Handley, Involvement of Proteoglycans in Tendinopathy. *J Musculoskelet Neuronal Interact* **11**, 86-93 (2011).
77. G. Nourissat, X. Houard, J. Sellam, D. Duprez, F. Berenbaum, Use of autologous growth factors in aging tendon and chronic tendinopathy. *Front Biosci. (Elite Ed)* **5**, 911-921 (2013).
78. M. MacKechnie *et al.*, Repair of full-thickness rotator cuff tears in patients aged younger than 55 years. *Arthroscopy* **30**, (2014).
79. F. Pegreffi, P. Paladini, F. Campi, G. Porcellini, Conservative Management of Rotator Cuff Tear. *Sports Medicine and Arthroscopy Review* **19**, (2011).
80. A. Mohamadi, J. Chan, F. Claessen, D. Ring, N. Chen, Corticosteroid Injections Give Small and Transient Pain Relief in Rotator Cuff Tendinosis: A Meta-analysis. *Clinical orthopaedics and related research* **475**, (2017).
81. R. Puzzitiello *et al.*, Adverse Impact of Corticosteroid Injection on Rotator Cuff Tendon Health and Repair: A Systematic Review - Arthroscopy. *The Journal of Arthroscopic and Related Surgery* **36**, 1468-1475 (2020).
82. E. Giovannetti de Sanctis *et al.*, The Efficacy of Injections for Partial Rotator Cuff Tears: A Systematic Review. *Journal of clinical medicine* **10**, (2020).
83. O. Dolkart *et al.*, Subacromial corticosteroid injections transiently decrease suture anchor pullout strength: biomechanical studies in rats. *Journal of shoulder and elbow surgery* **26**, (2017).
84. E. Maman *et al.*, Detrimental Effect of Repeated and Single Subacromial Corticosteroid Injections on the Intact and Injured Rotator Cuff: A Biomechanical and Imaging Study in Rats. *The American Journal of Sports Medicine* **44**, 177-182 (2015).
85. A. M. Cimino *et al.*, Corticosteroid Injections May Increase Retear and Revision Rates of Rotator Cuff Repair: A Systematic Review. *Arthroscopy: The Journal of Arthroscopic & Related Surgery* **36**, 2334-2341 (2020).
86. M. DeClercq *et al.*, Systematic Review of Platelet-Rich Plasma for Rotator Cuff Repair: Are We Adhering to the Minimum Information for Studies Evaluating Biologics in Orthopaedics? *Orthop J Sports Med* **9**, (2021).
87. C. Littlewood, A. Lowe, J. Moore, Rotator Cuff Disorders: A Survey of Current Uk Physiotherapy Practice - j.1758-5740.2011.00164.x. *Shoulder and Elbow* **4**, 64-71 (2012).
88. S. Moosmayer *et al.*, At a 10-Year Follow-up, Tendon Repair Is Superior to Physiotherapy in the Treatment of Small and Medium-Sized Rotator Cuff Tears. *J Bone Joint Surg Am* **101**, (2019).
89. S. Moosmayer *et al.*, Tendon repair compared with physiotherapy in the treatment of rotator cuff tears: a randomized controlled study in 103 cases with a five-year follow-up. *J Bone Joint Surg Am* **96**, (2014).
90. S. Moosmayer *et al.*, Comparison between surgery and physiotherapy in the treatment of small and medium-sized tears of the rotator cuff: A randomised controlled study of 103 patients with one-year follow-up. *The Journal of bone and joint surgery. British volume* **92**, (2010).
91. R. C. Mather, III *et al.*, The Societal and Economic Value of Rotator Cuff Repair. *JBJS* **95**, (2013).
92. ShoulderDoc, Rotator Cuff Classifications. https://www.shoulderdoc.co.uk/article/1456, (2022).
93. J. Davidson, S. Burkhart, The Geometric Classification of Rotator Cuff Tears: A System Linking Tear Pattern to Treatment and Prognosis - pdf. *Arthroscopy: The Journal of Arthroscopic and Related Surgery* **26**, 417-424 (2010).

94. S. Burkhart, The principle of margin convergence in rotator cuff repair as a means of strain reduction at the tear margin. *Annals of biomedical engineering* **32**, (2004).
95. M. Baldwin *et al.*, Use of implantable meshes for augmented rotator cuff repair: a systematic review and meta-analysis. *BMJ Open* **10**, (2020).
96. U. o. Washington, Arthroscopic shoulder surgery for the treatment of rotator cuff tears. *UW Orthopaedics and Sports Medicine*.
97. E. A. Codman, Complete rupture of the supraspinatus tendon. Operative treatment with report of two successful cases. *Journal of Shoulder and Elbow Surgery* **20**, 347-349 (2011).
98. M. Apreleva, M. Özbaydar, P. G. Fitzgibbons, J. J. P. Warner, Rotator cuff tears: The effect of the reconstruction method on three-dimensional repair site area. *Arthroscopy: The Journal of Arthroscopic & Related Surgery* **18**, 519-526 (2002).
99. B. J. Cole, N. S. ElAttrache, A. Anbari, Arthroscopic rotator cuff repairs: an anatomic and biomechanical rationale for different suture-anchor repair configurations. *Arthroscopy* **23**, 662--669 (2007).
100. J. Dines, A. Bedi, N. ElAttrache, D. Dines, Single-row versus double-row rotator cuff repair: techniques and outcomes. *The Journal of the American Academy of Orthopaedic Surgeons* **18**, (2010).
101. E. Urch *et al.*, Improved Rotator Cuff Footprint Contact Characteristics With an Augmented Repair Construct Using Lateral Edge Fixation. *The American Journal of Sports Medicine* **48**, 444-449 (2019).
102. D. Adla, M. Rowsell, R. Pandey, Cost-effectiveness of open versus arthroscopic rotator cuff repair. *Journal of Shoulder and Elbow Surgery* **19**, 258-261 (2010).
103. Y. Bedeir, A. Jimenez, B. Grawe, Recurrent tears of the rotator cuff: Effect of repair technique and management options. *Orthopedic Reviews* **10**, (2018).
104. C. A. Cummins, G. A. C. Murrell, Mode of failure for rotator cuff repair with suture anchors identified at revision surgery. *J Shoulder Elbow Surg* **12**, 128--133 (2003).
105. M. C. Park, N. S. Elattrache, C. S. Ahmad, J. E. Tibone, "Transosseous-equivalent" rotator cuff repair technique. *Arthroscopy* **22**, 1360 e1361-1365 (2006).
106. S. Park, B. Shim, H. Seok, How Much Will High Tension Adversely Affect Rotator Cuff Repair Integrity? *Arthroscopy : the journal of arthroscopic & related surgery : official publication of the Arthroscopy Association of North America and the International Arthroscopy Association* **35**, (2019).
107. T.-H. Yoon, S.-J. Kim, Y.-R. Choi, D.-S. Kim, Y.-M. Chun, Incomplete footprint coverage under tension in repair of isolated supraspinatus full-thickness tear. *Scientific Reports* **11**, 1-7 (2021).
108. H.-B. He *et al.*, Biomechanical comparison between single-row with triple-loaded suture anchor and suture-bridge double-row rotator cuff repair. *BMC Musculoskeletal Disorders* **21**, 629 (2020).
109. L. Li, S. L. Bokshan, L. V. Ready, B. D. Owens, The primary cost drivers of arthroscopic rotator cuff repair surgery: a cost-minimization analysis of 40,618 cases. *Journal of Shoulder and Elbow Surgery* **28**, 1977-1982 (2019).
110. J. Murphy *et al.*, Costs, quality of life and cost-effectiveness of arthroscopic and open repair for rotator cuff tears. *The Bone & Joint Journal* **98-B**, 1648-1655 (2016).
111. F. A. Barber, Biodegradable Shoulder Anchors Have Unique Modes of Failure. *Arthroscopy: The Journal of Arthroscopic & Related Surgery* **23**, 316-320 (2007).
112. U. G. Longo *et al.*, Metallic versus biodegradable suture anchors for rotator cuff repair: a case control study. *BMC Musculoskeletal Disorders* **20**, 477 (2019).
113. D. Hurwit, G. Fanton, M. Tella, A. Behn, K. J. Hunt, Viscoelastic Properties of Common Suture Material Used for Rotator Cuff Repair and Arthroscopic Procedures. *Arthroscopy: The Journal of Arthroscopic & Related Surgery* **30**, 1406-1412 (2014).
114. K. Swan , T. Baldini, E. McCarthy, Arthroscopic Suture Material and Knot Type. *The American Journal of Sports Medicine* **37**, (2009).
115. L. J. Bisson, L. M. Manohar, R. D. Wilkins, J. Gurske-Deperio, M. T. Ehrensberger, Influence of Suture Material on the Biomechanical Behavior of Suture-Tendon Specimens: A

Controlled Study in Bovine Rotator Cuff. *The American Journal of Sports Medicine* **36**, 907-912 (2008).
116. J. F. Williams *et al.*, Abrasiveness of high-strength sutures used in rotator cuff surgery: are they all the same? *J Shoulder Elbow Surg* **25**, 142--148 (2016).
117. S. S. Burkhart, J. L. Diaz Pagàn, M. A. Wirth, K. A. Athanasiou, Cyclic loading of anchor-based rotator cuff repairs: confirmation of the tension overload phenomenon and comparison of suture anchor fixation with transosseous fixation. *Arthroscopy* **13**, 720-724 (1997).
118. D. Wüst, D. Meyer, P. Favre, C. Gerber, Mechanical and handling properties of braided polyblend polyethylene sutures in comparison to braided polyester and monofilament polydioxanone sutures. *Arthroscopy : the journal of arthroscopic & related surgery : official publication of the Arthroscopy Association of North America and the International Arthroscopy Association* **22**, 1146-1153 (2006).
119. M. Lambrechts *et al.*, Comparison of the cheese-wiring effects among three sutures used in rotator cuff repair. *Int J Shoulder Surg* **8**, 81--85 (2014).
120. B. Owens, J. Algeri, V. Liang, S. DeFroda, Rotator cuff tendon tissue cut-through comparison between 2 high-tensile strength sutures. *Journal of shoulder and elbow surgery* **28**, (2019).
121. M. Kowalsky *et al.*, Evaluation of suture abrasion against rotator cuff tendon and proximal humerus bone. *Arthroscopy : the journal of arthroscopic & related surgery : official publication of the Arthroscopy Association of North America and the International Arthroscopy Association* **24**, (2008).
122. J. Deranlot *et al.*, Abrasive properties of braided polyblend sutures in cuff tendon repair: an in vitro biomechanical study exploring regular and tape sutures. *Arthroscopy : the journal of arthroscopic & related surgery : official publication of the Arthroscopy Association of North America and the International Arthroscopy Association* **30**, (2014).
123. M. Byrne, A. Aly, The Surgical Suture. *Aesthetic Surgery Journal* **39**, S67-S72 (2019).
124. A. Lock *et al.*, Induction of immune gene expression and inflammatory mediator release by commonly used surgical suture materials: an experimental in vitro study - s13037-017-0132-2.pdf. *Patient Safety in Surgery* **11**, (2017).
125. A. F. C. Aristizabal, F. A. Barber, Rotator cuff repair: technical considerations influencing optimum anchor choice in rotator cuff repair. *Annals of Joint*, (2020).
126. C. Cho, K. Bae, D. Kim, Biomaterials Used for Suture Anchors in Orthopedic Surgery. *Clinics in orthopedic surgery* **13**, (2021).
127. S. Chaudhry, K. Dehne, F. Hussain, A review of suture anchors. *Orthopaedics and Trauma* **33**, 263-270 (2019).
128. N. S. Nagra, N. Zargar, R. D. J. Smith, A. J. Carr, Mechanical properties of all-suture anchors for rotator cuff repair. *Bone Joint Res* **6**, 82--89 (2017).
129. A. Dhawan, N. Ghodadra, V. Karas, M. J. Salata, B. J. Cole, Complications of Bioabsorbable Suture Anchors in the Shoulder. *The American Journal of Sports Medicine* **40**, 1424-1430 (2012).
130. M. Sgroi, T. Friesz, M. Schocke, H. Reichel, T. Kappe, Biocomposite Suture Anchors Remain Visible Two Years After Rotator Cuff Repair. *Clin Orthop Relat Res* **477**, 1469-1478 (2019).
131. J. Bergsma, W. de Bruijn, F. Rozema, R. Bos, G. Boering, Late degradation tissue response to poly(L-lactide) bone plates and screws. *Biomaterials* **16**, (1995).
132. W. Warden, D. Chooljian, D. Jackson, en-Year Magnetic Resonance Imaging Follow-Up of Bioabsorbable Poly-L-Lactic Acid Interference Screws After Anterior Cruciate Ligament. *The Journal of Arthroscopic and Related Surgery* **24**, (2008).
133. M. Radford, J. Noakes, J. Read, D. Wood, The natural history of a bioabsorbable interference screw used for anterior cruciate ligament reconstruction with a 4-strand hamstring technique. *Arthroscopy : the journal of arthroscopic & related surgery : official publication of the Arthroscopy Association of North America and the International Arthroscopy Association* **21**, (2005).
134. A. F. Cobaleda Aristizabal, E. J. Sanders, F. A. Barber, Adverse Events Associated With Biodegradable Lactide-Containing Suture Anchors. *Arthroscopy: The Journal of Arthroscopic & Related Surgery* **30**, 555-560 (2014).

135. S. S. Hasan, Editorial Commentary: Biology and Biomechanics Must Be Carefully Balanced for a Durable Rotator Cuff Repair. *Arthroscopy: The Journal of Arthroscopic & Related Surgery* **37**, 38-41 (2021).
136. M. E. Bishop *et al.*, Biomechanical and Clinical Comparison of Suture Techniques in Arthroscopic Rotator Cuff Repair. *JBJS Rev* **5**, e3 (2017).
137. M. V. Wlk *et al.*, Biomechanical evaluation of suture–tendon interface and tissue holding of three suture configurations in torn and degenerated versus intact human rotator cuffs. *Knee Surgery, Sports Traumatology, Arthroscopy* **23**, 386-392 (2015).
138. R. Langer, J. Vacanti, Tissue engineering. *Science (New York, N.Y.)* **260**, (1993).
139. S. Shinde, O. Suman. (Allied Market Research, 2020).
140. Y. S. Kim, M. M. Smoak, A. J. Melchiorri, A. G. Mikos, An Overview of the Tissue Engineering Market in the United States from 2011 to 2018. *Tissue engineering. Part A* **25**, 1-8 (2019).
141. H. Quie, D. Nogueira, E. Vollebregt, How to use the Equivalence Pathway under MDR - Qserve Group. https://www.qservegroup.com/eu/en/i822/how-to-use-the-equivalence-pathway-under-mdr, (2020).
142. M. Baldwin, S. Snelling, S. Dakin, A. Carr, Augmenting endogenous repair of soft tissues with nanofibre scaffolds. *Journal of the Royal Society, Interface* **15**, 20180019 (2018).
143. F. J. O'Brien, Biomaterials & scaffolds for tissue engineering scaffolds for tissue engineering. *Materials Today* **14**, 88-95 (2011).
144. Y. Tyan, M. Yang, C. Chang, T. Chung, Biocompatibility of Materials for Biomedical Engineering. *Advances in experimental medicine and biology* **1250**, (2020).
145. B. Yue, Biology of the extracellular matrix: an overview. *Journal of glaucoma* **23**, (2014).
146. B. Smith, D. Grande, The current state of scaffolds for musculoskeletal regenerative applications. *Nature reviews. Rheumatology* **11**, (2015).
147. F. O'Brien, B. O'Connell, *Chapter IV: Biomaterials and Tissue Engineering*. T. Lee, P. Niederer, Eds., Basic Engineering for Medics and Biologists (2010), vol. 152.
148. M. S. Rashid *et al.*, Rotator cuff repair with biological graft augmentation causes adverse tissue outcomes. *Acta Orthopaedica* **91**, 782-788 (2020).
149. P. A. Mouthuy *et al.*, Biocompatibility of implantable materials: An oxidative stress viewpoint. *Biomaterials* **109**, 55-68 (2016).
150. R. Abhari, J. Martins, H. Morris, P. Mouthuy, A. Carr, Synthetic sutures: Clinical evaluation and future developments. *Journal of Biomaterials Applications* **32**, 410-421 (2017).
151. J. K. F. Wong, S. Alyouha, K. E. Kadler, M. W. J. Ferguson, D. A. McGrouther, The cell biology of suturing tendons. *Matrix Biology* **29**, 525-536 (2010).
152. R. Bell *et al.*, Inhibition of apoptosis exacerbates fatigue-damage tendon injuries in an in vivo rat model. *European cells & materials* **36**, (2018).
153. R. Hynes, Integrins: bidirectional, allosteric signaling machines. *Cell* **110**, (2002).
154. B. Shen, M. K. Delaney, X. Du, Inside-out, outside-in, and inside-outside-in: G protein signaling in integrin-mediated cell adhesion, spreading, and retraction. *Current opinion in cell biology* **24**, 600-606 (2012).
155. C. Jean, P. Gravelle, J. Fournie, G. Laurent, Influence of stress on extracellular matrix and integrin biology. *Oncogene* **30**, (2011).
156. M. Partridge, E. Marcantonio, Initiation of attachment and generation of mature focal adhesions by integrin-containing filopodia in cell spreading. *Molecular biology of the cell* **17**, (2006).
157. B. Geiger, A. Bershadsky, R. Pankov, K. Yamada, Transmembrane crosstalk between the extracellular matrix--cytoskeleton crosstalk. *Nature reviews. Molecular cell biology* **2**, (2001).
158. G. Lock, B. Wehrle-Haller, S. Stromblad, Cell–matrix adhesion complexes: Master control machinery of cell migration. *Seminars in Cancer Biology* **18**, 65-76 (2008).
159. R. Pankov, K. Yamada, Fibronectin at a glance. *Journal of cell science* **115**, (2002).
160. H. Bachman, J. Nicosia, M. Dysart, T. Barker, Utilizing Fibronectin Integrin-Binding Specificity to Control Cellular Responses. *Advances in wound care* **4**, (2015).

161. A. K. Gaharwar, I. Singh, A. Khademhosseini, Engineered biomaterials for in situ tissue regeneration. *Nature Reviews Materials* **5**, 686-705 (2020).
162. M.-D. Mechanobiology, What are cell-matrix adhesions? https://www.mechanobio.info/what-is-mechanosignaling/what-is-the-extracellular-matrix-and-the-basal-lamina/, (2018).
163. A. Nair, L. Tang, Influence of scaffold design on host immune and stem cell responses | Elsevier Enhanced Reader. *Seminars in Immunology* **29**, 62-71 (2017).
164. L. Tang, J. W. Eaton, Natural Responses to Unnatural Materials: A Molecular Mechanism for Foreign Body Reactions. *Molecular Medicine* **5**, 351-358 (1999).
165. G. Zhou, T. Groth, Host Responses to Biomaterials and Anti-Inflammatory Design—a Brief Review. *Macromolecular Bioscience* **18**, 1800112 (2018).
166. Y. Mao, J. Schwarzbauer, Stimulatory effects of a three-dimensional microenvironment on cell-mediated fibronectin fibrillogenesis. *Journal of cell science* **118**, (2005).
167. M. Larsen, V. Artym, J. Green, K. Yamada, The matrix reorganized: extracellular matrix remodeling and integrin signaling. *Current opinion in cell biology* **18**, (2006).
168. N. H. G. R. I. (NIH), Deoxyribonucleic Acid (DNA) Fact Sheet. https://www.genome.gov/about-genomics/fact-sheets/Deoxyribonucleic-Acid-Fact-Sheet, (2020).
169. A. Casamassimi, A. Ciccodicola, Transcriptional Regulation: Molecules, Involved Mechanisms, and Misregulation. *International journal of molecular sciences* **20**, 1281 (2019).
170. R. J. Mackenzie, RNA-Seq: Basics, Applications and Protocol. *Technology Networks - Genomis Research*, (2022).
171. T. Fee, S. Surianarayanan, D. Crawford, Y. Zhou, J. Berry, Nanofiber Alignment Regulates NIH3T3 Cell Orientation and Cytoskeletal Gene Expression on Electrospun PCL+Gelatin Nanofibers | PLOS ONE. *PLoS One* **11**, (2016).
172. M. Baldwin *et al.*, Electrospun Scaffold Micro-Architecture Induces an Activated Transcriptional Phenotype within Tendon Fibroblasts. *Frontiers in bioengineering and biotechnology* **9**, (2022).
173. A. Nezhentsev *et al.*, In vitro evaluation of the response of human tendon-derived stromal cells to a novel electrospun suture for tendon repair. *TRANSLATIONAL SPORTS MEDICINE* **4**, 409-418 (2021).
174. H. Chen *et al.*, Dissecting the microenvironment around biosynthetic scaffolds in murine skin wound healing. *Science Advances* **7**, (2021).
175. J. Shi *et al.*, Regulation of the inflammatory response by vascular grafts modified with Aspirin-Triggered Resolvin D1 promotes blood vessel regeneration. *Acta Biomaterialia* **97**, (2019).
176. V. Chernonosova, P. Laktionov, I. Murashov, A. Karpenko, P. Laktionov, Comparative gene expression profiling of human primary endotheliocytes cultivated on polyurethane-based electrospun 3D matrices and natural decellularized vein. *Biomedical materials* **15**, (2020).
177. M. Phelan *et al.*, Soy Protein Nanofiber Scaffolds for Uniform Maturation of Human Induced Pluripotent Stem Cell-Derived Retinal Pigment Epithelium. *Tissue engineering. Part C, Methods* **26**, (2020).
178. R. D. J. Smith *et al.*, Characterizing the macro and micro mechanical properties of scaffolds for rotator cuff repair. *J Shoulder Elbow Surg*, (2017).
179. M. Street *et al.*, Augmentation with an ovine forestomach matrix scaffold improves histological outcomes of rotator cuff repair in a rat model. *J Orthop Surg Res* **10**, 165 (2015).
180. M. Zhu *et al.*, Overlay repair with a synthetic collagen scaffold improves the quality of healing in a rat rotator cuff repair model. *J Shoulder Elbow Surg*, (2019).
181. D. Bryant *et al.*, A randomized clinical trial to compare the effectiveness of rotator cuff repair with or without augmentation using porcine small intestine submucosa for patients with moderate to large rotator cuff tears: a pilot study. *J Shoulder Elbow Surg* **25**, 1623-1633 (2016).

182. A. Sensini, G. Massafra, C. Gotti, A. Zucchelli, L. Cristofolini, Tissue Engineering for the Insertions of Tendons and Ligaments: An Overview of Electrospun Biomaterials and Structures. *Frontiers Bioengineering and Biotechnology* **9**, (2021).
183. J. P. Spalazzi *et al.*, In vivo evaluation of a multiphased scaffold designed for orthopaedic interface tissue engineering and soft tissue-to-bone integration. *J Biomed Mater Res A* **86**, 1--12 (2008).
184. S. Font Tellado *et al.*, Fabrication and Characterization of Biphasic Silk Fibroin Scaffolds for Tendon/Ligament-to-Bone Tissue Engineering. *Tissue Eng Part A* **23**, 859--872 (2017).
185. T. K. H. Teh, S.-L. Toh, J. C. H. Goh, Aligned Hybrid Silk Scaffold for Enhanced Differentiation of Mesenchymal Stem Cells into Ligament Fibroblasts. *Tissue Engineering Part C: Methods* **17**, 687-703 (2011).
186. G. Criscenti *et al.*, Triphasic scaffolds for the regeneration of the bone-ligament interface. *Biofabrication* **8**, 015009 (2016).
187. D. Sooriyaarachchi, H. J. Minière, S. Maharubin, G. Z. Tan, Hybrid Additive Microfabrication Scaffold Incorporated with Highly Aligned Nanofibers for Musculoskeletal Tissues. *Tissue engineering and regenerative medicine* **16**, 29-38 (2018).
188. J. A. Smith, E. Mele, Electrospinning and Additive Manufacturing: Adding Three-Dimensionality to Electrospun Scaffolds for Tissue Engineering. *Frontiers in bioengineering and biotechnology* **9**, 674738-674738 (2021).
189. Y. Yu *et al.*, Fabrication and characterization of electrospinning/3D printing bone tissue engineering scaffold. *RSC Advances* **6**, 110557-110565 (2016).
190. I. Calejo, R. Costa-Almeida, R. L. Reis, M. E. Gomes, Enthesis Tissue Engineering: Biological Requirements Meet at the Interface. *Tissue Eng Part B Rev* **25**, 330--356 (2019).
191. M. W. Hast, A. Zuskov, L. J. Soslowsky, The role of animal models in tendon research. *Bone Joint Res* **3**, 193-202 (2014).
192. G. Oreff, M. Fenu, C. Vogl, I. Ribitsch, F. Jenner, Species variations in tenocytes' response to inflammation require careful selection of animal models for tendon research. *Scientific Reports* **11**, (2021).
193. S. Rodeo, Translational Animal Models in Orthopaedic Research. *The American Journal of Sports Medicine* **45**, (2017).
194. C. Hull, US4575330A - Apparatus for production of three-dimensional objects by stereolithography. *United States Patent*, (1986).
195. E. Sachs, M. Cima, C. J, Three-Dimensional Printing: Rapid Tooling and Prototypes Directly from a CAD Model. *CIRP Annals* **39**, 201-204 (1990).
196. M. Gomes *et al.* (Elsevier Inc, 2013), pp. 385-425.
197. P. Gunatillake, R. Adhikari, BIODEGRADABLE SYNTHETIC POLYMERS FOR TISSUE ENGINEERING. *European Cells and Materials* **5**, 1-16 (2003).
198. J. J. Chung, H. Im, S. H. Kim, J. W. Park, Y. Jung, Toward Biomimetic Scaffolds for Tissue Engineering: 3D Printing Techniques in Regenerative Medicine. *Frontiers in bioengineering and biotechnology* **8**, 586406-586406 (2020).
199. J. Stansbury, M. Idacavage, 3D printing with polymers: Challenges among expanding options and opportunities. *Dental materials : official publication of the Academy of Dental Materials* **32**, (2016).
200. C. Mandrycky, Z. Wang, K. Kim, D. Kim, 3D bioprinting for engineering complex tissues. *Biotechnology advances* **34**, (2016).
201. T. Potyondy *et al.*, Recent advances in 3D bioprinting of musculoskeletal tissues. *Biofabrication* **13**, (2021).
202. N. Sears, P. Dhavalikar, M. Whitely, E. Cosgriff-Hernandez, Fabrication of biomimetic bone grafts with multi-material 3D printing - IOPscience. *Biofabrication* **9**, (2017).
203. Z. Jiang *et al.*, Extrusion 3D Printing of Polymeric Materials with Advanced Properties. *Advanced Science* **7**, 2001379 (2020).
204. M. Labet, W. Thielemans, Synthesis of polycaprolactone: a review. *Chemical Society Reviews* **38**, 3484-3504 (2009).
205. R. Dwivedi *et al.*, Polycaprolactone as biomaterial for bone scaffolds: Review of literature. *J Oral Biol Craniofac Res* **10**, 381-388 (2020).

206. M. Bartnikowski, T. R. Dargaville, S. Ivanovski, D. W. Hutmacher, Degradation mechanisms of polycaprolactone in the context of chemistry, geometry and environment. *Progress in Polymer Science* **96**, 1-20 (2019).
207. Y. Ikada, H. Tsuji, Biodegradable polyesters for medical and ecological applications. *Macromolecular Rapid Communications*, (2000).
208. E. Archer, M. Torretti, S. Madbouly, Biodegradable polycaprolactone (PCL) based polymer and composites. *Physical Sciences Reviews*, (2021).
209. M. Woodruff, D. Hutmacher, The return of a forgotten polymer— Polycaprolactone in the 21st century. *Progress in Polymer Science* **35**, 1217-1256 (2010).
210. A. Göpferich, Erosion of composite polymer matrices. *Biomaterials* **18**, 397-403 (1997).
211. L. A. Bosworth, S. Downes, Physicochemical characterisation of degrading polycaprolactone scaffolds. *Polymer Degradation and Stability* **95**, 2269-2276 (2010).
212. V. Sukanya, P. Mohanan, Degradation of Poly(ε-caprolactone) and bio-interactions with mouse bone marrow mesenchymal stem cells. *Colloids and surfaces. B, Biointerfaces* **163**, (2018).
213. S. Gerdes *et al.*, Process–Structure–Quality Relationships of Three-Dimensional Printed Poly(Caprolactone)-Hydroxyapatite Scaffolds. *Tissue Engineering Part A*. **26**, 279-291 (2020).
214. M. Bohner, B. L. G. Santoni, N. Döbelin, β-tricalcium phosphate for bone substitution: Synthesis and properties. *Acta Biomaterialia* **113**, 23-41 (2020).
215. E. Nyberg, A. Rindone, A. Dorafshar, W. L. Grayson, Comparison of 3D-Printed Poly-ε-Caprolactone Scaffolds Functionalized with Tricalcium Phosphate, Hydroxyapatite, Bio-Oss, or Decellularized Bone Matrix<sup/>. *Tissue Eng Part A* **23**, 503--514 (2017).
216. H. Park, J. Choi, W. Jeong, Clinical Application of Three-Dimensional Printing of Polycaprolactone/Beta-Tricalcium Phosphate Implants for Cranial Reconstruction. *The Journal of craniofacial surgery*, (2022).
217. H. Lee *et al.*, Designed hybrid scaffolds consisting of polycaprolactone microstrands and electrospun collagen-nanofibers for bone tissue regeneration. *Journal of Biomedical Materials Research Part B: Applied Biomaterials* **97B**, 263-270 (2011).
218. A. Zimmerling, Z. Yazdanpanah, D. M. L. Cooper, J. D. Johnston, X. Chen, 3D printing PCL/nHA bone scaffolds: exploring the influence of material synthesis techniques. *Biomaterials Research* **25**, 1-12 (2021).
219. E. S, D. S, Mechanical and microstructural properties of polycaprolactone scaffolds with one-dimensional, two-dimensional, and three-dimensional orthogonally oriented porous architectures produced by selective laser sintering. *Acta biomaterialia* **6**, (2010).
220. J. Más Estellés, A. Vidaurre, J. M. Meseguer Dueñas, I. Castilla Cortázar, Physical characterization of polycaprolactone scaffolds. *Journal of Materials Science: Materials in Medicine* **19**, 189-195 (2007).
221. J. H. Shim *et al.*, Porosity effect of 3D-printed polycaprolactone membranes on calvarial defect model for guided bone regeneration. *Biomed Mater* **13**, 015014 (2017).
222. A. Olubamiji *et al.*, Modulating mechanical behaviour of 3D-printed cartilage-mimetic PCL scaffolds: influence of molecular weight and pore geometry. *Biofabrication* **8**, (2016).
223. A. Rai, S. Senapati, S. K. Saraf, P. Maiti, Biodegradable poly(ε-caprolactone) as a controlled drug delivery vehicle of vancomycin for the treatment of MRSA infection. *Journal of Materials Chemistry B* **4**, 5151-5160 (2016).
224. J. Kim *et al.*, Biocompatibility and Pharmacokinetic Analysis of an Intracameral Polycaprolactone Drug Delivery Implant for Glaucoma. *Investigative ophthalmology & visual science* **57**, (2016).
225. B. Zhu *et al.*, A biodegradable long-term contraceptive implant with steady levonorgestrel release based on PLGA microspheres embedded in PCL-coated implant. *Journal of Drug Delivery Science and Technology* **67**, 102955 (2022).
226. K. Nanda, R. Callahan, L. Dorflinger, Addressing gaps in the contraceptive method mix: methods in development. *Women's health (London, England)* **11**, (2015).
227. Osteopore, www.osteopore.com/technology.

228. S.-H. Teoh, B.-T. Goh, J. Lim, Three-Dimensional Printed Polycaprolactone Scaffolds for Bone Regeneration Success and Future Perspective. *Tissue Engineering Part A* **25**, 931-935 (2019).
229. S. Lee, D. Choi, J.-H. Shim, W. Nam, Efficacy of three-dimensionally printed polycaprolactone/beta tricalcium phosphate scaffold on mandibular reconstruction. *Scientific Reports* **10**, 1-9 (2020).
230. W. Jeong *et al.*, Clinical Application of 3D-Printed Patient-Specific Polycaprolactone/Beta Tricalcium Phosphate Scaffold for Complex Zygomatico-Maxillary Defects. *Polymers* **14**, (2022).
231. Y. Park, J. Cha, S. Bang, S. Kim, Clinical Application of Three-Dimensionally Printed Biomaterial Polycaprolactone (PCL) in Augmentation Rhinoplasty. *Aesthetic plastic surgery* **43**, (2019).
232. M.-O. Christen, F. Vercesi, Polycaprolactone: How a Well-Known and Futuristic Polymer Has Become an Innovative Collagen-Stimulator in Esthetics. *Clin Cosmet Investig Dermatol* **13**, 31-48 (2020).
233. M. E. Cheng *et al.*, Pectus excavatum camouflage: a new technique using a tissue engineered scaffold. *European Journal of Plastic Surgery* **45**, 177-182 (2021).
234. G. Castrisos *et al.*, Regenerative matching axial vascularisation of absorbable 3D-printed scaffold for large bone defects: A first in human series. *Journal of plastic, reconstructive & aesthetic surgery*, (2022).
235. R. J. Morrison *et al.*, Mitigation of tracheobronchomalacia with 3D-printed personalized medical devices in pediatric patients. *Science translational medicine* **7**, 285ra264-285ra264 (2015).
236. E. D. Boland *et al.*, Electrospinning polydioxanone for biomedical applications. *Acta Biomaterialia* **1**, 115-123 (2005).
237. J. A. Ray, N. Doddi, D. Regula, J. A. Williams, A. Melveger, Polydioxanone (PDS), a novel monofilament synthetic absorbable suture. *Surgery, gynecology & obstetrics* **153**, 497-507 (1981).
238. N. Goonoo, R. Jeetah, A. Bhaw-Luximon, D. Jhurry, Polydioxanone-based bio-materials for tissue engineering and drug/gene delivery applications. *Eur J Pharm Biopharm* **97**, 371-391 (2015).
239. H. L. Lin, C. C. Chu, D. Grubb, Hydrolytic degradation and morphologic study of poly-p-dioxanone. *Journal of Biomedical Materials Research* **27**, 153-166 (1993).
240. W. Abbott, J. Megerman, J. Hasson, G. L'Italien, D. Warnock, Effect of compliance mismatch on vascular graft patency. *Journal of Vascular Surgery* **5**, 376-382 (1987).
241. C. Ping Ooi, R. E. Cameron, The hydrolytic degradation of polydioxanone (PDSII) sutures. Part I: Morphological aspects. *Journal of Biomedical Materials Research* **63**, 280-290 (2002).
242. H. Ramakrishna *et al.*, Tissue engineering a tendon-bone junction with biodegradable braided scaffolds. *Biomaterials Research* **23**, 11 (2019).
243. Y. Jiao *et al.*, Construction and application of textile-based tissue engineering scaffolds: a review. *Biomaterials Science* **8**, 3574-3600 (2020).
244. N. Tucker, H. Razzaq, K. Hofman, J. J. Stanger, M. P. Staiger, The History of the Science and Technology of Electrospinning from 1600 to 1995. *Journal of Engineered Fibers and Fabrics* **7**, 63-73 (2012).
245. A. Formhals, US2349950A - Method and apparatus for spinning. *Google Patents*, (1944).
246. Y.-Z. Long, X. Yan, X.-X. Wang, J. Zhang, M. Yu, in *Electrospinning: Nanofabrication and Applications,* B. Ding, X. Wang, J. Yu, Eds. (William Andrew Publishing, 2019), pp. 21-52.
247. A. Tamayol *et al.*, Fiber-based tissue engineering: Progress, challenges, and opportunities. *Biotechnology advances* **31**, (2013).
248. S. Ramakrishna *et al.*, Electrospun nanofibers: solving global issues. *Materials Today* **9**, 40-50 (2006).
249. H. Zhong, J. Huang, J. Wu, J. Du, Electrospinning nanofibers to 1D, 2D, and 3D scaffolds and their biomedical applications. *Nano Research* **15**, 787-804 (2021).
250. T. S. Sampath Kumar, V. Yogeshwar Chakrapani, Electrospun 3D Scaffolds for Tissue Regeneration. *Adv Exp Med Biol* **1078**, 29-47 (2018).

251. T. L. Jenkins, D. Little, Synthetic scaffolds for musculoskeletal tissue engineering: cellular responses to fiber parameters. *npj Regenerative Medicine* **4**, 1-14 (2019).
252. A. P. Kishan, E. M. Cosgriff-Hernandez, Recent advancements in electrospinning design for tissue engineering applications: A review. *Journal of Biomedical Materials Research Part A* **105**, 2892-2905 (2017).
253. C.-H. Shen, in *Diagnostic Molecular Biology,* C.-H. Shen, Ed. (Academic Press, 2019), pp. 87-116.
254. C. Lee *et al.*, Nanofiber alignment and direction of mechanical strain affect the ECM production of human ACL fibroblast. *Biomaterials* **26**, (2005).
255. S. Orr *et al.*, Aligned multilayered electrospun scaffolds for rotator cuff tendon tissue engineering. *Acta biomaterialia* **24**, 117-126 (2015).
256. J. Choi, S. Lee, G. Christ, A. Atala, J. Yoo, The influence of electrospun aligned poly(epsilon-caprolactone)/collagen nanofiber meshes on the formation of self-aligned skeletal muscle myotubes. *Biomaterials* **29**, (2008).
257. Z. Yin *et al.*, The regulation of tendon stem cell differentiation by the alignment of nanofibers. *Biomaterials* **31**, (2010).
258. S. Subramony *et al.*, The guidance of stem cell differentiation by substrate alignment and mechanical stimulation. *Biomaterials* **34**, (2013).
259. O. Hakimi *et al.*, A layered electrospun and woven surgical scaffold to enhance endogenous tendon repair. *Acta Biomater* **26**, 124-135 (2015).
260. A. Kendal *et al.*, Resorbable electrospun polydioxanone fibres modify the behaviour of cells from both healthy and diseased human tendons. *European cells & materials* **33**, (2017).
261. M. Rashid *et al.*, Histopathological and immunohistochemical evaluation of cellular response to a woven and electrospun polydioxanone (PDO) and polycaprolactone (PCL) patch for tendon repair. *Scientific reports* **10**, (2020).
262. B. B. Rothrauff *et al.*, The Rotator Cuff Organ: Integrating Developmental Biology, Tissue Engineering, and Surgical Considerations to Treat Chronic Massive Rotator Cuff Tears. *Tissue Eng Part B Rev* **23**, 318-335 (2017).
263. S. D. McCullen, C. M. Haslauer, E. G. Loboa, Fiber-reinforced scaffolds for tissue engineering and regenerative medicine: use of traditional textile substrates to nanofibrous arrays. *Journal of Materials Chemistry* **20**, 8776-8788 (2010).
264. B. B. Rothrauff *et al.*, Braided and Stacked Electrospun Nanofibrous Scaffolds for Tendon and Ligament Tissue Engineering. *Tissue Eng Part A* **23**, 378-389 (2017).
265. J. G. Barber, A. M. Handorf, T. J. Allee, W.-J. Li, Braided Nanofibrous Scaffold for Tendon and Ligament Tissue Engineering. *Tissue Engineering Part A* **19**, 1265-1274 (2011).
266. J. Freeman, M. Woods, C. Laurencin, Tissue engineering of the anterior cruciate ligament using a braid-twist scaffold design. *Journal of biomechanics* **40**, (2007).
267. S. Czaplewski, T. Tsai, S. Duenwald-Kuehl, R. Vanderby, W. Li, Tenogenic differentiation of human induced pluripotent stem cell-derived mesenchymal stem cells dictated by properties of braided submicron fibrous scaffolds. *Biomaterials* **35**, (2014).
268. I. Calejo, R. Costa-Almeida, R. L. Reis, M. E. Gomes, A Textile Platform Using Continuous Aligned and Textured Composite Microfibers to Engineer Tendon-to-Bone Interface Gradient Scaffolds. *Adv Healthc Mater* **8**, e1900200 (2019).
269. R. E. Abhari *et al.*, Using an industrial braiding machine to upscale the production and modulate the design of electrospun medical yarns. *Polymer Testing* **69**, 188-198 (2018).
270. P.-A. Mouthuy, N. Zargar, O. Hakimi, E. Lostis, A. Carr, Fabrication of continuous electrospun filaments with potential for use as medical fibres. *Biofabrication* **7**, 025006 (2015).
271. K. Yamaguchi *et al.*, The demographic and morphological features of rotator cuff disease. A comparison of asymptomatic and symptomatic shoulders. *J Bone Joint Surg Am* **88**, 1699--1704 (2006).
272. V. N. Gibbs, P. Raval, J. L. Rees, S. E. Gwilym, Rotator cuff tears: repair and reconstruction. *Orthopaedics and Trauma* **32**, 165-170 (2018).
273. L. S. Oh, B. R. Wolf, M. P. Hall, B. A. Levy, R. G. Marx, Indications for Rotator Cuff Repair: A Systematic Review. *Clinical Orthopaedics and Related Research®* **455**, (2007).

274. J. Apostolakos *et al.*, The enthesis: a review of the tendon-to-bone insertion. *Muscles Ligaments Tendons J* **4**, 333--342 (2014).
275. F. A. Barber, M. A. Herbert, R. C. Beavis, F. Barrera Oro, Suture anchor materials, eyelets, and designs: update 2008. *Arthroscopy* **24**, 859--867 (2008).
276. F. A. Barber, W. D. Dockery, C. H. Cowden, 3rd, The degradation outcome of biocomposite suture anchors made from poly L-lactide-co-glycolide and β-tricalcium phosphate. *Arthroscopy* **29**, 1834--1839 (2013).
277. A. J. Boys, M. C. McCorry, S. Rodeo, L. J. Bonassar, L. A. Estroff, Next Generation Tissue Engineering of Orthopedic Soft Tissue-to-Bone Interfaces. *MRS Commun* **7**, 289--308 (2017).
278. R. C. Locke, A. C. Abraham, M. L. Killian, Orthopedic Interface Repair Strategies Based on Native Structural and Mechanical Features of the Multiscale Enthesis. *ACS Biomater Sci Eng* **3**, 2633--2643 (2017).
279. R. E. Abhari, A. J. Carr, P.-A. Mouthuy, in *Electrofluidodynamic Technologies (EFDTs) for Biomaterials and Medical Devices,* V. Guarino, L. Ambrosio, Eds. (Woodhead Publishing, 2018), pp. 295-328.
280. N. Narayanan, L. Kuang, M. Del Ponte, C. Chain, M. Deng, in *Nanocomposites for Musculoskeletal Tissue Regeneration,* H. Liu, Ed. (Woodhead Publishing, Oxford, 2016), pp. 3-29.
281. S.-J. Lee, M. Nowicki, B. Harris, L. G. Zhang, Fabrication of a Highly Aligned Neural Scaffold via a Table Top Stereolithography 3D Printing and Electrospinning. *Tissue Engineering Part A* **23**, 491-502 (2017).
282. B. Huang *et al.*, Engineered dual-scale poly (ε-caprolactone) scaffolds using 3D printing and rotational electrospinning for bone tissue regeneration. *Additive Manufacturing* **36**, 101452 (2020).
283. M. Rampichová *et al.*, Composite 3D printed scaffold with structured electrospun nanofibers promotes chondrocyte adhesion and infiltration. *Cell Adhesion & Migration* **12**, 271-285 (2018).
284. N. W. Pensa *et al.*, 3D printed mesh reinforcements enhance the mechanical properties of electrospun scaffolds. *Biomaterials Research* **23**, 22 (2019).
285. C. Vyas *et al.*, Three-Dimensional Printing and Electrospinning Dual-Scale Polycaprolactone Scaffolds with Low-Density and Oriented Fibers to Promote Cell Alignment. *3D Printing and Additive Manufacturing* **7**, 105-113 (2020).
286. B. Huang *et al.*, Polymer-Ceramic Composite Scaffolds: The Effect of Hydroxyapatite and β-tri-Calcium Phosphate. *Materials (Basel)* **11**, (2018).
287. E. Itoi *et al.*, Tensile properties of the supraspinatus tendon. *J Orthop Res* **13**, 578-584 (1995).
288. E. Itoi, H. C. Hsu, S. W. Carmichael, B. F. Morrey, K. N. An, Morphology of the torn rotator cuff. *J Anat* **186 (Pt 2)**, 429-434 (1995).
289. T. Matsuhashi *et al.*, Tensile properties of a morphologically split supraspinatus tendon. *Clin Anat* **27**, 702-706 (2014).
290. M. Rickert, H. Georgousis, U. Witzel, The native tensile strength of the supraspinatus tendon. A biomechanical study. *Der Unfallchirurg* **101**, 265--270 (1998).
291. T. U. Rashid, R. E. Gorga, W. E. Krause, Mechanical Properties of Electrospun Fibers—A Critical Review. *Advanced Engineering Materials* **23**, 2100153 (2021).
292. A. A. Lach *et al.*, Pyridine as an additive to improve the deposition of continuous electrospun filaments. *PLoS One* **14**, e0214419--e0214419 (2019).
293. L. Savić *et al.*, Early development of a polycaprolactone electrospun augment for anterior cruciate ligament reconstruction. *Materials Science and Engineering: C* **129**, 112414 (2021).
294. H. Maleki, H. Barani, Morphological and mechanical properties of drawn poly(l-lactide) electrospun twisted yarns. *Polymer Engineering & Science* **58**, 1091-1096 (2018).
295. R. E. Abhari, P.-A. Mouthuy, N. Zargar, C. Brown, A. Carr, Effect of annealing on the mechanical properties and the degradation of electrospun polydioxanone filaments. *Journal of the Mechanical Behavior of Biomedical Materials* **67**, 127-134 (2017).
296. S. Tan, A. Su, W. Li, E. Zhou, New insight into melting and crystallization behavior in semicrystalline poly(ethylene terephthalate). *Journal of Polymer Science Part B: Polymer Physics* **38**, 53-60 (2000).

297. E. Lizundia, S. Petisco, J.-R. Sarasua, Phase-structure and mechanical properties of isothermally melt-and cold-crystallized poly (L-lactide). **17**, 242-251 (2013).
298. K. Ishikiriyama *et al.*, Heat capacity of poly-p-dioxanone. *Journal of Macromolecular Science, Part B* **37**, 27-44 (1998).
299. R. D. Smith *et al.*, The response of tenocytes to commercial scaffolds used for rotator cuff repair. *Eur Cell Mater* **31**, 107--118 (2016).
300. I. O. f. Standardization, in *Part 5: Tests for in Vitro Cytotoxicity*. (2009).
301. K. Balani, *Biosurfaces : a materials science and engineering perspective*. (ACerS--Wiley, Hoboken, New Jersey, 2014).
302. W. Zhang *et al.*, Fabrication and characterization of porous polycaprolactone scaffold via extrusion-based cryogenic 3D printing for tissue engineering. *Materials & Design* **180**, 107946 (2019).
303. D. J. Burlett, in *Handbook of Thermal Analysis and Calorimetry,* M. E. Brown, P. K. Gallagher, Eds. (Elsevier Science B.V., 2008), vol. 5, pp. 695-732.
304. M. Bonnet, K. D. Rogausch, J. Petermann, The endothermic "annealing peak" of poly(phenylene sulphide) and poly(ethylene terephthalate). *Colloid and Polymer Science* **277**, 513-518 (1999).
305. T. Mukhametzyanov *et al.*, Crystal Nucleation and Growth in Cross-Linked Poly(ε-caprolactone) (PCL). *Polymers* **13**, (2021).
306. M. A. Sabino, J. L. Feijoo, A. J. Müller, Crystallisation and morphology of poly(p-dioxanone). *Macromolecular Chemistry and Physics* **201**, 2687-2698 (2000).
307. H. K. Selle, B. Bar-On, G. Marom, H. D. Wagner, Gelatin yarns inspired by tendons--structural and mechanical perspectives. *Mater Sci Eng C Mater Biol Appl* **47**, 1-7 (2015).
308. N. Pan, D. Brookstein, Physical properties of twisted structures. II. Industrial yarns, cords, and ropes. *Journal of Applied Polymer Science* **83**, 610-630 (2002).
309. D. U. Shah, P. J. Schubel, M. J. Clifford, Modelling the effect of yarn twist on the tensile strength of unidirectional plant fibre yarn composites. *Journal of Composite Materials* **47**, 425-436 (2012).
310. A. A. Conte, K. Sun, X. Hu, V. Z. Beachley, Effects of Fiber Density and Strain Rate on the Mechanical Properties of Electrospun Polycaprolactone Nanofiber Mats. *Front Chem* **8**, 610-610 (2020).
311. J. A. Martins, A. A. Lach, H. L. Morris, A. J. Carr, P.-A. Mouthuy, Polydioxanone implants: A systematic review on safety and performance in patients. *Journal of Biomaterials Applications* **34**, 902-916 (2019).
312. O. S. Manoukian *et al.*, Biodegradable Polymeric Injectable Implants for Long-Term Delivery of Contraceptive Drugs. *Journal of applied polymer science* **135**, 46068 (2018).
313. L. Liverani, A. R. Boccaccini, Versatile Production of Poly(Epsilon-Caprolactone) Fibers by Electrospinning Using Benign Solvents. *Nanomaterials (Basel)* **6**, 75 (2016).
314. A. Salerno, D. Guarnieri, M. Iannone, S. Zeppetelli, P. A. Netti, Effect of micro- and macroporosity of bone tissue three-dimensional-poly(epsilon-caprolactone) scaffold on human mesenchymal stem cells invasion, proliferation, and differentiation in vitro. *Tissue Eng Part A* **16**, 2661--2673 (2010).
315. J. Xue, T. Wu, Y. Dai, Y. Xia, Electrospinning and Electrospun Nanofibers: Methods, Materials, and Applications. *Chem. Rev.* **119**, 5298-5415 (2019).
316. F. Qu, F. Guilak, R. L. Mauck, Cell migration: implications for repair and regeneration in joint disease. *Nature reviews. Rheumatology* **15**, 167-179 (2019).
317. M. Rashid *et al.*, Histological evaluation of cellular response to a multifilament electrospun suture for tendon repair. *PLOS ONE* **15**, e0234982 (2020).
318. S. R. Caliari *et al.*, Collagen Scaffolds Incorporating Coincident Gradations of Instructive Structural and Biochemical Cues for Osteotendinous Junction Engineering. *Adv Healthc Mater* **4**, 831--837 (2015).
319. S. Samavedi, P. Vaidya, P. Gaddam, A. R. Whittington, A. S. Goldstein, Electrospun meshes possessing region-wise differences in fiber orientation, diameter, chemistry and mechanical properties for engineering bone-ligament-bone tissues. *Biotechnol Bioeng* **111**, 2549--2559 (2014).

320. J. Xie *et al.*, "Aligned-to-random" nanofiber scaffolds for mimicking the structure of the tendon-to-bone insertion site. *Nanoscale* **2**, 923--926 (2010).
321. M. Ramalingam *et al.*, Nanofiber scaffold gradients for interfacial tissue engineering. *J Biomater Appl* **27**, 695--705 (2013).
322. C. Erisken, D. M. Kalyon, H. Wang, Functionally graded electrospun polycaprolactone and β-tricalcium phosphate nanocomposites for tissue engineering applications. *Biomaterials* **29**, 4065-4073 (2008).
323. X. Li *et al.*, Nanofiber Scaffolds with Gradations in Mineral Content for Mimicking the Tendon-to-Bone Insertion Site. *Nano Letters* **9**, 2763--2768 (2009).
324. Y. Cao *et al.*, Three-dimensional printed multiphasic scaffolds with stratified cell-laden gelatin methacrylate hydrogels for biomimetic tendon-to-bone interface engineering. *J Orthop Translat* **23**, 89-100 (2020).
325. C. R. Correia, R. L. Reis, J. F. Mano, Multiphasic, Multistructured and Hierarchical Strategies for Cartilage Regeneration. *Adv Exp Med Biol* **881**, 143-160 (2015).
326. A. Islam *et al.*, Biomechanical evaluation of a novel suturing scheme for grafting load-bearing collagen scaffolds for rotator cuff repair. *Clin Biomech (Bristol, Avon)* **30**, 669-675 (2015).
327. C. M. Jobe, J. P. Lannotti, Limits imposed on glenohumeral motion by joint geometry. *Journal of Shoulder and Elbow Surgery* **4**, 281-285 (1995).
328. L. F. Mellor *et al.*, Fabrication and Evaluation of Electrospun, 3D-Bioplotted, and Combination of Electrospun/3D-Bioplotted Scaffolds for Tissue Engineering Applications. *BioMed Research International* **2017**, 6956794 (2017).
329. B. M. Berghs, T. Derveaux, W. Speeckaert, K. Vanslambrouck, L. F. Wilde, Three-dimensional analysis of the orientation and the inclination of the rotator cuff footprint. *Journal of Shoulder and Elbow Surgery* **20**, 637-645 (2011).
330. A. D. Mazzocca, P. J. Millett, C. A. Guanche, S. A. Santangelo, R. A. Arciero, Arthroscopic single-row versus double-row suture anchor rotator cuff repair. *Am J Sports Med* **33**, 1861--1868 (2005).
331. C. Gerber, B. Fuchs, J. Hodler, The results of repair of massive tears of the rotator cuff. *J Bone Joint Surg Am* **82**, 505--515 (2000).
332. W. Z. Burkhead, Jr., J. G. Skedros, P. J. O'Rourke, W. A. Pierce, T. C. Pitts, A novel double-row rotator cuff repair exceeds strengths of conventional repairs. *Clin Orthop Relat Res* **461**, 106-113 (2007).
333. A. Inoue, E. Chosa, K. Goto, N. Tajima, Nonlinear stress analysis of the supraspinatus tendon using three-dimensional finite element analysis. *Knee Surg Sports Traumatol Arthrosc* **21**, 1151-1157 (2013).
334. C. Y. Huang *et al.*, Inhomogeneous mechanical behavior of the human supraspinatus tendon under uniaxial loading. *J Orthop Res* **23**, 924-930 (2005).
335. T. Nakajima, N. Rokuuma, K. Hamada, T. Tomatsu, H. Fukuda, Histologic and biomechanical characteristics of the supraspinatus tendon: Reference to rotator cuff tearing. *J Shoulder Elbow Surg* **3**, 79-87 (1994).
336. M. J. Bey, H. K. Song, F. W. Wehrli, L. J. Soslowsky, Intratendinous strain fields of the intact supraspinatus tendon: the effect of glenohumeral joint position and tendon region. *J Orthop Res* **20**, 869-874 (2002).
337. A. Sensini, L. Cristofolini, Biofabrication of Electrospun Scaffolds for the Regeneration of Tendons and Ligaments. *Materials (Basel, Switzerland)* **11**, 1963 (2018).
338. R. L. Waltrip, N. Zheng, J. R. Dugas, J. R. Andrews, Rotator Cuff Repair: A Biomechanical Comparison of Three Techniques. *The American Journal of Sports Medicine* **31**, 493-497 (2003).
339. D. Zhang *et al.*, Dealing with the Foreign-Body Response to Implanted Biomaterials: Strategies and Applications of New Materials. *Advanced Functional Materials* **31**, 2007226 (2021).
340. M. J. Webber, O. F. Khan, S. A. Sydlik, B. C. Tang, R. Langer, A Perspective on the Clinical Translation of Scaffolds for Tissue Engineering. *Annals of Biomedical Engineering* **43**, 641-656 (2015).

341. C. Kengla, A. Kidiyoor, S. V. Murphy, in *Kidney Transplantation, Bioengineering and Regeneration,* G. Orlando, G. Remuzzi, D. F. Williams, Eds. (Academic Press, 2017), pp. 957-971.
342. S. Caddeo, M. Boffito, S. Sartori, Tissue Engineering Approaches in the Design of Healthy and Pathological In Vitro Tissue Models. *Front Bioeng Biotechnol* **5**, 40 (2017).
343. K. H. Benam *et al.*, Engineered in vitro disease models. *Annu Rev Pathol* **10**, 195-262 (2015).
344. Y. Chen *et al.*, Characterization and optimization of cell seeding in scaffolds by factorial design: quality by design approach for skeletal tissue engineering. *Tissue Eng Part C Methods* **17**, 1211-1221 (2011).
345. P. Borbas *et al.*, High-Strength Suture Tapes Are Biomechanically Stronger Than High-Strength Sutures Used in Rotator Cuff Repair. *Arthrosc Sports Med Rehabil* **3**, e873-e880 (2021).
346. O. Arda, N. Göksügür, Y. Tüzün, Basic histological structure and functions of facial skin. *Clinics in Dermatology* **32**, 3-13 (2014).
347. W. Liu *et al.*, Repair of tendon defect with dermal fibroblast engineered tendon in a porcine model. *Tissue Eng* **12**, 775-788 (2006).
348. D. Deng *et al.*, Engineering human neo-tendon tissue in vitro with human dermal fibroblasts under static mechanical strain. *Biomaterials* **30**, 6724-6730 (2009).
349. W. Wang *et al.*, Induction of predominant tenogenic phenotype in human dermal fibroblasts via synergistic effect of TGF-β and elongated cell shape. *American Journal of Physiology-Cell Physiology* **310**, C357-C372 (2015).
350. J. R. Mackley, J. Ando, P. Herzyk, S. J. Winder, Phenotypic responses to mechanical stress in fibroblasts from tendon, cornea and skin. *Biochem J* **396**, 307-316 (2006).
351. R. J. Geraghty *et al.*, Guidelines for the use of cell lines in biomedical research. *Br J Cancer* **111**, 1021-1046 (2014).
352. E. G. Hayman, M. D. Pierschbacher, S. Suzuki, E. Ruoslahti, Vitronectin--a major cell attachment-promoting protein in fetal bovine serum. *Exp Cell Res* **160**, 245-258 (1985).
353. C.-T. Hsiao *et al.*, Fibronectin in cell adhesion and migration via N-glycosylation. *Oncotarget* **8**, 70653-70668 (2017).
354. T. Tsuji, Physiological and Pathological Roles of α3β1 Integrin. **200**, 115-132 (2004).
355. A. Kurzyk, B. Ostrowska, W. Święszkowski, Z. Pojda, Characterization and Optimization of the Seeding Process of Adipose Stem Cells on the Polycaprolactone Scaffolds.
356. Z. Research, RNA Clean & Concentrator ™ - 5. https://files.zymoresearch.com/protocols/_r1013_r1014_r1015_r1016_rna_clean_concentrator-5.pdf.
357. N. S. Nagra, D. Prieto Alhambra, S. Snelling, T. Vincent, A. Carr, N. S. Nagra, Eds. (2019).
358. F. AM, H. T, S. C, R. P, B. J, DNase I treatment of cDNA first strands prevents RT-PCR amplification of contaminating DNA sequences. *BioTechniques* **35**, (2003).
359. B. Matlock. (Thermo Fisher Scientific, Wilmington, MA, USA, 2022).
360. O. N. D, G. H, S. M, Ribosomal RNA depletion for efficient use of RNA-seq capacity. *Current protocols in molecular biology* **Chapter 4**, (2013).
361. S. Zhao, Y. Zhang, R. Gamini, B. Zhang, D. von Schack, Evaluation of two main RNA-seq approaches for gene quantification in clinical RNA sequencing: polyA+ selection versus rRNA depletion. *Scientific Reports* **8**, 1-12 (2018).
362. N. Zou, S. Ditty, B. Li, S. Lo, Random priming PCR strategy to amplify and clone trace amounts of DNA. *BioTechniques* **35**, (2003).
363. S. Zhao *et al.*, Comparison of stranded and non-stranded RNA-seq transcriptome profiling and investigation of gene overlap. *BMC Genomics* **16**, 1-14 (2015).
364. Anaconda Software Distribution. *Anaconda Inc.* **Vers. 2-2.4.0**, (2020).
365. S. Andrews, FastQC: A Quality Control Tool for High Throughput Sequence Data [Online]. Available online at: http://www.bioinformatics.babraham.ac.uk/projects/fastqc/. (2015).
366. P. Ewels, M. Magnusson, S. Lundin, M. Käller, MultiQC: summarize analysis results for multiple tools and samples in a single report. *Bioinformatics* **32**, 3047-3048 (2016).

367. N. L. Bray, H. Pimentel, P. Melsted, L. Pachter, Near-optimal probabilistic RNA-seq quantification. *Nature Biotechnology* **34**, 525-527 (2016).
368. F. Cunningham *et al.*, Ensembl 2022. *Nucleic Acids Research* **50**, D988-D995 (2022).
369. E. Project, http://ftp.ensembl.org/pub/release-104/fasta/homo_sapiens/cdna/.
370. K. Pearson, LIII. On lines and planes of closest fit to systems of points in space. *The London, Edinburgh, and Dublin Philosophical Magazine and Journal of Science* **2**, 559-572 (1901).
371. M. I. Love, W. Huber, S. Anders, Moderated estimation of fold change and dispersion for RNA-seq data with DESeq2. *Genome Biology* **15**, 550 (2014).
372. M. I. Love, S. Anders, W. Huber. (bioconductor.org), vol. 2022.
373. R. Khetani, M. Mistry, J. Liu, W. Gammerdinger. vol. 2022.
374. S. F. Berry Alexander *et al.*, An Open-Source Toolkit To Expand Bioinformatics Training in Infectious Diseases. *mBio* **12**, e01214-01221.
375. K. Blighe, S. Rana, M. Lewis, EnhancedVolcano: Publication-ready volcano plots with enhanced colouring and labeling. https://github.com/kevinblighe/EnhancedVolcano., (2022).
376. H. Wickham, *ggplot2: Elegant Graphics for Data Analysis*. https://ggplot2.tidyverse.org/. *Springer-Verlag New York*, (2016).
377. T. Wu *et al.*, clusterProfiler 4.0: A universal enrichment tool for interpreting omics data. *The Innovation* **2**, 100141 (2021).
378. R. Bourgon, R. Gentleman, W. Huber, Independent filtering increases detection power for high-throughput experiments. *Proceedings of the National Academy of Sciences* **107**, 9546-9551 (2010).
379. M. Stephens, False discovery rates: a new deal. *Biostatistics* **18**, 275-294 (2017).
380. C. Evans *et al.*, Selecting between-sample RNA-Seq normalization methods from the perspective of their assumptions. *Briefings in Bioinformatics* **19**, 776-792 (2017).
381. S. Anders, W. Huber, Differential expression analysis for sequence count data. *Genome Biology* **11**, 1-12 (2010).
382. G. P. Wagner, K. Kin, V. J. Lynch, Measurement of mRNA abundance using RNA-seq data: RPKM measure is inconsistent among samples. *Theory in Biosciences* **131**, 281-285 (2012).
383. A. Mortazavi, B. A. Williams, K. McCue, L. Schaeffer, B. Wold, Mapping and quantifying mammalian transcriptomes by RNA-Seq. *Nature Methods* **5**, 621-628 (2008).
384. Y. Zhao *et al.*, TPM, FPKM, or Normalized Counts? A Comparative Study of Quantification Measures for the Analysis of RNA-seq Data from the NCI Patient-Derived Models Repository. *Journal of Translational Medicine* **19**, 1-15 (2021).
385. S. Zhao, Z. Ye, R. Stanton, Misuse of RPKM or TPM normalization when comparing across samples and sequencing protocols. *RNA* **26**, 903-909 (2020).
386. S. Wold, K. Esbensen, P. Geladi, Principal component analysis. *Chemometrics and Intelligent Laboratory Systems* **2**, 37-52 (1987).
387. R. Bro, A. K. Smilde, Principal component analysis. *Analytical Methods* **6**, 2812-2831 (2014).
388. K. Blighe, Haplotype Classification Using Copy Number Variation and Principal Components Analysis. *The Open Bioinformatics Journal* **7**, 19-24 (2013).
389. B. Boehmke, B. Greenwell, *Chapter 17 Principal Components Analysis*. Hands-On Machine Learning with R (Taylor & Francis Group, 2020).
390. Pythagorean theorem | Definition & History. https://www.britannica.com/science/Pythagorean-theorem.
391. R. Kolde, Pretty Heatmaps (pheatmaps package). (2018).
392. S. C. Hicks, F. W. Townes, M. Teng, R. A. Irizarry, Missing data and technical variability in single-cell RNA-sequencing experiments. *Biostatistics* **19**, 562-578 (2018).
393. A. JL *et al.*, The Vertebrate Genome Annotation (Vega) database. *Nucleic acids research* **33**, (2005).
394. O. A. Shchelochkov, Open Reading Frame. https://www.genome.gov/genetics-glossary/Open-Reading-Frame, (2022).

395. K. Rustad, V. Wong, G. Gurtner, The role of focal adhesion complexes in fibroblast mechanotransduction during scar formation. *Differentiation; research in biological diversity* **86**, (2013).
396. P. Reddig, R. Juliano, Clinging to life: cell to matrix adhesion and cell survival. *Cancer metastasis reviews* **24**, (2005).
397. V. Ruprecht *et al.*, How cells respond to environmental cues – insights from bio-functionalized substrates. *Journal of Cell Science* **130**, 51-61 (2017).
398. D. E. A *et al.*, Tendon-Derived Biomimetic Surface Topographies Induce Phenotypic Maintenance of Tenocytes In Vitro. *Tissue engineering. Part A* **27**, (2021).
399. V. M. Wang *et al.*, Medial versus lateral supraspinatus tendon properties: implications for double-row rotator cuff repair. *Am J Sports Med* **38**, 2456-2463 (2010).
400. C. Erisken, X. Zhang, K. L. Moffat, W. N. Levine, H. H. Lu, Scaffold Fiber Diameter Regulates Human Tendon Fibroblast Growth and Differentiation. https://home.liebertpub.com/tea, (2012).
401. D. S. Musson *et al.*, In Vitro Evaluation of a Novel Non-Mulberry Silk Scaffold for Use in Tendon Regeneration. https://home.liebertpub.com/tea, (2015).
402. H. J. Chung, J. Uitto, Type VII collagen: the anchoring fibril protein at fault in dystrophic epidermolysis bullosa. *Dermatologic clinics* **28**, (2010).
403. J. H. Mortensen, M. A. Karsdal, in *Biochemistry of Collagens, Laminins and Elastin,* M. A. Karsdal, Ed. (Academic Press, 2016), pp. 57-60.
404. D. A. Culton, L. A. Diaz, Treatment of subepidermal immunobullous diseases. *Clinics in Dermatology* **30**, 95-102 (2012).
405. M. Hosio *et al.*, Primary Ciliary Signaling in the Skin—Contribution to Wound Healing and Scarring. *Frontiers in Cell and Developmental Biology* **8**, (2020).
406. F. Fang, M. Sup, A. Luzzi, X. Ferrer, S. Thomopoulos, Hedgehog signaling underlying tendon and enthesis development and pathology. *Matrix biology : journal of the International Society for Matrix Biology* **105**, (2022).
407. M. Spasic, C. Jacobs, Lengthening primary cilia enhances cellular mechanosensitivity. *European cells & materials* **33**, (2017).
408. M. Kunova Bosakova *et al.*, Fibroblast growth factor receptor influences primary cilium length through an interaction with intestinal cell kinase. *Proceedings of the National Academy of Sciences* **116**, 4316-4325 (2019).
409. I. Sánchez, B. Dynlacht, Cilium assembly and disassembly. *Nature cell biology* **18**, (2016).
410. M. Meyer *et al.*, FGF receptors 1 and 2 are key regulators of keratinocyte migration in vitro and in wounded skin. *Journal of cell science* **125**, (2012).
411. Y. Koike, M. Yozaki, A. Utani, H. Murota, Fibroblast growth factor 2 accelerates the epithelial–mesenchymal transition in keratinocytes during wound healing process. *Scientific Reports* **10**, 1-13 (2020).
412. M. Abdelhakim, X. Lin, R. Ogawa, The Japanese Experience with Basic Fibroblast Growth Factor in Cutaneous Wound Management and Scar Prevention: A Systematic Review of Clinical and Biological Aspects. *Dermatology and therapy* **10**, (2020).
413. Y. Liu, Y. Liu, J. Deng, W. Li, X. Nie, Fibroblast Growth Factor in Diabetic Foot Ulcer: Progress and Therapeutic Prospects. *Frontiers in Endocrinology* **12**, (2021).
414. H. Peng, W. Gao, F. Chong, H. Liu, J. Zhang, Semaphorin 4A enhances lung fibrosis through activation of Akt via PlexinD1 receptor. *Journal of biosciences* **40**, (2015).
415. T. Carvalheiro *et al.*, Induction of Inflammation and Fibrosis by Semaphorin 4A in Systemic Sclerosis. *Arthritis & rheumatology (Hoboken, N.J.)* **71**, (2019).
416. X. Zhao *et al.*, Focal Adhesion Kinase Regulates Fibroblast Migration via Integrin beta-1 and Plays a Central Role in Fibrosis. *Scientific reports* **6**, (2016).
417. N. Chiarelli *et al.*, Transcriptome-Wide Expression Profiling in Skin Fibroblasts of Patients with Joint Hypermobility Syndrome/Ehlers-Danlos Syndrome Hypermobility Type. *PLoS One* **11**, (2016).
418. G. Li, J. Deng, Y. Qi, R. Liu, Z. Liu, COLEC12 regulates apoptosis of osteosarcoma through Toll-like receptor 4-activated inflammation. *Journal of clinical laboratory analysis* **34**, (2020).

419. A. Goss *et al.*, Wnt2 signaling is necessary and sufficient to activate the airway smooth muscle program in the lung by regulating myocardin/Mrtf-B and Fgf10 expression. *Developmental biology* **356**, (2011).
420. N. P. Fusté *et al.*, Cytoplasmic cyclin D1 regulates cell invasion and metastasis through the phosphorylation of paxillin. *Nature Communications* **7**, 1-14 (2016).
421. M. A. Velasco-Velázquez *et al.*, Examining the role of cyclin D1 in breast cancer. *Future Oncology* **7**, 753-765 (2011).
422. Z. Zhong *et al.*, Cyclin D1/cyclin-dependent kinase 4 interacts with filamin A and affects the migration and invasion potential of breast cancer cells. *Cancer research* **70**, (2010).
423. Z. Li , C. Wang, G. Prendergast, R. Pestell, Cyclin D1 functions in cell migration. *Cell Cycle* **5**, (2006).
424. V. Adorno-Cruz, H. Liu, Regulation and functions of integrin α2 in cell adhesion and disease. *Genes Dis* **6**, 16-24 (2018).
425. J. Heino, The collagen receptor integrins have distinct ligand recognition and signaling functions. *Matrix biology : journal of the International Society for Matrix Biology* **19**, (2000).
426. M. Barczyk, S. Carracedo, D. Gullberg, Integrins. *Cell and tissue research* **339**, (2010).
427. J. San Antonio *et al.*, A key role for the integrin alpha2beta1 in experimental and developmental angiogenesis. *The American journal of pathology* **175**, (2009).
428. K. R. Turner, C. Adams, S. Staelens, H. Deckmyn, J. San Antonio, Crucial Role for Endothelial Cell α2β1 Integrin Receptor Clustering in Collagen-Induced Angiogenesis. *The Anatomical Record* **303**, 1604-1618 (2020).
429. R. Kendall, C. Feghali-Bostwick, Fibroblasts in fibrosis: novel roles and mediators. *Frontiers in pharmacology* **5**, (2014).
430. M. Tonnesen, X. Feng, R. Clark, Angiogenesis in wound healing. *The journal of investigative dermatology. Symposium proceedings* **5**, (2000).
431. P. G. Murphy, B. J. Loitz, C. B. Frank, D. A. Hart, Influence of exogenous growth factors on the synthesis and secretion of collagen types I and III by explants of normal and healing rabbit ligaments. *Biochemistry and Cell Biology* **72**, 403-409 (1994).
432. M. Lampugnani, Endothelial adherens junctions and the actin cytoskeleton: an 'infinity net'? *Journal of biology* **9**, (2010).
433. Y. Wang *et al.*, Single-cell analysis of murine fibroblasts identifies neonatal to adult switching that regulates cardiomyocyte maturation. *Nature Communications* **11**, 1-18 (2020).
434. P. Cai *et al.*, Comparison of rheumatoid arthritis (RA) and osteoarthritis (OA) based on microarray profiles of human joint fibroblast-like synoviocytes. *Cell Biochemistry and Function* **37**, 31-41 (2019).
435. S. Gaffen, Structure and signalling in the IL-17 receptor family. *Nature reviews. Immunology* **9**, (2009).
436. A. Beringer, P. Miossec, Systemic effects of IL-17 in inflammatory arthritis. *Nature reviews. Rheumatology* **15**, (2019).
437. W. Liu *et al.*, Fanconi anemia pathway as a prospective target for cancer intervention. *Cell & Bioscience* **10**, 1-14 (2020).
438. HFF-1 | SCRC-1041. *ATCC*, (2022).
439. R. N. Gomes, F. Manuel, D. S. Nascimento, The bright side of fibroblasts: molecular signature and regenerative cues in major organs. *npj Regenerative Medicine* **6**, 1-12 (2021).
440. D. Janson, G. Saintigny, A. van Adrichem, C. Mahé, A. El Ghalbzouri Different gene expression patterns in human papillary and reticular fibroblasts. *The Journal of investigative dermatology* **132**, (2012).
441. R. A. Harper, G. Grove, Human Skin Fibroblasts Derived from Papillary and Reticular Dermis: Differences in Growth Potential in Vitro. *Science* **204**, (1979).
442. J. Sorrell, M. Baber, A. Caplan, Human dermal fibroblast subpopulations; differential interactions with vascular endothelial cells in coculture: nonsoluble factors in the extracellular matrix influence interactions. *Wound repair and regeneration : official publication of the Wound Healing Society [and] the European Tissue Repair Society* **16**, (2008).

443. Y. J. No, M. Castilho, Y. Ramaswamy, H. Zreiqat, Role of Biomaterials and Controlled Architecture on Tendon/Ligament Repair and Regeneration. *Advanced Materials* **32**, 1904511 (2020).
444. F. A. Barber, S. M. Feder, S. S. Burkhart, J. Ahrens, The relationship of suture anchor failure and bone density to proximal humerus location: A cadaveric study. *Arthroscopy: The Journal of Arthroscopic & Related Surgery* **13**, 340--345 (1997).
445. D. J. Rossouw, B. J. McElroy, A. A. Amis, R. J. H. Emery, A BIOMECHANICAL EVALUATION OF SUTURE ANCHORS IN REPAIR OF THE ROTATOR CUFF. *The Journal of Bone and Joint Surgery. British volume* **79-B**, 458-461 (1997).
446. J. Barth *et al.*, Critical period and risk factors for retear following arthroscopic repair of the rotator cuff. *Knee Surgery, Sports Traumatology, Arthroscopy* **25**, 2196-2204 (2016).
447. J. P. Iannotti *et al.*, Time to Failure After Rotator Cuff Repair: A Prospective Imaging Study. *JBJS* **95**, (2013).
448. K. Shea, E. Obopilwe, J. Sperling, J. Iannotti, A biomechanical analysis of gap formation and failure mechanics of a xenograft-reinforced rotator cuff repair in a cadaveric model. *Journal of shoulder and elbow surgery* **21**, (2012).
449. A. S. Curtis, K. M. Burbank, J. J. Tierney, A. D. Scheller, A. R. Curran, The insertional footprint of the rotator cuff: an anatomic study. *Arthroscopy* **22**, 609 e601 (2006).
450. W. Lumsdaine *et al.*, Morphology of the humeral insertion of the supraspinatus and infraspinatus tendons: Application to rotator cuff repair. *Clin Anat* **28**, 767-773 (2015).
451. W. C. Sessions, Thickness of the Rotator Cuff Tendons at the Articular Margin: An Anatomic Cadaveric Study. *Iowa Orthop J* **37**, 85–89 (2017).
452. A. G. Volk, C. T. Vangsness, Jr., An anatomic study of the supraspinatus muscle and tendon. *Clin Orthop Relat Res*, 280-285 (2001).
453. M. S. Roh *et al.*, Anterior and posterior musculotendinous anatomy of the supraspinatus. *J Shoulder Elbow Surg* **9**, 436-440 (2000).
454. C. Ruotolo, J. E. Fow, W. M. Nottage, The supraspinatus footprint: an anatomic study of the supraspinatus insertion. *Arthroscopy* **20**, 246-249 (2004).
455. A. Nimura *et al.*, The superior capsule of the shoulder joint complements the insertion of the rotator cuff. *J Shoulder Elbow Surg* **21**, 867-872 (2012).
456. N. Naidoo, L. Lazarus, K. S. Satyapal, The Rotator Cuff Footprint: A Cadaveric Study of the Morphometry and Morphology. *International Journal of Morphology* **34**, 975-985 (2016).
457. T. Matsuhashi *et al.*, Tensile properties of a morphologically split supraspinatus tendon. *Clin Anat* **27**, 702--706 (2014).
458. Y. S. Kim, J. M. Kim, L. U. Bigliani, H. J. Kim, H. W. Jung, In vivo strain analysis of the intact supraspinatus tendon by ultrasound speckles tracking imaging. *J Orthop Res* **29**, 1931-1937 (2011).
459. C. Kirchhoff *et al.*, Assessment of bone quality within the tuberosities of the osteoporotic humeral head: relevance for anchor positioning in rotator cuff repair. *Am J Sports Med* **38**, 564--569 (2010).
460. N. Aydin, B. Karaismailoglu, M. Gurcan, M. K. Ozsahin, Arthroscopic double-row rotator cuff repair: a comprehensive review of the literature. *SICOT J* **4**, 57-57 (2018).
461. T. Rodet, F. Noo, M. Defrise, The cone-beam algorithm of Feldkamp, Davis, and Kress preserves oblique line integrals. *Medical physics* **31**, (2004).
462. P. W. Jost *et al.*, Suture Number Determines Strength of Rotator Cuff Repair. *JBJS* **94**, (2012).
463. M. J. Feucht *et al.*, Biomechanical evaluation of different suture materials for arthroscopic transtibial pull-out repair of posterior meniscus root tears. *Knee Surgery, Sports Traumatology, Arthroscopy* **23**, 132-139 (2015).
464. G. E. S. University of Reading Archaeology, Pig - Humerus - 3D model. https://sketchfab.com/3d-models/pig-humerus-0ca7a67074b743c2b0ad799d5ba03a98, (2021).
465. *Húmero – Anatomía Humana 3D*. https://anatomiahumana3d.com/ (Instituto de Anatomía, Histología y Patología de la Facultad de Medicina de la Universidad Austral de Chile).

466. A. I. Pearce, R. G. Richards, S. Milz, E. Schneider, S. G. Pearce, Animal models for implant biomaterial research in bone: a review. *Eur Cell Mater* **13**, 1-10 (2007).
467. J. Aerssens, S. Boonen, G. Lowet, J. Dequeker, Interspecies differences in bone composition, density, and quality: potential implications for in vivo bone research. *Endocrinology* **139**, 663-670 (1998).
468. S. Cone, P. Warren, M. Fisher, Rise of the Pigs:Utilization of the Porcine Model to Study MusculoskeletalBiomechanics and Tissue Engineering During Skeletal Growth. *Tissue Engineering: Part C* **23**, 763-780 (2017).
469. Burkhart, The Deadman Theory of Suture Anchors: observations along a south Texas fence line. *Arthroscopy* **11**, 119-123 (1995).
470. N. Keough, T. de Beer, A. Uys, E. Hohmann, An anatomical investigation into the blood supply of the proximal humerus: surgical considerations for rotator cuff repair. *JSES Open Access* **3**, 320-327 (2019).
471. B. O'Neill, Nozzle diameter and layer height explained. https://www.wevolver.com/article/nozzle-diameter-and-layer-height-explained, (2022).
472. A. L. Seitz, P. W. McClure, S. Finucane, N. D. Boardman, 3rd, L. A. Michener, Mechanisms of rotator cuff tendinopathy: intrinsic, extrinsic, or both? *Clin Biomech (Bristol, Avon)* **26**, 1-12 (2011).
473. C.-K. Hong *et al.*, When deadman theory meets footprint decortication: a suture anchor biomechanical study. *Journal of Orthopaedic Surgery and Research* **14**, 157 (2019).
474. H. Nagamoto, N. Yamamoto, H. Sano, E. Itoi, A biomechanical study on suture anchor insertion angle: Which is better, 90° or 45°? *Journal of Orthopaedic Science* **22**, 56-62 (2017).
475. E. Strauss, D. Frank, E. Kubiak, F. Kummer, A. Rokito, The Effect of the Angle of Suture Anchor Insertion on Fixation Failure at the Tendon--Suture Interface After Rotator Cuff Repair: Deadman's Angle Revisited. *Arthroscopy: The Journal of Arthroscopic & Related Surgery* **25**, 597--602 (2009).
476. T. Clevenger, M. Beebe, E. Strauss, E. Kubiak, The effect of insertion angle on the pullout strength of threaded suture anchors: a validation of the deadman theory. *Arthroscopy : the journal of arthroscopic & related surgery : official publication of the Arthroscopy Association of North America and the International Arthroscopy Association* **30**, (2014).
477. H. Nagamoto, N. Yamamoto, E. Itoi, Effect of anchor threads on the pullout strength: A biomechanical study. *Journal of orthopaedics* **15**, (2018).
478. R. N. Green, O. W. Donaldson, M. Dafydd, S. L. Evans, R. Kulkarni, Biomechanical Study: Determining the Optimum Insertion Angle for Screw-In Suture Anchors—Is Deadman's Angle Correct? *Arthroscopy: The Journal of Arthroscopic & Related Surgery* **30**, 1535-1539 (2014).
479. S. S. Burkhart, Suture anchor insertion angle and the deadman theory. *Arthroscopy : the journal of arthroscopic & related surgery : official publication of the Arthroscopy Association of North America and the International Arthroscopy Association* **25**, (2009).
480. S. S. Burkhart, The Deadman Theory Is Alive and Well. *Arthroscopy* **30**, 1049-1050 (2014).
481. S. S. Burkhart, Can the Deadman Be Killed? *Arthroscopy: The Journal of Arthroscopic & Related Surgery* **31**, 181-182 (2015).
482. K. Robi, N. Jakob, K. Matevz, V. Matjaz, The Physiology of Sports Injuries and Repair Processes. *Current Issues in Sports and Exercise Medicine*, (2013).
483. J. Maquirriain, Achilles tendon rupture: avoiding tendon lengthening during surgical repair and rehabilitation. *Yale J Biol Med* **84**, 289-300 (2011).
484. L. Linnanmäki *et al.*, Gap Formation During Cyclic Testing of Flexor Tendon Repair. *The Journal of Hand Surgery* **43**, 570.e571-570.e578 (2018).
485. K. Wieser *et al.*, Suture slippage in knotless suture anchors as a potential failure mechanism in rotator cuff repair. *Arthroscopy : the journal of arthroscopic & related surgery : official publication of the Arthroscopy Association of North America and the International Arthroscopy Association* **28**, (2012).

486. R. Thal, A Knotless Suture Anchor: Design, Function, and Biomechanical Testing. *The American Journal of Sports Medicine* **29**, 646-649 (2001).
487. K. A. Burns *et al.*, Rotator Cuff Repair With Knotless Technique Is Quicker and More Cost-Effective Than Knotted Technique. *Arthrosc Sports Med Rehabil* **1**, e123-e130 (2019).
488. D. H. Kim *et al.*, Biomechanical comparison of a single-row versus double-row suture anchor technique for rotator cuff repair. *Am J Sports Med* **34**, 407-414 (2006).
489. T. A. Sgroi, M. Cilenti, Rotator cuff repair: post-operative rehabilitation concepts. *Curr Rev Musculoskelet Med* **11**, 86-91 (2018).
490. S. Zhang *et al.*, Delayed early passive motion is harmless to shoulder rotator cuff healing in a rabbit model. *The American journal of sports medicine* **41**, (2013).
491. C. Peltz *et al.*, The effect of postoperative passive motion on rotator cuff healing in a rat model. *J Bone Joint Surg Am* **91**, (2009).
492. K. Chang *et al.*, Early Versus Delayed Passive Range of Motion Exercise for Arthroscopic Rotator Cuff Repair: A Meta-analysis of Randomized Controlled Trials. *The American journal of sports medicine* **43**, (2015).
493. N. Bakti, T. Antonios, A. Phadke, B. Singh, Early versus delayed mobilization following rotator cuff repair. *J Clin Orthop Trauma* **10**, 257-260 (2019).
494. C. Capelli, S. Schievano, in *3D Printing in Medicine,* D. M. Kalaskar, Ed. (Woodhead Publishing, 2017), pp. 73-90.
495. K. Deshmukh *et al.*, in *Biopolymer Composites in Electronics,* K. K. Sadasivuni, D. Ponnamma, J. Kim, J. J. Cabibihan, M. A. AlMaadeed, Eds. (Elsevier, 2017), pp. 27-128.
496. Z. Yang, Z. Song, X. Nie, K. Guo, Y. Gu, A smart scaffold composed of three-dimensional printing and electrospinning techniques and its application in rat abdominal wall defects. *Stem cell research & therapy* **11**, (2020).
497. S. Naghieh, E. Foroozmehr, M. Badrossamay, M. Kharaziha, Combinational processing of 3D printing and electrospinning of hierarchical poly(lactic acid)/gelatin-forsterite scaffolds as a biocomposite: Mechanical and biological assessment. *Materials & Design* **133**, 128-135 (2017).
498. I. Rajzer *et al.*, Layered gelatin/PLLA scaffolds fabricated by electrospinning and 3D printing- for nasal cartilages and subchondral bone reconstruction. *Materials & Design* **155**, 297-306 (2018).
499. C. Mota *et al.*, Dual-Scale Polymeric Constructs as Scaffolds for Tissue Engineering. *Materials (Basel, Switzerland)* **4**, 527-542 (2011).
500. Y. Pan *et al.*, Small-diameter hybrid vascular grafts composed of polycaprolactone and polydioxanone fibers. *Scientific Reports* **7**, 1-11 (2017).
501. M. J. McClure, S. A. Sell, D. G. Simpson, G. L. Bowlin, Electrospun Polydioxanone, Elastin, and Collagen Vascular Scaffolds: Uniaxial Cyclic Distension. *Journal of Engineered Fibers and Fabrics* **4**, 155892500900400204 (2009).
502. P.-A. Mouthuy *et al.*, Investigating the use of curcumin-loaded electrospun filaments for soft tissue repair applications. *Int J Nanomedicine* **12**, 3977--3991 (2017).
503. P. Fathi *et al.*, Computed tomography-guided additive manufacturing of Personalized Absorbable Gastrointestinal Stents for intestinal fistulae and perforations. *Biomaterials* **228**, 119542 (2020).
504. N. Goonoo *et al.*, Improved Multicellular Response, Biomimetic Mineralization, Angiogenesis, and Reduced Foreign Body Response of Modified Polydioxanone Scaffolds for Skeletal Tissue Regeneration. *ACS applied materials & interfaces* **11**, (2019).
505. P. Madurantakam *et al.*, Multiple factor interactions in biomimetic mineralization of electrospun scaffolds. *Biomaterials* **30**, (2009).
506. I. A. Rodriguez *et al.*, Mineralization Potential of Electrospun PDO-Hydroxyapatite-Fibrinogen Blended Scaffolds. *International Journal of Biomaterials* **2012**, 159484 (2012).
507. L. Chung *et al.*, Interleukin 17 and senescent cells regulate the foreign body response to synthetic material implants in mice and humans. *Science translational medicine* **12**, eaax3799 (2020).
508. S. A. Sell *et al.*, Electrospun polydioxanone–elastin blends: potential for bioresorbable vascular grafts. *Biomedical Materials* **1**, 72-80 (2006).

509. M. J. Smith *et al.*, Suture-reinforced electrospun polydioxanone–elastin small-diameter tubes for use in vascular tissue engineering: A feasibility study. *Acta Biomaterialia* **4**, 58-66 (2008).
510. S. Heene *et al.*, Vascular Network Formation on Macroporous Polydioxanone Scaffolds. *Tissue engineering. Part A* **27**, (2021).
511. X. Liu *et al.*, The Role of Vascular Endothelial Growth Factor in Tendon Healing. *Frontiers in Physiology* **12**, (2021).
512. J. Yao, T. Korotkova, R. Smith, Viability and proliferation of pluripotential cells delivered to tendon repair sites using bioactive sutures--an in vitro study. *The Journal of Hand Surgery* **36**, (2011).
513. O. Hakimi, S. Chaudhury, R. Murphy, A. Carr, Differential growth on sutures of tendon cells derived from torn human rotator cuff. *J Biomed Mater Res B Appl Biomater* **100**, 685-692 (2012).
514. B. J. Ollivere, H. A. Bosman, P. W. Bearcroft, A. H. Robinson, Foreign body granulomatous reaction associated with polyethelene 'Fiberwire(®)' suture material used in Achilles tendon repair. *Foot Ankle Surg* **20**, e27-29 (2014).
515. A. W. Mack *et al.*, Wound complications following the use of fiberwire In lower-extremity traumatic amputations. *Journal of Bone and Joint Surgery* **91**, 680-685 (2009).
516. P. Storey, R. J. Gadd, C. Blundell, M. B. Davies, Complications of Suture Button Ankle Syndesmosis Stabilization with Modifications of Surgical Technique. *Foot & Ankle International* **33**, 717-721 (2012).
517. T. Yokoe, T. Tajima, N. Yamaguchi, Y. Morita, E. Chosa, Surgical Wound Complications after Knee Cruciate Ligament Reconstruction in Patients with Atopic Dermatitis. *J Knee Surg* **34**, 1237-1242 (2021).
518. M. T. Galloway, A. L. Lalley, J. T. Shearn, The role of mechanical loading in tendon development, maintenance, injury, and repair. *J Bone Joint Surg Am* **95**, 1620-1628 (2013).
519. C. Woon *et al.*, Three-dimensional-construct bioreactor conditioning in human tendon tissue engineering. *Tissue engineering. Part A* **17**, (2011).
520. P.-A. Mouthuy *et al.*, Humanoid robots to mechanically stress human cells grown in soft bioreactors. *Communications Engineering* **1**, 1-11 (2022).
521. U. Longo, S. Buchmann, A. Berton, N. Maffulli, V. Denaro, Arthroscopic knots and strength sutures for rotator cuff repair. *Sports medicine and arthroscopy review* **19**, (2011).
522. J. A. Calvo-Haro *et al.*, Conceptual evolution of 3D printing in orthopedic surgery and traumatology: from “do it yourself” to “point of care manufacturing”. *BMC Musculoskeletal Disorders* **22**, 360 (2021).
523. J. J. Otero, A. Vijverman, M. Y. Mommaerts, Use of fused deposit modeling for additive manufacturing in hospital facilities: European certification directives. *Journal of Cranio-Maxillofacial Surgery* **45**, 1542-1546 (2017).
524. G. Repetto, A. del Peso, J. L. Zurita, Neutral red uptake assay for the estimation of cell viability/cytotoxicity. *Nature Protocols* **3**, 1125-1131 (2008).
525. L. P. Freedman *et al.*, The culture of cell culture practices and authentication—Results from a 2015 Survey. *BioTechniques* **59**, 189-192 (2015).
526. P. Hughes, D. Marshall, Y. Reid, H. Parkes, C. Gelber, The costs of using unauthenticated, over-passaged cell lines: how much more data do we need? *BioTechniques* **43**, (2007).

Appendices

Appendix A. Pipeline for RNA-Seq analysis

A.1 Pipeline for *kallisto* pseudoalignment and QC

Once you have your sequencing files, you need to download them and align them to a reference genome. I have used the kallisto pipeline to do so, adapted from Dr Adam Cribbs.
The following code will be run from the Terminal (Linux/Mac), NOT from the Python environment!
To start, download and install *Miniconda* first by following instructions here: https://docs.conda.io/en/latest/miniconda.html.

NB: this does NOT work on Windows machines!
NB2: If any of the commands return authentication errors, run it with '*sudo*' in front of it

Sources:

- https://diytranscriptomics.com/project/lecture-02
- https://developer.basespace.illumina.com/docs/content/documentation/cli/cli-overview

```
# Install mamba and set up your environment
$ conda env list
$ conda install -n base -c conda-forge mamba
$ conda config --add channels bioconda
$ conda config --add channels conda-forge
$ cd ~/Documents #the cd command brings you to the directory of choice

# Clone the github repository of Dr Adam Cribbs
$ git clone https://github.com/Acribbs/cribbslab.git
$ cd cribbslab
$ mamba env create -f conda/environments/cribbslab.yml
$ conda activate cribbslab  # this will be the main environment!
$ python setup.py develop
$ git clone https://github.com/Acribbs/deseq2_report.git

# Install Illumina BaseSpace (BS)– two ways of doing this
1. Run following commands (NB: this did not work for me)
$ mkdir $HOME/bin
$ wget "https://launch.basespace.illumina.com/CLI/latest/amd64-osx/bs" -O
$HOME/bin/bs

2. If HomeBrew is installed run the following:
$ brew tap basespace/basespace && brew install bs-cli

# Set up directory and build index in same directory as FastQ files will be in
$ mkdir sequencing
$ cd sequencing
$ mamba install wget
$ wget http://ftp.ensembl.org/pub/release-
104/fasta/homo_sapiens/cdna/Homo_sapiens.GRCh38.cdna.all.fa.gz
# If using another species, please make sure to use the relevant genome!

# Download your files. NB: if these commands don't work, add ./ in front of it
```

```
$ bs projects list # pulls up a list of available projects on BS
$ bs project download -i 273727480 -o . --extension=fastq.gz # replace red numbers with your own project

# Merging READ 1 and READ 2 of each sample into one file
$ find . -name "*R1_001.fastq.gz"| sort | paste - - - -
$ find . -name '*R1_001.fastq.gz' -exec mv fastq \;
$ cat sample1_L00*_R1_001.fastq.gz > sample1_R1.fastq.gz
$ cat sample1_L00*_R2_001.fastq.gz > sample1_R2.fastq.gz

$ fastqc *.gz # check quality of your files

# Building kallisto index for HUMAN samples
$ kallisto index -i Homo_sapiens.GRCh38.cdna.all.index
Homo_sapiens.GRCh38.cdna.all.fa

# Mapping paired-end data using kallisto – repeat this code for EVERY sample you have!
$ kallisto quant \ # calling program and function
-i Homo_sapiens.GRCh38.cdna.all.index \ # name and path of index
-o sample1 \ # name of output folder
-t 8 \ # number of threads to use
sample1_R1.fastq.gz \ # name of read 1 fastq file
sample1_R2.fastq.gz \ # name of read 2 fastq file
&> sample1.log # name of resulting log file

# Collate all QC reports into one
$ multiqc .
```

A.2 Pipeline for using DESeq2 in R Studio

This Rmarkdown document was compiled using different sources and is intended for analyzing bulk RNA-seq data that has been processed using pseudoalignment with kallisto. I've written this document with my samples in mind, so please remember to change relevant code chunks to suit your experimental set-up. Please make sure you have all packages installed before running the codes - this can be quite time consuming depending on your machine! NB: I've included the code for ONE comparison to save the space – when looking at multiple comparisons, obviously you will need to repeat certain code chunks.
https://diytranscriptomics.com/
https://www.hadriengourle.com/tutorials/rna/
http://bioconductor.org/packages/devel/bioc/vignettes/DESeq2
https://github.com/hbctraining/DGE_workshop/blob/master/lessons/
https://www.youtube.com/watch?v=tlf6wYJrwKY&list=PLblh5JKOoLUJo2Q6xK4tZElbIvAACEykp (videos to understand basic RNASeq stats)

```
# Set directory and sub files etc
# Load libraries
library("DESeq2")
library("tidyverse")
library("pheatmap")
library("rhdf5")
library("ensembldb")
library("tximport")
library("DT")
library("knitr")
library("EnsDb.Hsapiens.v86") # if using another species install the relevant package
library("RColorBrewer")
```

```
library("gplots")
library("EnhancedVolcano")
library("pathview")
library("clusterProfiler")
library("AnnotationHub")
library("annotables")
library("org.Hs.eg.db")
library("enrichplot")
library("ggpubr")
library("PPInfer")

# Read in metadata file
targets <- read.csv("studydesign4.csv") # metadata file
path <- file.path(targets$sampleID, "abundance.tsv")
rownames(targets) <- targets$sample # this is to make the first row the samplenames

# Read in kallisto output
Tx <- transcripts(EnsDb.Hsapiens.v86, columns=c("tx_id", "gene_name"))
Tx <- as_tibble(Tx)
Tx <- dplyr::rename(Tx, target_id = tx_id)
Tx <- dplyr::select(Tx, "target_id", "gene_name")

Txi_gene <- tximport(path,
                     type = "kallisto",
                     tx2gene = Tx,
                     txOut = FALSE,
                     countsFromAbundance = "lengthScaledTPM",
                     ignoreTxVersion = TRUE)

        TXI-gene[1:10:,:]

# Create DESeq2Dataset object and specify design
dds <- DESeqDataSetFromTximport(Txi_gene, colData=targets, design=~group) dds$group <-
factor(paste0(dds$material, dds$timepoint)) # Group the factors together
design(dds) <- ~ group
keep <- rowSums(counts(dds)) >= 10 # Filter out low count genes
dds <- dds[keep,]
dds <- DESeq(dds)
resultsNames(dds) # Look at what kind of contrasts you have
plotDispEsts(dds, main="Dispersion plot") # Plot dispersion estimates

# Transform counts for data visualisation
rld <- rlog(dds, blind=TRUE)
rld@colData@rownames<-targets$sample
DESeq2::plotPCA(rld, intgroup="group") # Generate PCA plot

rld_mat <- assay(rld) # Extract the rlog matrix from the object
rld_cor <- cor(rld_mat) # Compute pairwise correlation values (Pearson coefficient)

# Plot additional PCs - input is a matrix of log transformed values
pca2 <- prcomp(t(rld_mat))
df <- cbind(targets, pca2$x)
ggplot(df) + geom_point(aes(x=PC1, y=PC2, color = group)) #pick whichever PCs you want to plot

# Generate screeplot
rv <- rowVars(assay(rld)) # calculate the variance for each gene
select <- order(rv, decreasing=TRUE)[seq_len(min(500, length(rv)))] # select the ntop genes by
variance
pca <- prcomp(t(assay(rld)[select,])) # perform a PCA on the data in assay(x) for the selected genes
percentVar <- pca$sdev^2 / sum( pca$sdev^2 ) # the contribution to the total variance for each
component
scree_plot=data.frame(percentVar)
scree_plot[,2]<- c(1:24)
colnames(scree_plot)<-c("variance","PC")
scree_plot<-ggplot(scree_plot, mapping=aes(x=PC, y=variance))+geom_bar(stat="identity")

# Plot heatmap (sample-sample distance)
colnames(rld_cor) <- paste( rld$sample, sep="-")
rownames(rld_cor) <- paste( rld$sample, sep="-")

sample1_meta <- targets %>%
  rownames_to_column(var="samplename") %>%
  as_tibble()
```

```
annotation <- sample1_meta %>%
     dplyr::select(samplename, material, timepoint) %>%
     data.frame(row.names = "samplename")

pheatmap(rld_cor, annotation=annotation)

# Create sample-sample heatmap
sampleDists <- dist(t(assay(rld))) #calculates Euclidean distance. Rld to ensure we have a roughly
equal contribution from all genes
sampleDistMatrix <- as.matrix( sampleDists )
rownames(sampleDistMatrix) <- paste( rld$material, rld$timepoint, sep = " - " )
colnames(sampleDistMatrix) <- NULL
colors <- colorRampPalette( rev(brewer.pal(9, "Blues")) )(255)
pheatmap(sampleDistMatrix,
          clustering_distance_rows = sampleDists,
          clustering_distance_cols = sampleDists,
          col = colors)

# Generate cluster dendogram
library(matrixStats)
o <- order(rv,decreasing=TRUE)
dists <- dist(t(assay(rld)[head(o,500),]))
hc <- hclust(dists)
plot(hc, labels=rld$sample)
plot(hc, labels=rld$group)
distd <- dist(t(assay(rld)[head(o,500),]))
hc <- hclust(distd)
dend <- as.dendrogram(hc)

# Output results of Wald test for contrast - the second variable will be the baseline that is compared
against
res <- results(dds,alpha = 0.05)
res1 <- results(dds, contrast=c("group","electrospunfourteen","fiberwirefourteen"),alpha = 0.05)

# Look at the number of DEGs per contrast
summary(res)

# Apply shrinkage per contrast
res_shrink<-lfcShrink(dds, res=res, type="ashr") #apply shrinkage, note I'm using "ashr" instead of
"apeglm"

res1_shrink <- lfcShrink(dds, contrast=c("group","electrospunfourteen","fiberwirefourteen"), res=res1,
type="ashr")

# Generate MA plots
par(mfrow=c(2,2))
DESeq2::plotMA(res_shrink, ylim=c(-2,2), main = "MA plot - overall")
DESeq2::plotMA(res1_shrink, ylim=c(-2,2), main = "ES 14 vs FW 14")

# Genenerate volcano plot per contrast
vp1<-EnhancedVolcano(res1,
    lab = rownames(res1),
    x = 'log2FoldChange',
    y = 'pvalue',
    title = "ES 14 vs FW 14",
    titleLabSize = 12,
    xlim =c(-10,10), #makes all graphs equal in x axis
    subtitle = NULL,
    caption = NULL) # if this isn't set, EnhancedVolcano will by default put a subtitle here

# Arrange volcano plots in a grid
ggarrange(vp2, vp4, vp1, vp7,
          labels = c("A", "B", "C", "D"),
          #ncol = 2,
          common.legend = TRUE, legend = "bottom")

# Set cut off values
padj.cutoff <- 0.05
lfc.cutoff <- 1

# Convert results PER contrast into tibble
res_shrink_tb <- res_shrink %>%
  data.frame() %>%
  rownames_to_column(var="gene") %>%
```

```
  as_tibble()

res1_shrink_tb <- res1_shrink %>%
  data.frame() %>%
  rownames_to_column(var="gene") %>%
  as_tibble()
# Keep significant genes only
sigRes <- res_shrink_tb %>%
        dplyr::filter(padj < padj.cutoff & abs(log2FoldChange) > lfc.cutoff)

# Normalized counts
normalized_counts <- counts(dds, normalized=TRUE)
colnames(normalized_counts) <- rownames(targets)

normalized_counts <- normalized_counts %>%
  data.frame(check.names=FALSE) %>%
  rownames_to_column(var="gene") %>%
  as_tibble()

# Extract top 20 genes PER CONTRAST
top20_sigRes_genes <- res_shrink_tb %>%
        arrange(padj) %>%   #Arrange rows by padj values
        pull(gene) %>%      #Extract character vector of ordered genes
        head(n=20)      #Extract the first 20 genes

top20_sigRes_genes1 <- res1_shrink_tb %>%
        arrange(padj) %>%   #Arrange rows by padj values
        pull(gene) %>%      #Extract character vector of ordered genes
        head(n=20)      #Extract the first 20 genes

# Extract normalized counts for top 20 significant genes
top20_sigRes_norm <- normalized_counts %>%
        dplyr::filter(gene %in% top20_sigRes_genes)

top20_sigRes_norm1 <- normalized_counts %>%
        dplyr::filter(gene %in% top20_sigRes_genes1)

# Gathering the columns to have normalized counts to a single column
gathered_top20_sigRes <- top20_sigRes_norm %>%
  gather(colnames(top20_sigRes_norm)[2:25], key = "samplename", value = "normalized_counts") #for all
samples

# Specify which columns are of interest for the specific contrast
gathered_top20_sigRes1 <- top20_sigRes_norm1 %>%
  gather(colnames(top20_sigRes_norm1)[c(3,5,9,11,15,17,21,23)], key = "samplename", value =
"normalized_counts")
# Join two metaframes
gathered_top20_sigRes_joined <- inner_join(sample1_meta, gathered_top20_sigRes)

gathered_top20_sigRes1_joined <- inner_join(sample1_meta, gathered_top20_sigRes1)

# Plot DEGs per  contrast
top20<-ggplot(gathered_top20_sigRes_joined) +
        geom_point(aes(x = gene, y = normalized_counts, color = group)) +
        scale_y_log10() +
        xlab("Genes") +
        ylab("log10 Normalized Counts") +
        ggtitle("Top 20 Significant DE Genes - overall") +
        theme_bw() +
    theme(axis.text.x = element_text(angle = 45, hjust = 1)) +
    theme(plot.title = element_text(hjust = 0.5))

top20_1<-ggplot(gathered_top20_sigRes1_joined) +
        geom_point(aes(x = gene, y = normalized_counts, color = group)) +
        scale_y_log10() +
        xlab("Genes") +
        ylab("log10 Normalized Counts") +
        ggtitle("Top 20 Significant DE Genes - ES14 vs FW14") +
        theme_bw() +
    theme(axis.text.x = element_text(angle = 45, hjust = 1)) +
    theme(plot.title = element_text(hjust = 0.5))
```

```
# Arrange plots into a grid
ggarrange(top20, top20_1, top20_2, top20_4,
          labels = c("A", "B", "C", "D"))

# Generate heatmap from DEGs
normalized_counts <- normalized_counts[which(duplicated(normalized_counts$gene) == FALSE),]
norm_sig <- normalized_counts
norm_sig <- data.frame(norm_sig)
norm_sig <- norm_sig %>%
  filter(normalized_counts$gene %in% sigRes$gene) %>%
  data.frame(check.names = FALSE)

column_to_rownames(norm_sig, var = "gene")
rownames(norm_sig) <- norm_sig$gene

sample1_meta <- targets %>%
  rownames_to_column(var="samplename") %>%
  as_tibble()

annotation <- sample1_meta %>%
     dplyr::select(sample, material, timepoint) %>%
     data.frame(row.names = "sample")

heat_colors <- brewer.pal(9, "YlOrRd")

pheatmap<-pheatmap(norm_sig[ ,2:length(colnames(norm_sig))],
         color = heat_colors,
         cluster_rows = T,
         show_rownames = F,
         annotation = annotation,
         border_color = NA,
         fontsize = 10,
         scale = "row",
         fontsize_row = 10,
         height = 20)

# Generate top 20 genes heatmap
pheatmap50<-pheatmap(top20_sigRes_norm[ ,2:length(colnames(top20_sigRes_norm))],
         color = heat_colors,
         cluster_rows = T,
         show_rownames =T,
         labels_row=rownames(top20_sigRes_norm), #if this shows up numeric, make sure to subset the
rownames first: rownames(top20_sigRes_norm) <- top20_sigRes_norm$gene
         annotation = annotation,
         border_color = NA,
         fontsize = 10,
         scale = "row",
         fontsize_row = 10,
         height = 20)

# Return the IDs for the gene symbols in the DE results. Note I'm using grch38 here but there are also
other versions!
idx <- grch38$symbol %in% rownames(res_shrink)
ids <- grch38[idx, ]

idx_1 <- grch38$symbol %in% rownames(res1_shrink)
ids_1 <- grch38[idx, ]

# Gene names can map to more than one Ensembl ID, so remove duplicates
non_duplicates <- which(duplicated(ids$symbol) == FALSE)
ids <- ids[non_duplicates, ]

non_duplicates <- which(duplicated(ids_1$symbol) == FALSE)
ids_1 <- ids_1[non_duplicates, ]

# Merge the IDs with the results
res_ids <- inner_join(res_shrink_tb, ids, by=c("gene"="symbol"))
res1_ids <- inner_join(res1_shrink_tb, ids_1, by=c("gene"="symbol"))

# Create background dataset for hypergeometric testing using all genes tested for significance in the
results
allSig_genes <- as.character(res_ids$ensgene)

# Extract significant results
```

```
sig <- dplyr::filter(res_ids, padj < 0.05) #if no genes are returned in EGO, then this cut-off can be
changed. Usually set at 0.05.
sig_genes <- as.character(sig$ensgene)

sig1 <- filter(res1_ids, padj < 0.05)
sig_genes1 <- as.character(sig1$ensgene)

# GO pathway analysis
ego <- enrichGO(gene = sig_genes,
                universe = allSig_genes,
                keyType = "ENSEMBL",
                OrgDb = org.Hs.eg.db,
                ont = "BP",
                pAdjustMethod = "BH",
                qvalueCutoff = 0.05, #change if no genes! Normally at 0.05
                readable = TRUE)

ego1 <- enrichGO(gene = sig_genes1,
                universe = allSig_genes,
                keyType = "ENSEMBL",
                OrgDb = org.Hs.eg.db,
                ont = "BP",
                pAdjustMethod = "BH",
                qvalueCutoff = 0.05,
                readable = TRUE)


# Output results from GO analysis to a table
cluster_summary <- data.frame(ego2)
write.csv(cluster_summary, "results/clusterProfiler_ego2.csv")

 # Generate dotplots and arrange them in a grid
dp2<-dotplot(ego2, showCategory=25, title="ES14 vs ES0")

ggarrange(dp2, dp4,
          labels = c("A", "B"),
          common.legend = TRUE, legend = "bottom")

# Prepare count matrix for GSEA

res_entrez1 <- filter(res1_ids, entrez != "NA") # Remove any NA values
res_entrez1 <- res_entrez1[which(duplicated(res_entrez1$entrez) == F), ] # Remove any Entrez
duplicates
foldchanges1 <- res_entrez1$log2FoldChange # Extract the foldchanges
names(foldchanges1) <- res_entrez1$entrez # Name each fold change with the corresponding Entrez ID
foldchanges1 <- sort(foldchanges1, decreasing = TRUE) # Sort fold changes in decreasing order

# GSEA using gene sets from KEGG pathways
gseaKEGG1 <- gseKEGG(geneList = foldchanges1, # ordered named vector of fold changes (Entrez IDs are
the associated names)
              organism = "hsa", # supported organisms listed below
              #nPerm = 1000, # default number permutations
              minGSSize = 20, # minimum gene set size (# genes in set) - change to test more sets or
recover sets with fewer genes
              pvalueCutoff = 0.05, # padj cutoff value --> change this if no enriched genes, default
is 0.05
              verbose = FALSE)

#Extract results and write them to file
gseaKEGG_results1 <- gseaKEGG1@result

write.csv(gseaKEGG_results2, "results/gsea_2_kegg.csv", quote=F)

# Generate plots for GSEA output and arrange them

GSEA.bp2<-GSEA.barplot(gseaKEGG_results2, category = 'Description', score = 'NES',
             pvalue = 'pvalue', sort = 'NES', decreasing = TRUE, title="ES14 vs ES0")

ggarrange(GSEA.bp2, GSEA.bp4,
          common.legend = TRUE, legend = "top")
```

Appendix B. Pathway analysis method

Pathway analysis was done in two ways. The first step was to perform an over-representation analysis (ORA) using the Gene Ontology (GO) database, which contains information on genes and interactions and is based on *in silico* data (i.e., via computer simulations) or confirmed laboratory experimental evidence. It categorizes genes based on shared functions or pathways for many kinds of organisms and determines whether any category is over-represented, i.e., enriched, in a list of experimentally derived DEGs. It classifies relationships between genes according to three different vocabularies (ontologies): molecular function (MF), cellular component (CC) or biological process (BP) and annotates genes accordingly. ORA is performed using a hypergeometric distribution to calculate the p-value (also known as the Fisher's exact test). Briefly, the probability of the number of genes in the DEGs list that is associated with a category is determined based on the number of genes associated with the same category in the background set – relating to the specific organism. This gives the following equation – which is used to calculate the adjusted p-value (p) for each category:

$$p = \frac{\left(\frac{k}{n}\right)\left(\frac{N-K}{n-k}\right)}{\left(\frac{N}{n}\right)}$$

N = total number of genes in the organism's specific genome (background set)
n = total number of genes in the list of DEGs (experimental set)
K = probability of x number of genes in N associated with category A
k = probability of x number of genes in n associated with a category A

The GSEA method is based on a weighted Kolmogorov–Smirnov-like statistic: briefly, a list of genes is the output of the DESeq2 analysis. This list gets ranked according to fold change by GSEA. Then, the distribution of genes across this list is assessed by walking down the list and using a running-sum statistic: this means that the statistic value increases when a gene in the list is found that belongs to a certain set and it decreases when it does not, see Figure B.1.

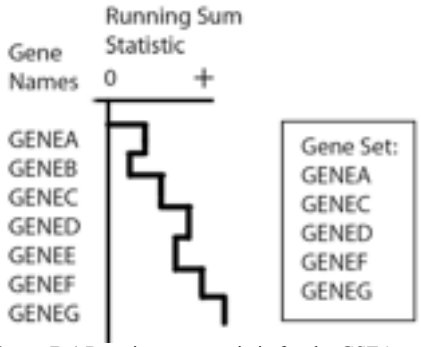

Figure B.1 Running-sum statistic for the GSEA method.

During this 'walk' through the list, the maximum deviation from zero is also calculated which is called the enrichment score (ES): this reflects how far removed a gene is from the top or bottom of a list. If a gene set is not enriched, then those specific genes will be spread through the list uniformly (the null hypothesis), but if it is enriched then these genes will largely be either at the top or bottom of the list. Then, the p-values for the ES are calculated and adjusted for multiple hypothesis testing by normalizing the ES for each gene set: the number of false positives is controlled by calculating the false discovery rate (FDR) and the result is a normalized enrichment score (NES). A negative NES means that the genes belonging to that set will be mostly at the bottom of the list and a positive NES means the opposite. The closer the score is to 0, the more uniformly genes in each gene set are distributed through the list.

Appendix C. Measurements for prototypes

Table C.1 Specifications of measurements obtained from the literature study. All measurements are given in mm.

	Specimen information	**M-L**	**A-P**	**S-I**	**CSA**	**Shape**
Curtis (*449*)	**Age:** unknown **N**: sex unknown, 26 fresh frozen cadaveric shoulders **NB**: specimens with rotator cuff tearing or osteophytic changes were excluded	12-21	18-33			trapezoidal
Rickert (*290*)	**Age**: 23-94 **N:** 18 male and 7 female, 25 fresh frozen cadavers **NB:** articular or bursal partial-thickness tears were excluded		22.1 ± 3.3	3.30 ± 0.97; 2.59 ± 0.99; 2.21 ± 1.04		
Lumsdaine (*450*)	**Age**: 49 - 96 (range) **N**: 15 male and 12 female, 43 embalmed cadavers **NB:** Australian Caucasoid donors, no "pre-mortem anatomical disruption"	6.7 ± 2.6	20.9 ± 3.9 (medial) 6.4 ± 1.5 (lateral)		122 ± 66.6	triangular
Mochizuki (*16*)	**Age:** 77.3 (average) **N**: 25 males and 39 females, 113 cadaveric shoulders fixed in 8% formalin and preserved in 30% ethanol **NB:** Japanese donors	6.9 ± 1.4	12.6 ± 2.0		43.5	triangular
Sessions (*451*)	**Age**: 59 - 101 (range) **N:** 11 male and 10 female, 21 embalmed cadaveric shoulders **NB:** no direct rotator cuff pathology			4.9 ± 2.1		
Volk (*452*)	**Age**: 48-76 (range) **N**: 10 male, 10 female, 20 embalmed cadavers **NB:** no rotator cuff tears	42–77; 20-37				
Kim (*458*)	**Age**: 61.9 ± 16 (mean) **N:** 10 male, 10 formalin embalmed cadaveric specimens **NB:** "no evidence of rotator cuff pathology"	61.0 ± 7.0; 29.0 ± 6.0	8.0 ± 2.0; 16.0 ± 3.0			cord-like; quadrangular
Roh (*453*)	**Age**: 82 (mean) **N:** 10 male and 15 female, 25 embalmed shoulders **NB:** intact supraspinatus muscle and tendon was harvested from each specimen		8.4 ± 2.1; 12.8 ± 2.8	3.1 ± 0.7; 2.5 ± 0.7	26.4±11.3; 31.1±10.1	
Dugas (*21*)	**Age**: 48-88 (range) **N:** 20 fresh frozen cadaveric upper-extremity specimens **NB**: "no evidence of previous shoulder surgery or visible gross shoulder abnormality. No rim rents or craters"	12.7 ± 63	16.3 ± 0.6		155 ± 66	
Ruotolo (*454*)	**Age**: 70 (average) **N:** 17 cadaver shoulders **NB:** no partial- or full-thickness tears	11.6±1.84	25.2 ± 2.4			
Nimura (*455*)	**Age**: 77.3 (average) **N:** 2 males and 4 females, 12 cadaveric shoulders fixed in 8% formalin and preserved in 30% ethanol **NB:** Japanese cadavers	3.5±2.3; 7.6±1.9				triangular
Itoi (*288*)	**Age**: 56-69 (range) **N**: 5 male and 6 female, 11 fresh frozen cadaver shoulders **NB:** no partial- or full-thickness tears		7.4 ± 0.7; 7.0 ± 1.2; 7.5 ± 1.2	3.5 ± 0.5; 3.6 ± 0.7; 2.9 ± 0.5	25.5 ± 4.3; 24.7 ± 5.8; 21.9 ± 5.3	

Itoi (*287*)	**Age**: 64-96 **(**range) **N**: 41 embalmed cadaveric shoulders **NB:** the measurements of the 11 shoulders with intact rotator cuffs are presented in this table	18.2 ± 2.8	15.3 ± 3.0	2.2 ± 0.4	70 ± 20	
Matsuhashi (*289*)	**Age**: 68.3 ± 15.0 (mean) **N**: 3 male and 4 female; 7 freshly frozen cadaveric specimens **NB**: no "disease of the shoulder detectable by direct inspection or radiograms"		13.3 (0.9); 15.8 (1.5)	4.8 ± 0.8; 2.7 ± 0.4	50.3 ±9.1; 32.8 ±4.9	
Smith (*178*)	**Age**: 60-93 (range) **N**: 5 fresh frozen cadaveric specimens **NB**: "no macroscopic signs of tissue damage"			2.0 ± 0.33		
Naidoo (*456*)	**Age**: 54-94 (range) **N**: 24 male and 16 female, 40 cadaveric specimens **NB**: "38 white and 2 black individuals"	20.1 ± 5.4	15.2 ± 4.3			rectangular (76.3%); round (23.8%)
Minagawa (*20*)	**Age**: 54-92 (range) **N**: 4 male and 5 female, 10 embalmed shoulders **NB**: "without rotator cuff tears or any other abnormalities of soft tissue/bony str uctures"		22.5 ± 3.1			
	Age range: 23 - 101	**3.5 - 61**	**6.4 - 25.2**	**2.0 - 4.9**	**21.9 - 155**	

Appendix D. Additional figures Chapter 4

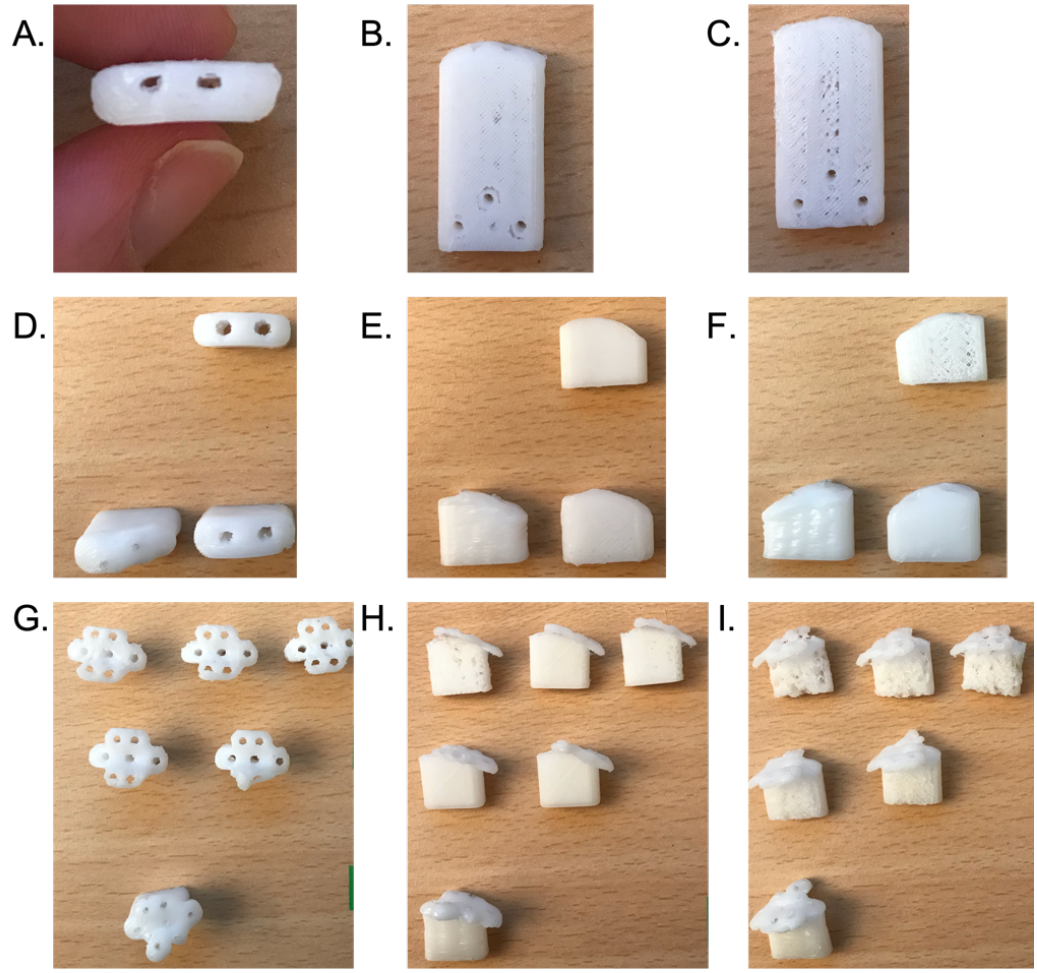

Figure D.1 Printing of the scaffolds in various tries with a top view (A, D, G), lateral view of the bottom layer (B, E, H) and lateral view of the top layer (C, F, I).

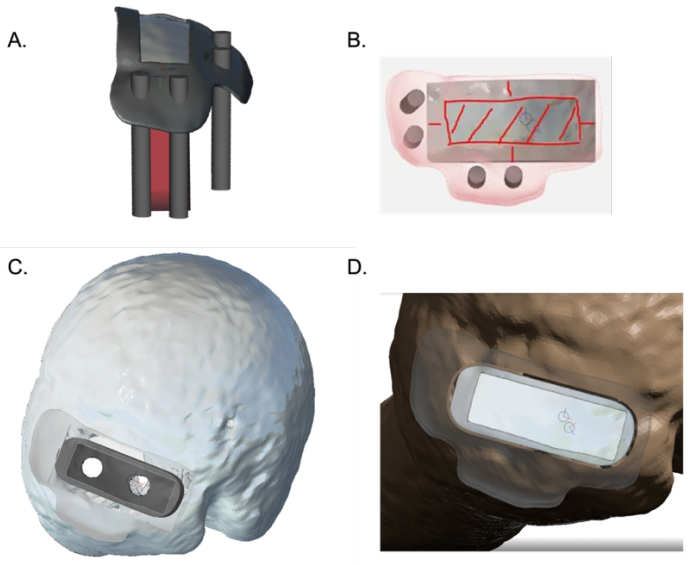

Figure D.2 Printing of the scaffold with the metal casing (A) resulted in a larger sized block (grey area in B compared to the red shaded area of the original size), to secure the implant within the GT (C and D).

Appendix E. Automation of the current manufacturing process

A project by **Alexander Witt** (MSc student) conducted as an internship funded by the Engineering and Physical Sciences Research Council (EPSRC).

E.1 First design concept

Figure E.1 shows the first overall concept with two key subsections: the fibre spool [1] and the fibre guide, with its associated supports ([2] and [3]). The spool is free to rotate about its own support and feeds the fibres through the guide. It logically follows that the fibres need to be guided onto the print surface accurately and quickly, while also not placing them under too much tension to prevent damage. To achieve this, a smooth walled guide was designed which acted in a similar fashion to a guillotine. Figures E.1B and C show the entry and exit points for the fibres, as well the system of servos that are designed to hold and cut the fibres once they have been drawn across the printing surface. The intention for the spool guides was to move the spool along its support without having to motorise that process, increasing the simplicity and guaranteeing accuracy. In Figure E.1D the fibre guide is mounted to the print bed, with an extra servo that was required to raise the lower arm off the level of the print bed when the fibre carriage system returns to collect more fibres. The fibre carriage itself would use a system of motorised springs and strings to move across the print bed (not shown), and a pair of servos to actuate the gripping function and move it vertically.

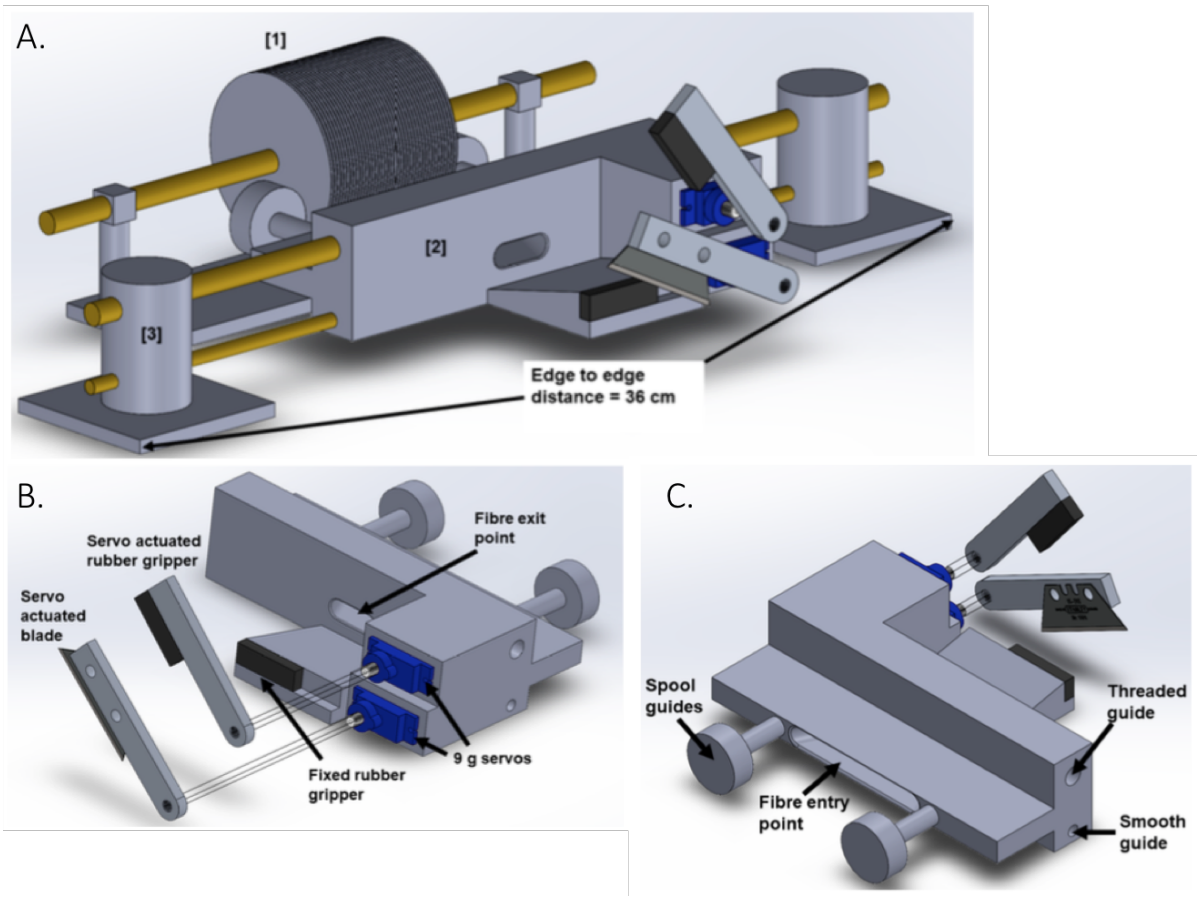

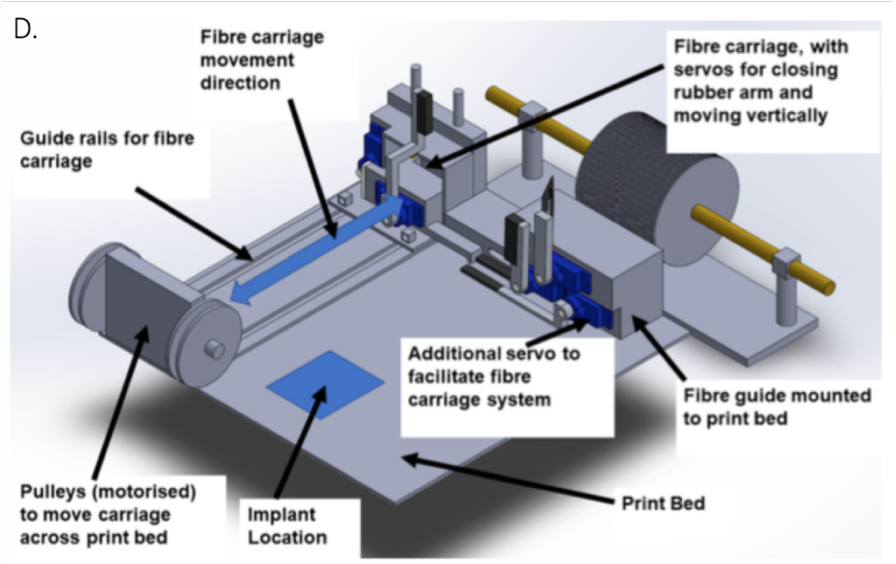

Figure E.1 First design with a diagram illustrating the overall initial concept (A): [1] fibre spool, [2] fibre guide and [3] motorised guide supports. An exploded frontal diagram of the fibre guide with labelled components in B and exploded rear diagram with remaining components labelled in C. The fibre guide mounted to the printing bed is pictured in D.

E.2 Second design concept

This second concept was postulated as a method of fixing a roll of fibres and then rotating a set of forks to collect the fibres, before laying them onto the print bed using a system of bearings (Figure E.2).

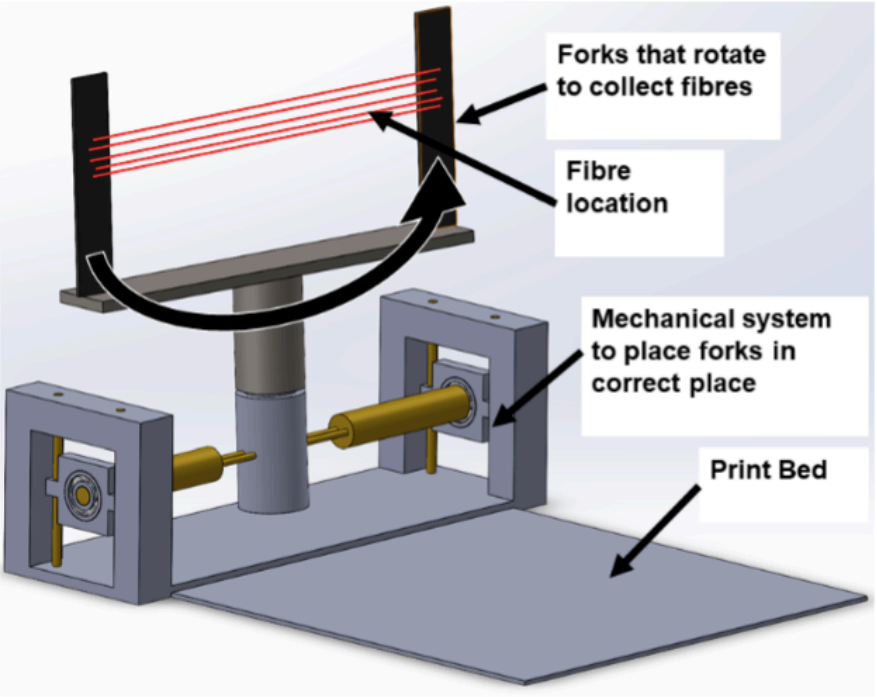

Figure E.2 Second design concept

E.3 Third design concept

Figure E.3 shows the overall extruder assembly in place on the 3D printer frame, with the original FDM printer head visible for scale. There is a reliance on maintaining tension across the print bed to ensure correct printing of the scaffold. Therefore, a system of laying down double-sided tape around the perimeter of the print bed onto which the fibres can be pressed

was chosen to achieve this. Figure E.3B shows a top down view of the extruder assembly into which the fibres would be fed. There are a pair of rubber rollers, much like a treadmill, to facilitate the fibres being drawn onto the print bed. The passive roller can be moved back and forth to allow the fibres to be loaded at the beginning of each period of printing. The driven roller is driven by the same motor used on the Prusa MK3S that the concept is designed around. Figure E.3C shows the fibre nozzle through which the fibres are drawn. This has a leaf spring which enables it to be pressed into the surface without damaging it. There is then a servo operated cutting element which would be a heated tungsten wire, much like a filament light bulb, to slice the fibres to length. Since this method of moving fibres across the print bed is governed by the speed at which the print head can move, this would mean that the top surface of the scaffold would no longer be tacky for every fibre. This means that heating elements would be required to re-melt the top surface to enable fibre adhesion. There are four of these to enable fibres to be laid in all directions, and can be moved up and down using servos, so as not to interfere with the fibre laying process.

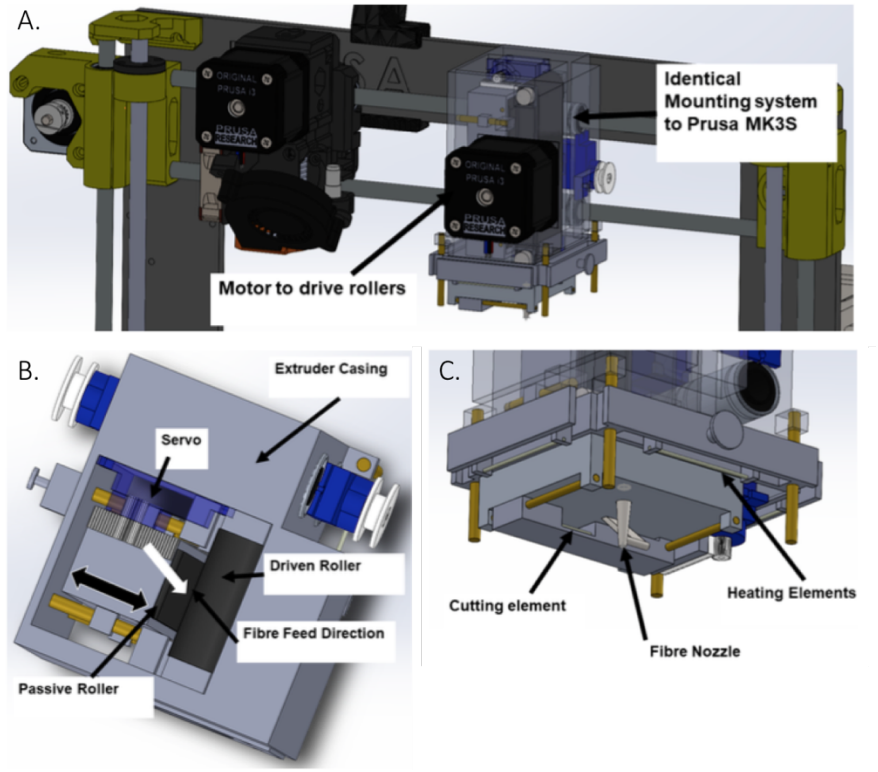

Figure E.3 Third design concept with the extruder assembly in place with the standard head visible for scale (A), a top down view of the extruder assembly (B) and a diagram of the fibre laying section (C).